Development of Multifunctional Polyphenolic Coatings for Improved Peri-Implant Healing

A Doctoral Thesis by
Florian Weber

Department of Biomaterials
Institute of Clinical Dentistry
Faculty of Dentistry
University of Oslo
Norway

Series of dissertations submitted to the
Faculty of Dentistry, University of Oslo

ISBN 978-82-8327-056-3

Cover: Hanne Baadsgaard Utigard.
Print production: Reprosentralen, University of Oslo.

"If your experiment needs statistics, you ought to have done a better experiment."

— Ernest Rutherford

Acknowledgments

I would like to thank Professor Håvard J. Haugen for the opportunity to follow my PhD program at the Department of Biomaterials. Without the welcoming environment during my master's internship, I would not have continued my research at this department. Further, I would like to thank Professor Janne E. Reseland, Head of the Oral Research Laboratory, for providing an open and unrestricted working environment.

During my time as a PhD candidate, I was able to join many interesting seminars, research schools, and conferences. Many thanks to everyone at the Digital Life Norway Research School. I am very grateful to have received all of the financial and scientific support to be part of them.

Speaking of scientific support, I specially have to thank my supervisors, Hanna Tiainen and Alejandro Barrantes. Their ability to set up and manage a proper project was a key element for the work that has been achieved. Despite having a specific goal, I could always follow my own ideas and interests for which I am very grateful. Throughout all the years in the lab, we have also grown together socially and it has been a great time. Without a doubt, I will miss International Lunches, gym sessions, and most of all the Friday Sauna Club. I would not have survived without the last one.

It is needless to say that all of the work was not only a burden on my shoulders, so thank you to each of the coauthors who contributed to the project. Particularly, I acknowledge Wei-Chi Liao and Mattias Edén, for their patience with typesetting, Einar Sagstuen for his endless knowledge about radicals, Qi-Zhi Zong for his AFM skills, Louise Dornelas for teaching me how to work with fungi, and Quang Huy Quach for his seemingly endless work effort. Further, I acknowledge all students who were subjected to repetitive tasks and thereby contributed with their results to this project.

To all my colleagues in the Biomaterials Group, thank you for being part of this special period of my life. I hope to stay in contact and meet with you again in future. Since I was lucky to spend some time at other institutes, I thank Marité Cardenas for her help with neutron reflectometry, Pentti Tengvall for support with ellipsometry, and Bryan Coad for having me over in Adelaide. Thanks to all the people I have met abroad. It was a truly memorable time and an experience I will carry with me for life.

Finally, I want to thank my family and friends for their support. I know I complained a lot but in the end, I have no regrets.

Florian Weber
Oslo, June 2021

Preface

This thesis is submitted in partial fulfillment of the requirements for the degree of *Philosophiae Doctor* at the University of Oslo. The research presented here was conducted at the University of Oslo, under the supervision of Associate Professor Hanna Tiainen and Doctor Alejandro Barrantes.

The thesis is a collection of five papers, presented in chronological order of writing. The papers are preceded by an introductory chapter that provides the motivation for the work and background information on titanium dental implants, tissue integration, and oral infections. After an outline of the research structure together with its aims and hypothesis, the methodological considerations are described to give the rationality of experiments employed in this thesis. Succeeding, the main results of the studies are summed up, discussed, and put into context with the general hypothesis. Finally, concluding remarks are drawn and an outlook to future perspectives is given.

List of Papers

Paper I **Silicic Acid-Mediated Formation of Tannic Acid Nanocoatings**

Florian Weber, Alejandro Barrantes, and Hanna Tiainen.
Published in: *Langmuir*, **2019**, Vol. 35(9), pp. 3327–3336. DOI: 10.1021/acs.langmuir.8b04208.

Paper II **Silicate-Phenolic Networks: Coordination-Mediated Deposition of Bioinspired Tannic Acid Coatings**

Florian Weber, Wei-Chih Liao, Alejandro Barrantes, Matthias Edén, and Hanna Tiainen.
Published in: *Chemistry – A European Journal*, **2019**, Vol. 25, pp. 9870–9874. DOI: 10.1002/chem.201902358.

Paper III **Tannic Acid Radicals in the Presence of Alkali Metal Salts and Their Impact on the Formation of Silicate-Phenolic Networks**

Florian Weber, Einar Sagstuen, Qi-Zhi Zong, Tian Zheng, and Hanna Tiainen.
Published in: *ACS Applied Materials & Interfaces*, **2020**, Vol. 12 (47), pp. 52457–52466. DOI: 10.1021/acsami.0c16946.

Paper IV **Anti-Inflammatory Properties and Innate Immune Response towards Polyphenolic Coatings for Titanium Dental Implants**

Florian Weber, Quang Huy Quach, Mathias Reiersen, Sadaf Yosef Sarraj, Dyala Bakir, Victor Aleksander Jankowski, Per H. Nilsson, Hanna Tiainen.
Submitted manuscript, **February 2021**.

Paper V **Polyphenolic Surface Modifications for the Prevention of Fungal Colonization of Titanium Dental Implants**

Florian Weber, Louise Morais Dornelas-Figueira, Nora Hafiane, Alejandro Barrantes, Fernanda Cristina Petersen, Hanna Tiainen.
Prepared manuscript.

Table of Contents

Acknowledgments iv

Preface v

List of Papers vi

Table of Contents vii

List of Figures ix

1 Introduction 1
- 1.1 Dental implants . . . 1
- 1.2 Tissue integration and wound healing . . . 2
- 1.3 Inflammation and infectious diseases around dental implants . . . 5
- 1.4 Strategies to improve host tissue integration . . . 7
- 1.5 Polyphenols . . . 9

2 Research Concept 15
- 2.1 Aims and hypothesis . . . 15
- 2.2 Research structure . . . 15

3 Experimental Considerations 17
- 3.1 Preparation of modified surfaces . . . 17
- 3.2 Characterization of the polyphenolic coating process . . . 19
- 3.3 Analysis of the surface chemistry . . . 24
- 3.4 Polyphenolic radical formation . . . 28
- 3.5 Protein interactions with polyphenolic surfaces . . . 29
- 3.6 Blood compatibility . . . 31
- 3.7 Cellular response . . . 32
- 3.8 Adhesion and biofilm formation of *Candida albicans* . . . 34

4 Summary of Key Findings 37
- 4.1 Chemistry of polyphenolic coatings . . . 37
- 4.2 Biological response . . . 38

5 Discussion 39
- 5.1 Formation and characterization of polyphenolic coatings . . . 39
- 5.2 Effect of polyphenolic coatings on wound healing . . . 42
- 5.3 Can polyphenolic coatings prevent peri-implant infections? . . . 44

6 Concluding Remarks 47

Glossary **49**

Bibliography **53**

A Appendix **73**

Papers **82**

I Silicic Acid-Mediated Formation of Tannic Acid Nanocoatings **83**

II Silicate-Phenolic Networks: Coordination-Mediated Deposition of Bioinspired Tannic Acid Coatings **115**

III Tannic Acid Radicals in the Presence of Alkali Metal Salts and Their Impact on the Formation of Silicate-Phenolic Networks **141**

IV Anti-Inflammatory Properties and Innate Immune Response towards Polyphenolic Coatings for Titanium Dental Implants **185**

V Polyphenolic Surface Modifications for the Prevention of Fungal Colonization of Titanium Dental Implants **223**

List of Figures

1.1 Endosseous titanium dental implants . . . 2
1.2 Phases of wound healing . . . 3
1.3 Activation pathways of complement and coagulation system . . . 4
1.4 The role of cytokines and signaling pathways in inflammation . . . 6
1.5 Strategies for bioactive surface modifications . . . 9
1.6 Classification of polyphenolic molecules . . . 10
1.7 The structure of polyphenols used in this work . . . 11
1.8 Reaction chemistry of polyphenols . . . 12
1.9 Adhesion of polyphenols on titanium surfaces . . . 13
1.10 Polymerization and coating formation of polyphenols . . . 14

2.1 Research concept . . . 16

3.1 Deposition of polyphenolic coatings . . . 18
3.2 The QCM–D setup to monitor the coating formation . . . 20
3.3 Principle of QCM–D and NPS technology . . . 21
3.4 Analysis of free radicals by EPR . . . 29
3.5 Schematic setup of experiments with blood . . . 31
3.6 Schematic setup of experiments with *C. albicans* . . . 35

5.1 Structure of silicate–TA networks and PG polymers . . . 40

6.1 TA coated dental implant . . . 48

A1 Batch-to-batch variation of tannic acid . . . 73
A2 Buffer compatibility for the deposition of TA coatings . . . 74
A3 Neutron reflectometry data . . . 75
A4 Layer properties and their effect on neutron reflectometry . . . 76
A5 TOF-SIMS coating analysis . . . 77
A6 MALDI-TOF coating analysis . . . 78
A7 Raman coating analysis . . . 79
A8 Radial diffusion antioxidant capacity assay . . . 79
A9 SDS-PAGE of salivary proteins . . . 80

Chapter 1

Introduction

Good oral health is important for the quality of life of every person. However, the quality of live can be significantly impaired by tooth loss.[1] Patients with missing teeth often report loss of phonetic function, eating disability, and social stigma.[2] Tooth loss can occur through either trauma or oral diseases such as caries, periodontitis, and cancer. Oral diseases are one of the most common public health issues, affecting around 3.5 billion people worldwide.[3] Caries and periodontal diseases are the most prevalent conditions which can lead to tooth loss in severe cases.[4] It is estimated that about 10 % of the European population suffer from severe periodontal diseases.[5] Historically, bridges have been used to restore aesthetics, masticatory and phonetic function after tooth loss. Nowadays, the placing of dental implants has become more popular due to the high success rate of 95 %.[6] Therefore, the global market for dental implants is currently estimated to be worth $5 billion and predicted to grow even further.[7] In Norway, 15 000 dental implants were placed annually in the period from 2014 to 2017.[8] This frequent use of dental implants highlights their importance in the current clinical treatment of tooth loss.

1.1 Dental implants

The development of modern dental implants started in the early 20$^{\text{th}}$ century, although it took until 1965 before the first titanium dental implant was placed by Brånemark.[9,10] Today, there are many types of implants produced by different manufacturers. Despite differences in the implant design, a fundamental build-up is commonly shared as depicted in **Figure 1.1**. Simplified, endosseous implants consist of an implant body, an abutment, and a crown. The implant body is anchored in the jawbone and provides a firm base for the crown. The crown is connected to the implant via the abutment. Depending on the implant design, either the implant body (tissue level implant), or the abutment (bone level implant) is in contact with the gingival soft tissue.

Titanium (Ti) has become very popular as biocompatible implant material due to its good mechanical properties and corrosion resistance.[11–13] Titanium and its alloys provide sufficient mechanical strength compared to noble metals, such as gold, and are less brittle than ceramics.[14,15] The excellent biocompatibility of Ti originates from the TiO, TiO_2, and Ti_2O_3 containing oxide layer, which forms at the metallic Ti surface instantly upon contact with air or water.[16] This passivation layer is the reason for corrosion resistance of Ti implants and their minimal release of metal ions into the surrounding tissue.[17] The biocompatibility of Ti as an implant material is also manifested in a low foreign body reaction.[18] Specifically the absence of fibrous encapsulation enables the close contact of titanium with bone, which is an inevitable requirement for a firm placement of dental implants.[11,19] These properties led to the definition of *osseointegrated* implants.[10,20]

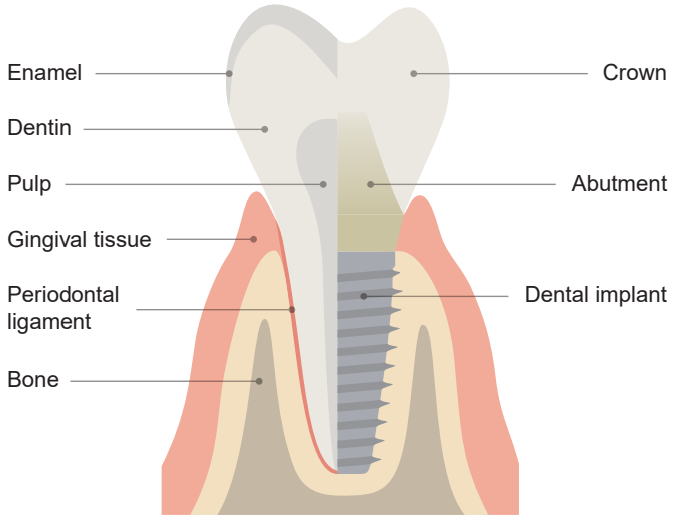

Figure 1.1: The endosseous titanium dental implant consists of three parts to replace natural tooth. In comparison to an intact tooth, the implant body is in direct contact with bone. The visible part of the restoration, the crown, is fixed to the implant via the abutment. Depending on the implant design, either abutment or the top part of the implant is in contact with the gingival soft tissue.

1.2 Tissue integration and wound healing

Placing the implant in the prepared jawbone marks the start of the foreign body reaction. This host response to foreign objects affects the subsequent wound healing process and dictates the final tissue integration of the implant. Wound healing is often separated into three phases. In the beginning, the body responds with acute inflammation to the surgical trauma and the implant surface. Thereafter, a regeneration phase and a remodeling phase follow during which new soft and hard tissue is formed in the peri-implant area (**Figure 1.2**).[12,21] In the following, the distinct processes for each of these phases are described in more detail.

In the first phase, tissue damage and contact of the implant with blood at the wound site activate the coagulation and complement system (**Figure 1.3**). The complement system is part of the innate immune response and plays a critical role in the defense mechanism against pathogens and foreign objects.[26] The complement system flags the implant as foreign object for elimination by the recruited phagocytic cells, such as neutrophils, monocytes, and macrophages. Further, cell lysis complexes are formed, which are able to attack the cell membrane of pathogens.[27] Activation of the complement system occurs either via antibody adsorption in the classical pathway or via hydrolysis (tickover) of the complement component C3 in the alternative pathway. In the following cascade, amplification of the activation marker by C3– and C5–convertase results in the formation of terminal complement complex (TCC), which is responsible for lysis of pathogenic cells.[28] During the amplification cascade, the subunits C3a and C5a are released, which act as pro-inflammatory signaling molecules.[29]

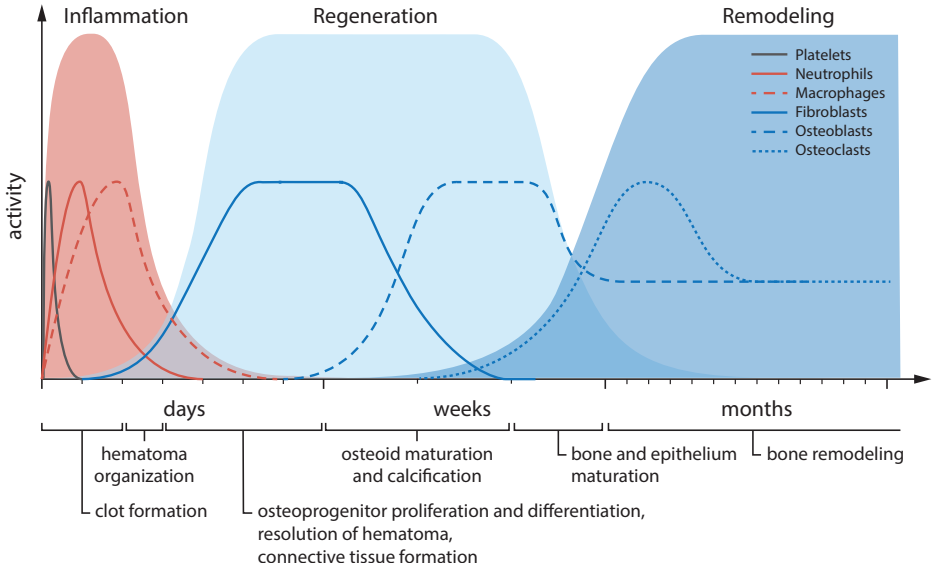

Figure 1.2: The three phases of wound healing start with inflammation and the formation of a blood clot to stop bleeding. It is followed by a regenerative phase in which the blood clot is being resolved by fibrinolysis. Thereafter, bone is generated by osteoblast and osteoclast activity.[22,23] Simultaneously, gingival soft tissue is regenerated and a barrier epithelium is established.[24,25] In the final phase, the newly formed bone is transformed and remodeled to yield the final osseointegrated structure.

Simultaneously, activation of the coagulation system starts the wound healing process. Blood coagulation inhibits bleeding by forming a blood clot that consists of extracellular matrix components and platelets. Both the tissue damage and the implant surface trigger the extrinsic and intrinsic coagulation pathway. In both pathways, tissue factors (TFs) are released and amplified as shown in **Figure 1.3**. The pathways converge in the cleavage of prothrombin (TF–II) to thrombin (TF–IIa) and prothrombin fragment 1 and 2 (F1+2). During hemostasis, thrombin is regulated by antithrombin, which forms a thrombin–antithrombin complex (TAT).[30] However, during activation of coagulation, thrombin levels increase and activate the assembly of fibrinogen to fibrin.[31,32] The various coagulation factors, such as thrombin, subsequently activate platelets, which in turn increase the formation of thrombin.[33] Thus, a feedback loop is created, forming the blood clot consisting of a fibrin mesh forms and entrapped platelets. Coagulation plays a decisive role in inflammation, as thrombin induces pro-inflammatory cytokine expression.[34] Further, prolonged inflammation and a continuous activation of platelets reduces fibrinolysis. This can lead to fibrous encapsulation, preventing a close contact of the implant with bone.[35,36]

After the acute inflammatory phase, the regeneration phase starts with the reorganization of the hematoma (**Figure 1.2**). During this phase, a variety of cytokines and growth factors affect the attraction of leukocytes and fibroblasts to the wound site. Fibroblasts proliferate and form extracellular matrix (ECM) as a framework for tissue remodeling.[37] Further, expression of pro-inflammatory

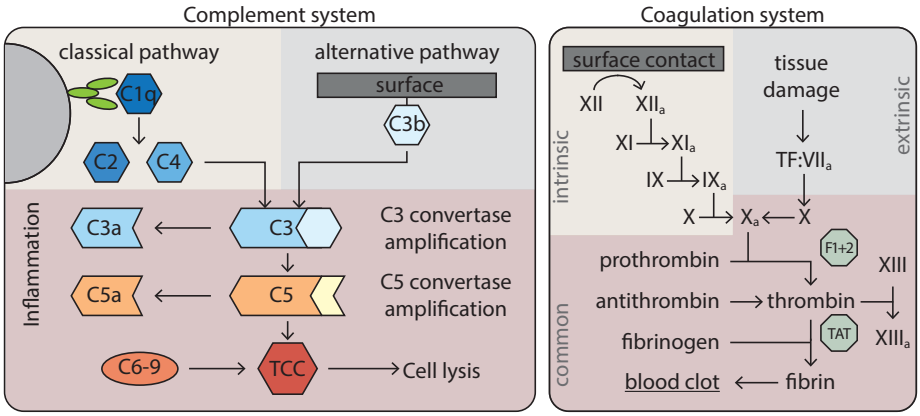

Figure 1.3: As part of the innate immune response, the complement system is activated by surfaces via either the classical or the alternative pathway. Similarly, surfaces trigger the coagulation cascade leading to the formation of a blood clot. Both systems are complex interconnected pathways relying on several stimuli-response actions. In combination they define the foreign body response and affect the subsequent regenerative processes.

cytokines by leukocytes ceases and changes towards anti-inflammatory cytokines to relieve inflammation.[38] During the progression of the regeneration phase, the initial ECM deposited by fibroblasts is then remodeled. We now have to distinguish between hard and soft tissue remodeling. Hard tissue is formed through osteogenic and angiogenic processes. Osteoprogenitor cells migrate from the bone marrow towards the wound site, where these type of mesenchymal stem cells proliferate and differentiate into osteoblasts. These osteoblasts start to deposit bone on the surface of the surrounding bone (distant osteogenesis) and on the implant surface (contact osteogenesis).[39] Subsequently, the deposited immature woven bone formed within the first few days is gradually replaced with dense lamellar bone by osteoblast and osteoclast activity. This final adaption to the environment is a persisting process, causing constant remodeling throughout life.[23,39] In contrast to hard tissue formation, the remodeling of granular tissue to mucosal soft tissue starts by forming the initial junctional epithelium after two weeks. Thereafter, organization of collagen fibers and full development of the epithelial barrier occurs.[24,25]

Under ideal circumstances, the acute inflammation abates within a few days, passing over to the healing processes. After a few months, the implant presents close contact with the surrounding soft tissue and the newly formed bone holds the implant firmly in position. The implant is now called osseointegrated. At this point, the survival rate of the implant is around 95 %.[6,10] A well established soft tissue integration plays a vital role for the survival of the implant as it is the barrier against microbial invasion at the interface of the abutment or tissue level implant.[40] However, for patients with impaired wound healing or an chronic infection, the acute inflammation is prolonged and the healing process is disturbed. Thereby, bacterial invasion of the peri-implant environment can cause peri-implant diseases, such as peri-implant mucositis and peri-implantitis. The latter can lead to major bone resorption, which ultimately results in failure of the implant.

1.3 Inflammation and infectious diseases around dental implants

Peri-implant mucositis and peri-implantitis are inflammatory oral diseases caused by bacteria.[41] In the previous section, we encountered inflammation as part of the wound healing and we will now expand on its causes in more detail to explain how cells react to external stimuli. This allows us to present strategies how inflammation can be tackled. It is important to discern inflammation caused by invasive pathogens, the surgical trauma, and the foreign body response. However, there are common principles associated with how cells respond to pathogen-associated molecular patterns (PAMPs) and damage-associated molecular patterns (DAMPs).

1.3.1 Inflammation

As described earlier, inflammation is connected to the innate immune response of the human body to foreign objects, such as bacteria or an implant. Activation of the complement system by these foreign objects recruits circulating leukocytes.[26] Neutrophils are the dominant species of leukocytes, responding initially to the anaphylatoxins C5a and C3a (**Figure 1.2**).[34,42,43] The expression of chemokines by leukocytes subsequently attracts monocytes, which differentiate to macrophages (**Figure 1.4**).[42,44] Macrophages and neutrophils are considered as some of the most important cells of the innate immune system as they can express various inflammatory cytokines and eliminate foreign objects by phagocytosis. While macrophages can easily take up micro-organism, they enter a state of frustrated phagocytosis at the implant surface as the foreign body cannot be internalized.[45] During phagocytosis, neutrophils and macrophages also express reactive oxygen species (ROS) and cause local acidosis, damaging all surrounding cells without discrimination.[46] To combat foreign objects more efficiently, pro-inflammatory M1 polarized macrophages express cytokines, which attract more leukocytes and trigger inflammation in surrounding cells (**Figure 1.4**).[47,48] Once the cause of inflammation is resolved, macrophages enter a M2 polarized state, supporting wound healing and tissue repair processes.[49] This transition is activated by anti-inflammatory cytokines, which are expressed by T_H2-cells.[50,51]

It is evident that cytokines are important in cell communication and modulation of inflammation. These signaling molecules are being processed by cells via different signaling pathways as shown in **Figure 1.4**. After the recognition by cytokine specific receptor complexes, the signal cascades activate gene expression in the cell nucleus. For example, tissue necrosis factor alpha (TNF-α) and interleukin–1 (IL-1) activate toll-like receptors and cause a turnover of nuclear factor kappa B (NF-κB) via the MyD88/IRAK pathway.[52] They also activate the mitogen-activated protein kinase (MAPK) pathway,[53] whereas IL-6 activates the STAT3 signal transduction.[54] However, this inflammatory response can also be triggered by micro-organisms. Recognition of bacterial and fungal LPSs by toll-like receptors activate the MAPK pathway and results in inflammatory cytokine expression.[55]

Tackling inflammation can thus be achieved at different stages. Inhibition of the complement activation as part of the immune system may reduce the number of activated leukocytes. Alternatively, the macrophage polarization and expression of ROS and pro-inflammatory cytokines can be suppressed. Thereby,

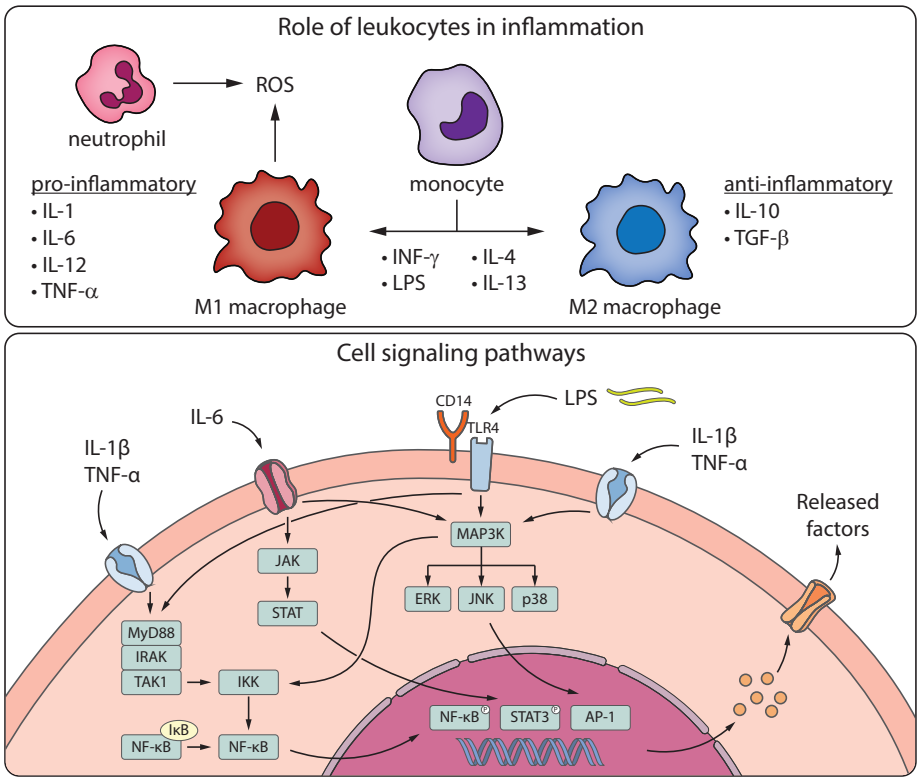

Figure 1.4: Upon inflammation, recruited monocytes are polarized by inflammatory cytokines. During phagocytosis, M1 macrophages and neutrophils release ROS and further pro-inflammatory cytokines. Once inflammation is relieved, anti-inflammatory cytokines mediate a M2 macrophage polarization. DAMPs, such as cytokines, and PAMPs, such as lipopolysaccharide (LPS), are recognized by cells via receptors and activate various signaling pathways leading to gene activation and expression of further signaling molecules.

the tissue destructive processes are lowered, which supports wound healing. Once inflammation sets in and pro-inflammatory cytokines or PAMPs are present, the intercellular signaling pathway can still be blocked to prevent the further progression of inflammation. However, fighting inflammation by suppressing the immune response comes with a trade-off. It potentially opens the door for uncontrolled microbial growth.

1.3.2 Peri-implant diseases

There is a broad variety of bacteria in the oral cavity that can invade the peri-implant environment and cause infection and inflammation. Implanted devices further pose a risk of carrying dormant bacteria that cause infection after the wound has healed.[56,57] Once micro-organisms start to colonize the implant surface and invade the gingival tissue patients develop peri-implant diseases such as peri-implant mucositis and peri-implantitis.

Peri-implantitis is defined as destructive inflammatory process caused by bacteria that affects the soft and hard tissues around osseointegrated implants.[58,59] Peri-implantitis is often preceded by peri-implant mucositis, which describes the inflammation of the gingival tissue surrounding the implant.[60] Only a few years after the introduction of osseointegrated implants, peri-implant diseases were observed and associated with subgingival plaque.[61] Plaque probes typically show a multi-species biofilm, which contain bacteria from the orange complex, such as *P. indermedia* and *F. nucleatum.* Progression of peri-implant mucositis to peri-implantitis further shifts the composition to the red complex, which includes *P. gingivalis* and *T. forsythia.*[41,62,63] These micro-organisms have also been identified in patients with periodontitis.[64] Thus, it is discussed whether patients who suffered periodontal diseases before receiving implants are at higher risk of developing peri-implantitis.[41,65] Besides these common oral bacteria, other biofilm-forming micro-organisms such as *Staphyloccus spp.* and *Candida spp.* have been detected.[66,67] These organisms play an important role in the early colonization of surfaces and the establishment of biofilms.[67] After their initial colonization of the implant surface, other common oral bacteria are able to attach and grow protected by the biofilm.[68]

Today, the prevalence of peri-implantitis ranges between 10 % to 30 %, but can exceed 70 % depending on the assessment criteria.[58,59,69,70] In particular, the patients with pre-existing diseases or habits affecting wound healing, such as auto-immune diseases, diabetes, and smoking, are at higher risk of developing peri-implant diseases.[71,72] An important factor affecting the prevalence of biofilm accumulation and the risk of infection is the implant design. An increased colonization has been observed especially on rough surfaces.[73] This is related to the protection of bacterial cells against mechanical removal forces during oral hygiene measures.[74,75] Hence, most clinically used surfaces which are in contact with soft tissue are polished. However, the progressive bone loss caused by peri-implantitis exposes the predominantly rough implant surface and the implant site becomes more difficult to adequately disinfect.[63] Treatment of peri-implantitis commonly consists of mechanical debridement with adjunctive use of chemical disinfectants or antibiotics.[76] However, with the rising incidence of antimicrobial resistance, a sufficient treatment may not be guaranteed.[77] Indeed, there is already evidence that on rough surfaces the efficacy of decontamination with antimicrobial agents is limited.[78]

It is evident that we need new ways to fight peri-implant infections. Currently, no implant exists, which meets all desired characteristics. An ideal implant should be antimicrobial, promote tissue integration, and offer appropriate mechanical strength. Thus, efforts are being made to change the surface chemistry of established dental implants with the aim to prevent the initial colonization by bacteria and support soft-tissue attachment as natural barrier against microbial invasion.

1.4 Strategies to improve host tissue integration

Advances in biomaterial science has shaped the modern idea of biocompatible materials.[79] Through the continuous study of surface properties and their effect on the clinical performance, the host response to materials can be predicted.[80]

Currently, research tries to find a solution for the balance between tissue integration and prevention of microbial colonization. This fight between cells and bacteria over the surface has been termed as *'race to the surface'* by Anthony Gristina.[81]

1.4.1 The initial contact counts

Cell and microbial adhesion to surfaces is influenced not only by surface morphological features but also by the physico-chemical properties of the surface. Differences in wettability, polarity, and charge are known to influence cell adhesion.[82] Although the surface chemistry of any material may technically be well defined, cells may not experience the same properties *in vivo*. Upon first contact with body fluids, such as blood or saliva, various biomolecules will adsorb onto the surface and form a conditioning film. The formation of this film is surface dependent, and influences the foreign body reaction and cell adhesion.[83,84] A general observation is that hydrophobic surfaces adsorb more proteins, however, biomolecules often exhibit changes in conformation upon adsorption, which may impact their biological activity.[85,86] The conformation the proteins adopt further depends on the surface charge of the biomaterial, and can be of reversible or irreversible nature. During physical adsorption of proteins, the composition of the protein layer is subject to changes over time, as the initially adsorbed low molecular weight (LMW) proteins are gradually exchanged by larger molecules with higher surface affinity. This process is known as Vroman effect.[57,87]

1.4.2 Current implant surface modifications

There are two principle strategies to change surface properties, i) changing the topography, or ii) the chemistry. As mentioned before, rough surfaces show clinically better integrated dental implants due to the increased contact area and retention.[88–90] Further, rough surfaces promote bone formation.[91,92] Thus, almost all current dental implant surfaces are treated in a way to increase their surface roughness. In contrast, surfaces in contact to soft tissue are primarily smooth to reduce bacterial invasion. However, these surfaces do not show close attachment of the gingival tissue.[73]

Promoting direct attachment of soft and hard tissue to the implant surface, while simultaneously reducing microbial attachment, still remains a challenge. Improved cell adhesion and proliferation requires a positive stimulus through signaling motifs on the surface. To address this problem, various biomimetic approaches to modify surfaces have been proposed as shown in **Figure 1.5**.[93,94] Soft and hard tissue integration can exemplary be promoted by tethering bone morphogenetic proteins (BMPs) and cell adhesion domains (RGDs) onto surfaces.[95–98]

Simultaneously, microbial attachment and proliferation of bacteria has to be prevented by either non-adhesive surfaces or molecules, which inhibit growth of potential pathogens. Continuous efforts are made to inhibit surface colonization by studying topographical features on the nanometer scale. Although correlations of bacterial adhesion and nanoscale surface features have been obtained, no surface that is universally resistant to all microbes has been found so far.[99,100] An alternative to nanopatterned surfaces are brush-like polyethylene glycol (PEG) polymer coatings. These render the surface hydrophilic, and create a viscoelastic

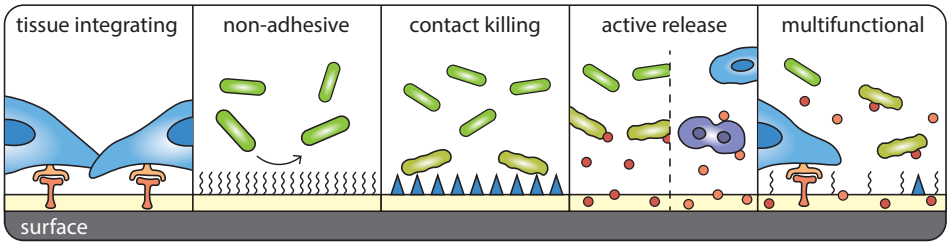

Figure 1.5: Different coating strategies exist to support tissue integration and reduce microbial colonization. Cellular interactions can be facilitated with specific motifs for attachment and release of growth factors. In contrast, microbial adhesion has to be prevented by reducing their ability to attach to surfaces, or by killing them upon contact. Similar to the stimulation of human cells, controlled release of antimicrobial molecules can affect the growth of bacteria or fungi. The ultimate goal is a multifunctional surface uniting all principles.

surface that is unfavorable for bacterial attachment and protein adsorption.[101–103] Further, reduction of microbial colonization can be obtained by biocidal molecules bound onto the surface or released from coatings. Broadly studied materials in this context are silver doped materials,[104] quaternary ammonium compounds, antibacterial peptides, and various enzymes.[104–107]

All these different goals ultimately have to be combined in a multifunctional, bioactive surface that maintains its properties for an appropriate time after implantation. Recently, polyphenolic molecules attracted attention in the quest to create such multifunctional coatings.[108–113] Polyphenols exhibit a number of desired attributes, such as antimicrobial, anti-inflammatory, and antioxidant properties, which make them interesting candidates to tackle inflammation and infections. Further, the ability to adhere to most surfaces and form coatings can be utilized to equip surfaces with these attributes. In the following section, polyphenols will be introduced and their structural features are put into relation with their biological function.

1.5 Polyphenols

1.5.1 Definition

Polyphenols are a class of compounds bearing multiple hydroxyl groups on an aromatic benzene ring. Historically, they are also known as tannins, due to their use in the leather manufacturing process.[114] Based on these tanning properties polyphenols were defined by White, Bate-Smith, Swayne, and Haslam (WBSSH) as high molecular weight compounds with several phenolic hydroxyl groups, which precipitate proteins from solution.[115] The WBSSH definition includes condensed tannins, hydrolyzable tannins, and phlorotannins. Later, the strict classification of plant polyphenols was expanded by Quideau to accommodate other plant secondary metabolites derived from the shikimate pathway, such as lignans, stilbenes, and other low molecular weight molecules.[114] Following this approach, we can divide the diverse group of molecules in classes with similar structure, as illustrated in

(**Figure 1.6**). The great variability of polyphenols is caused by changes in the number and arrangement of the hydroxyl groups on benzene. Beyond the simple phenol molecule bearing one hydroxyl group, polyhydroxy phenolic motifs are classified as pyrocatechol, pyrogallol, resorcinol, or phloroglucinol (**Figure 1.7**). In this work, we focus on the polyphenolic molecules tannic acid (TA), gallic acid (GA), ellagic acid (EA), and pyrogallol (PG), which are depicted in **Figure 1.7**.

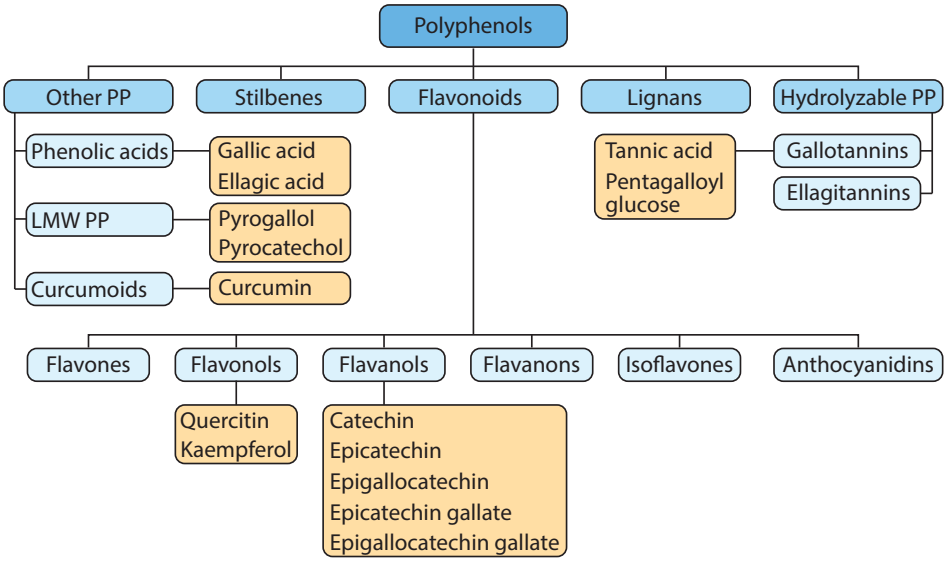

Figure 1.6: Classification of polyphenols according to their fundamental structure. Commonly, this group of molecules comprise hydrolyzable polyphenols, lignans, stilbenes, and flavonoids (condensed polyphenols). In addition to these structures based on the classical WBSSH definition, secondary plant metabolites as defined by Quideau are included. These are phenolic acids, LMW polyphenols, and curcumoids. Examples of commonly studied molecules are highlighted in yellow.

1.5.2 Chemical properties and biologic implications

The phenolic group is the most important constituent of polyphenols, resulting in their unique properties (**Figure 1.8**). The phenolic hydroxyl group is mildly acidic with pK_a values of 8 to 10. Additional hydroxyl groups on the benzene ring can further lower the pK_a value through intramolecular hydrogen interactions.[116] Thereby, the hydroxyl groups are responsible for polar interactions, resulting in the hydrophilic character of many polyphenols.[114] In contrast, the benzene ring allows hydrophobic interactions by π-stacking,[117] cation-π stacks,[118] and cation-π-anion interactions.[119]

This chemical variety enables interactions with many organic biomolecules. Especially hydrogen bonding and hydrophobic interactions cause aggregation of proteins and enzymes. In particular, uncharged proline-rich proteins (PRPs), albumins, mucins, and collagen are denatured by polyphenolic molecules.[120] These interactions have been suggested to reduce oxidative stress caused by pro-

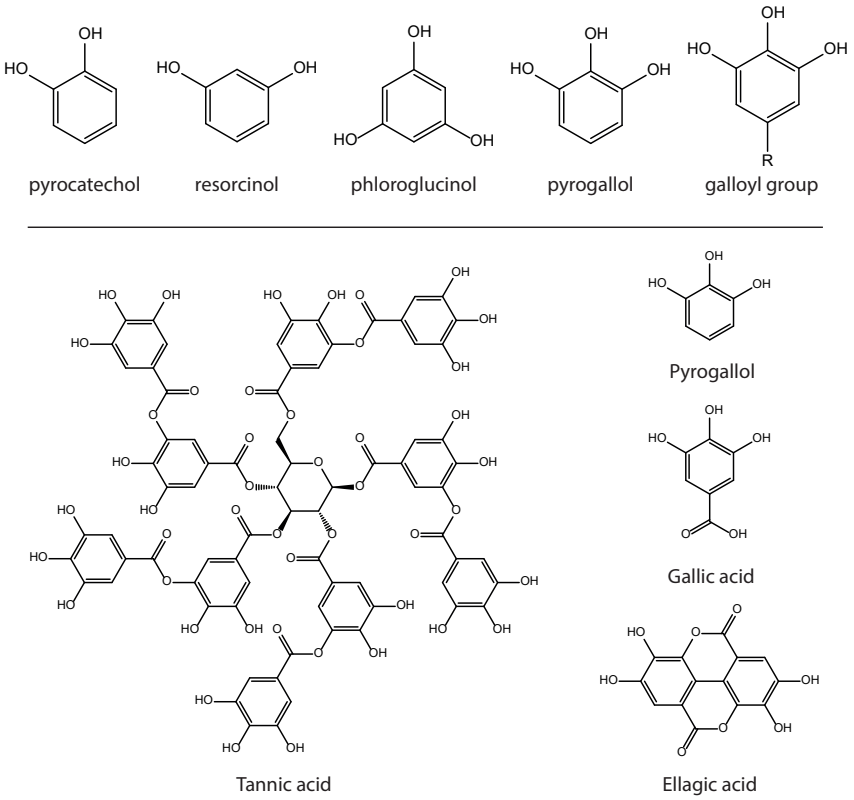

Figure 1.7: *Top*: Polyphenolic molecules consist of one or more benzene rings with at least two hydroxyl groups attached. *Bottom*: Structures of polyphenols used in this work. TA is a high molecular weight compound consisting of a central glucose unit with up to ten galloyl groups attached. Hydrolysis of these subunits yields GA, which can in turn dimerize to form EA. PG represents GA without the carboxylic acid group.

inflammatory enzymes.[121] The most studied anti-inflammatory mechanism of polyphenols is the interaction with redox active cell signaling molecules, and the inhibition of myeloid differentiation primary response 88 (MyD88) dependent NF-κB phosphorylation shown in **Figure 1.4**.[122,123] Thereby, the expression of pro-inflammatory cytokines can be modulated.[122,124,125] In addition to effects on human cells, a variety of antimicrobial activities have been reported. For example, interactions of polyphenolic molecules with bacterial cell membranes result in bactericidal effects.[126] Further, the interaction with transmembrane proteins can block efflux pumps.[127,128]

Polyphenols with either pyrocatechol or pyrogallol groups are further able to coordinate metal cations.[129] Thereby, reactive metal ions, such as Fe^{3+}, can be scavenged to avoid ROS production via Fenton reactions.[130,131] It is also suggested that chelation of ions, which are vital for bacterial metabolism, can have an antimicrobial effect.[132] Alternatively, the coordination of metal ions can be used to as a nucleation point for antimicrobial silver deposition.[133]

In oxidative environment, phenolic compounds react to form quinones

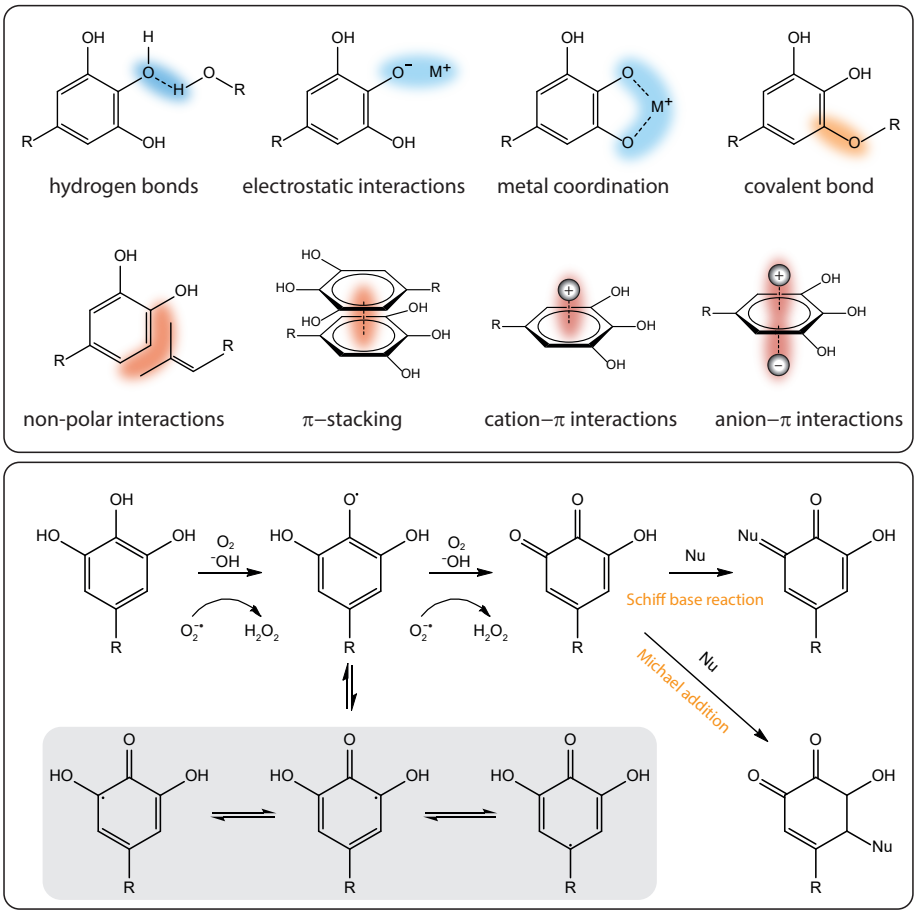

Figure 1.8: *Top panel.* The phenolic hydroxyl group is the origin of a variety of interactions. Besides hydrogen bonding and ionic interactions, vicinal hydroxyl groups chelate metal ions. Further, the benzene ring allows interactions via its delocalized π-electron system in π-stacks and ion-π complexes. *Bottom panel.* The oxidation of polyphenols occurs spontaneously in slightly alkaline conditions with dissolved oxygen. During the oxidation to quinones, mesomerically stabilized radical intermediates are formed. Subsequently, quinones can undergo polymerization and coupling reactions via Schiff-base or Michael-addition reactions.

(**Figure 1.8**). During this process, semi-quinone radical intermediates are formed.[134–138] Thereby, the proton is removed from the hydroxyl group, followed by electron transfer. This mechanism is referred to as SPLET.[139,140] Auto-oxidation commonly involves dissolved oxygen and it is suggested that superoxide radicals ($O_2^{-\cdot}$) are formed, which subsequently react to hydrogen peroxide (H_2O_2).[141–143] Phenolic radicals are relatively stable compared to other organic radicals due to the mesomeric stabilization in the conjugated π-system.[144] The delocalization of the radical spreads out the charge density and lowers the energy level of the radical. Hence, polyphenols are broadly considered as antioxidant radical scavenging

molecules. This antioxidant effect also depends on the degree of substitution and increases from phenol < catechol < pyrogallol due to an increase in radical stability by the electron donating hydroxyl groups.[145] Once polyphenols have been oxidized to quinones, they react with nucleophiles via Schiff-base formation or Michael addition (**Figure 1.8**).[115,146] This also leads to spontaneous self-polymerization of polyphenolic molecules, forming high molecular weight polymers in alkaline conditions.[147]

However, there is an unresolved dispute as to whether redox cycling has an overall pro-oxidant or antioxidant effect.[148,149] Most *in vivo* studies related to dietary uptake of plant polyphenols support the antioxidant effect.[150,151] In contrast, cancer researchers claim opposite effects.[152] Thus, whether the antioxidant property of polyphenolic molecules prevents inflammatory conditions remains an application specific effect.

1.5.3 Polyphenols at interfaces

The investigation of polyphenols for surface modifications began after the pioneering work on the adhesive properties of catechol containing biopolymers.[153] The first studies following this discovery then focused on the interaction of dopamine with various surfaces.[154,155] In these investigations, it was found that dopamine adheres to a broad variety of different materials, such as oxides, metals, and polymers. The driving force for this surface independent adsorption phenomenon is the previously described variety in reactivity of polyphenolic molecules (**Figure 1.8**). Thereby, polyphenolic groups are able to coordinate to metal ions on the surface, react covalently with nucleophilic groups, form hydrogen bonds, and coordinate to polymeric materials through hydrophobic interactions.[156,157] On titanium surfaces, catechol groups first form labile hydrogen bonds before stable coordination to Ti centers via mono- and bidentate links (**Figure 1.9**).[158,159]

The adhesive properties of dopamine were then used to create coatings via oxidation of dopamine to dopa-quinone, which undergoes polymerization to form polydopamine (eumelanin).[160,161] In the further development of functional surface modification, the substrate-independent adsorption and coating formation of a variety of different polyphenolic molecules was established (**Figure 1.10**).[113,162]

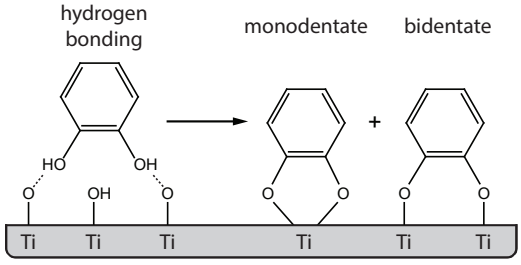

Figure 1.9: Polyphenolic molecules are able to interact with a variety of different surfaces via polar, ionic, covalent, and hydrophobic interactions. On titanium surfaces, the catechol group first adheres through hydrogen bonding followed by mono- and bidentate coordination with Ti.

Based on these results, kinetic studies extended the knowledge about interface chemistry and assembly of polyphenolic layers.[163,164] Their main findings were that the coating formation is highly dependent on reaction conditions such as pH and ionic strength. Simultaneously, studies with TA–based metal phenolic networks (MPNs) progressed and opened the field for facile surface functionalization by dip-coating.[165] Contrary to oxidative polymerization, MPNs can form in non-oxidative environments based on the cross-linking of polyphenolic molecules with transition metal ions, such as Fe^{3+} (**Figure 1.10**).[155] In order to build a cross-linked network structure, molecules with more than one catechol group are required. Thus, most MPN research is based on TA due to its high number of galloyl groups available for cross-linking (**Figure 1.7**). The knowledge acquired over the past decade is able to shed light on some of the physical and chemical interactions during the formation of polyphenolic surface modifications,[166–168] and a variety of different biomedical applications were proposed thereafter.[169] With regard to wound healing, polyphenolic molecules have also been studied for soft and hard tissue regeneration.[170] However, little research has yet been done on the use of polyphenolic coatings to improve the foreign body response and support the wound healing process.

In addition, there are still open questions regarding the chemistry of polyphenolic coatings and the differences between oxidative polymerization and MPNs Additional knowledge is needed particularly with respect to the change in chemistry and biological function of polyphenols once they are deposited in a surface confined layer. The main influencing factor in this regard is the reaction conditions applied to induce oxidative polymerization or cross-linking of MPNs. Thus, investigation of the coating deposition process of polyphenols and the characterization of the physical and chemical properties of the coating is necessary to understand the biologic response.

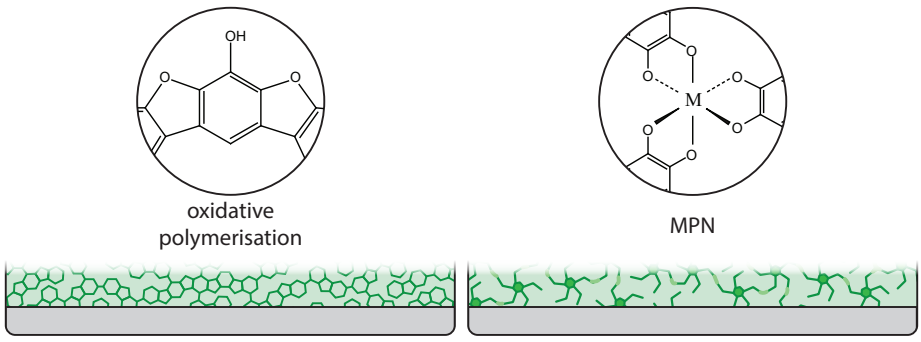

Figure 1.10: After the initial adhesion a layer can be built up either via oxidative polymerization or via cross-linking of either catechol, or galloyl groups with metal ions. Oxidative polymerization is mostly encountered in polydopamine or pyrogallol coatings, whereas Fe-based MPN are commonly used with TA.

Chapter 2

Research Concept

2.1 Aims and hypothesis

The general hypothesis of this work was that Ti dental implant surfaces modified with polyphenolic compounds improve the wound healing process. Therefore, polyphenolic molecules ought to retain their intrinsic anti-inflammatory and antimicrobial properties after being deposited as coatings. Consequently, an improved host tissue integration of titanium implants is elicited by reducing the inflammatory response and inhibiting microbial colonization.

Therefore, the aim was to investigate the mechanisms involved in the surface deposition of polyphenolic molecules and to characterize the physical, chemical, and structural properties of coatings obtained under different experimental conditions. After that, the biocompatibility, antioxidant capacity, and anti-inflammatory properties of functionalized Ti surfaces towards blood and primary human cells was assessed. Finally, microbial surface colonization was studied by evaluating the adhesion and growth of oral pathogens on polyphenolic coatings in a condition mimicking the oral environment.

2.2 Research structure

Before the *in vitro* performance of polyphenolic coatings was evaluated, the deposition mechanisms of TA and PG were studied in more detail. Thus, the project was divided into two main blocks according to **Figure 2.1**. First, the chemical reactions involved in the coating formation of TA were characterized and compared to other polyphenols, such as GA and EA. These experiments were focused on the real-time kinetics and coating chemistry involved in the assembly of polyphenolic molecules on Ti surfaces under different experimental conditions. The main aim was to find out how aqueous silicic acid (Si_{aq}) enables the continuous formation of TA coatings and how pH and ionic strength influence the deposition of polyphenolic coatings.

After establishing the difference between the assembly mechanisms of TA and PG coatings, a set of three coated surfaces was defined. Thereby, the anti-inflammatory and antimicrobial properties and the host response in relation to the surface chemistry was determined *in vitro*. TA coatings represent cross-linked network structures similar to MPN and were prepared at pH = 6.8 or pH = 7.8 to test different oxidation states. PG coatings represent oxidatively polymerized coatings similar to polydopamine coatings. First, the interaction of the modified surfaces with blood and the capability to reduce oxidative stress and inflammation was studied. Second, the ability to inhibit biofilm formation by reducing fungal growth and attachment to the modified surfaces was analyzed.

These objectives were addressed in five articles and manuscripts with individual research questions as outlined below.

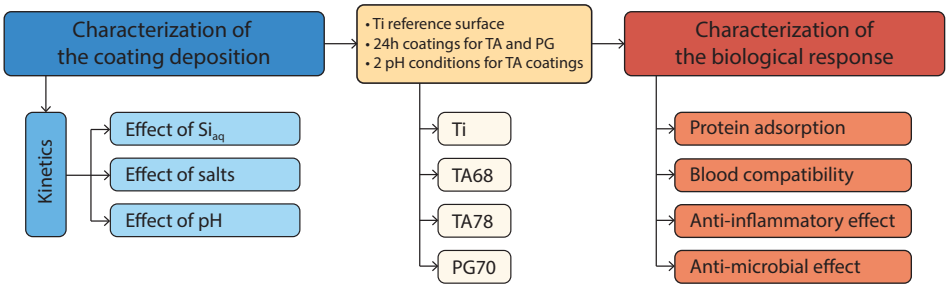

Figure 2.1: The research presented in this thesis is split into characterization of the coating formation and assessment of the biological response for four different surfaces.

Characterization of the coating deposition

Paper I

- What is the mechanism in the formation of TA and PG coatings?
- What are the structural requirements for the coating formation and can the results be extrapolated for other polyphenolic molecules?
- Do both coatings vary in physical and morphological properties, which could affect the subsequent stability and behavior in clinical applications?

Paper II

- Are TA coatings based on coordination chemistry with silicic acid?
- How can the efficiency of the TA coating process be improved?

Paper III

- Why is a high ionic strength required for the formation of TA and PG coatings?
- Can sodium salts be exchanged with any other alkali metal salt?
- Are salts involved in the polyphenolic radical formation?

Anti-inflammatory and antimicrobial properties of polyphenolic coatings

Paper IV

- Are polyphenolic coatings blood compatible?
- Do polyphenolic coatings activate the complement and coagulation system?
- Do polyphenols retain the antioxidant effect after being deposited on surfaces and reduce intracellular ROS?
- Can polyphenolic coatings reduce the cytokine expression in inflamed fibroblasts?

Paper V

- Are polyphenolic coatings able to reduce the adhesion, growth, and biofilm formation of *Candida albicans*?
- Do salivary protein layers affect the antimicrobial properties of polyphenolic coatings?

Chapter 3

Experimental Considerations

3.1 Preparation of modified surfaces

3.1.1 Commercial tannic acid

TA is an easily available and affordable plant-derived product with potent anti-inflammatory and antioxidant properties.[171] However, due its biological origin, commercial TA is subject to batch-to-batch variations. Ideally, a purification step is performed before use to remove contaminants and degradation products. After we noticed that the coating formation was dependent on the TA batch, the composition was analyzed by high–performance liquid chromatography (HPLC) (**Figure A1**). For the majority of this work, we used a singular batch, which showed only GA contamination, and thereby circumvented a laborious purification process.

Besides TA, we studied several other polyphenolic molecules in this work to compare the coating formation and biologic response. GA was used to represent the main structural component of TA (**Figure 1.7**). However, GA does not form coatings.[162] Therefore, PG was used as the simplest molecule, which has three phenolic hydroxyl groups and forms coatings. Further, EA was taken into consideration as a dimer of GA, but poor water solubility at neutral pH prevented the use in our experiments.

3.1.2 Coating deposition

Although the deposition of polyphenolic coatings is surface independent,[113] titanium was chosen as the model surface representing the material of most dental implants. To study the biological response of cells to the coated surfaces, polished Ti coins were used as substrates mimicking the smooth abutment surface of titanium dental implants. A smooth surface finish further allows the characterization of physical properties and cell response without the overlaying effects of surface roughness. Polyphenolic coatings were obtained by immersing the coins in the solutions containing the dissolved polyphenolic molecule for 24 h with gentle agitation on a rocking platform (**Figure 3.1**). This allows oxygen to diffuse and participate in the oxidative reactions.[142] From previous research on the formation of polyphenolic coatings, it is known that many parameters influence the coating formation.[164] Therefore, systematic studies with different parameters had to be conducted. One of the major factors affecting the coating formation is the pH, a driving force of the oxidation.[162] To maintain a steady pH level throughout the coating process, the solutions had to be buffered. However, not all buffers are compatible with the polyphenolic molecules or salts required to adjust the ionic strength (**Figure A2**). While bicine was commonly used in previous studies,[164,172] we used HEPES in this work as it offered a more suitable buffer range and did not interact with any of the components.

For experiments which require a defined surface roughness and surface chemistry, Si wafers were used instead of Ti coins. This was the case for (i) surface energy and wettability studies using contact angle measurements, (ii) studies of the coating thickness by ellipsometry that are affected by the roughness and inhomogeneous oxide layer on Ti, and (iii) coating topography studies. To avoid polyphenolic polymer particles, which form during the oxidation reaction and sediment on the surfaces, Si wafers were mounted vertically (**Figure 3.1**). Due to issues with coatings peeling off the Si substrate during rinsing, the native oxide layer of the wafers was removed by HF treatment before the coating process. Problems with the deposition of polyphenols on SiO_2 layers are known and initially suggested to originate in the dissolution of the oxide layer by polyphenols.[162] However, it has also been shown that the adsorption energy of catechols on silica can be as low as that for water, which could cause the detachment of the polyphenolic layer upon rinsing.[173]

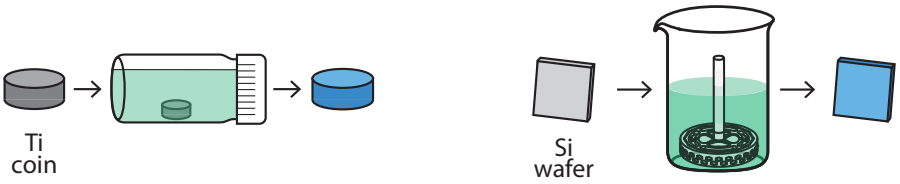

Figure 3.1: Ti surfaces are coated by immersion in 10 mL polyphenolic solution under gentle rocking motion. For the deposition of ideal smooth coatings on Si wafers, substrates were mounted vertically using a custom-made 3D-printed holder.

3.1.3 Monitoring polyphenolic oxidation reactions

Both the polymerization of polyphenols and the formation of MPNs are connected to spontaneous oxidation in slightly alkaline solution.[155,162] To determine the progress of oxidation, the change in the absorbance of UV–visible light (UV–vis) in the range between $\lambda = 200\,\text{nm} to 800\,\text{nm}$ was monitored. In this energy range, the absorption of light originating from the transition of π–electrons from bonding to anti-bonding orbitals can be used to interpret the electronic configuration of molecules.[174] Once polyphenols change their chemical structure upon oxidation, these transitions are affected and can be easily detected by this spectroscopic method.

Since UV–vis spectroscopy does not result in a detailed molecular structure of the polyphenols after the oxidation reaction, additional Fourier transform infrared (FTIR) spectroscopy was used as a complementary technique. In contrast to UV–vis spectroscopy, analysis of aqueous polyphenolic solutions using a ZnSe flow chamber was, however, dominated by the water signal at the concentration of $1\,\text{mg}\,\text{mL}^{-1}$ TA or PG. This problem was circumvented by placing droplets of polyphenolic solutions on the crystal of an attenuated total reflection (ATR) module. The ATR unit directs the IR beam to the solid interface where it interacts with the material and reflects off to the detector. After evaporation of the solvent from the sample, a quantifiable signal was obtained. Additionally, once the oxidation reaction of

polyphenols forms polymers, particles can be filtered off and analyzed by FTIR. However, these particles can be chemically different from the coating and should not be used to make statements about the chemical structure of the coating.[164]

Alternative standard techniques to investigate the chemical structure of polyphenols, such as ^{13}C and ^{1}H nuclear magnetic resonance (NMR) spectroscopy, were considered, but exact conditions as employed during the coating formation could not be established. Structural analysis of organic compounds using NMR is typically conducted in heavy water (D_2O). While D_2O is mandatory for proton spectra, 10 % D_2O is enough for the instruments magnetic field lock in ^{13}C.[175] However, we observed that TA dissolved in D_2O did not oxidize equally to respective H_2O based solutions. Thus, we could not determine the structure of polyphenols after the oxidation reaction. Further, due to issues with salt solubility in other solvents, such as EtOH, and the precipitation of polyphenols during long experiments, more elaborate studies could not be performed.

3.2 Characterization of the polyphenolic coating process

3.2.1 Kinetics of the coating process

For the kinetic analysis of the coating deposition, a quartz crystal microbalance with dissipation monitoring (QCM–D) was used. This instrument allows monitoring the formation of polyphenolic coating in real-time and in an aqueous environment. However, for the deposition of the coating on the sensor, the solution has to be pumped through a measurement chamber (**Figure 3.2**). This causes slight differences in the coating formation compared to the deposition process in vials due to limitations in mass transport. To balance these limitations with the required reaction volume, a flow speed of 100 µL min^{-1} was chosen.[164] Since QCM–D was used in many of the experiments in this thesis, its fundamental principles are elucidated in more detail.

QCM–D utilizes the piezoelectric effect of quartz to excite the acoustic resonance of the sensor. Fundamentally, the oscillation frequency depends on the physical properties of the quartz sensor according to Equation 3.1 established by Sauerbrey.[176] This equation correlates the change in frequency (f) as a result of a change in mass (m) for a sensor with fixed density (ρ_0) and thickness (t_0). The sensors used in this work are available with different surface, such as Ti, and have a fundamental frequency (f_0) of 5 MHz.

$$\Delta f = -\frac{f_0}{\rho_0 t_0}\Delta m \tag{3.1}$$

The Sauerbrey model was originally used for measurements in air and is only valid for rigid layers with a thickness below the acoustic shear wave penetration depth (δ_{acc}). Under these boundary conditions, the change in frequency is directly proportional to the change in mass and the instrument can detect changes of 18 ng/(Hz cm^2).[176] In addition to measuring the response of the sensor's fundamental frequency, the response of odd harmonics can be recorded. The probing depth depends on the oscillation frequency of the sensor and the viscosity (η_l) and density (ρ_l) of the surrounding environment according to Equation 3.2. A typical probing depth (δ_{acc}) at 5 MHz in water is approximately 250 nm (**Figure 3.3**).[177]

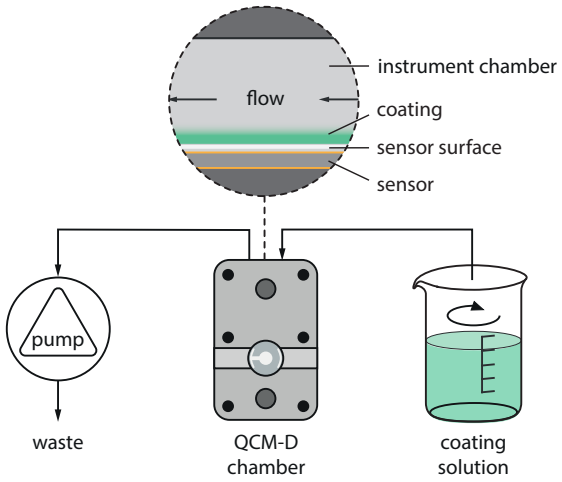

Figure 3.2: QCM–D was used to investigate the deposition kinetic of polyphenols. The polyphenolic solution was flown at a flow rate of 100 µL min^{-1} through the chamber to balance the required reaction volumes and restrictions in mass transport. The increase in mass of the sensor upon formation of coatings causes a change in resonance frequency, which can be monitored continuously to determine the coating kinetics.

$$\delta_{acc} = \frac{1}{\sqrt{\pi f \rho_l / \eta_l}} \tag{3.2}$$

However, in liquid environment, a rigid film cannot always be assumed, since coupled liquid dampens the oscillation of the sensor. This is measured as the dissipation (D) of the signal. Therefore, the Sauerbrey model has been expanded to attribute signal dampening. In the Kelvin-Voigt model, viscoelastic properties of an adsorbed layer on the sensor surface are used to correlate changes in mass. Thereby, changes in frequency and dissipation become functions of shear modulus (μ) and viscosity (η) of the adsorbed layer and the surrounding liquid.[178] While the properties of bulk fluids are commonly known, the density, shear modulus, and viscosity of an adsorbed film or coating are parameters of particular interest. However, the Voigt model only yields the η and μ of the layer. Thus, the layer density (ρ) has to be known before or measured separately. While densities for protein layers are available in literature, the layer properties of polyphenolic coatings have not yet been investigated. Consequently, we estimated the layer density by nanoplasmonic sensing (NPS) as described later. It should be mentioned that the theoretical models do not always result in physically logic parameters. Polymeric layers are not always ideal Newtonian fluids and model constraints, such as including frequency dependent viscoelastic properties, cause significant differences in the fitted parameters. Thus, in some cases a qualitative analysis according to changes in Δf and ΔD may be more suitable.[179]

QCM–D also presents some other disadvantages which complicate the data interpretation. The oscillation of the sensor is largely determined by the viscoelastic properties of the surrounding liquid. Thus, changes in the environmental conditions,

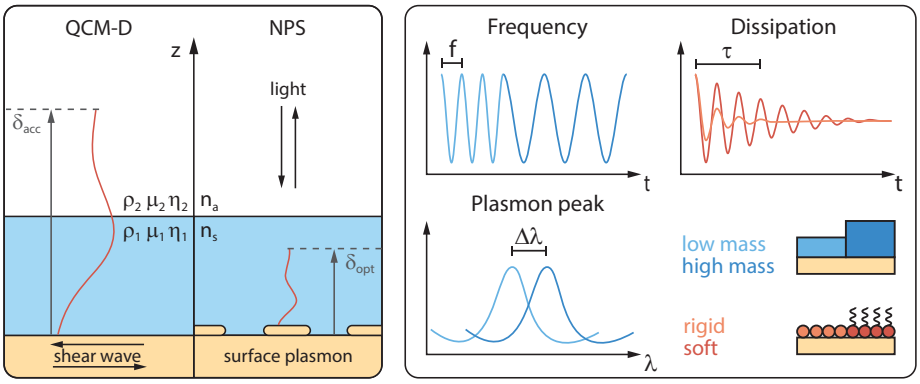

Figure 3.3: The principle of QCM–D is based on acoustic shear waves elicited by a quartz sensor. In contrast, NPS is an optical measurement technique using surface plasmon interactions to obtain the density of adsorbed layers. QCM–D is able to probe the viscoelastic properties of molecules coupled to the surrounding fluid by monitoring changes in resonance frequency (f) and signal dissipation (D). In comparison, NPS senses changes in refractive index (n) caused by the adsorption of molecules to the solid-liquid interface.

such as changing buffers and the temperature, contribute to the measured Δf and ΔD values. For measurements, where the coating formation is followed by adsorption or desorption studies in a different buffer, the shift in frequency and dissipation caused by the different solution must be accounted for. Therefore, it is necessary to record these changes before the experiment on clean sensors. Further, a final measurement in the original solution after the experiment verifies that the signal was not caused by the change in bulk liquid properties. Additionally, the presence of particles on the sensor surface contributes to the dissipation of the QCM–D signal by dissipating energy.[180] This is important to consider during the formation of polyphenolic coatings, since polyphenols polymerize during the coating process. These resulting particles accumulate in the measurement chamber and distort the signal. In this work, the effect has been addressed by flipping the instrument upside down. Consider the chamber shown in **Figure 3.2** rotated by 180°. This avoids particle sedimentation on the surface of the sensor. However, the drawback is that air bubbles can rise to the interface of the sensor in this orientation. Since air bubbles result in sudden spikes in the signal and render modeling impossible, we rather took the presence of particles into account as the cause for a higher dissipation.

3.2.2 Thickness, hydration, and density of polyphenolic coatings

As previously mentioned, the density of polyphenolic coatings was not known, and thus, the thickness of the coatings in liquid cannot be estimated correctly. Therefore, we used nanoplasmonic sensing (NPS) to obtain the density of polyphenolic layers in liquid state. NPS is an optical method using local plasmon resonance. In contrast to dedicated surface plasmon resonance (SPR) instruments, NPS can be conducted on special QCM–D sensors plated with gold nanodisks (**Figure 3.3**).

This allows obtaining data from two individual instruments on the same sample and can be used to directly correlate measured parameters.

Equal to the acoustic shear wave in QCM–D, the surface plasmon decays exponentially and displays a characteristic probing depth (δ_{opt}) of 30 nm (Equation 3.3).[181] At a layer thickness beyond the probing depth, the equation can be reduced, which allowed for the estimation of the density (ρ_{s}) of the layer (**Equation 3.4**). This density can then be used to calculate the layer thickness in QCM–D. Since QCM–D measures the mass of the coating coupled to water, we have now obtained the wet–mass and the thickness of the polyphenolic layer. Since the wet–mass is strongly dependent on the hydration of different polyphenols, QCM–D can overestimate the amount of molecules in the coating. To compensate the influence of coupled water, the thickness determined by QCM–D was used in **Equation 3.5**, to calculate the dry–mass based on NPS measurements. The necessary refractive index increment ($\mathrm{d}n_{\mathrm{s}}/\mathrm{d}c$) was measured to be 0.173.

$$\Delta\lambda = S_0 \cdot \Delta n_s = \frac{2}{\delta_{opt}} \int_0^{d_s} S_0 e^{-2z/\delta_{opt}} \cdot \Delta n(z) \tag{3.3}$$

$$\rho_s = \frac{\Delta\lambda}{S_0 \cdot dn_s/dc} \tag{3.4}$$

$$\Gamma_s = d_s \cdot \frac{\Delta n_s}{dn_s/dc} = d_s \frac{\Delta\lambda}{S_0(1 - e^{-2d_s/\delta_{opt}}) \cdot dn_s/dc} \tag{3.5}$$

The drawback of the NPS method is a short penetration depth, which excludes studies of coatings with a thickness above 100 nm. A slightly higher penetration depth could be obtained with SPR instruments to obtain the dry–mass and layer thickness.[161] Alternatively, a method has recently been described to determine a correct dry mass with QCM–D. The method describes the decoupling of the kinematic viscosity from the density of the bulk liquid. Thereby, the signal change for viscosity-matched liquids can be extrapolated to yield an accurate dry mass.[182] An additional limitation of the NPS system lies in the instrument setup, in which the light has to pass through the solution before being reflected at the sensor surface (**Figure 3.3**). Changes in the bulk solution, such as high absorption during oxidation of polyphenols, or particles scattering light, reduce the signal quality. This could have affected the calculation of the TA layer density, which resulted in values below the density of protein layers. For measurements where this can be avoided, the benefit of using NPS in combination with QCM–D is the simultaneous measurement of dry–mass and wet–mass characteristics in the same experiment. Thus, differences caused by the change in experimental setup can be avoided.

Neutron reflectometry (NR) is an alternative technique to evaluate the density, thickness, or roughness of thin layers *in situ*. While the principle of NR is similar to X–ray scattering techniques, the use of neutrons has the advantage of being able to study organic compounds which have low X–ray contrast. In NR, the interference pattern of the neutron beam is measured after being reflected at the interfaces of the coating. The reflectivity (R) of a surface depends on the wavelength λ, the angle (θ) of the incident beam and the integrated density of the material according to Equation 3.6 and 3.7.[183] The density is usually expressed as the scattering length density (SLD) and can be estimated by the scattering length of each atom

and its number density. The SLD of the compound of interest should ideally differ significantly from the surrounding medium. Measurements were performed in both H_2O (SLD_{H_2O} = -0.56) and D_2O (SLD_{D_2O} = 6.40).[184] As a control, contrast matched solvent was further used to verify that the assumed SLD of the polyphenolic layer was correct ($SLD_{cmc} = SLD_{TA}$ = 4.34).

$$q = \frac{4\pi \sin\theta}{\lambda} \tag{3.6}$$

$$R = \frac{16\pi^2}{q^4} \left| \int SLD(z)dz \right|^2 \tag{3.7}$$

However, the attempt to characterize the coating formation of polyphenols by NR did not result in sufficiently reliable data to model the desired parameters (**Figure A3**). Although the experiments were performed on the D17 instrument at the Institute Laue Langevin (ILL, Grenoble, France), which features the highest neutron flux to date,[185] data quality was poor. Thickness measurements were conducted at intervals of 10 min with reduced q–range. To cover the full q–range, the detector had to be moved to take measurements at two incident angles. Moving the detector requires time and therefore, the full q–range was recorded only at the beginning, once every hour, and at end of the experiment. The poor data quality may be caused by the rapid coating kinetics, which changes the layer thickness during each scan interval and obscures the data (**Figure A4**). Further, a roughness above 50 Å significantly affects the distinct fringe pattern. We have also observed that oxidation in D_2O did not progress as in H_2O at pH = 7.8, even though the pD was adjusted to the same level as the pH (pD = pH + 0.4).[186] Hence, regular water was used during the coating formation. For the characterization under different solvent contrast, the instrument chamber was flushed with heavy water after the formation process. To avoid these drawbacks, coatings could be deposited on the NR substrate before the experiment and analyzed by complementary dry–state techniques, such as atomic force microscopy (AFM) and ellipsometry. Subsequently the layer thickness and hydration could be studied in liquid environment by NR

So far, the described methods were all used to measure the coating thickness continuously during the formation of the coating. In addition to the *in situ* analysis, the coatings were also characterized in dry state, which allowed us to estimate the hydration of coatings by comparing the wet–mass obtained with QCM–D to the thickness determined by a complementary technique that probes the coating in dry state.

Amongst the various approaches to measure the coating thickness in dry state, null–ellipsometry was the preferred method for its high throughput. In principle, ellipsometry measures the change of the amplitude (Ψ) and phase (Δ) of polarized light after interacting with a thin film.[187] Null–ellipsometry operates by modulating the phase and amplitude of light to create a linear polarized beam after its reflection from a surface. An analyzer then determines the angle for which the intensity of the detected beam is minimal. Thereby, the thickness and refractive index (n_r) of the coating can be calculated. However, the numerical solution does not always guarantee accurate refractive indices.[188] For a relative

approximation, a single layer model was applied, which treated the coating and the SiO_2 oxide layer on Si substrates as one layer with the refractive index of SiO_2 ($n_{r,SiO_2} = 1.46$). For absolute values of the coating thickness, n_r of the coating has to be known. The refractive index can be obtained by either measuring a thin film with known thickness or by using a spectroscopic ellipsometer. The latter allows for the collection of enough data to fit the recorded data with optical models, obtaining the complex refractive index.

To support our ellipsometry data, we obtained the required thickness by height measurements of the coating using an AFM. For this measurement, the coating was scratched off the Si wafer using the tip of the AFM cantilever. Thereby, we determined that the layer thickness in the simplified ellipsometry model was over estimated by approximately 25 %. Hence, the correct refractive index of the polyphenolic layer is approximately $n_{r,\,TA} = 1.88$. This is in good agreement to the estimated values for polyphenolic compounds ranging from 1.70 to 1.92[189,190]

3.2.3 Surface topography

Besides using AFM as a method to determine the thickness of the polyphenolic coatings, we also used this method to image the surface topography and calculate the surface roughness. AFM offers a very high spatial resolution of up to 1 nm by using piezoelectric drivers. The downside of this contact-based method is creating artifacts on steep inclines or surface features the cantilever tip cannot reach due to its own shape.[191] Further, the scan area is below 100 µm × 100 µm. Thus, we used profilometry and scanning electron microscopy (SEM) as complementary techniques to describe the surface morphology on a larger length scale. While SEM only allows qualitative images for visualization of surfaces, profilometry also offers quantification of surface roughness. Using a 20 × objective, the area measured by profilometry is approximately 850 µm × 700 µm. The spatial resolution of optical measurements depends on the wavelength, properties of the objective, and the image sensor.[191] Therefore, profilometry typically has a lower resolution than AFM. In contrast to AFM, profilometry is contactless and allows measurements of complex surfaces. Depending on the scale of the roughness, different measurement modes are available. As mentioned previously, the influences in surface roughness by variations of the substrate were minimized by using Si wafers. On these smooth surfaces, roughness measurements were conducted in interferometry mode.

3.3 Analysis of the surface chemistry

3.3.1 Structural chemistry

In the further analysis of the chemical structure, SEM was used in combination with energy dispersive x–ray spectroscopy (EDS) to obtain an initial estimate of the elemental composition. EDS allows the analysis of characteristic X–rays generated by the interaction of atoms with the electron beam. While SEM can offer a high spatial resolution, EDS detectors only allow the detection of elements in relatively low resolution due to the high interaction volume of the electron beam. During the analysis of nanometer thick coatings, the signal is mostly dominated by the underlying substrate. Therefore, a more surface-specific technique was

required. To evaluate the presence and chemistry of silica in the coatings, we used X–ray photoelectron spectroscopy (XPS). Similar to EDS, XPS is a method which characterizes the elemental composition, but with a typical probing depth of 10 nm, XPS is much more surface sensitive.[192] In contrast to SEM–EDS, XPS uses a defined monochromatic X–ray beam to eject electrons from atomic orbitals. The characteristic energy of electrons is then analyzed in either hemispherical or cylindrical detectors. Hemispherical detectors are highly energy sensitive and allow conclusions on the binding state of atoms.[193] Cylindrical detectors are less sensitive to the binding energy but allow mapping of specific elements across the surface. Also the spatial resolution of these detectors is relatively low with 3 µm. Since this resolution was not high enough to exclude that the signal originated from silica particles, previously observed in SEM, complementary time-of-flight – secondary ion mass spectroscopy (TOF–SIMS) analysis was performed. This method allows a higher spatial resolution by irradiating the sample surface with a focused Ga^+ ion beam similar to the electron beam in SEM.[194] The fragments ejected from the surface are then analyzed by mass spectroscopy. Thereby, we addressed the distribution of Si within the polyphenolic coatings.

In addition to mapping individual elements, TOF–SIMS can also be used to analyze the structural integrity of the polyphenolic molecules in the coating. In contrast to mapping experiments using Ga^+ ions, C_{60} clusters were used to eject fragment from the surface.[195] Irradiation with C_{60} clusters lead to softer ionization of the polyphenolic molecules and lower fragmentation compared to Ga^+. However, the obtained spectra mainly showed low molecular weights fragments below 600 Da (**Figure A5**). Since we wanted to verify whether TA maintained its structure and molecular weight up to 1700 Da, an alternative method with less ionization energy had to be used. Thus, we utilized the low energy of matrix-assisted laser desorption ionization – time-of-flight mass spectroscopy (MALDI–TOF) to ionize components of the coating.[196] Therefore, stainless steel MALDI–TOF plates were coated. In the subsequent analysis using 2,5-dihydroxybenzoic acid (DHB) as matrix, the high molecular weight components of TA were verified (**Figure A6**).

As an alternative to studying the molecular structure in the coating, molecules in solution can be analyzed by liquid chromatography (LC), which separates compounds according to their polarity. Often, a comparison of the sample to internal standards, such as gallic acid, can result in an estimate of the eluted compound. However, only coupling to a mass spectrometer (MS) allows the analysis of unknown compounds in more detail. In the study of oxidative polymerization products of polyphenols, the drawback of the LC–MS system was the sensitivity of its electro–spray ionization (ESI) unit to inorganic ions. Since the coating solutions contain a high amount of salts, these cause contamination of the ion source.[197] In order to separate salts before MS analysis, the first part of the eluting solution was discarded. This bears the possibility of excluding parts of the components from the analysis.

Since elemental composition and mass fragments are ambiguous and difficult to interpret, functional groups were studied by their distinct molecular vibration pattern. Therefore, ATR–FTIR spectroscopy was used to investigate the structural chemistry of coatings. As described earlier the principle of FTIR spectroscopy is to measure the absorption of IR light by atomic bonds. Thus, the IR beam has to penetrate the material of interest. In contrast to solid bulk material, thin

films with a thickness in the range of nanometers result in poor signal yield. This could be counteracted by using a grazing angle ATR module or multi-bounce ATR modules. Both systems increase the interaction path length and reduce interfacial reflectivity to obtain an improved signal.[198,199] Probing characteristic bands for polyphenol oxidation in coatings was possible, but less pronounced peaks, for example originating in the interaction of Si with polyphenols, could not be detected. As complementary technique to study functional chemical groups, Raman spectroscopy was used. However, as an inelastic scattering technique, Raman spectroscopy often has a low signal strength.[200] Hence, evidence for interaction between polyphenols and Si could not be obtained due to weak Raman absorption of Si components.[201] Further, the Raman laser quickly caused sample degradation and elicited background-fluorescence of the phenolic coating (**Figure A7**).

Since neither Raman nor FTIR spectroscopy were able to detect Si bonds, NMR was the only option to elucidate the role of Si in the formation of TA coatings. In contrast to studying the oxidation of polyphenols in solution by liquid state NMR, we now focused our interest on the solid coating. Since solid compounds cannot be probed with conventional NMR, a solid-state nuclear magnetic resonance (ss-NMR) technique had to be employed. ^{29}Si magic angle spinning NMR (MAS–NMR) was then used to analyze the specific Si bonds. To probe the coating, we deposited polyphenolic layers on TiO_2 carrier particles. By limiting the coating time to 2 h, polymerized polyphenol particles could be excluded from the analysis. In contrast to conventional NMR, MAS–NMR generally has a lower signal strength. Further, the low amount of coating per TiO_2 particle reduces the signal strength. Last, the natural abundance of NMR–active ^{29}Si is only 4.67 %. To improve the NMR signal, the coatings were prepared with a ^{29}Si enriched coating solutions. Therefore, $^{29}SiO_2$ was dissolved in NaOH and added to the coating solution before pH adjustment. After the coating deposition, the TiO_2 were filtered off, washed, and dried before MAS–NMR measurements.

3.3.2 Physical surface chemistry

The difference in structural chemistry of polyphenolic coatings further manifests in the apparent physical properties of the modified surface. These surface properties, such as wettability, surface energy, and surface zeta potential, are important factors determining the adsorption of proteins and molecules that form the initial conditioning film on implant surfaces. Surface wettability describes the spreading behavior of a liquid on the surface and can be quantified by measuring the contact angle that defines the shape of a liquid droplet on the surface. Since the wettability is influenced by the roughness of the surface, contact angles were measured on optically flat Si wafers to eliminate the influence of varying surface morphology.[202] On ideal flat surfaces, the contact angle (Θ) can be correlated to the surface energy (γ_S) according to Young's equation, which describes the force equilibrium at the phase boundary.

$$\gamma_S = \gamma_{SL} + \gamma_L \cos\Theta \tag{3.8}$$

By measuring several contact angles of different liquids with known interfacial energies (γ_L), the surface energy can be deduced via linear regression. There

are different models for the calculation of surface energies. These models either take polar and dispersive components or acid-base reactions into account.[203] To accounts for both polar and non-polar interactions of polyphenols with biomolecules, the universal model by OWRK was chosen. This model includes polar and dispersive forces for both the liquid and the solid surface according to Equation 3.9. In the OWRK model, the polar part (γ^{P}) of the surface energy is derived from the intercept (a) and the dispersive part (γ^{D}) from the slope (m) in the linear equation $y = mx + a$.[204] Addition of γ^{D} and γ^{P} then results in the total surface energy.

$$
\begin{gathered}
y = \frac{1 + \cos\Theta}{2} \cdot \frac{\gamma_L}{\sqrt{\gamma_L^D}} \\
x = \sqrt{\frac{\gamma_L^P}{\gamma_L^D}} \; ; \quad m = \sqrt{\gamma_S^P} \; ; \quad a = \sqrt{\gamma_S^D} \\
\gamma = \gamma^P + \gamma^D
\end{gathered}
\tag{3.9}
$$

However, wettability studies do not fully describe the surface properties of the coatings especially for polar surfaces, which can have different charges. Therefore, the apparent surface charge, commonly known as the surface zeta potential, was obtained via electrophoretic light scattering. The principle of this method is based on the mobility of tracer particles in an electrical field depending on the distance to the surface.[205] For a correct analysis of the electro–osmotic flow (EOF), the tracer particles should not interact with the surface. Therefore, negatively charged colloidal polystyrene beads ($\varnothing = 100\,\mathrm{nm}$) were used. Due to the application of an electrical field, the conductivity of the solution has to be set below $1\,\mathrm{mS\,m^{-1}}$, which corresponds to a 10 mM NaCl solution. This means that coating conditions at 600 mM NaCl cannot be achieved with this method. This is important since the zeta potential depends on the concentration of ions.[206] This limitation is common to all EOF based techniques, and the zeta potential at high salinity can only be measured indirectly by extrapolation.[207,208]

3.3.3 Antioxidant properties

As described in the introductory chapter, the antioxidant properties of polyphenolic compounds are in part associated with their ability to scavenge radicals.[144] For the quantification of the antioxidant capacity of polyphenols the reduction of the $\mathrm{ABTS}^{\bullet+}$ radical cation was measured.[209] This is a colorimetric assay suitable for water-soluble antioxidants, such as TA and PG used in this work. Alternatively, lipid peroxidation and antioxidant assays are often described in literature.[210] However, in these methods, polyphenols have to be dissolved in non-polar solvents, such as EtOH. Since the coating was intended to have antioxidant properties in aqueous environment, the ABTS assay was chosen. The antioxidant capacity of pristine polyphenols was determined by normalization to trolox. Trolox is a vitamin E analogue with antioxidant properties commonly used in literature as positive control in antioxidant assays. Thereby, results expressed as trolox equivalent anti-oxidant capacity (TEAC) can be compared to values in literature.

The assay was also used to determine the antioxidant performance of the coated surfaces. The coated coins were incubated in the solution and the reduction

in absorbance of the supernatant was subsequently measured. For the assay with coatings, a pooled sample setup was chosen in which several coins per group were incubated with 1 mL solution per coin. From this bulk solution, 200 µL aliquots were then analyzed over a period of time. Pooling several coins per group increases the volume and ensures that removing several aliquots is not significantly affecting the overall volume per group. Adjusting the volume after taking the aliquots changed the absorbance and was therefore avoided. While the quantification by spectrophotometry only allows the quantification of the bulk supernatant, a radial diffusion experiment showed that coated surfaces release polyphenolic molecules (**Figure A8**). For this experiment 40 µL mL^{-1} was added to a 1.5 % agarose solutions and the gel was casted in 6-well plates. However, the quantitative analysis of pictures, taken over 24 h, is often complicated due to varying light conditions and a gradual diffusion front.

3.4 Polyphenolic radical formation

The radical formation of polyphenolic molecules is not only important for the antioxidant properties, but it is also considered to play a major role in the oxidation of polyphenols and the subsequent coating formation.[146,211] The formation of polyphenolic radicals was investigated by electron paramagnetic resonance (EPR) spectroscopy, which allows a direct analysis of unpaired electrons. In comparison to many short-lived reactive radicals, such as $^{\bullet}OH$ or $^{\bullet}O_2^-$, studying of polyphenolic radicals by EPR is much simpler due to their high stability. Thus, the measurement of phenolic radicals is possible without using spin-traps. Polyphenols were dissolved in water without the addition of buffer molecules, which could potentially interact with radicals. The radical formation was then initiated by adjusting the pH immediately before the analysis to avoid a time-dependent change in radical intensity. Further, equal mixing and oxygen uptake was taken into account for all samples to guarantee constant conditions. The samples were then taken up in capillaries, which were placed in the sample cavity of the EPR instrument.

The principle of EPR is similar to NMR. However, EPR probes the energy of electrons upon interaction with a static external magnetic field.[212] This Zeeman effect causes the electron spin to align either parallel or anti-parallel (**Figure 3.4**). Both states are different in energy, which can be probed by applying an electric field according to Equation 3.10.[212] The electric field, described by Plank's constant(h) and the frequency (ν), correlates to the electron specific g-value, the Bohr magneton (μ_B) and the magnetic field (B_0).

$$E = h\nu = g\mu_B B_0 \tag{3.10}$$

Interaction of free radical electrons with their surrounding atoms further becomes evident in the hyperfine structure of the signal (**Figure 3.4**). Depending on the number of chemical equivalent nuclei (N), a number of hyperfine lines are obtained according to $2\,N \cdot I + 1$.[213] In the case of polyphenolic molecules consisting of C, O, and H, the interaction pattern can be simplified since ^{12}C and ^{16}O have a spin I = 0. Hence, only H atoms with spin I = 1/2 contribute to the spectra. However, due to the delocalization of the electron system in polyphenolic molecules, the radical electron can couple to either equivalent or non-equivalent

protons. The resulting splitting pattern can be predicted using a binomial tree illustrating the multiplicity and intensity of the obtained signal (**Figure 3.4**). From the resulting spectra, various parameters describing the coupling constants, were then modeled using isotropic EPR simulation software. Thereby, the location of the free electron can be determined.

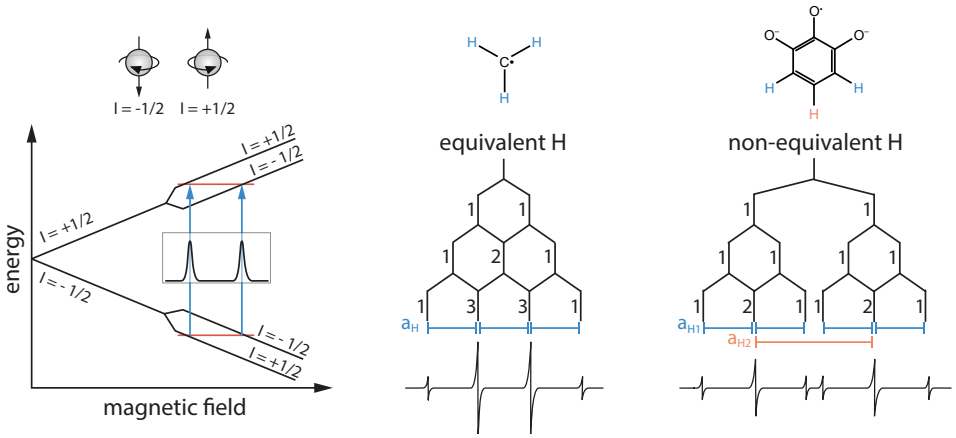

Figure 3.4: Electrons with spin $I = \pm\frac{1}{2}$ align parallel or anti-parallel to an external magnetic field. Upon interaction of the electron with other nuclei, the energy splits again depending on the alignment of the spin. This causes a hyperfine structure of the EPR signal. Nuclei with high spin density cause a high splitting constant (a_{H2}), whereas nuclei with lower spin density result in a lower value a_{H1}.

Since EPR is very sensitive in detecting different radicals, it is important to test pure chemicals. Since commercial TA also contained GA, as pointed out earlier (**Figure A1**), it was necessary to separate GA from TA by liquid chromatography. The TA fraction was collected, reduced under vacuum, and freeze-dried to avoid degradation. As reference for the TA EPR signal, we used pentagalloyl glucose (PGG).

3.5 Protein interactions with polyphenolic surfaces

The adsorption of a protein conditioning film occurs as the initial process after placing any object into human tissue. In the case of dental implants, this conditioning film originates from blood plasma and saliva. As described in the introduction, the surface-dependent adsorption of different proteins directs the foreign body response.[83,84]

We studied the formation of protein layers on polyphenolic surfaces by QCM–D to assess whether the coatings change the structural properties of the adsorbed protein layer. A fundamental understanding of the composition of this protein film may eventually allow the prediction of the host response. Proteins, saliva, and blood plasma were diluted in phosphate buffered saline (PBS) at pH = 7.0 to study the adsorption, without instantly saturating the sensor surface. The experiments were performed at 21 °C instead of physiological 37 °C due to degassing of water upon heating in the instrument chamber. In experiments, which last longer than

1 h, air bubbles form and distort the QCM–D signal. Further, the QCM–D signal is temperature-dependent and a switch in temperature during a measurement would require a calibration for each experiment. In addition, the viscous properties and density of the buffer influence QCM–D signal. This influence was reduced by forming the coatings in phosphate buffer instead of HEPES. Yet the change in ionic strength affecting the density of the buffer had to be compensated. Therefore, the baseline for the coating buffer and the protein buffer was recorded on the clean sensor before each experiment. After the coating deposition, a rinsing step with the protein buffer was conducted for up to 1 h until the signal was stable. Subsequently, the adsorption of proteins was recorded.

The protein layer was then analyzed using Voigt viscoelastic modeling as described in subsection 3.2.1. While the mass of the protein layer is rather simple to obtain, the structural and conformational changes are not straight-forward to interpret. Computing the viscoelastic properties of adsorbed protein layers results in the complex shear modulus (G). It is composed of the storage modulus (G') and the loss modulus (G''), according to Equation 3.11.

$$\begin{aligned} G &= \mu + i2\pi\eta f = G' + iG'' \\ tan(\theta) &= \frac{G''}{G'} \end{aligned} \tag{3.11}$$

Analysis of the loss tangent ($tan(\delta)$) can be used to quantify whether the layer behaves more solid-like ($tan(\delta) < 1$) or liquid-like ($tan(\delta) > 1$). However, this notation is strictly only allowed for Newtonian fluids.[214] Further, the required modeling of the adsorbed layer has to take the frequency dependent rheological properties of adsorbed films into account.[215] This limitation is overcome by a frequency-dependent shear (μ) and viscosity (η) model. It is obvious that mathematical modeling of complex protein layers is highly dependent on the model parameters and assumptions made. Therefore, changes in frequency and dissipation can also be obtained by analysis of $\Delta D/\Delta F$ plots.[179] This allows for a more qualitative analysis based on the shape analysis. Further, slopes derived from the obtained curves can be used to compare the adsorption behavior of proteins on different surfaces.

Although QCM–D is a powerful technique for studying adsorption, it lacks the ability to give a quantitative answer regarding the individual components adsorbing from complex protein systems. Further, denaturation of the protein upon adsorption to a surface cannot be measured and requires other methods, such as circular dichroism.[216] For a more precise answer regarding the composition, an attempt was made to form protein pellicles on Ti coins with subsequent desorption and sodium dodecyl sulfate polyacrylamide gel electrophoresis (SDS–PAGE) analysis (**Figure A9**). However, the dynamic range to resolve especially the low concentrated components is limited. Either weak bands are dominated by the high content of proline rich proteins or they disappear once the total protein concentration is reduced. This drawback may be resolved by a proteomic analysis based on HPLC.

3.6 Blood compatibility

Following the non-specific protein adsorption, the foreign body response is triggered by activating the complement and coagulation system. The complement system is part of the innate immune system, and affects inflammation and stimulates leukocytes. The coagulation system initiates the formation of a blood clot, which serves as a provisional tissue matrix for wound healing. To study how polyphenolic coatings alter the response of the complement and coagulation system, blood samples were taken and incubated with coated Ti coins as shown in **Figure 3.5**. Complement and coagulation activation was assessed after 30 min since these processes happen quickly after the initial contact of blood with the surfaces. Similarly, the activation of monocytes, granulocytes, and platelets was determined after 30 min to evaluate the response directly after contact with the surface. In contrast, cytokine expression was determined after 4 h, allowing cells to react to stress signals.

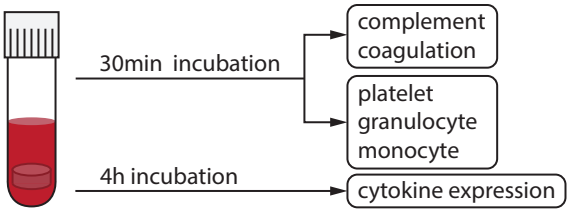

Figure 3.5: To analyze the host response towards polyphenolic coatings, coatings were incubated with human whole blood. After 30 min, the activation of the complement and coagulation system was assessed by ELISA. Further, the activation of monocytes, granulocytes, and platelets was quantified by flow cytometry. After 4 h, the expression of inflammatory cytokines was determined by multiplex analysis.

Coagulation activation markers TAT and F1+2 were quantified by enzyme linked immunosorbent assay (ELISA) to determine the activation in the common pathway of the coagulation system (**Figure 1.3**). Similarly, complement activation markers were analyzed using ELISA kits detecting the markers of the classical pathway (C4d), the alternative pathway (C3bBbP), and the final cell lysis complex (TCC). Sample dilution is an important factor during the quantification of these markers by sandwich ELISA. Since the assay uses well plates with pre-adsorbed antigens, saturation can occur if the sample concentration is too high. Thus, the experiments were conducted in appropriate dilution, which was later corrected for during the calculation of the expressed markers.

To supplement the data on activation markers for the coagulation and complement activation, the response on a cellular level was determined by studying the activation of monocytes, granulocytes, and platelets. Therefore, the cells were stained for activation markers on the cell membrane and analyzed by flow cytometry. Platelets were discerned from granulocytes and monocytes by expression of CD42 compared to CD45/CD15 for granulocytes and CD45/CD14 for monocytes. Activation of granulocytes and monocytes was quantified by CD11b and CD35 staining, respectively. Platelets were stained for two markers to determine their activation (CD62P) and change in morphology (CD63). As an alternative to flow

cytometry, a qualitative assessment of platelet activation based on the morphology could have been conducted by SEM. Visual inspection may, however, be biased by the operator compared to flow cytometry, where a large cell population can be assessed. However, flow cytometry may tent to quantify suspended non-activated cells, as activated platelets stick to the surface. Thus, incubated surfaces were extensively washed with PBS before sample transfer.

The subsequent inflammatory response of the activated blood cells was studied by measuring the expression of cytokines and chemokines after incubating blood with surfaces for 4 h. The response was quantified by a multiplex assay using a panel of 27 markers associated with inflammation. Multiplex generally relies on the same principle as ELISA. However, multiplexing is faster when several markers are determined in one experiment. Since the different antibodies are immobilized on color-coded polymer beads instead of a well plate, samples can be incubated with a mixture of different beads binding potential markers. Thereafter, fluorescent labeling with a detection antibody produces an active signal response. While Luminex beads are separated and individually analyzed by a flow cytometer, MagPix magnetic beads are captured with a magnet and evaluated by imaging. Magnetic beads have the advantage of being easily captured during sample preparation, when washing steps are required.

Since the experiment was designed in a way that all activation markers were analyzed from the same sample (**Figure 3.5**), a positive control, which can activate complement, coagulation, and inflammatory cytokine expression needed to be used. In this work, *E. coli* was used. While *E. coli* is a good positive control for inflammatory response and complement activation, it is not ideal as a positive control for coagulation. However, bare Ti itself can be used as positive control since it is a highly thrombogenic surface.[217] Alternatively, kaolin could also have been used for coagulation activation.

3.7 Cellular response

3.7.1 Cytotoxicity and genotoxicity

In the wound healing process, the provisional blood clot is subsequently remodeled by fibroblasts, which form granulation tissue to seal the wound.[218] The biocompatibility of polyphenolic molecules was first tested since interactions of polyphenols with cell membranes could lead to cytotoxic effects. Therefore, the lactate dehydrogenase (LDH) activity was measured. LDH is an enzyme in the cytosol of most cells. The assay primarily tests if the cell membrane is damaged upon which LDH is released into the culture medium. Since this assay does not determine whether cells are metabolically active, it cannot indicate whether polyphenols impaired the cells in other ways such as causing apoptosis or a cell circle arrest. For these specific tests, a variety of other assays is available, such as the MTT assay.[219] The advantage of the LDH is the simple colorimetric quantification of LDH activity in the cell medium in comparison to live/dead staining of cells for imaging or flow cytometry. The assay is also non-destructive to the sample, which allows further analysis of the cells in separate experiments.

Although polyphenolic molecules may not cause immediate cell death, their accumulation in the nucleus may have genotoxic effects based on their interaction

with DNA. Mutagenic effects are particularly known for the oxidized quinone forms of polyphenols, which cause DNA damage.[220] Hence, DNA damage was studied by a comet assay. This test separates intact DNA in the nucleus (comet head) from strand breaks that create the comet tail via electrophoresis. This method is highly sensitive and can be conducted in either neutral or alkaline condition.[221] In this study, the alkaline condition was chosen as it detects both single- and double-strand breaks. Analysis of the intact DNA in the comet head versus the damaged DNA in the tail area of the comet was performed with the OpenComet plug-in for ImageJ. The tool analyzes images of comets based on the intensity of the comet or its shape. The image quality and alignment largely dictate the ability to detect comets correctly. Since out-of-focus comets and misinterpreted comets contribute to a high error rate, they were manually removed from the analysis.

3.7.2 Intracellular reactive oxygen species

Although polyphenolic molecules may show antioxidant properties in the ABTS assay, interaction with proteins and other cellular components may reduce the capacity to scavenge intracellular radicals *in vitro*. To quantify the ability of polyphenols to reduce oxidative stress, intracellular ROS was quantified with a cell membrane permeable stain. A popular cell permeable stain for this purpose is H_2DCFDA. This stain is, however, susceptible to the presence of serum.[222] In contrast, CellROX stains are compatible with serum-containing cell medium. Oxidative stress was elicited by tert-butyl hydroperoxide (TBHP), as model for ROS released by leukocytes, and LPS.[223]

In an initial test, we imaged stained cells and obtained a rather inhomogeneous staining. Thus, analysis by flow cytometry was conducted to evaluate a more representative cell population. However, experiments with CellROX–Green showed a high background signal of the cells. Therefore, CellROX–DeepRed was finally used, as the unstained cells did not emit any background fluorescence at the detection wavelength of the stain. We still noticed background signal the in non-inflamed cells, which could originate from sample handling and the stress induced during the trypsination and resuspenion of the adherent fibroblasts for flow cytometry. Since CellROX–DeepRed mainly accumulates in the cytosol, co-staining the cell DNA with propidium iodide (PI) allowed for the distinction between live and dead cells. CellROX stains are unspecific towards ROS, meaning they quantify all oxygen radicals. This is beneficial if the radical type is not known or the total oxidative stress should be addressed. To discern specific stress factors, such as superoxide, nitric oxide, or hydrogen peroxide, specific ROS or reactive nitrogen species (RNS) stains have to be used.[224]

3.7.3 Anti-inflammatory effect

Besides reducing intracellular reactive oxygen species, polyphenols reportedly inhibit the inflammatory signaling pathways in cells. Thereby, the inflammation caused by either pathogens or trauma could be relieved to improve wound healing. Since the soft tissue around the implant is particularly prone to invasion of oral bacteria, we tested whether polyphenols reduce the inflammatory response in human gingival fibroblasts (hGFs) stimulated by LPS derived from *P. gingivalis*.

Cells were seeded on coated Ti coins and incubated for 2 h to allow cell adhesion. Subsequently, LPS was added to the cell culture medium to induce inflammation. However, the primary hGFs used in the cell experiments did not respond to LPS. After testing several batches of LPS and successfully evoking an inflammatory response in human osteoblasts (hOBs), we chose to induce inflammation in hGFs by IL-1β. IL-1β is a pleiotropic cytokine expressed in a variety of cells upon infection and injury.[225] Hence, assessing the expression of inflammatory cytokines upon stimulation with IL-1β shifts the analysis towards the trauma-induced inflammation.

The expression of pro-inflammatory markers and the activation of the NF-κB signaling pathway was assessed by multiplex and ELISA, respectively. Since cytokines are expressed and released into the cell culture medium after the inflammatory stimulus has been processed, the levels were quantified after 6 h, 24 h, and 48 h. In contrast to cytokine expression, phosphorylation of NF-κB requires cell lysis and thus, the temporal activation cannot be obtained for the same sample. Further, activation of the NF-κB signaling pathway occurs early after stimulation with IL-1β. Therefore, 0.5 h, 1 h, and 2 h time points were chosen for analysis.

3.8 Adhesion and biofilm formation of *Candida albicans*

The oral microbiome consists of a broad variety of micro-organisms which can colonize surfaces in the oral cavity including implants.[226] Some species form biofilms, which can harbor different commensal and pathogenic bacteria.[67] These multi-species biofilms pose a risk for the infections and inflammation of the gingival tissue. A commonly neglected micro-organism forming oral biofilms is *C. albicans*. Recent studies have shown that this fungus may play an important role in oral health as it can facilitate the adhesion of other oral pathogens.[227] Therefore, the effect of polyphenolic coatings on the growth and adhesion of *C. albicans* was assessed.

Growth inhibition of *C. albicans* was assessed in a biofilm model in which coins were incubated with yeast cells at 37 °C (**Figure 3.6**). After 6 h, 24 h, and 48 h the coins were rinsed and sonicated to determine the amount of cells in early, mature, and late biofilms.[228] In order to quantify the cell growth, a *C. albicans* strain which expresses click beetle luciferase during activation of the ACT1 gene was chosen.[229] ACT1 is a housekeeping gene responsible for the transcription of the cytoskeletal protein actin. This enables the assessment of the overall growth associated with ACT1, which is proportional to the amount of expressed luciferase.

The cell growth was then quantified by luminescence reading. Therefore, luciferin has to be supplemented as substrate for luciferase. However, luciferin is not cell permeable and cell lysis is required for the analysis at discrete time points. This increases the necessary steps and the required time for the analysis compared to other methods, such as the colorimetric detection of the metabolic activity by a XTT assay. Yet, this method is a simple alternative for assessing gene expression compared to polymerase chain reaction (PCR) analysis. However, in our study, we observed that the number of cells in biofilms was not high enough to produce a distinguishable luminescence signal. Therefore, colony forming units (CFUs), optical density (OD), and total biomass were also quantified to support the luminescence data. Further, the biofilms were fixed and dehydrated to image

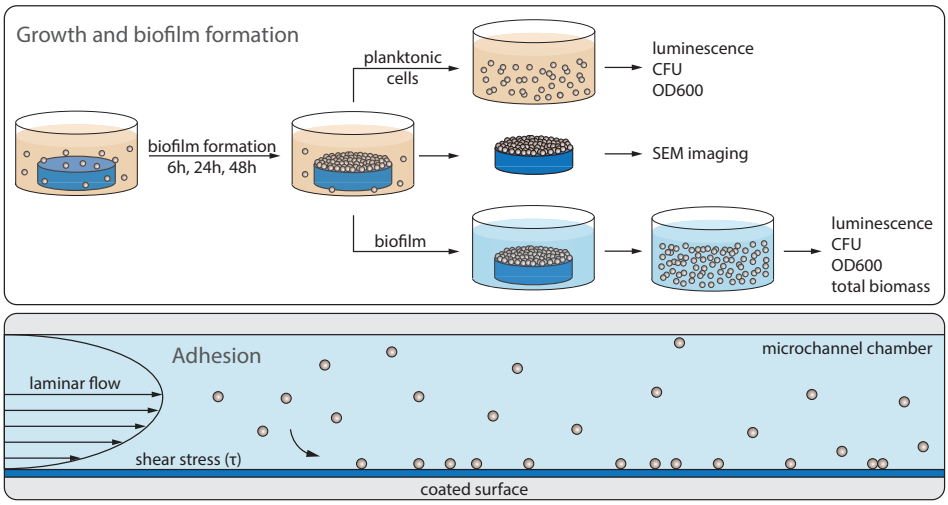

Figure 3.6: Experimental setup to determine the growth and adhesion of *C. albicans*. Biofilm formation was assessed after incubating fungal cells for 6 h, 24 h, and 48 h on coated Ti coins. The adhesion was studied using microchannel slides under constant flow resulting in shear forces of 0.1 dyn cm^{-2}.

the cells by SEM. However, the biofilms were found to disrupt during the sample preparation for SEM. Thus, the biofilm should be imaged, for example, by confocal microscopy after staining the cells with SYTO–9 dye.

In this work, the growth rate of *C. albicans* was determined in yeast–peptone–dextrose (YPD) medium at 37 °C. These conditions favors the growth of the fungus in yeast form. For a more virulent filamentous growth, hyphae formation can be induced by supplementing serum, or changing to anaerobic culture conditions.[230,231] For this purpose, the *C. albicans* HWP17 strain is also available with modifications encoding the luciferase sequence in relation to EFG1 and HWP1 promotors. Thereby, filamentation and hyphae formation of *C. albicans* can be studied by luminescence on a gene level.

Besides inhibition of fungal growth, reduced adhesion may also curb the colonization of implant surfaces. Since the oral cavity is subject to salivary flow, an experimental setup was chosen where cells are subject to constant flow in a microchannel (**Figure 3.6**). A key factor in studies determining the adhesion of cells under flow condition is the flow speed, which determines the shear stress of cells on the surface. In the oral cavity, the shear stress can reach up to 1 Pa (10 dyn cm^{-2}).[232] However, in interstitial spaces, the fluid flow may be lower and biofilm models typically adopt shear stresses in the order of 0.1 dyn cm^{-2}.[233] Thus, a flow chamber was chosen that elicits a fluid shear stress (τ) of 0.1 dyn cm^{-2} under a flow rate (Φ) of 100 µL min^{-1} and the dynamic viscosity (η) of PBS according to Equation 3.12.[1] Laminar flow was confirmed according to the Reynolds number ($Re = 10$), correlating the fluid density (ρ), η, and the flow speed (v) of PBS with the hydraulic diameter (D_H) of the flow chamber (Equation 3.13).

[1] 104.7 = empirical value for 0.4 mm channel slides provided by the manufacturer

$$\tau = \eta \cdot 104.7 \cdot \Phi \tag{3.12}$$

$$Re = \frac{\rho \, v \, D_H}{\eta} \tag{3.13}$$

To monitor the adhesion of fungal cells using fluorescent microscopy, *C. albicans* was dispersed in PBS. The stock solution was diluted to OD600 = 0.03 and stained with SYTO–9 dye. The stained cells were then continuously flown through the microchannel slide at a flow speed of 100 µL min^{-1} and the adhesion was monitored for 30 min until the surface was saturated. To further mimic surfaces in the oral cavity, a salivary pellicle was formed on coated substrates for 30 min before the yeast cells were allowed to adhere. Several images were then taken after rinsing with PBS and adherent cells were counted by ImageJ software.

Chapter 4

Summary of Key Findings

4.1 Chemistry of polyphenolic coatings

In Paper I, the use of silicic acid (Si_{aq}) for a surface independent formation of TA coatings was shown for the first time. The TA coating formation depended on the Si_{aq} concentration and was most effective around 100 µM. Compared to Si_{aq}, boric acid inhibited the coating formation and the polymerization reaction of TA without influencing its oxidation reaction. Germanic acid on the other hand enabled the deposition of TA, but it caused more precipitation compared to Si_{aq}. Transition metal cations, such as Fe^{3+} instantly reacted with polyphenols, precipitating and inhibiting any continuous coating formation. While Si_{aq} had no effect on PG and GA deposition, a positive correlation was observed for EA. Since EA possesses two sites with vicinal hydroxyl groups similar to TA, a cross-linking mechanism was proposed.

Direct evidence for the complexation of Si_{aq} with TA in the coating was then obtained by MAS–NMR in Paper II. Once the cross-linking mechanism was established, the requirement for oxidative conditions to deposit TA was questioned. Successful formation of coatings based on such silicate–TA networks in acidic environment proved that oxidation was not required. In addition, the coating formation at slightly acidic levels reduced the formation of byproducts and precipitates caused by the oxidation reactions. Thus, the layer thickness obtained during a 24 h coating process could be increased by approximately 50 %. The kinetic analysis showed a faster initial coating rate in alkaline conditions suggesting the involvement of base catalyzed deprotonation of hydroxyl groups. Hence, a continuously stirred tank reactor (CSTR) type setup was proposed in Paper II to enable a high deposition rate with limited side reactions. The change in pH further allowed us to prepare TA coatings with different oxidation states. TA coatings obtained at pH = 6.8 (TA68) showed less oxidization compared to TA coatings obtained at pH = 7.8 (TA78), as was shown by FTIR and the increasing Ag^{+} reduction on TA68 in Paper V.

In Paper III, we have shown the influence of the ionic strength on the deposition of TA coatings. Besides investigating the ionic strength, we also showed how the type of cation in LiCl and KCl impairs the layer formation compared to NaCl. K^{+} primarily results in strong cation-π interactions and precipitation of TA in the range of pH = 6 to 11, whereas Li^{+} inhibited the coating formation. The latter was mainly attributed to the hydrolytic action of Li^{+} forming GA radicals. In addition, we observed potential interaction between Li^{+} and Si_{aq} using QCM–D.

In contrast to the cross–linked TA network structures, PG coatings were based on auto-oxidative polymerization. Despite the oxidation reaction, pyrogallol coatings obtained at pH = 7.0 (PG70) were equally antioxidant as TA68 coatings (Paper V). The difference between the coating mechanisms of these polyphenolic molecules was also reflected in the obtained layer density. TA layers were less

dense and more hydrated than PG layers. Consequently, the different formation mechanisms and layer properties affected the stability of the coating under different pH conditions. Silicate–TA networks were more susceptible to disassembly at low pH values compared to PG coatings, as shown in Paper IV. In regard to surface chemistry, both TA and PG coatings were hydrophilic and negatively charged (Paper V).

4.2 Biological response

4.2.1 Effect on early wound healing processes

In Paper IV, we have shown how Ti surfaces coated with TA and PG may impact the foreign body reaction. Upon initial contact of the modified surfaces with blood, plasma protein adsorption was increased compared to Ti. The coatings changed particularly the adsorption kinetics of principal blood components, such as albumin, fibrinogen, and immunoglobulin G (IgG). The altered conditioning film subsequently affected the innate immune response. Activation factors for both the classical (C4d) and the alternative (C3bBbP) complement pathways were found. However, the coatings reduced the formation of TCC, suggesting the inhibition of the subsequent amplification cascade. In contrast, high concentrations of TAT and F1+2 verified that the blood coagulation was not affected. These results were corroborated by activation of platelets. In contrast, monocytes and granulocytes were not activated, which was in accordance with a low expression of inflammatory cytokines.

We found that the antioxidant properties of TA and PG were maintained in TA68, TA78, and PG70 coatings. Studying the response of hGFs towards the polyphenolic coatings attested their cytocompatibility but showed signs of DNA damage in the cells. In contrast, the capacity of the coatings to scavenge radicals resulted in the reduction of intracellular ROS after the exposure of hGFs to TBHP. TA68 showed best protection against oxidative stress amongst the tested coatings, due to their less oxidized nature and higher amount of released molecules compared to TA78 and PG70. None of the modified surfaces were able to inhibit the LPS/IL-1β induced inflammatory response in hGFs. The proposed inhibitory mechanism by blocking the NF-κB signaling pathway was not observed.

4.2.2 Antimicrobial activity

In Paper V, the inhibition of surface colonization of *Candida albicans* by polyphenolic coatings was investigated. The growth and biofilm formation of *C. albicans* was not affected by either TA68, TA78, or PG70 due to a low concentration of released molecules. Although we observed a slight reduction of fungal cell adhesion on the coatings, the colonization could not be inhibited under flow condition. To mimic the oral environment the formation of salivary pellicles on coated surfaces was studied. We found that the structure of the protein film was influenced by the coatings. However, *C. albicans* adhered to the protein layer similarly to the bare polyphenolic coatings. Despite the adhesion of the *C. albicans* cells was not inhibited, the pH-responsive disassembly of polyphenolic layers allowed to detach adherent yeast cells.

Chapter 5

Discussion

Dental implants are transmucosal implants and their interface is constantly challenged by microbial invasion in the oral cavity. To ensure that microbes do not colonize the implant surface, control of the early phase in wound healing is important to form a close seal between the wound and the oral environment, resulting in a well-integrated implant. Although titanium dental implants are for the most part fully osseointegrated, peri-implant mucositis and peri-implantitis still affect a significant portion of the patients.[234] Particularly, patients with a history of periodontitis or autoimmune diseases show a higher prevalence of peri-implantitis, due to impaired wound healing and chronic inflammation caused by infection of the peri-implant soft tissue.[41]

To support tissue integration of dental implants, a variety of surface modifications have been studied.[9,95] So far, more focus has been put on the bone interface, neglecting the gingival soft tissue.[39] This trend is also represented in current commercially available implants, which feature different topographical surface modifications of the implant body. While increasing the roughness of an implant surface results in a firmer anchoring in bone tissue,[92] the problem with rough or even porous surfaces is that they also present a niche for bacterial colonization.[40,235] Therefore, the interface in contact to the soft tissue is typically smooth. However, this does not promote attachment of connective tissue.[236] In the resulting peri-implant pocket subgingival plaque can be formed.[67]

To counteract and treat infections around dental implants, antibiotics are commonly administered.[60,237] With the emergence of antibiotic resistances, there is, however, a growing risk that this method will no longer be effective and justifiable in the future.

Therefore, alternative strategies need to be developed to support wound healing and prevent microbial colonization of implants. This has led to the emergence of biochemical surface modification to evoke a desired cell response through signaling molecules, growth factors, or bioactive drugs tethered to the surface.[95,238] For this purpose, polyphenolic molecules have attracted interest in recent years due to their anti-inflammatory and antimicrobial properties.[132,239] Since these molecules feature the ability to form surface independent coatings,[113] they are potential candidates to create multifunctional biomedical surfaces.

5.1 Formation and characterization of polyphenolic coatings

After the first report on the adhesive properties of polyphenols, studies on the adsorption and coating formation found that a broad array of polyphenolic molecules are able to form surface coatings.[113,162] Thereafter, first kinetics studies of the coating formation of TA brought further knowledge on the adsorption process under different conditions.[163,164] These studies suggested that TA and PG coatings were formed via oxidative polymerization under alkaline conditions. However, after

further research we suggested in Paper I that TA coating formation is mediated by aqueous silicic acid (Si_{aq}). This was then confirmed in Paper II, where we showed direct evidence that Si_{aq} acts as a cross-linker of TA molecules (**Figure 5.1**). Thus, coatings based on silicate–TA networks are closely related to the formation of Fe^{3+}-based metal phenolic network (MPN) structures. MPNs have been thoroughly investigated for a facile surface modification of various materials as well as drug encapsulation.[240] Based on the broad research on the physical and chemical interactions of these cross-linked networks,[165,241,242] similarities can be drawn in the behavior of silicate–phenolic networks and MPNs. Both systems depend on the ionic strength and the pH of the coating solution.[243,244] In contrast to Si_{aq}, the complexes of TA and Fe^{3+} form rapidly due to the high affinity of catechol to Fe^{3+}.[245] This renders a continuous deposition of MPN difficult and requires a controlled conversion of Fe^{2+} to Fe^{3+}.[246,247] Besides cross-linking by iron, most other transition metal cations have also been suggested for this purpose.[244] Although the type of cross-linking ion affects the stability of the coordination complexes,[248] the possibility to change the ion allows the use of functional ions. Cu^{2+} or Re^{3+}-based MPNs for example have shown potent antimicrobial properties.[249,250] However, due to the cytotoxicity of some of these transition metal ions, issues with biocompatibility have to be considered.

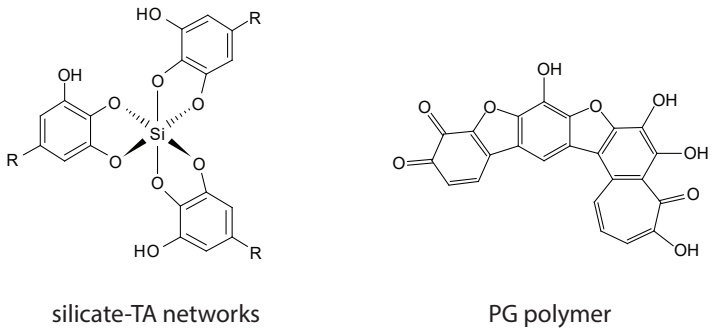

Figure 5.1: TA coatings are assembled trough silica cross-linking. PG coatings form trough the oxidation of PG resulting in irregular polymeric structures.

Although iron-based MPN have been suggested for a variety of biomedical applications,[166] their use for antioxidant and anti-inflammatory coatings is has not yet been well studied. Indeed, it may even be detrimental to use Fe^{3+}-based MPNs in these applications. Since these structures disassemble in acidic environment,[155] potential Fenton reactive Fe ions are released.[130,251] Silicate–phenolic networks also disassemble in acidic environment (Paper IV), but the release of $Si(OH)_4$ may in fact be beneficial in supporting wound healing by increasing the proliferation rate of fibroblasts.[252] Alternatively, boron and germanium can be used as inert cross-linkers. Similar to Si, B and Ge form tetravalent complexes with catechol molecules.[253,254] Using boron, cross-linked TA hydrogels are reportedly formed at pH = 7.4.[255–257] However, we did not obtain TA coatings when using boron as cross-linker (Paper I). In contrast, germanate complexation led to the deposition of TA. However, the most effective deposition of TA was obtained using Si_{aq} for which layers with thickness beyond 100 nm can be formed. The amount of

deposited polyphenolic molecules was of particular interest, since TA and PG coatings previously showed the release of molecules into solution.[172] We harnessed the release behavior and opted for an increase of the mass of the polyphenolic coatings. Thereby, reported concentrations for antimicrobial, antioxidant, and anti-inflammatory properties could be reached.[258–260]

The assembly of MPNs is also affected by the ionic strength.[241,243] Adding inert counter ions is required to overcome the electrostatic interactions of the negatively charged phenolic molecules (TA $pK_a^1 = 7.9$).[116,241] While iron-based MPN are formed under various different ionic strengths and different salts,[241,243] the formation of silicate–phenolic networks was more susceptible to changes in the ionic strength and the type of cation in the coating solution (Paper III). On the other hand, the type of anion was not found to affect the formation of TA coatings (**Figure A2**).[261] In general, cations are more important than anions as they can interact with deprotonated, negatively charged polyphenols and participate in cation-π interactions.[262] These interactions depend on the cation size, electronegativity and hydration shell.[118] Further, factors of the solution, such as the pH and polarity, affect cation-π interactions.[263,264] Such cation-π complexes were observed between TA and K^+, which inhibited the formation of TA coatings in a range from pH = 6 to 11 (Paper III). Li^+ also showed inhibitory effect on the coating formation, however, the mechanism was different to K^+. In solutions containing LiCl, we observed changes in the electronic structure of TA and its hydrolytic cleavage yielding GA. This may be caused by the tendency of Li^+ to form σ–type interactions with catechols compared to a predominantly π–type interaction of Na^+ and K^+.[265]

In comparison to silicate–phenolic networks, PG coatings rely on auto-oxidative polymerization. This mechanism is analogous to the formation of polydopamine coatings and proceeds through radical intermediate steps.[154,160] This radical formation proceeds through proton abstraction in alkaline environment, followed by electron transfer to dissolved oxygen.[138,139,146,266] (**Figure 1.8**). Oxidative polymerization is commonly induced by alkaline pH and dissolved oxygen, but enzymatically driven processes and the use of chemical oxidants are also being investigated.[267–270] An important consequence of the different coating mechanism is the condition in which TA and PG coatings can be deposited. In contrast to oxidative polymerization, we have shown that silicate–phenolic networks also form in anoxic environment (Paper I). In addition, the formation of TA coatings in acidic solutions suggest that oxidation is not required in the formation of silica coordination bonds. Since the requirement for both alkaline pH and dissolved oxygen in the formation of TA coatings was excluded, we suggest that the formation of silicate–phenolic networks does not involve formation of polyphenolic radicals. Yet, the increased kinetics of the TA coating formation at slightly alkaline conditions indicates a base catalyzed process.

While there is direct evidence for the polymeric nature of polydopamine coatings,[271,272] there is a variety of polymeric structures that have been proposed for PG (**Figure 5.1**).[273,274] These structures differ due to the uncontrolled radical-mediated reaction and the formation of cation-π assemblies.[262] In Paper III, we have shown that the formation of PG coatings is also dependent on the type of cation present in the coating solution. While monovalent ions did not inhibit the PG deposition, Mg^{2+} resulted in thicker PG coatings.[164] Mg^{2+} could either

form a more stable cation-π interaction compared to monovalent ions, or support the radical-mediated polymerization through spin stabilization of the radical intermediate.[275,276]

Evidently, the nature of polyphenolic coatings is complex. Due to the broad variety of interactions, the coating formation may not follow a straightforward chemical route. It is likely that ionic interaction and covalent polymerization occur simultaneously, depending on the coating conditions.[277] The variation in chemistry can subsequently affect the properties of the molecules released from the surface. While TA molecules in the silicate–TA networks appear to stay rather intact (**Figure A6**), partial oxidation or hydrolysis of TA can occur, forming EA.[263] The auto-oxidative polymerization of PG allows an even greater variability of formed polymers. Therefore, a more detailed study of the chemical structure of the coatings is required. Since FTIR spectra did not provide sufficient information for a full structural determination (Paper V), mass spectroscopy and NMR of the released molecules may reveal their structure. Fundamental understanding of the structure of the coating and the released molecules is important to correlate their chemical properties with the biologic response of cells and human tissue.

5.2 Effect of polyphenolic coatings on wound healing

Although the structure of polyphenolic coatings is not fully clarified, their ability to change the surface chemistry is used in a variety of biomedical applications.[166,169,170] While some studies have shown improved cell attachment and proliferation on polyphenolic coatings,[278,279] the overall effect of the coatings on wound healing *in vivo* has not yet been reported. Indications for their antioxidant and anti-inflammatory properties are mostly studied in *in vitro* using dissolved polyphenols.[125,280] Further, research using polyphenolic coatings has thus far focused on osseointegration and not on the soft tissue response.[172,281] However, positive results on soft tissue repair have been obtained for the release of polyphenols from hydrogels.[282,283] Thus, modifying implant surfaces with polyphenols as a source of anti-inflammatory molecules may improve wound healing and tissue integration.

However. the polyphenolic surface is not directly exposed to cells. Directly after placing the dental implant, its surface will be covered by blood and saliva. The initial adsorption of proteins and signaling molecules determines the response of cells recruited to the implant surface. Activation of the complement system can trigger the inflammatory response and the coagulation cascade starts to form a blood clot, providing the initial matrix for tissue remodeling. In Paper IV, we have shown how the polyphenolic surfaces change the blood plasma protein adsorption compared to bare Ti surfaces. Since polyphenols can react with proteins and bind them irreversibly, they generally show a high adsorption of proteins.[284] Adsorption of proteins onto surfaces can also induce conformational changes, especially on hydrophobic surfaces.[86] Although polyphenolic coatings are hydrophilic in nature (Paper V), changes in protein conformation on TA surfaces have been reported.[285] Further, we have observed that the irreversible binding of LMW proteins impairs the subsequent adsorption of other proteins (Paper V). This may also affect the cell adhesion, which is facilitated by binding of fibronectin to fibrin during blood

coagulation.[286,287]

Despite the changes in protein adsorption on polyphenolic coatings, our study showed that the coagulation system was equally activated compared to native Ti surfaces.[217] The activation of coagulation is important to form a blood clot, which closes the wound and prevents microbial invasion. Further, the formation of thrombin is also linked to increased osteogenic differentiation enhancing bone formation.[217,288]

While activation of the coagulation is beneficial, the activation of the complement system by the implant surface causes further stimulation of the inflammation in addition to the surgical trauma.[289] The alternative and classical complement pathways are triggered through the adsorption of complement components and antibodies.[26] The subsequent attraction of leukocytes and their inflammatory stimulation can affect the wound healing process.[290,291] In our study, we have observed activation markers for both complement pathways. This is caused by the protein conditioning film, which generally causes adsorption of complement components.[84] However, the formation of terminal complement complex (TCC) was inhibited and monocytes and granulocytes were not activated to express inflammatory cytokines. However, PG70 coatings increased the expression of IL-8, a potent chemoattractant for leukocytes,[292] which could influence the foreign body response.

In case of trauma induced inflammation or microbial invasion of the peri-implant tissue, the antioxidant and anti-inflammatory properties of polyphenols could reduce the further amplification of the inflammatory response and prevent tissue damage. As mentioned previously, TA and PG coatings release molecules from the surface.[172] In particular, the disassembly of TA coatings in acidic conditions could be utilized under inflammatory condition, where local acidosis triggers the release of polyphenolic molecules into the surrounding environment. These released molecules have an anti-inflammatory effect as they scavenge ROS and reduce the intracellular oxidative stress in hGFs (Paper IV). Thereby, the inflammatory feedback loop can be stopped and hGFs can be protected from ROS released by neutrophils and macrophages.[293] In addition, the ROS induced DNA damage in hGFs was reduced in the presence of polyphenolic coatings, which supports their antioxidant properties. However, without external ROS, polyphenols increased DNA damage compared to Ti surfaces. Evidence for pro-oxidant effects of polyphenolic molecules have been reported previously.[149] However, polyphenols have also been found to stimulate DNA repair mechanisms.[294] Hence, there is a conflict about the pro- or antioxidant effect of polyphenols in literature.[152] In our experiments, we observed that the cells proliferated phenotypically normal without clear indications of cytotoxic effects of the coatings. This is in good accordance with a previous study, in which the coatings did not evoke an inflammatory or cytotoxic response in hOBs.[172]

Besides scavenging ROS, polyphenols have also shown to modulate the DAMP associated signaling pathways to reduce the inflammatory cytokine expression.[295–297] Upon infection of the oral tissue by microbes, cells recognize LPS, which typically induces inflammation through activation of the NF-κB signal transduction.[55] Similar to LPS, IL-1β activates the NF-κB signaling pathway.[298] However, under IL-1β stimulation, we did not observe reduced expression of pro-inflammatory cytokines in hGFs or the inhibition of NF-κB phosphorylation. A

similar result has previously been obtained with quercitrin coatings,[299] suggesting that hGFs are under too much stress by stimulation with IL-1β. IL-1β is a pleiotropic cytokine and could activate also other signaling pathway besides the classical NF-κB activation.[52,300] This could have bypassed the inhibitory function of polyphenols affecting the MyD88-NF-κB signal transduction.[122] Moreover, the effect of polyphenols on cell signaling pathways is strongly dependent on the cell type. In macrophages for example, the anti-inflammatory effect of polyphenols reduces the pro-inflammatory M1 polarization (**Figure 1.4**).[301,302] Thus, polyphenols have a broad variety of targets to reduce the initial inflammatory response in different cell types.

Regarding the late wound healing stage, polyphenolic coatings show promising results for supporting osseointegration through stimulation of osteoblasts and inhibition of osteoclast activity.[281,303,304] Several studies have reported osteogenic properties of polyphenolic coatings towards stem cells.[111,305–307] However, our previous studies with hOBs indicated that TA and PG delayed osteoblast maturation.[172] Finding the correct balance in osteoblast and osteoclast activity is important since reduced activity of either cells could impose negative effects on the bone remodeling process. In addition, more evidence is required for the soft tissue attachment on polyphenolic coatings. There is initial evidence that polyphenolic coatings improve cell attachment, which could strengthen the soft tissue integration.[279] Further increase of cell attachment and proliferation could be achieved by tethering growth factors to the implant surface via polyphenolic coatings.[308,309] Ultimately, there is a need for convincing *in vivo* data on tissue integration of polyphenolic-modified surfaces. Only a few studies suggest a beneficial bone regeneration and improved wound healing *in vivo* using coated surfaces or polyphenolic gels.[282,310,311] Thus, further studies are needed to evaluate the overall effect of polyphenolic coatings on wound healing.

5.3 Can polyphenolic coatings prevent peri-implant infections?

In addition to supporting tissue integration through the modulation of the cell response, polyphenols may also prevent microbial colonization and infection of the implant. Inhibition of microbial growth and adhesion is the main factor affecting the race to the surface determining the long-term success of the dental implant.[81]

In our previous studies, TA and PG coatings did not prevent staphylococcal biofilm formation but affected their planktonic growth.[172] In this work, we studied the biofilm formation of *Candida albicans*, which is an important but largely ignored fungus in terms of periodontal and peri-implant plaque formation.[227,312] Our polyphenolic coatings could not inhibit biofilm formation or the growth of *C. albicans* (Paper V), despite numerous studies reporting growth inhibitory effects of polyphenols.[313–315] Interestingly, growth inhibition in relation to cell wall damage is suggested to be connected to lipid peroxidation.[316,317] Thus, these studies utilized the pro-oxidant effect of polyphenols. Although various polyphenolic molecules have shown potential antimicrobial effect on oral pathogens,[259,318,319] the required minimum inhibitory concentration (MIC) for fungal growth is mostly above 100 µg mL^{-1}. Polyphenolic coatings, which have a thickness in the nanometer

range, did not release such a large amount of molecules from their surface (Paper IV). In addition, *in vitro* experiments typically challenge the coatings with a high number of microbial cells. Thereby, the surfaces may quickly be saturated by cells, which subsequently grow rapidly under sub-inhibitory concentration of antimicrobial molecules.

The effect of polyphenolic coatings on the virulence of *C. albicans* has not been addressed in our study. Investigating the hyphae formation would relate to a more clinically relevant situation, in which the fungal cells attempt to invade gingival tissue. A suppressed change in phenotype has been shown to reduce the biofilm formation of *C. albicans*.[320] Since hyphae allow the adhesion of other oral pathogens, inhibition of hyphae formation could inhibit the development of multispecies biofilms harboring pathogenic oral bacterial.[227,321,322]

Apart from growth inhibition, a reduction of adhesion is a frequent approach to prevent microbial biofilm formation.[323] Our results in Paper V, however, showed no reduction of adherent cells to a degree that can be claimed to prevent *C. albicans* colonization. Although less cells adhered to the surface under flow, it is expected that due to the rapid growth, a biofilm will be establish after a longer incubation time.[228] These results are in accordance with a recent study utilizing MPN coatings to reduce microbial adhesion. The MPN-modified surfaces were not intrinsically antimicrobial but required subsequent sulfonate modification.[108] Another approach is the formation of structured TA multilayer films, which showed bactericidal effects and reduction in adhesion.[111,324]

It is however questionable whether adhesion studies are clinically relevant since they are often conducted in PBS and ignore the presence of proteins and other biomolecules. With regard to the oral environment, the formation of a salivary protein conditioning film masks the underlying surface properties and allows fungal adhesion.[325] *C. albicans* particularly recognizes mucins, which usually cover mucosal soft tissue.[326] Therefore, we evaluated the formation of salivary pellicles on the polyphenolic surfaces and found differences in their viscoelastic properties among the tested surfaces. This indicated changes in their structure but the fungal adhesion was not affected.

Since polyphenolic coatings did not show a reduction in adhesion or growth inhibition *in vitro*, a balance has to be found in the simultaneous inhibition of the immune response and suppressed inflammatory response.[327,328] Since polyphenols affect the microbial cell wall integrity and inhibit of efflux pumps,[127,128,132,329] a further possible option to elicit a antimicrobial effect is the combination with antibiotics. Utilizing this synergistic effect may increase the susceptibility of fungi to antibiotics and reduce the emergence of drug-resistant cells.[330]

It is worth mentioning that the oral microbiome is a dynamic environment and studies of few selected bacteria or fungi do not represent the response *in vivo*.[331] Reducing one species may cause others to take over. Further, different species may express biomolecules, which protect the whole community in the biofilm.[332] Thus, strategies developed *in vitro* require verification in more biologically relevant conditions. Currently, this means *in vivo* studies are required since complex *in vitro* co-culture models are difficult to develop.

Chapter 6

Concluding Remarks

Polyphenolic molecules offer a broad spectrum of interactions to modulate cell signaling pathways and relieve oxidative stress. The deposition of these molecules on implant surfaces in the form of coatings was hypothesized to constitute a facile method to create functionalized implant surfaces, which deliver active molecules to the wound site in a controlled manner after implant surgery. Further, the foreign body response may be modulated by the specific polyphenolic surface chemistry. Thus, the aim was to reduce local inflammatory reactions to support the wound healing processes and implant integration.

Therefore, this work investigated how coatings of the two polyphenolic molecules TA and PG are formed and how they may affect wound healing and infections around dental implants. Comparing the coating mechanisms between the two molecules, we have determined that TA builds Si_{aq} cross-linked network structures, whereas PG polymerizes via an auto-oxidative route. The use of silicate–phenolic networks allowed us to change the oxidative state of the coating and control the deposition process. In further studies, it may be of interest to study whether silicate–phenolic networks form through a radical intermediate step. Analysis of the deposition in a radical scavenging environment may give some further insight into the reaction pathway to increase the control over the deposition of polyphenolic coatings. Changing the polymerization of PG via alternative mechanisms, such as enzymatically or chemically controlled oxidation, could result in more defined polymeric structures. This may enable the use of other polyphenols available in the diverse library of anti-inflammatory and antimicrobial polyphenolic molecules as surface independent nanocoatings on various implant surfaces.

The interaction of coatings with human whole blood showed that the coagulation system was activated, which retained the thrombogenic effect of Ti surfaces. In contrast, complement activation was reduced, which suppressed monocyte and granulocyte activation and inflammatory cytokine expression. Therefore, we expect an improved foreign body response on our coatings compared to Ti surfaces. The coatings also showed potent antioxidant properties and released active molecules, which reduced the intracellular reactive oxygen species and inhibited DNA damage caused by oxidative stress. However, mitigation of the inflammatory response induced by the pro-inflammatory cytokine IL-1β was not observed for human gingival fibroblasts. This could be due to either the cells used in this work or the use of IL-1β as the inflammatory stimulus. Thus, future studies are needed investigate the modulating effect of polyphenols in other cells stimulated by either LPS or IL-1β. The polyphenol-mediated response in leukocytes and macrophages exposed to inflammatory stimuli should be a particular focus in the investigation of the potential benefits of polyphenolic coatings in the early wound healing processes. Thereby, a compromised immune response to infection should also be considered.

With regard to inflammation by invading pathogens, polyphenolic compounds reportedly have antimicrobial effects against a broad variety of oral pathogens.

However, our polyphenolic coatings did not inhibit the growth and biofilm formation of *C. albicans*. Further, no reduction of fungal adhesion was observed either on TA and PG coatings or on saliva-coated surfaces. In future studies, reduction of hyphae formation of *C. albicans* by the polyphenolic molecules could be evaluated as a strategy to reduce the virulence of *C. albicans*. Additionally, microbial colonization of modified surfaces should be considered in experimental setups which challenge the surfaces in conditions that match the oral environment.

In case TA and PG modified surfaces do not present appropriate anti-inflammatory and antimicrobial properties, additional modifications can be realized by harnessing the known reactivity of polyphenols.[167] Potential options for secondary functionalization are the incorporation of drugs, ions, or growth-factors into the layer to support regenerative processes. Alternatively, build-up of multilayers or tethering bioactive molecules onto the final polyphenolic coating are possible strategies to obtain multifunctional coatings with improved wound healing properties.

In summary, we have obtained control over the deposition of TA and PG to create nanocoatings with a thickness above 100 nm. Thereby, the release of anti-inflammatory molecules from the surface was increased. However, the biological response should be investigated in more detail, and whether or not these polyphenolic coatings are able to reduce infections and inflammation in a clinical setting remains to be tested. In particular, the selective reduction of the immune reaction to implant surfaces whilst not compromising the capacity to fight infectious microorganisms will be a challenge. This ultimately determines whether future implants can be envisioned similar to those pictured in **Figure 6.1**.

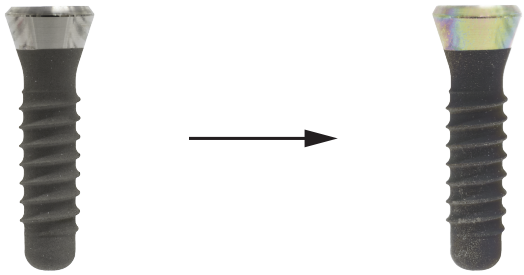

Figure 6.1: If the future research on polyphenolic surface modifications shows a significant improvement in wound healing in a clinical setting, a new generation of titanium dental implants may look like the coated implant on the right.

Glossary

Notation	Description
ABTS	2,2'-azino-bis(3-ethylbenzothiazoline-6-sulfonic acid, a radical used in colorimetric antioxidant assays. 27, 28, 33, 79
ACT1	actin protein 1. 34
AFM	atomic force microscopy. 23, 24
ATR	attenuated total reflection. 18, 25, 26
BMP	bone morphogenetic protein. 8
C	complement component. C3. 2 C3a. 2, 5 C3bBbP. 31, 38 C4d. 31, 38 C5. 2 C5a. 2, 5
CFU	colony forming unit. 34
CSTR	continuously stirred tank reactor. 37
DAMP	damage-associated molecular pattern. 5, 6, 43
DPPH	2,2-diphenyl-1-picrylhydrazyl, a radical trap to study chemical reactions involving radicals. 27
EA	ellagic acid. 10, 11, 15, 17, 37, 42, 77
ECM	extracellular matrix. 3, 4
EDS	energy dispersive x–ray spectroscopy. 24, 25
EFG1	enhanced filamentous growth protein 1. 35
ELISA	enzyme linked immunosorbent assay. 31, 32, 34
EOF	electro–osmotic flow. 27
EPR	electron paramagnetic resonance. 28, 29
ESI	electro–spray ionization. 25
F1+2	prothrombin fragment 1 and 2. 3, 31, 38
FTIR	Fourier transform infrared. 18, 19, 25, 26, 37, 42, 79
GA	gallic acid. 10, 11, 15, 17, 29, 37, 41, 73, 77, 78
H_2DCFDA	2',7'-dichlorodihydrofluorescein diacetate, a cell-permeant indicator for reactive oxygen species. 33
hGF	human gingival fibroblast. 33, 34, 38, 43, 44
hOB	human osteoblast. 34, 43, 44

Notation	Description
HPLC	high–performance liquid chromatography. 17, 30, 73
HWP1	hyphal wall protein 1. 35
IgG	immunoglobulin G. 38
IL	interleukin. IL–1. 5, 34, 38, 43, 44, 47 IL–6. 5 IL–8. 43
IRAK	interleukin–1 receptor associated kinase. 5
LC	liquid chromatography. 25
LDH	lactate dehydrogenase. 32
LIFT	process of elevating the potential of the ions. 78
LMW	low molecular weight. 8, 10, 42
LPS	lipopolysaccharide. 5, 6, 33, 34, 38, 43, 47
MALDI–TOF	matrix-assisted laser desorption ionization – time-of-flight mass spectroscopy. 25, 77, 78
MAPK	mitogen-activated protein kinase. 5
MAS–NMR	magic angle spinning NMR. 26, 37
MIC	minimum inhibitory concentration. 44
MPN	metal phenolic network. 14, 15, 18, 40, 41, 45
MS	mass spectrometer. 25
MTT	3-(4,5-dimethylthiazol-2-yl)-2,5-diphenyltetrazolium bromide, a tetrazole dye used in colorimetric assay for assessing cell metabolic activity. 32
MyD88	myeloid differentiation primary response 88. 5, 11, 44
NF-κB	nuclear factor kappa B. 5, 11, 34, 38, 43, 44
NMR	nuclear magnetic resonance. 19, 26, 28, 42
NPS	nanoplasmonic sensing. 20–22
NR	neutron reflectometry. 22, 23, 75
OD	optical density. 34
OWRK	Owens, Wendt, Rabel, and Kaelble defined a standard method for calculating the surface free energy. 27
PAMP	pathogen-associated molecular pattern. 5, 6
PBS	phosphate buffered saline. 29, 32, 35, 36, 45
PCR	polymerase chain reaction. 34
PEG	polyethylene glycol. 8
PG	pyrogallol. 10, 11, 15–18, 27, 37–44, 47, 48
PG70	pyrogallol coatings obtained at pH = 7.0. 37, 38, 43
PGG	pentagalloyl glucose. 29
PI	propidium iodide. 33
PRP	proline-rich protein. 10
QCM–D	quartz crystal microbalance with dissipation monitoring. 19–23, 29, 30, 37

Notation	Description
RGD	cell adhesion domain. 8
RNS	reactive nitrogen species. 33
ROS	reactive oxygen species. 5, 6, 11, 16, 33, 38, 43
SDS–PAGE	sodium dodecyl sulfate polyacrylamide gel electrophoresis. 30, 80
SEM	scanning electron microscopy. 24, 25, 32, 35
Si_{aq}	aqueous silicic acid. 15, 37, 40, 47, 79
SLD	scattering length density. 22, 23, 76
SPLET	sequential proton loss electron transfer. 12
SPR	surface plasmon resonance. 21, 22
ss-NMR	solid-state nuclear magnetic resonance. 26
STAT3	signal transducer and activator of transcription 3. 5
TA	tannic acid. 10, 11, 14–19, 22, 25–27, 29, 37–45, 47, 48, 73–75, 77–79
TA68	TA coatings obtained at pH = 6.8. 37, 38
TA78	TA coatings obtained at pH = 7.8. 37, 38
TAT	thrombin–antithrombin complex. 3, 31, 38
TBHP	tert-butyl hydroperoxide. 33, 38
TCC	terminal complement complex. 2, 31, 38, 43
TEAC	trolox equivalent anti-oxidant capacity. 27
TF	tissue factor. 3
TNF-α	tissue necrosis factor alpha. 5
TOF–SIMS	time-of-flight – secondary ion mass spectroscopy. 25, 77
UV–vis	UV–visible light. 18
WBSSH	White, Bate-Smith, Swayne, and Haslam defined polyphenols. 9, 10
XPS	X–ray photoelectron spectroscopy. 25
XTT	2,3-bis-(2-methoxy-4-nitro-5-sulfophenyl)-2H-tetrazolium-5-carboxanilide, tetrazole dye used in colorimetric assay for assessing cell metabolic activity. 34
YPD	yeast–peptone–dextrose. 35

Bibliography

[1] A. E. Gerritsen, P. F. Allen, D. J. Witter, E. M. Bronkhorst, N. H. J. Creugers, "Tooth Loss and Oral Health-Related Quality of Life: A Systematic Review and Meta-Analysis", *Health and Quality of Life Outcomes* **2010**, *8*, 126.

[2] P. F. Allen, "Assessment of Oral Health Related Quality of Life", *Health and Quality of Life Outcomes* **2003**, *1*, 40.

[3] T. Vos, A. A. Abajobir, C. Abbafati, K. M. Abbas, K. H. Abate, "Global, Regional, and National Incidence, Prevalence, and Years Lived with Disability for 328 Diseases and Injuries for 195 Countries, 1990–2016: A Systematic Analysis for the Global Burden of Disease Study 2016", *Lancet* **2018**, *392*, 1789–1858.

[4] B. L. Pihlstrom, B. S. Michalowicz, N. W. Johnson, "Periodontal Diseases", *The Lancet* **2005**, *366*, 1809–1820.

[5] A. Sheiham, G. S. Netuveli, "Periodontal Diseases in Europe", *Periodontology 2000* **2002**, *29*, 104–121.

[6] V. Moraschini, L. A. d. C. Poubel, V. F. Ferreira, E. d. S. P. Barboza, "Evaluation of Survival and Success Rates of Dental Implants Reported in Longitudinal Studies with a Follow-up Period of at Least 10 Years: A Systematic Review", *International Journal of Oral and Maxillofacial Surgery* **2015**, *44*, 377–388.

[7] H. W. Elani, J. R. Starr, J. D. Da Silva, G. O. Gallucci, "Trends in Dental Implant Use in the U.S., 1999-2016, and Projections to 2026", *Journal of Dental Research* **2018**, *97*, 1424–1430.

[8] S. A. Lie, G. B. Lygre, I. Reichhelm, E. Eggum, V. H. Bull, H. Gjengedal, "Data Fra Helfo Og Norsk Pasientskadeerstatning Gir Liten Informasjon Om Kvalitet Og Omfang Av Behandling Med Tannimplantater I Norge", *Norske Tannlegeforeningengs Tidende* **2019**, *129*, 776–782.

[9] L. Gaviria, J. P. Salcido, T. Guda, J. L. Ong, "Current Trends in Dental Implants", *Journal of the Korean Association of Oral and Maxillofacial Surgeons* **2014**, *40*, 50–60.

[10] R. Adell, U. Lekholm, B. Rockler, P. I. Brånemark, "A 15-year Study of Osseointegrated Implants in the Treatment of the Edentulous Jaw", *International Journal of Oral Surgery* **1981**, *10*, 387–416.

[11] R. Van Noort, "Titanium: The Implant Material of Today", *Journal of Materials Science* **1987**, *22*, 3801–3811.

[12] D. M. Brunette, P. Tengvall, M. Textor, P. Thomsen, *Titanium in Medicine: Material Science, Surface Science, Engineering, Biological Responses and Medical Applications*, Springer Science & Business Media, **2012**.

[13] D. F. Williams, "On the Mechanisms of Biocompatibility", *Biomaterials* **2008**, *29*, 2941–2953.

[14] K. J. Anusavice, C. Shen, H. R. Rawls, *Phillips' Science of Dental Materials*, Elsevier Health Sciences, **2012**.

[15] B. R. Osman, V. M. Swain, "A Critical Review of Dental Implant Materials with an Emphasis on Titanium Versus Zirconia", *Materials* **2015**, *8*.

[16] M. J. Donachie, *Titanium: A Technical Guide*, ASM international, **2000**.

[17] D. F. Williams, "Corrosion of Implant Materials", *Annual Review of Materials Science* **1976**, *6*, 237–266.

[18] B. D. Ratner, D. M. Brunette, P. Tengvall, M. Textor, P. Thomsen in *Titanium in Medicine: Material Science, Surface Science, Engineering, Biological Responses and Medical Applications*, Springer, **2001**, Chapter A Perspective on Titanium Biocompatibility, pp. 1–12.

[19] I. Gotman, "Characteristics of Metals Used in Implants", *Journal of Endourology* **1997**, *11*, 383–389.

[20] T. Albrektsson, P.-I. Brånemark, H.-A. Hansson, J. Lindström, "Osseointegrated Titanium Implants: Requirements for Ensuring a Long-Lasting, Direct Bone-to-Implant Anchorage in Man", *Acta Orthopaedica Scandinavica* **1981**, *52*, 155–170.

[21] G. Byrne, *Fundamentals of Implant Dentistry*, John Wiley & Sons, **2014**.

[22] J. E. Park, A. Barbul, "Understanding the Role of Immune Regulation in Wound Healing", *The American Journal of Surgery* **2004**, *187*, S11–S16.

[23] E. F. Eriksen, "Cellular Mechanisms of Bone Remodeling", *Reviews in Endocrine and Metabolic Disorders* **2010**, *11*, 219–227.

[24] G. E. Salvi, D. D. Bosshardt, N. P. Lang, I. Abrahamsson, T. Berglundh, J. Lindhe, S. Ivanovski, N. Donos, "Temporal Sequence of Hard and Soft Tissue Healing around Titanium Dental Implants", *Periodontology 2000* **2015**, *68*, 135–152.

[25] A. Turabelidze, S. Guo, A. Y. Chung, L. Chen, Y. Dai, P. T. Marucha, L. A. DiPietro, "Intrinsic Differences between Oral and Skin Keratinocytes", *PLOS ONE* **2014**, *9*, e101480–e101480.

[26] N. S. Merle, S. E. Church, V. Fremeaux-Bacchi, L. T. Roumenina, "Complement System Part I - Molecular Mechanisms of Activation and Regulation", *Frontiers in Immunology* **2015**, *6*, 262.

[27] N. S. Merle, R. Noe, L. Halbwachs-Mecarelli, V. Fremeaux-Bacchi, L. T. Roumenina, "Complement System Part II: Role in Immunity", *Frontiers in Immunology* **2015**, *6*, 257.

[28] J. V. Sarma, P. A. Ward, "The Complement System", *Cell and Tissue Research* **2011**, *343*, 227–235.

[29] K. Murphy, C. Weaver, *Janeway's Immunobiology*, 8th Edition, Garland science, **2012**.

[30] N. S. Quinsey, A. L. Greedy, S. P. Bottomley, J. C. Whisstock, R. N. Pike, "Antithrombin: In Control of Coagulation", *The International Journal of Biochemistry & Cell Biology* **2004**, *36*, 386–389.

[31] S. Antoniak, "The Coagulation System in Host Defense", *Research and Practice in Thrombosis and Haemostasis* **2018**, *2*, 549–557.

[32] M. Hoffman, "Remodeling the Blood Coagulation Cascade", *Journal of Thrombosis and Thrombolysis* **2003**, *16*, 17–20.

[33] J. W. M. Heemskerk, E. M. Bevers, T. Lindhout, "Platelet Activation and Blood Coagulation", *Thrombosis and Haemostasis* **2002**, *88*, 186–193.

[34] M. Levi, T. van der Poll, "Inflammation and Coagulation", *Critical Care Medicine* **2010**, *38*.

[35] J. Petäjä, "Inflammation and Coagulation. an Overview", *Thrombosis Research* **2011**, *127*, S34–S37.

[36] A. Arys, C. Philippart, N. Dourov, Y. He, Q. T. Le, J. J. Pireaux, "Analysis of Titanium Dental Implants After Failure of Osseointegration: Combined Histological, Electron Microscopy, and X-Ray Photoelectron Spectroscopy Approach", *Journal of Biomedical Materials Research* **1998**, *43*, 300–312.

[37] S. Barrientos, O. Stojadinovic, M. S. Golinko, H. Brem, M. Tomic-Canic, "Growth Factors and Cytokines in Wound Healing", *Wound Repair and Regeneration* **2008**, *16*, 585–601.

[38] C. Susin, T. Fiorini, J. Lee, J. A. De Stefano, D. P. Dickinson, U. M. E. Wikesjö, "Wound Healing Following Surgical and Regenerative Periodontal Therapy.", *Periodontology 2000* **2015**, *68*, 83–98.

[39] N. P. Lang, "Oral Implants: The Paradigm Shift in Restorative Dentistry", *Journal of Dental Resesearch* **2019**, *98*, 1287–1293.

[40] B. Zhao, H. C. van der Mei, G. Subbiahdoss, J. de Vries, M. Rustema-Abbing, R. Kuijer, H. J. Busscher, Y. Ren, "Soft Tissue Integration Versus Early Biofilm Formation on Different Dental Implant Materials", *Dental Materials* **2014**, *30*, 716–727.

[41] M. Quirynen, M. De Soete, D. van Steenberghe, "Infectious Risks for Oral Implants: A Review of the Literature", *Clinical Oral Implants Research* **2002**, *13*, 1–19.

[42] J. M. Anderson, "Mechanisms of Inflammation and Infection with Implanted Devices", *Cardiovascular Pathology* **1993**, *2*, 33–41.

[43] M. J. Flick, X. Du, J. L. Degen, "Fibrin(ogen)-$\alpha_M\beta_2$ Interactions Regulate Leukocyte Function and Innate Immunity *In Vivo*", *Experimental biology and medicine* **2004**, *229*, 1105–1110.

[44] H. Mitani, N. Katayama, H. Araki, K. Ohishi, K. Kobayashi, H. Suzuki, K. Nishii, M. Masuya, K. Yasukawa, N. Minami, H. Shiku, "Activity of Interleukin 6 in the Differentiation of Monocytes to Macrophages and Dendritic Cells", *British Journal of Haematology* **2000**, *109*, 288–295.

[45] P. M. Henson, "The Immunologic Release of Constituents from Neutrophil Leukocytes", *Journal of Immunology* **1971**, *107*, 1547.

[46] C. N. Serhan, P. A. Ward, D. W. Gilroy, *Fundamentals of Inflammation*, Cambridge University Press, **2010**.

[47] R. W. Johnson, "Inhibition of Growth by Pro-Inflammatory Cytokines: An Integrated View", *Journal of Animal Science* **1997**, *75*, 1244–1255.

[48] A. Cerami, "Inflammatory Cytokines", *Clinical Immunology and Immunopathology* **1992**, *62*, S3–S10.

[49] C. Mills, "M1 and M2 Macrophages: Oracles of Health and Disease", *Critical Reviews in Immunology* **2012**, *32*.

[50] S. M. Opal, V. A. DePalo, "Anti-Inflammatory Cytokines", *Chest* **2000**, *117*, 1162–1172.

[51] P. J. Murray, "Macrophage Polarization", *Annual Reviews Physiology* **2017**, *79*, 541–566.

[52] S.-C. Sun, "The Non-Canonical NF-κB Pathway in Immunity and Inflammation.", *Nature Reviews. Immunology* **2017**, *17*, 545–558.

[53] K. Grynberg, F. Y. Ma, D. J. Nikolic-Paterson, "The Jnk Signaling Pathway in Renal Fibrosis", *Frontiers in Physiology* **2017**, *8*, 829.

[54] C. Gabay, "Interleukin-6 and Chronic Inflammation", *Arthritis Research & Therapy* **2006**, *8*, S3.

[55] E. M. Pålsson-McDermott, L. A. J. O'Neill, "Signal Transduction by the Lipopolysaccharide Receptor, Toll-like Receptor-4.", *Immunology* **2004**, *113*, 153–62.

[56] K. Lewis, "Persister Cells, Dormancy and Infectious Disease", *Nature Reviews Microbiology* **2007**, *5*, 48–56.

[57] B. Gottenbos, H. J. Busscher, H. C. van der Mei, P. Nieuwenhuis, "Pathogenesis and Prevention of Biomaterial Centered Infections", *Journal of Materials Science: Materials in Medicine* **2002**, *13*, 717–722.

[58] N. U. Zitzmann, T. Berglundh, "Definition and Prevalence of Peri-Implant Diseases", *Journal of Clinical Periodontology* **2008**, *35*, 286–91.

[59] A. Mombelli, N. Müller, N. Cionca, "The Epidemiology of Peri-Implantitis", *Clinical Oral Implants Research* **2012**, *23*, 67–76.

[60] N. P. Lang, T. G. Wilson, E. F. Corbet, "Biological Complications with Dental Implants: Their Prevention, Diagnosis, and Treatment", *Clinical Oral Implants Research* **2000**, *11*, 146–155.

[61] A. Mombelli, M. A. C. van Oosten, E. Schürch Jr., N. P. Lang, "The Microbiota Associated with Successful or Failing Osseointegrated Titanium Implants", *Oral Microbiology and Immunology* **1987**, *2*, 145–151.

[62] R. Pokrowiecki, A. Mielczarek, T. Zareba, S. Tyski, "Oral Microbiome and Peri-Implant Diseases: Where Are We Now?", *Therapeutics and Clinical Risk Management* **2017**, *13*, 1529–1542.

[63] A. Mombelli, "Microbiology and Antimicrobial Therapy of Peri-Implantitis", *Periodontology 2000* **2002**, *28*, 177–189.

[64] P. J. Perez-Chaparro, C. Goncalves, L. C. Figueiredo, M. Faveri, E. Lobao, N. Tamashiro, P. Duarte, M. Feres, "Newly Identified Pathogens Associated with Periodontitis: A Systematic Review", *Journal of Dental Research* **2014**, *93*, 846–858.

[65] G. Polizzi, U. Grunder, R. Goené, N. Hatano, P. Henry, W. J. Jackson, K. Kawamura, F. Renouard, R. Rosenberg, G. Triplett, "Immediate and Delayed Implant Placement into Extraction Sockets: A 5-year Report", *Clinical Implant Dentistry and Related Research* **2000**, *2*, 93–99.

[66] J. Slots, T. E. Rams, "New Views on Periodontal Microbiota in Special Patient Categories", *Journal of Clinical Periodontology* **1991**, *18*, 411–420.

[67] W. Heuer, C. Elter, A. Demling, A. Neumann, S. Suerbaum, M. Hannig, T. Heidenblut, B. F. W., M. Stiesch-Scholz, "Analysis of Early Biofilm Formation on Oral Implants in Man", *Journal of Oral Rehabilitation* **2007**, *34*, 377–382.

[68] A. Bridier, P. Sanchez-Vizuete, M. Guilbaud, J. C. Piard, M. Naïtali, R. Briandet, "Biofilm-Associated Persistence of Food-Borne Pathogens", *Food Microbiology* **2015**, *45*, 167–178.

[69] E. Elemek, O. B. Agrali, B. Kuru, L. Kuru, "Peri-Implantitis and Severity Level", *Eur J Dent* **2020**, *14*, 024–030.

[70] M. Krebs, N. Kesar, A. Begić, N. von Krockow, G.-H. Nentwig, P. Weigl, "Incidence and Prevalence of Peri-Implantitis and Peri-Implant Mucositis 17 to 23 (18.9) Years Postimplant Placement", *Clinical Implant Dentistry and Related Research* **2019**, *21*, 1116–1123.

[71] A. Turri, P. H. Orlato Rossetti, L. Canullo, M. G. Grusovin, C. Dahlin, "Prevalence of Peri-Implantitis in Medically Compromised Patients and Smokers: A Systematic Review.", *International Journal of Oral and Maxillofacial Implants* **2016**, *31*.

[72] L. Levin, D. Schwartz-Arad, "The Effect of Cigarette Smoking on Dental Implants and Related Surgery", *Implant Dentistry* **2005**, *14*.

[73] J. Cosyn, M. M. Sabzevar, P. De Wilde, T. De Rouck, "Commentary: Two-Piece Implants with Turned Versus Microtextured Collars", *Journal of Periodontology* **2007**, *78*, 1657–1663.

[74] M. Esposito, J.-M. Hirsch, U. Lekholm, P. Thomsen, "Failure Patterns of Four Osseointegrated Oral Implant Systems", *Journal of Materials Science: Materials in Medicine* **1997**, *8*, 843–847.

[75] M. Quirynen, H. C. Van Der Mei, C. M. L. Bollen, A. Schotte, M. Marechal, G. I. Doornbusch, I. Naert, H. J. Busscher, D. Van Steenberghe, "An *In Vivo* Study of the Influence of the Surface Roughness of Implants on the Microbiology of Supra- and Subgingival Plaque", *Journal of Dental Research* **1993**, *72*, 1304–1309.

[76] F. Javed, A. S. T. AlGhamdi, A. Ahmed, T. Mikami, H. B. Ahmed, H. C. Tenenbaum, "Clinical Efficacy of Antibiotics in the Treatment of Peri-Implantitis", *International Dental Journal* **2013**, *63*, 169–176.

[77] T. E. Rams, J. E. Degener, A. J. van Winkelhoff, "Antibiotic Resistance in Human Peri-Implantitis Microbiota", *Clinical Oral Implants Research* **2014**, *25*, 82–90.

[78] O. Carcuac, J. Derks, G. Charalampakis, I. Abrahamsson, J. Wennström, T. Berglundh, "Adjunctive Systemic and Local Antimicrobial Therapy in the Surgical Treatment of Peri-Implantitis: A Randomized Controlled Clinical Trial", *Journal of Dental Research* **2015**, *95*, 50–57.

[79] D. G. Castner, B. D. Ratner, "Biomedical Surface Science: Foundations to Frontiers", *Surface Science* **2002**, *500*, 28–60.

[80] B. D. Ratner, "New Ideas in Biomaterials Science – A Path to Engineered Biomaterials", *Journal of Biomedial Materials Research* **1993**, *27*, 837–850.

[81] A. G. Gristina, "Biomaterial-Centered Infection: Microbial Adhesion versus Tissue Integration", *Science* **1987**, *237*, 1588–1595.

[82] K. Cai, M. Frant, J. Bossert, G. Hildebrand, K. Liefeith, K. D. Jandt, "Surface Functionalized Titanium Thin Films: Zeta-Potential, Protein Adsorption and Cell Proliferation", *Colloids and Surfaces B: Biointerfaces* **2006**, *50*, 1–8.

[83] D. R. Schmidt, H. Waldeck, W. J. Kao in *Biological Interactions on Materials Surfaces: Understanding and Controlling Protein, Cell, and Tissue Responses*, (Eds.: D. A. Puleo, R. Bizios), Springer US, New York, NY, **2009**, Chapter Protein Adsorption to Biomaterials, pp. 1–18.

[84] J. Andersson, K. N. Ekdahl, J. D. Lambris, B. Nilsson, "Binding of C3 Fragments on Top of Adsorbed Plasma Proteins during Complement Activation on a Model Biomaterial Surface", *Biomaterials* **2005**, *26*, 1477–1485.

[85] H. Fabre, D. Mercier, A. Galtayries, D. Portet, N. Delorme, J.-F. Bardeau, "Impact of Hydrophilic and Hydrophobic Functionalization of Flat Tio2/ti Surfaces on Proteins Adsorption", *Applied Surface Science* **2018**, *432*, 15–21.

[86] P. Roach, D. Farrar, C. C. Perry, "Interpretation of Protein Adsorption: Surface-induced Conformational Changes", *Journal of the American Chemical Society* **2005**, *127*, 8168–8173.

[87] L. Vroman, A. L. Adams, G. C. Fischer, P. C. Munoz, "Interaction of High Molecular Weight Kininogen, Factor XII, and Fibrinogen in Plasma at Interfaces", **1980**.

[88] D. Buser, R. K. Schenk, S. Steinemann, J. P. Fiorellini, C. H. Fox, H. Stich, "Influence of Surface Characteristics on Bone Integration of Titanium Implants. a Histomorphometric Study in Miniature Pigs", *Journal of Biomedical Materials Research* **1991**, *25*, 889–902.

[89] I. Abrahamsson, T. Berglundh, E. Linder, N. P. Lang, J. Lindhe, "Early Bone Formation Adjacent to Rough and Turned Endosseous Implant Surfaces", *Clinical Oral Implants Research* **2004**, *15*, 381–392.

[90] T. Ma, X. Ge, Y. Zhang, Y. Lin in *Interface Oral Health Science 2016*, Springer, **2017**, Chapter Effect of Titanium Surface Modifications of Dental Implants on Rapid Osseointegration, pp. 247–256.

[91] L. Marinucci, S. Balloni, E. Becchetti, S. Belcastro, M. Guerra, M. Calvitti, C. Lull, E. M. Calvi, P. Locci, "Effect of Titanium Surface Roughness on Human Osteoblast Proliferation and Gene Expression *In Vitro*", *International Journal of Oral and Maxillofacial Implants* **2006**, *21*.

[92] C. N. Elias, L. Meirelles, "Improving Osseointegration of Dental Implants", *Expert Review of Medical Devices* **2010**, *7*, 241–256.

[93] H. J. Busscher, H. C. van der Mei, G. Subbiahdoss, P. C. Jutte, J. J. A. M. van den Dungen, S. A. J. Zaat, M. J. Schultz, D. W. Grainger, "Biomaterial-Associated Infection: Locating the Finish Line in the Race for the Surface", *Science Translational Medicine* **2012**, *4*, 153rv10.

[94] C. Stewart, B. Akhavan, S. G. Wise, M. M. M. Bilek, "A Review of Biomimetic Surface Functionalization for Bone-Integrating Orthopedic Implants: Mechanisms, Current Approaches, and Future Directions", *Progress in Materials Science* **2019**, *106*, 100588.

[95] J. E. Ellingsen, P. Thomsen, S. P. Lyngstadaas, "Advances in Dental Implant Materials and Tissue Regeneration", *Periodontology 2000* **2006**, *41*, 136–156.

[96] D. M. Ferris, G. D. Moodie, P. M. Dimond, C. W. D. Giorani, M. G. Ehrlich, R. F. Valentini, "RGD-Coated Titanium Implants Stimulate Increased Bone Formation *In Vivo*", *Biomaterials* **1999**, *20*, 2323–2331.

[97] S. E. Kim, C.-S. Kim, Y.-P. Yun, D. H. Yang, K. Park, S. E. Kim, C.-M. Jeong, J.-B. Huh, "Improving Osteoblast Functions and Bone Formation upon BMP-2 Immobilization on Titanium Modified with Heparin", *Carbohydrate Polymers* **2014**, *114*, 123–132.

[98] Y. Yang, N. Oh, Y. Liu, W. Chen, S. Oh, M. Appleford, S. Kim, K. Kim, S. Park, J. Bumgardner, W. Haggard, J. Ong, "Enhancing Osseointegration Using Surface-Modified Titanium Implants", *JOM Journal of the Minerals Metals and Materials Society* **2006**, *58*, 71–76.

[99] L.-C. Xu, C. A. Siedlecki, "*Staphylococcus epidermidis* Adhesion on Hydrophobic and Hydrophilic Textured Biomaterial Surfaces", *Biomedical Materials* **2014**, *9*, 035003.

[100] V. M. Graham, C. N. Cady, "Nano and Microscale Topographies for the Prevention of Bacterial Surface Fouling", *Coatings* **2014**, *4*.

[101] P. Kingshott, H. J. Griesser, "Surfaces that Resist Bioadhesion", *Current Opinion in Solid State and Materials Science* **1999**, *4*, 403–412.

[102] R. R. Maddikeri, S. Tosatti, M. Schuler, S. Chessari, M. Textor, R. G. Richards, L. G. Harris, "Reduced Medical Infection Related Bacterial Strains Adhesion on Bioactive RGD Modified Titanium Surfaces: A First Step toward Cell Selective Surfaces", *Journal of Biomedial Materials Research* **2008**, *84A*, 425–435.

[103] I. Francolini, C. Vuotto, A. Piozzi, G. Donelli, "Antifouling and Antimicrobial Biomaterials: An Overview", *APMIS* **2020**, *125*, 392–417.

[104] C. Pan, Z. Zhou, X. Yu, "Coatings As the Useful Drug Delivery System for the Prevention of Implant-Related Infections", *Journal of Orthopaedic Surgery and Research* **2018**, *13*, 220–220.

[105] R. Kaur, S. Liu, "Antibacterial Surface Design – Contact Kill", *Progress in Surface Science* **2016**, *91*, 136–153.

[106] K. E. Uhrich, S. M. Cannizzaro, R. S. Langer, K. M. Shakesheff, "Polymeric Systems for Controlled Drug Release", *Chemical Reviews* **1999**, *99*, 3181–3198.

[107] R. Langer, "Invited Review Polymeric Delivery Systems for Controlled Drug Release", *Chemical Engineering Communications* **1980**, *6*, 1–48.

[108] M.-P. Ko, C.-J. Huang, "A Versatile Approach to Antimicrobial Coatings Via Metal–Phenolic Networks", *Colloids and Surfaces B: Biointerfaces* **2020**, 110771.

[109] D. Pranantyo, L. Q. Xu, K.-G. Neoh, E.-T. Kang, Y. X. Ng, S. L.-M. Teo, "Tea Stains-Inspired Initiator Primer for Surface Grafting of Antifouling and Antimicrobial Polymer Brush Coatings", *Biomacromolecules* **2015**, *16*, 723–732.

[110] Z.-Q. Xu, X. Wang, X. Liu, Z. Cui, X. Yang, K. W. K. Yeung, J. C. Chung, P. K. Chu, S. Wu, "Tannic Acid/Fe^{3+}/Ag Nanofilm Exhibiting Superior Photodynamic and Physical Antibacterial Activity", *ACS Applied Materials & Interfaces* **2017**.

[111] S. Yang, Y. Wang, X. Wu, S. Sheng, T. Wang, X. Zan, "Multifunctional Tannic Acid (TA) and Lysozyme (LYS) Films Built Layer by Layer for Potential Application on Implant Coating", *ACS Biomaterials Science & Engineering* **2019**, *5*, 3582–3594.

[112] S. Yang, Y. Xu, Q. Lin, Y. Bai, X. Zan, Q. Ye, "A Bio-Inspired, One-Step but Versatile Coating onto Various Substrates with Strong Antibacterial and Enhanced Osteogenesis", *Chemical Communications* **2019**, *55*, 2058–2061.

[113] T. S. Sileika, D. G. Barrett, R. Zhang, K. H. A. Lau, P. B. Messersmith, "Colorless Multifunctional Coatings Inspired by Polyphenols Found in Tea, Chocolate, and Wine", *Angewandte Chemie International Edition* **2013**, *52*, 10766–10770.

[114] S. Quideau, D. Deffieux, C. Douat-Casassus, L. Pouységu, "Plant Polyphenols: Chemical Properties, Biological Activities, and Synthesis", *Angewandte Chemie International Edition* **2011**, *50*, 586–621.

[115] E. Haslam, *Practical Polyphenolics: From Structure to Molecular Recognition and Physiological Action*, **1998**.

[116] N. P. Slabbert, "Ionisation of Some Flavanols and Dihydroflavonols", *Tetrahedron* **1977**, *33*, 821–824.

[117] C. Lim, J. Huang, S. Kim, H. Lee, H. Zeng, D. S. Hwang, "Nanomechanics of Poly(catecholamine) Coatings in Aqueous Solutions", *Angewandte Chemie International Edition* **2016**, *55*, 3342–3346.

[118] R. Kumpf, D. Dougherty, "A Mechanism for Ion Selectivity in Potassium Channels: Computational Studies of Cation-π Interactions", *Science* **1993**, *261*, 1708–1710.

[119] J. Zhang, L. Xiang, B. Yan, H. Zeng, "Nanomechanics of Anion-π Interaction in Aqueous Solution", *Journal of the American Chemical Society* **2020**.

[120] A. E. Hagerman in *Recent Advances in Polyphenol Research*, *Vol. 3*, John Wiley & Sons, **2012**, Chapter Fifty Years of Polyphenol-Protein Complexes, pp. 71–97.

[121] B. Frei, J. V. Higdon, "Antioxidant Activity of Tea Polyphenols *In Vivo*: Evidence from Animal Studies", *The Journal of Nutrition* **2003**, *133*, 3275S–3284S.

[122] S.-E. Jang, S. R. Hyam, J.-J. Jeong, M. J. Han, D.-H. Kim, "Penta-o-Galloyl-β-D-Glucose Ameliorates Inflammation by Inhibiting MYD88/NF-κB and MYD88/MAPK Signalling Pathways", *British Journal of Pharmacology* **2013**, *170*, 1078–1091.

[123] Y. Kabe, K. Ando, S. Hirao, M. Yoshida, H. Handa, "Redox Regulation of NF-κB Activation: Distinct Redox Regulation between the Cytoplasm and the Nucleus", *Antioxidants and Redox Signaling* **2005**, *7*, 395–403.

[124] I. Rahman, S. K. Biswas, P. A. Kirkham, "Regulation of Inflammation and Redox Signaling by Dietary Polyphenols", *Biochemical Pharmacology* **2006**, *72*, 1439–1452.

[125] X. Han, T. Shen, H. Lou, "Dietary Polyphenols and Their Biological Significance", *International Journal of Molecular Sciences* **2007**, *8*, 950–988.

[126] H. Ikigai, T. Nakae, Y. Hara, T. Shimamura, "Bactericidal Catechins Damage the Lipid Bilayer", *Biochimica et Biophysica Acta* **1993**, *1147*, 132–6.

[127] J. F. S. dos Santos, S. R. Tintino, T. S. de Freitas, F. F. Campina, I. R. de A. Menezes, J. P. Siqueira-Júnior, H. D. M. Coutinho, F. A. B. Cunha, "*In Vitro* e *In Silico* Evaluation of the Inhibition of *Staphylococcus aureus* Efflux Pumps by Caffeic and Gallic Acid", *Comparative Immunology Microbiology and Infectious Diseases* **2018**, *57*, 22–28.

[128] V. B. Maisuria, M. Okshevsky, E. Déziel, N. Tufenkji, "Proanthocyanidin Interferes with Intrinsic Antibiotic Resistance Mechanisms of Gram-negative Bacteria", *Advanced Science* **2019**, *0*, 1802333.

[129] N. Slabbert in *Plant Polyphenols*, Springer, **1992**, Chapter Complexation of Condensed Tannins with Metal Ions, pp. 421–436.

[130] C. C. Winterbourn, "Toxicity of Iron and Hydrogen Peroxide: The Fenton Reaction", *Toxicology Letters* **1995**, *82-83*, 969–974.

[131] N. R. Perron, J. L. Brumaghim, "A Review of the Antioxidant Mechanisms of Polyphenol Compounds Related to Iron Binding", *Cell Biochemistry and Biophysics* **2009**, *53*, 75–100.

[132] M. Daglia, "Polyphenols As Antimicrobial Agents", *Current Opinion in Biotechnology* **2012**, *23*, 174–81.

[133] C. Zhao, N. S. Nguyen, X. Li, D. McCarthy, H. Wang, "Tannic Acid Coating and *In Situ* Deposition of Silver Nanoparticles to Improve the Antifouling Properties of an Ultrafiltration Membrane", *Journal of Applied Polymer Science* **2018**, *136*, 47314.

[134] Y. Song, G. R. Buettner, "Thermodynamic and Kinetic Considerations for the Reaction of Semiquinone Radicals to Form Superoxide and Hydrogen Peroxide", *Free Radical Biology and Medicine* **2010**, *49*, 919–962.

[135] H. I. Abrash, "The Air Oxidation of 4,6-Di(2-Phenyl-2-Propyl)Pyrogallol. Spectroscopic and Kinetic Studies of the Intermediates", *Carlsberg Research Communications* **1977**, *42*, 11–25.

[136] M. Adams, M. S. B. Jr., R. H. Sands, "Paramagnetic Resonance Spectra of Some Semiquinone Free Radicals", *The Journal of Chemical Physics* **1958**, *28*, 774–776.

[137] E. R. Altwicker, "The Chemistry of Stable Phenoxy Radicals", *Chemical Reviews* **1967**, *67*, 475–531.

[138] S. Steenken, P. Neta in *The Chemistry of Phenols*, John Wiley & Sons, **2016**, Chapter Transient Phenoxyl Radicals: Formation and Properties in Aqueous Solutions.

[139] Z. Markovic, D. Milenkovic, J. Dorovic, J. M. Dimitrid Markovic, B. Lucid, D. Amic, "A DFT and PM6 Study of Free Radical Scavenging Activity of Ellagic Acid", *Monatshefte Für Chemie - Chemical Monthly* **2013**, *144*, 803–812.

[140] J. Dorovic, J. M. D. Markovic, V. Stepanic, N. Begovic, D. Amic, Z. Markovic, "Influence of Different Free Radicals on Scavenging Potency of Gallic Acid", *Journal of Molecular Modeling* **2014**, *20*, 2345.

[141] S. Marklund, G. Marklund, "Involvement of the Superoxide Anion Radical in the Autoxidation of Pyrogallol and a Convenient Assay for Superoxide Dismutase", *European Journal of Biochemistry* **1974**, *47*, 469–474.

[142] H. R. Devlin, I. J. Harris, "Mechanism of the Oxidation of Aqueous Phenol with Dissolved Oxygen", *Industrial & Engineering Chemistry Fundamentals* **1984**, *23*, 387–392.

[143] M. Akagawa, T. Shigemitsu, K. Suyama, "Production of Hydrogen Peroxide by Polyphenols and Polyphenol-Rich Beverages under Quasi-Physiological Conditions", *Bioscience Biotechnology and Biochemistry* **2003**, *67*, 2632–2640.

[144] F. Shahidi, P. K. Janitha, P. D. Wanasundara, "Phenolic Antioxidants", *Critical Reviews in Food Science and Nutrition* **1992**, *32*, 67–103.

[145] K. Zhan, H. Ejima, N. Yoshie, "Antioxidant and Adsorption Properties of Bioinspired Phenolic Polymers: A Comparative Study of Catechol and Gallol", *ACS Sustainable Chemistry & Engineering* **2016**, *4*, 3857–3863.

[146] A. I. Scott, "Oxidative Coupling of Phenolic Compounds", *Quarterly Reviews Chemical Society* **1965**, *19*, 1–35.

[147] C. Poncet-Legrand, B. Cabane, A. B. Bautista-Ortin, S. Carrillo, H. Fulcrand, J. Perez, A. Vernhet, "Tannin Oxidation: Intra- Versus Intermolecular Reactions", *Biomacromolecules* **2010**, *11*, 2376–86.

[148] J.-P. Salminen, M. Karonen, J. Sinkkonen, "Chemical Ecology of Tannins: Recent Developments in Tannin Chemistry Reveal New Structures and Structure–activity Patterns", *Chemistry – a European Journal* **2011**, *17*, 2806–2816.

[149] N. S. Khan, A. Ahmad, S. M. Hadi, "Anti-Oxidant, Pro-Oxidant Properties of Tannic Acid and Its Binding to DNA", *Chemico-biological Interactions* **2000**, *125*, 177–189.

[150] K. M. Riedl, S. Carando, H. M. Alessio, M. McCarthy, A. E. Hagerman in *Free Radicals in Food*, *Vol. 807*, 807, American Chemical Society, **2002**, Chapter Antioxidant Activity of Tannins and Tannin-Protein Complexes: Assessment *In Vitro* and *In Vivo*, pp. 188–200.

[151] C. Sánchez-Moreno, J. A. Larrauri, F. Saura-Calixto, "Free Radical Scavenging Capacity and Inhibition of Lipid Oxidation of Wines, Grape Juices and Related Polyphenolic Constituents", *Food Research International* **1999**, *32*, 407–412.

[152] J. D. Lambert, R. J. Elias, "The Antioxidant and Pro-Oxidant Activities of Green Tea Polyphenols: A Role in Cancer Prevention", *Archives of Biochemistry and Biophysics* **2010**, *501*, 65–72.

[153] J. L. Dalsin, B.-H. Hu, B. P. Lee, P. B. Messersmith, "Mussel Adhesive Protein Mimetic Polymers for the Preparation of Nonfouling Surfaces", *Journal of the American Chemical Society* **2003**, *125*, 4253–4258.

[154] H. Lee, S. M. Dellatore, W. M. Miller, P. B. Messersmith, "Mussel-Inspired Surface Chemistry for Multifunctional Coatings", *Science* **2007**, *318*, 426–430.

[155] H. Ejima, J. J. Richardson, K. Liang, J. P. Best, M. P. van Koeverden, G. K. Such, J. Cui, F. Caruso, "One-Step Assembly of Coordination Complexes for Versatile Film and Particle Engineering", *Science* **2013**, *341*, 154–157.

[156] A. H. Hofman, I. A. van Hees, J. Yang, M. Kamperman, "Bioinspired Underwater Adhesives by Using the Supramolecular Toolbox", *Advanced Materials* **2018**, *30*, 1704640.

[157] J. Saiz-Poseu, J. Mancebo-Aracil, F. Nador, F. Busque, D. Ruiz-Molina, "The Chemistry behind Catechol-Based Adhesion", *Angewandte Chemie. International Edition* **2018**, *58*, 696–714.

[158] J. Yu, W. Wei, M. S. Menyo, A. Masic, J. H. Waite, J. N. Israelachvili, "Adhesion of Mussel Foot Protein-3 to TiO_2 Surfaces: The Effect of pH", *Biomacromolecules* **2013**, *14*, 1072–1077.

[159] Q. Ye, F. Zhou, W. Liu, "Bioinspired Catecholic Chemistry for Surface Modification", *Chemical Society Reviews* **2011**, *40*, 4244–4258.

[160] F. Bernsmann, V. Ball, F. Addiego, A. Ponche, M. Michel, J. J. d. A. Gracio, V. Toniazzo, D. Ruch, "Dopamine–Melanin Film Deposition Depends on the Used Oxidant and Buffer Solution", *Langmuir* **2011**, *27*, 2819–2825.

[161] Y. Liu, K. Ai, L. Lu, "Polydopamine and Its Derivative Materials: Synthesis and Promising Applications in Energy, Environmental, and Biomedical Fields", *Chemical Reviews* **2014**, *114*, 5057–5115.

[162] D. G. Barrett, T. S. Sileika, P. B. Messersmith, "Molecular Diversity in Phenolic and Polyphenolic Precursors of Tannin-Inspired Nanocoatings", *Chemical Communications* **2014**, *50*, 7265–7268.

[163] V. Ball, F. Meyer, "Deposition Kinetics and Electrochemical Properties of Tannic Acid on Gold and Silica", *Colloids and Surfaces a: Physicochemical and Engineering Aspects* **2016**, *491*, 12–17.

[164] S. Geißler, A. Barrantes, P. Tengvall, P. B. Messersmith, H. Tiainen, "Deposition Kinetics of Bioinspired Phenolic Coatings on Titanium Surfaces", *Langmuir* **2016**, *32*, 8050–60.

[165] M. A. Rahim, H. Ejima, K. L. Cho, K. Kempe, M. Müllner, J. P. Best, F. Caruso, "Coordination-driven Multistep Assembly of Metal–Polyphenol Films and Capsules", *Chemistry of Materials* **2014**, *26*, 1645–1653.

[166] J. Guo, T. Suma, J. J. Richardson, H. Ejima, "Modular Assembly of Biomaterials Using Polyphenols As Building Blocks", *ACS Biomaterials Science & Engineering* **2019**.

[167] J. H. Ryu, P. B. Messersmith, H. Lee, "Polydopamine Surface Chemistry: A Decade of Discovery", *ACS Applied Materials & Interfaces* **2018**, *10*, 7523–7540.

[168] H. A. Lee, Y. Ma, F. Zhou, S. Hong, H. Lee, "Material-independent Surface Chemistry beyond Polydopamine Coating", *Accounts of Chemical Research* **2019**.

[169] W. Cheng, X. Zeng, H. Chen, Z. Li, W. Zeng, L. Mei, Y. Zhao, "Versatile Polydopamine Platforms: Synthesis and Promising Applications for Surface Modification and Advanced Nanomedicine", *ACS Nano* **2019**.

[170] A. Shavandi, A. E.-D. A. Bekhit, P. Saeedi, Z. Izadifar, A. A. Bekhit, A. Khademhosseini, "Polyphenol Uses in Biomaterials Engineering", *Biomaterials* **2018**, *167*, 91–106.

[171] M. Shin, E. Park, H. Lee, "Plant-Inspired Pyrogallol-Containing Functional Materials", *Advanced Functional Materials* **2019**, *29*, 1903022.

[172] S. Geißler, M. Gomez-Florit, D. Wiedmer, A. Barrantes, F. C. Petersen, H. Tiainen, "*In Vitro* Performance of Bioinspired Phenolic Nanocoatings for Endosseous Implant Applications", *ACS Biomaterials Science & Engineering* **2019**.

[173] S. A. Mian, L. C. Saha, J. Jang, L. Wang, X. Gao, S. Nagase, "Density Functional Theory Study of Catechol Adhesion on Silica Surfaces", *Journal of Physical Chemistry C* **2010**, *114*, 20793–20800.

[174] A. S. Franca, L. M. L. Nollet in *Spectroscopic Methods in Food Analysis*, Food Analysis & Properties, CRC Press, **2017**, Chapter UV–Vis Spectroscopy.

[175] A. Tampieri, M. Szabó, F. Medina, H. Gulyás, "A Brief Introduction to the Basics of Nmr Spectroscopy and Selected Examples of Its Applications to Materials Characterization", *Physical Sciences Reviews* **2020**, *just accepted*, DOI `10.1515/psr-2019-0086`.

[176] G. Sauerbrey, "Verwendung Von Schwingquarzen Zur Wägung Dünner Schichten Und Zur Mikrowägung", *Zeitschrift Für Physik* **1959**, *155*, 206–222.

[177] K. Keiji Kanazawa, J. G. Gordon, "The Oscillation Frequency of a Quartz Resonator in Contact with Liquid", *Analytica Chimica Acta* **1985**, *175*, 99–105.

[178] M. V. Voinova, M. Rodahl, M. Jonson, B. Kasemo, "Viscoelastic Acoustic Response of Layered Polymer Films at Fluid-solid Interfaces: Continuum Mechanics Approach", *Physica Scripta* **1999**, *59*, 391.

[179] G. A. McCubbin, S. Praporski, S. Piantavigna, D. Knappe, R. Hoffmann, J. H. Bowie, F. Separovic, L. L. Martin, "QCM-D Fingerprinting of Membrane-Active Peptides", *European Biophysics Journal* **2011**, *40*, 437–446.

[180] D. Johannsmann, I. Reviakine, R. P. Richter, "Dissipation in Films of Adsorbed Nanospheres Studied by Quartz Crystal Microbalance (QCM-D)", *Analytical Chemistry* **2009**, *81*, 8167–8176.

[181] A. Dmitriev, *Nanoplasmonic Sensors*, Springer Science & Business Media, **2012**.

[182] A. Armanious, B. Agnarsson, A. Lundgren, V. P. Zhdanov, F. Höök, "Determination of Adsorbate Mass in Solution Using QCM: Elimination of the Inseparable Liquid Contribution", *Arxiv Preprint* **2020**.

[183] J. Penfold, R. M. Richardson, A. Zarbakhsh, J. R. P. Webster, D. G. Bucknall, A. R. Rennie, R. A. L. Jones, T. Cosgrove, R. K. Thomas, J. S. Higgins, P. D. I. Fletcher, E. Dickinson, S. J. Roser, I. A. McLure, A. R. Hillman, R. W. Richards, E. J. Staples, A. N. Burgess, E. A. Simister, J. W. White, "Recent Advances in the Study of Chemical Surfaces and Interfaces by Specular Neutron Reflection", *Journal of the Chemical Society Faraday Transactions* **1997**, *93*, 3899–3917.

[184] P. Kienzle, Scattering Calculations, Webpage, **2020**.

[185] T. Saerbeck, R. Cubitt, A. Wildes, G. Manzin, K. H. Andersen, P. Gutfreund, "Recent Upgrades of the Neutron Reflectometer D17 at ILL", *Journal of Applied Crystallography* **2018**, *51*, 249–256.
[186] A. Krężel, W. Bal, "A Formula for Correlating pKa Values Determined in D_2O and H_2O", *Journal of Inorganic Biochemistry* **2004**, *98*, 161–166.
[187] H. Fujiwara, *Spectroscopic Ellipsometry: Principles and Applications*, Wiley, **2007**.
[188] K. Hinrichs, K.-J. Eichhorn, *Ellipsometry of Functional Organic Surfaces and Films*, *Vol. 52*, Springer, **2018**.
[189] Chemspider, Tannic Acid, Webpage, **2020**.
[190] F. Gharagheizi, P. Ilani-Kashkouli, A. Kamari, A. H. Mohammadi, D. Ramjugernath, "Group Contribution Model for the Prediction of Refractive Indices of Organic Compounds", *Journal of Chemical and Engineering Data* **2014**, *59*, 1930–1943.
[191] M. Conroy, J. Armstrong in, *Vol. 13*, IOP Publishing, **2005**, p. 458.
[192] D. Briggs, *Surface Analysis of Polymers by XPS and Static SIMS*, Cambridge University Press, **1998**.
[193] K. M. R. Kallury, U. J. Krull, M. Thompson, "X-Ray Photoelectron Spectroscopy of Silica Surfaces Treated with Polyfunctional Silanes", *Analytical Chemistry* **1988**, *60*, 169–172.
[194] R. N. S. Sodhi, "Time-of-Flight Secondary Ion Mass Spectrometry (TOF-SIMS):–Versatility in Chemical and Imaging Surface Analysis", *Analyst* **2004**, *129*, 483–487.
[195] C. M. Mahoney, "Cluster Secondary Ion Mass Spectrometry of Polymers and Related Materials", *Mass Spectrometry Reviews* **2010**, *29*, 247–293.
[196] H. J. Griesser, P. Kingshott, S. L. McArthur, K. M. McLean, G. R. Kinsel, R. B. Timmons, "Surface-MALDI Mass Spectrometry in Biomaterials Research", *Biomaterials* **2004**, *25*, 4861–4875.
[197] J. J. Pitt, "Principles and Applications of Liquid Chromatography-Mass Spectrometry in Clinical Biochemistry", *The Clinical Biochemist. Reviews* **2009**, *30*, 19–34.
[198] Y. Ishino, H. Ishida, "Grazing Angle Metal-Overlayer Infrared ATR Spectroscopy", *Applied Spectroscopy* **1988**, *42*, 1296–1302.
[199] B. L. Mojet, S. D. Ebbesen, L. Lefferts, "Light at the Interface: The Potential of Attenuated Total Reflection Infrared Spectroscopy for Understanding Heterogeneous Catalysis in Water", *Chemical Society Reviews* **2010**, *39*, 4643–4655.
[200] J. R. Ferraro, *Introductory Raman Spectroscopy*, Elsevier, **2003**.
[201] G. Socrates, *Infrared and Raman Characteristic Group Frequencies : Tables and Charts*, **2004**.
[202] T. S. Chow, "Wetting of Rough Surfaces", *Journal of Physics: Condensed Matter* **1998**, *10*, L445–L451.
[203] R. R. Deshmukh, A. R. Shetty, "Comparison of Surface Energies Using Various Approaches and Their Suitability", *Journal of Applied Polymer Science* **2008**, *107*, 3707–3717.
[204] K.-Y. Law, H. Zhao, K.-Y. Law, H. Zhao in *Surface Wetting: Characterization, Contact Angle, and Fundamentals*, Springer International Publishing, **2016**, Chapter Determination of Solid Surface Tension by Contact Angle, pp. 135–148.
[205] J. C. W. Corbett, F. McNeil-Watson, R. O. Jack, M. Howarth, "Measuring Surface Zeta Potential Using Phase Analysis Light Scattering in a Simple Dip Cell Arrangement", *Colloids and Surfaces a: Physicochemical and Engineering Aspects* **2012**, *396*, 169–176.

[206] S. Salgin, U. Salgin, S. Bahadir, "Zeta Potentials and Isoelectric Points of Biomolecules: The Effects of Ion Types and Ionic Strengths", *International Journal of Electrochemical Science* **2012**, *7*, 12404–12414.

[207] O. Plohl, L. F. Zemljic, S. Potrc, T. Luxbacher, "Applicability of Electro-Osmotic Flow for the Analysis of the Surface Zeta Potential", *RSC Advances* **2020**, *10*, 6777–6789.

[208] B. D. Coday, T. Luxbacher, A. E. Childress, N. Almaraz, P. Xu, T. Y. Cath, "Indirect Determination of Zeta Potential at High Ionic Strength: Specific Application to Semipermeable Polymeric Membranes", *Journal of Membrane Science* **2015**, *478*, 58–64.

[209] R. Re, N. Pellegrini, A. Proteggente, A. Pannala, M. Yang, C. Rice-Evans, "Antioxidant Activity Applying an Improved Abts Radical Cation Decolorization Assay", *Free Radical Biology and Medicine* **1999**, *26*, 1231–1237.

[210] J.-K. Moon, T. Shibamoto, "Antioxidant Assays for Plant and Food Components", *Journal of Agriculture and Food Chemistry* **2009**, *57*, 1655–1666.

[211] I. Y. Tóth, M. Szekeres, R. Turcu, S. Sáringer, E. Illés, D. Nesztor, E. Tombácz, "Mechanism of in-situ Surface Polymerization of Gallic Acid in an Environmental-inspired Preparation of Carboxylated Core–Shell Magnetite Nanoparticles", *Langmuir* **2014**, *30*, 15451–15461.

[212] G. R. Eaton, S. S. Eaton, D. P. Barr, R. T. Weber, *Quantitative EPR*, Springer Science & Business Media, **2010**.

[213] J. A. Pedersen, *Handbook of EPR Spectra from Quinones and Quinols*, CRC press, **2018**.

[214] D. Johannsmann, *The Quartz Crystal Microbalance in Soft Matter Research*, Springer, **2015**, pp. 191–204.

[215] A. R. Patel, B. A. Kerwin, S. R. Kanapuram, "Viscoelastic Characterization of High Concentration Antibody Formulations Using Quartz Crystal Microbalance with Dissipation Monitoring", *Journal of Pharmaceutical Sciences* **2009**, *98*, 3108–3116.

[216] N. Poklar Ulrih, "Analytical Techniques for the Study of Polyphenol–Protein Interactions", *Critical Reviews in Food Science and Nutrition* **2017**, *57*, 2144–2161.

[217] J. Hong, J. Andersson, K. N. Ekdahl, G. Elgue, N. Axen, R. Larsson, B. Nilsson, "Titanium Is a Highly Thrombogenic Biomaterial: Possible Implications for Osteogenesis", *Thrombosis and Haemostasis* **1999**, *82*, 58–64.

[218] P. Bainbridge, "Wound Healing and the Role of Fibroblasts", *Journal of Wound Care* **2013**, *22*, 407–412.

[219] G. Fotakis, J. A. Timbrell, "*In Vitro* Cytotoxicity Assays: Comparison of LDH, Neutral Red, MTT and Protein Assay in Hepatoma Cell Lines Following Exposure to Cadmium Chloride", *Toxicology Letters* **2006**, *160*, 171–177.

[220] M. T. Smith, "Quinones As Mutagens, Carcinogens, and Anticancer Agents: Introduction and Overview", *Journal of Toxicology and Environmental Health* **1985**, *16*, 665–672.

[221] S. Perez-Cerezales, A. Miranda, A. Gutierrez-Adan, "Comparison of Four Methods to Evaluate Sperm DNA Integrity between Mouse Caput and Cauda Epididymidis", *Asian Journal of Andrology* **2012**, *14*, 335–337.

[222] K. A. Szychowski, K. Rybczynska-Tkaczyk, M. L. Leja, A. K. Wojtowicz, J. Gminski, "Tetrabromobisphenol a (TBBPA)-stimulated Reactive Oxygen Species (ROS) Production in Cell-free Model Using the 2',7'-dichlorodihydrofluorescein Diacetate (H_2DCFDA) Assay – Limitations of Method", *Environmental Science and Pollution Research* **2016**, *23*, 12246–12252.

[223] D. Y. Kim, J.-H. Jun, H.-L. Lee, K. M. Woo, H.-M. Ryoo, G.-S. Kim, J.-H. Baek, S.-B. Han, "N-Acetylcysteine Prevents LPS-lnduced Pro-Inflammatory Cytokines and MMP-2 Production in Gingival Fibroblasts", *Archives of Pharmacal Research* **2007**, *30*, 1283.

[224] B. Kalyanaraman, V. Darley-Usmar, K. J. A. Davies, P. A. Dennery, H. J. Forman, M. B. Grisham, G. E. Mann, K. Moore, L. J. Roberts, H. Ischiropoulos, "Measuring Reactive Oxygen and Nitrogen Species with Fluorescent Probes: Challenges and Limitations", *Free Radical Biology and Medicine* **2012**, *52*, 1–6.

[225] C. A. Dinarello, "Biology of Interleukin 1", *The FASEB Journal* **1988**, *2*, 108–115.

[226] W. G. Wade, "The Oral Microbiome in Health and Disease", *Pharmacological Research* **2013**, *69*, 137–143.

[227] B. P. Krom, S. Kidwai, J. M. ten Cate, "*Candida* and Other Fungal Species: Forgotten Players of Healthy Oral Microbiota", *Journal of Dental Research* **2014**, *93*, 445–451.

[228] J. Chandra, D. M. Kuhn, P. K. Mukherjee, L. L. Hoyer, T. McCormick, M. A. Ghannoum, "Biofilm Formation by the Fungal Pathogen *Candida albicans*: Development, Architecture, and Drug Resistance", *Journal of Bacteriology* **2001**, *183*, 5385–5394.

[229] M. Kapitan, I. Eichhof, Q. Lagadec, J. F. Ernst, "Click Beetle Luciferases As Dual Reporters of Gene Expression in *Candida albicans*", *Microbiology* **2016**, *162*, 1310–1320.

[230] F. Cottier, F. A. Mühlschlegel, "Sensing the Environment: Response of *Candida albicans* to the X Factor", *Fems Microbiology Letters* **2009**, *295*, 1–9.

[231] Y. W. Cavalcanti, M. Wilson, M. Lewis, A. A. Del-Bel-Cury, W. J. da Silva, D. W. Williams, "Modulation of *Candida albicans* Virulence by Bacterial Biofilms on Titanium Surfaces", *Biofouling* **2016**, *32*, 123–134.

[232] D. J. Cook, T. A. Hollowood, R. S. T. Linforth, A. J. Taylor, "Oral Shear Stress Predicts Flavour Perception in Viscous Solutions", *Chemical Senses* **2003**, *28*, 11–23.

[233] C. E. Fernández, M. B. Aspiras, M. W. Dodds, C. González-Cabezas, A. H. Rickard, "The Effect of Inoculum Source and Fluid Shear Force on the Development of *In Vitro* Oral Multispecies Biofilms", *Journal of Applied Microbiology* **2017**, *122*, 796–808.

[234] J. Lindhe, J. Meyle, "Peri-Implant Diseases: Consensus Report of the Sixth European Workshop on Periodontology", *Journal of Clinical Periodontology* **2008**, *35*, 282–285.

[235] M. Quirynen, C. M. L. Bollen, "The Influence of Surface Roughness and Surface-free Energy on Supra- and Subgingival Plaque Formation in Man", *Journal of Clinical Periodontology* **1995**, *22*, 1–14.

[236] R. Glauser, P. Schüpbach, J. Gottlow, C. H. F. Hämmerle, "Peri-Implant Soft Tissue Barrier at Experimental One-Piece Mini-Implants with Different Surface Topography in Humans: A Light-Microscopic Overview and Histometric Analysis", *Clinical Implant Dentistry and Related Research* **2005**, *7*, s44–s51.

[237] M. Esposito, M. G. Grusovin, H. V. Worthington, "Interventions for Replacing Missing Teeth: Antibiotics at Dental Implant Placement to Prevent Complications", *Cochrane Database of Systematic Reviews* **2013**, DOI `10.1002/14651858.CD004152.pub4`.

[238] S. Kuroda, R. Smeets, B. Stadlinger, F. Schwarz, B. Beck-Broichsitter, O. Jung, C. Precht, F. Kloss, A. Gröbe, M. Heiland, T. Ebker, "Impact of Dental Implant Surface Modifications on Osseointegration", *Biomed Research International* **2016**, *2016*, 6285620.

[239] H. Zhang, R. Tsao, "Dietary Polyphenols, Oxidative Stress and Antioxidant and Anti-Inflammatory Effects", *Current Opinion in Food Science* **2016**, *8*, 33–42.

[240] H. Ejima, J. J. Richardson, F. Caruso, "Metal–Phenolic Networks As a Versatile Platform to Engineer Nanomaterials and Biointerfaces", *Nano Today* **2017**, *12*, 136–148.

[241] J. Guo, J. J. Richardson, Q. A. Besford, A. J. Christofferson, Y. Dai, C. W. Ong, B. L. Tardy, K. Liang, G. H. Choi, J. Cui, P. J. Yoo, I. Yarovsky, F. Caruso, "Influence of Ionic Strength on the Deposition of Metal–Phenolic Networks", *Langmuir* **2017**, *33*, 10616–10622.

[242] Q.-Z. Zhong, S. Li, J. Chen, K. Xie, S. Pan, J. J. Richardson, F. Caruso, "Oxidation-Mediated Kinetic Strategies for Engineering Metal–Phenolic Networks", *Angewandte Chemie International Edition* **2019**, *58*, 12563–12568.

[243] T. Park, W. I. Kim, B. J. Kim, H. Lee, I. S. Choi, J. H. Park, W. K. Cho, "Salt-induced, Continuous Deposition of Supramolecular Iron(III)–Tannic Acid Complex", *Langmuir* **2018**, *34*, 12318–12323.

[244] J. Guo, Y. Ping, H. Ejima, K. Alt, M. Meissner, J. J. Richardson, Y. Yan, K. Peter, D. von Elverfeldt, C. E. Hagemeyer, F. Caruso, "Engineering Multifunctional Capsules through the Assembly of Metal–Phenolic Networks", *Angewandte Chemie. International Edition* **2014**, *53*, 5546–51.

[245] C. G. Pierpont, C. W. Lange in *Progress in Inorganic Chemistry*, **1994**, Chapter The Chemistry of Transition Metal Complexes Containing Catechol and Semiquinone Ligands, pp. 331–442.

[246] H. Lee, W. I. Kim, W. Youn, T. Park, S. Lee, T.-S. Kim, J. F. Mano, I. S. Choi, "Iron Gall Ink Revisited: In-Situ Oxidation of Fe(II)–Tannin Complex for Fluidic Interface Engineering", *Advanced Materials* **2018**, *30*, 1805091.

[247] C. Maerten, L. Lopez, P. Lupattelli, G. Rydzek, S. Pronkin, P. Schaaf, L. Jierry, F. Boulmedais, "Electrotriggered Confined Self-Assembly of Metal–Polyphenol Nanocoatings Using a Morphogenic Approach", *Chemistry of Materials* **2017**, *29*, 9668–9679.

[248] Z. Xu, "Mechanics of Metal-Catecholate Complexes: The Roles of Coordination State and Metal Types", *Scientific Reports* **2013**, *3*, 2914.

[249] X. Li, P. Gao, J. Tan, K. Xiong, M. F. Maitz, C. Pan, H. Wu, Y. Chen, Z. Yang, N. Huang, "Assembly of Metal–Phenolic/Catecholamine Networks for Synergistically Anti-Inflammatory, Antimicrobial, and Anticoagulant Coatings", *ACS Applied Materials & Interfaces* **2018**, *10*, 40844–40853.

[250] L. Liu, X. Xiao, K. Li, X. Li, K. Yu, X. Liao, B. Shi, "Prevention of Bacterial Colonization Based on Self-Assembled Metal–Phenolic Nanocoating from Rare Earth Ions and Catechin", *ACS Applied Materials & Interfaces* **2020**.

[251] N. R. Perron, H. C. Wang, S. N. DeGuire, M. Jenkins, M. Lawson, J. L. Brumaghim, "Kinetics of Iron Oxidation upon Polyphenol Binding", *Dalton Transactions* **2010**, *39*, 9982–9987.

[252] S. Quignard, T. Coradin, J. J. Powell, R. Jugdaohsingh, "Silica Nanoparticles As Sources of Silicic Acid Favoring Wound Healing *In Vitro*", *Colloids and Surfaces B: Biointerfaces* **2017**, *155*, 530–537.

[253] K. Yoshino, M. Kotaka, M. Okamoto, H. Kakihana, "^{11}B-NMR Study of the Complex Formation of Borate with Catechol and L-Dopa", *Bulletin of the Chemical Society of Japan* **1979**, *52*, 3005–3009.

[254] P. Pichet, R. L. Benoit, "Complexes of Germanium (IV) with Anions of O-Diphenols and Their Stability Constants", *Inorganic Chemistry* **1967**, *6*, 1505–1509.

[255] M. Pasdeloup, C. Brisson, "Nmr Study of the Complexation of Boric Acid with Catechol (1,2-dihydroxybenzene)", *Org. Magn. Reson.* **2020**, *16*, 164–167.

[256] M. Vatankhah-Varnoosfaderani, S. Hashmi, A. GhavamiNejad, F. J. Stadler, "Rapid Self-Healing and Triple Stimuli Responsiveness of a Supramolecular Polymer Gel Based on Boron–Catechol Interactions in a Novel Water-Soluble Mussel-Inspired Copolymer", *Polymer Chemistry* **2014**, *5*, 512–523.

[257] X. Cheng, M. Li, H. Wang, Y. Cheng, "All-Small-Molecule Dynamic Covalent Gels with Antibacterial Activity by Boronate-Tannic Acid Gelation", *Chinese Chemical Letters* **2019**.

[258] G. Xiong, W. Ji, F. Wang, F. Zhang, P. Xue, M. Cheng, Y. Sun, X. Wang, T. Zhang, "Quercetin Inhibits Inflammatory Response Induced by LPS from *Porphyromonas gingivalis* in Human Gingival Fibroblasts via Suppressing NF-κB Signaling Pathway", *BioMed Research International* **2019**, *2019*, 6282635.

[259] D. Seleem, V. Pardi, R. M. Murata, "Review of Flavonoids: A Diverse Group of Natural Compounds with Anti-*Candida albicans* Activity *In Vitro*", *Archives of Oral Biology* **2017**, *76*, 76–83.

[260] S. Sakanaka, M. Aizawa, M. Kim, T. Yamamoto, "Inhibitory Effects of Green Tea Polyphenols on Growth and Cellular Adherence of an Oral Bacterium, *Porphyromonas gingivalis*", *Bioscience Biotechnolgy & Biochemistry* **2011**, *60*, 745–749.

[261] G. Yun, D. G. Kang, H. B. Rheem, H. Lee, S. Y. Han, J. Park, W. K. Cho, S. M. Han, I. S. Choi, "Reversed Anionic Hofmeister Effect in Metal–Phenolic-based Film Formation", *Langmuir* **2020**, *36*, 15552–15557.

[262] S. Hong, Y. Wang, S. Y. Park, H. Lee, "Progressive Fuzzy Cation-π Assembly of Biological Catecholamines", *Science Advances* **2018**, *4*, eaat7457.

[263] R. Ou, J. Wei, C. Zhao, Q. Gu, H. Zhu, X. Li, N. S. Nguyen, L. Wan, M. Forsyth, H. Wang, "Monovalent Cation-Phenolic Crystals with pH Reversible Crystal Transformation", *Chemistry – a European Journal* **2019**, *25*, 12281.

[264] K. K. Bania, A. K. Guha, P. K. Bhattacharyya, S. Sinha, "Effect of Substituent and Solvent on Cation-π Interactions in Benzene and Borazine: A Computational Study", *Dalton Transactions* **2014**, *43*, 1769–1784.

[265] G. Prampolini, M. d'Ischia, A. Ferretti, "The Phenoxyl Group-Modulated Interplay of Cation-π and σ-type Interactions in the Alkali Metal Series", *Physical Chemistry Chemical Physics* **2020**, *22*, 27105–27120.

[266] A. C. Eslami, W. Pasanphan, B. A. Wagner, G. R. Buettner, "Free Radicals Produced by the Oxidation of Gallic Acid: An Electron Paramagnetic Resonance Study", *Chemistry Central Journal* **2010**, *4*, 15.

[267] J.-R. Jeon, J.-H. Kim, Y.-S. Chang, "Enzymatic Polymerization of Plant-derived Phenols for Material-independent and Multifunctional Coating", *Journal of Materials Chemistry B* **2013**, *1*, 6501–6509.

[268] J. J. Roberts, P. Naudiyal, K. S. Lim, L. A. Poole-Warren, P. J. Martens, "A Comparative Study of Enzyme Initiators for Crosslinking Phenol-Functionalized Hydrogels for Cell Encapsulation", *Biomater Res* **2016**, *20*, 30.

[269] Q.-Z. Zhong, J. J. Richardson, S. Li, W. Zhang, Y. Ju, J. Li, S. Pan, J. Chen, F. Caruso, "Expanding the Toolbox of Metal–Phenolic Networks Via Enzyme-mediated Assembly", *Angewandte Chemie International Edition* **2020**, *59*, 1711–1717.

[270] Y. Chen, Q. Liu, "Oxidant-Induced Plant Phenol Surface Chemistry for Multifunctional Coatings: Mechanism and Potential Applications", *Journal of Membrane Science* **2018**, *570-571*, 176–183.

[271] P. Delparastan, K. Malollari, H. Lee, P. Messersmith, "Direct Evidence for the Polymeric Nature of Polydopamine", *Angewandte Chemie International Edition* **2018**, *58*, 6.

[272] Y. Ding, L.-T. Weng, M. Yang, Z. Yang, X. Lu, N. Huang, Y. Leng, "Insights into the Aggregation/Deposition and Structure of a Polydopamine Film", *Langmuir* **2014**, *30*, 12258–12269.

[273] F. Behboodi-Sadabad, H. Zhang, V. Trouillet, A. Welle, N. Plumeré, P. A. Levkin, "UV-Triggered Polymerization, Deposition, and Patterning of Plant Phenolic Compounds", *Advanced Functional Materials* **2017**, 1700127.

[274] A. Critchlow, E. Haslam, R. D. Haworth, P. B. Tinker, N. M. Waldron, "The Oxidation of Some Pyrogallol and Purpurogallin Derivatives", *Tetrahedron* **1967**, *23*, 2829–2847.

[275] A. S. Reddy, G. N. Sastry, "Cation [M = H^+, Li^+, Na^+, K^+, Ca^{2+}, Mg^{2+}, $NH_4{}^+$, and $NMe_4{}^+$] Interactions with the Aromatic Motifs of Naturally Occurring Amino Acids: a Theoretical Study", *The Journal of Physical Chemistry A* **2005**, *109*, 8893–8903.

[276] B. Kalyanaraman, P. I. Premovic, R. C. Sealy, "Semiquinone Anion Radicals from Addition of Amino Acids, Peptides, and Proteins to Quinones Derived from Oxidation of Catechols and Catecholamines. an ESR Spin Stabilization Study", *Journal of Biological Chemistry* **1987**, *262*, 11080–11087.

[277] H. Xu, J. Nishida, W. Ma, H. Wu, M. Kobayashi, H. Otsuka, A. Takahara, "Competition between Oxidation and Coordination in Cross-linking of Polystyrene Copolymer Containing Catechol Groups", *ACS Macro Letters* **2012**, *1*, 457–460.

[278] F. Reitzer, M. Allais, V. Ball, F. Meyer, "Polyphenols at Interfaces", *Advances in Colloid and Interface Science* **2018**, *257*, 31–41.

[279] M. Gomez-Florit, M. A. Pacha-Olivenza, M. C. Fernández-Calderón, A. Córdoba, M. L. González-Martín, M. Monjo, J. M. Ramis, "Quercitrin-nanocoated Titanium Surfaces Favour Gingival Cells against Oral Bacteria", *Scientific Reports* **2016**, *6*, 22444.

[280] C. Torres-León, J. Ventura-Sobrevilla, L. Serna-Cock, J. A. Ascacio-Valdés, J. Contreras-Esquivel, C. N. Aguilar, "Pentagalloylglucose (PGG): A Valuable Phenolic Compound with Functional Properties", *Journal of Functional Foods* **2017**, *37*, 176–189.

[281] C. Steffi, Z. Shi, C. H. Kong, W. Wang, "Bioinspired Polydopamine and Polyphenol Tannic Acid Functionalized Titanium Suppress Osteoclast Differentiation: A Facile and Efficient Strategy to Regulate Osteoclast Activity at Bone-Implant Interface", *Journal of the Royal Society Interface* **2019**, *16*, 20180799.

[282] Y. Huan, P. Ke-jun, W. Qiu-lin, G. Zheng-yi, L. Yao-qin, Z. Jun, X. Fang, L. Yi-lun, T. Ying, D. Feng-mei, Z. Peng, J. Jia-gui, W. Xin-chun, "Effect of Pomegranate Peel Polyphenol Gel on Cutaneous Wound Healing in Alloxan-Induced Diabetic Rats", *Chinese Medical Journal* **2013**, *126*.

[283] N. Ninan, A. Forget, V. P. Shastri, N. H. Voelcker, A. Blencowe, "Antibacterial and Anti-Inflammatory pH-Responsive Tannic Acid-Carboxylated Agarose Composite Hydrogels for Wound Healing", *ACS Applied Material Interfaces* **2016**, *8*, 28511–28521.

[284] B. Tardy, J. J. Richardson, V. Nithipipat, K. Kempe, J. Guo, K. L. Cho, M. A. Rahim, H. Ejima, F. Caruso, "Protein Adsorption and Coordination-based End-tethering of Functional Polymers on Metal–Phenolic Network Films", *Biomacromolecules* **2019**, *20*, 1421–1428.

[285] L. Yang, L. Han, Q. Liu, Y. Xu, L. Jia, "Galloyl Groups-Regulated Fibrinogen Conformation: Understanding Antiplatelet Adhesion on Tannic Acid Coating", *Acta Biomaterialia* **2017**, *64*, 187–199.

[286] Y. Yang, R. Cavin, J. L. Ong, "Protein Adsorption on Titanium Surfaces and Their Effect on Osteoblast Attachment", *Journal of Biomedial Materials Research* **2003**, *67A*, 344–349.

[287] M. S. Hansen, "Fibronectin and Coagulation Factor XIII Increases Blood Platelet Adhesion to Fibrin", *Thrombosis Research* **1984**, *34*, 551–556.

[288] A. Thor, L. Rasmusson, A. Wennerberg, P. Thomsen, J.-M. Hirsch, B. Nilsson, J. Hong, "The Role of Whole Blood in Thrombin Generation in Contact with Various Titanium Surfaces", *Biomaterials* **2007**, *28*, 966–974.

[289] D. Perala, R. Chapman, J. Gelfand, "Complement Activation by Dental Implants.", *International Journal of Oral & Maxillofacial Implants* **1991**, *6*.

[290] M. Källtorp, A. Askendal, P. Thomsen, P. Tengvall, "Inflammatory Cell Recruitment, Distribution, and Chemiluminescence Response at IgG Precoated- and Thiol Functionalized Gold Surfaces", *Journal of Biomedial Materials Research* **1999**, *47*, 251–259.

[291] N. Harmankaya, K. Igawa, P. Stenlund, A. Palmquist, P. Tengvall, "Healing of Complement Activating Ti Implants Compared with Non-Activating Ti in Rat Tibia", *Acta Biomaterialia* **2012**, *8*, 3532–3540.

[292] M. Baggiolini, I. Clark-Lewis, "Interleukin-8, a Chemotactic and Inflammatory Cytokine", *Febs Letters* **1992**, *307*, 97–101.

[293] M. Mittal, M. R. Siddiqui, K. Tran, S. P. Reddy, A. B. Malik, "Reactive Oxygen Species in Inflammation and Tissue Injury", *Antioxidants & Redox Signaling* **2014**, *20*, 1126–1167.

[294] J. P. Silva, A. C. Gomes, O. P. Coutinho, "Oxidative DNA Damage Protection and Repair by Polyphenolic Compounds in PC12 Cells", *European Journal of Pharmacology* **2008**, *601*, 50–60.

[295] C. Bodet, F. Chandad, D. Grenier, "Cranberry Components Inhibit Interleukin-6, Interleukin-8, and Prostaglandin E2 Production by Lipopolysaccharide-Activated Gingival Fibroblasts", *European Journal of Oral Sciences* **2007**, *115*, 64–70.

[296] D. S. Wheeler, J. D. Catravas, K. Odoms, A. Denenberg, V. Malhotra, H. R. Wong, "Epigallocatechin-3-gallate, a Green Tea-derived Polyphenol, Inhibits Il-1β-dependent Proinflammatory Signal Transduction in Cultured Respiratory Epithelial Cells", *Journal of Nutrition* **2004**, *134*, 1039–1044.

[297] S. Agarwal, C. Baran, N. P. Piesco, J. C. Quintero, H. H. Langkamp, L. P. Johns, C. S. Chandra, "Synthesis of Proinflammatory Cytokines by Human Gingival Fibroblasts in Response to Lipopolysaccharides and Interleukin-1β", *Journal of Periodontal Research* **1995**, *30*, 382–389.

[298] G. Bonizzi, M. Karin, "The Two NF-κB Activation Pathways and Their Role in Innate and Adaptive Immunity", *Trends in Immunology* **2004**, *25*, 280–288.

[299] M. Gómez-Florit, M. Monjo, J. M. Ramis, "Quercitrin for Periodontal Regeneration: Effects on Human Gingival Fibroblasts and Mesenchymal Stem Cells", *Scientific Reports* **2015**, *5*, 16593.

[300] K. Kuno, K. Matsushima, "The Il-1 Receptor Signaling Pathway", *Journal of Leukocyte Biology* **1994**, *56*, 542–547.

[301] S. Aharoni, Y. Lati, M. Aviram, B. Fuhrman, "Pomegranate Juice Polyphenols Induce a Phenotypic Switch in Macrophage Polarization Favoring a M2 Anti-Inflammatory State", *Biofactors* **2015**, *41*, 44–51.

[302] H. Zhang, X. Wu, G. Wang, P. Liu, S. Qin, K. Xu, D. Tong, H. Ding, H. Tang, F. Ji, "Macrophage Polarization, Inflammatory Signaling, and NF-κB Activation in Response to Chemically Modified Titanium Surfaces", *Colloids and Surfaces B: Biointerfaces* **2018**, *166*, 269–276.

[303] V. Nicolin, N. De Tommasi, S. L. Nori, F. Costantinides, F. Berton, R. Di Lenarda, "Modulatory Effects of Plant Polyphenols on Bone Remodeling: A Prospective View from the Bench to Bedside", *Frontiers in Endocrinology* **2019**, *10*, 494–494.

[304] R. He, X. Hu, H. C. Tan, J. Feng, C. Steffi, K. Wang, W. Wang, "Surface Modification of Titanium with Curcumin: A Promising Strategy to Combat Fibrous Encapsulation", *Journal of Materials Chemistry B* **2015**, *3*, 2137–2146.

[305] E. Torre, G. Iviglia, C. Cassinelli, M. Morra, N. Russo, "Polyphenols from Grape Pomace Induce Osteogenic Differentiation in Mesenchymal Stem Cells", *International Journal of Molecular Medicine* **2020**, *45*, 1721–1734.

[306] M. Cazzola, S. Ferraris, F. Boschetto, A. Rondinella, E. Marin, W. Zhu, G. Pezzotti, E. Vernè, S. Spriano, "Green Tea Polyphenols Coupled with a Bioactive Titanium Alloy Surface: *In Vitro* Characterization of Osteoinductive Behavior through a KUSA A1 Cell Study", *International Journal of Molecular Sciences* **2018**, *19*, 2255.

[307] A. Córdoba, M. Satué, M. Gómez-Florit, M. Hierro-Oliva, C. Petzold, S. P. Lyngstadaas, M. L. González-Martín, M. Monjo, J. M. Ramis, "Flavonoid-Modified Surfaces: Multifunctional Bioactive Biomaterials with Osteopromotive, Anti-Inflammatory, and Anti-Fibrotic Potential", *Advanced Healthcare Materials* **2015**, *4*, 540–549.

[308] Z. Yang, J. Wu, X. Wang, J. Wang, N. Huang, "Inspired Chemistry for a Simple but Highly Effective Immobilization of Vascular Endothelial Growth Factor on Gallic Acid-functionalized Plasma Polymerized Film", *Plasma Processes and Polymers* **2012**, *9*, 718–725.

[309] J. S. Lee, J.-C. Lee, J. S. Heo, "Polydopamine-Assisted BMP-2 Immobilization on Titanium Surface Enhances the Osteogenic Potential of Periodontal Ligament Stem Cells Via Integrin-Mediated Cell-Matrix Adhesion", *Journal of Cell Communication and Signaling* **2018**, *12*, 661–672.

[310] S. Lee, Y.-Y. Chang, J. Lee, S. K. Madhurakkat Perikamana, E. M. Kim, Y.-H. Jung, J.-H. Yun, H. Shin, "Surface Engineering of Titanium Alloy Using Metal–Polyphenol Network Coating with Magnesium Ions for Improved Osseointegration", *Biomaterial Science* **2020**, *8*, 3404–3417.

[311] S. Yang, Y. Wang, S. Luo, C. Shan, Y. Geng, T. Zhang, S. Sheng, X. Zan, "Building Polyphenol and Gelatin Films As Implant Coating, Evaluating from *In Vitro* and *In Vivo* Performances", *Colloids and Surfaces B: Biointerfaces* **2019**, *181*, 549–560.

[312] B. A. Peters, J. Wu, R. B. Hayes, J. Ahn, "The Oral Fungal Mycobiome: Characteristics and Relation to Periodontitis in a Pilot Study.", *BMC Microbiology* **2017**, *17*, 157.

[313] M. Hirasawa, K. Takada, "Multiple Effects of Green Tea Catechin on the Antifungal Activity of Antimycotics against *Candida albicans*", *Journal of Antimicrobial Chemotherapy* **2004**, *53*, 225–229.

[314] K. Ishida, J. C. P. de Mello, D. A. G. Cortez, B. P. D. Filho, T. Ueda-Nakamura, C. V. Nakamura, "Influence of Tannins from *Stryphnodendron adstringens* on Growth and Virulence Factors of *Candida albicans*", *Journal of Antimicrobial Chemotherapy* **2006**, *58*, 942–949.

[315] E. H. Endo, D. A. Garcia Cortez, T. Ueda-Nakamura, C. V. Nakamura, B. P. Dias Filho, "Potent Antifungal Activity of Extracts and Pure Compound Isolated from Pomegranate Peels and Synergism with Fluconazole against *Candida albicans*", *Research in Microbiology* **2010**, *161*, 534–540.

[316] M. Sharma, R. Manoharlal, A. S. Negi, R. Prasad, "Synergistic Anticandidal Activity of Pure Polyphenol Curcumin I in Combination with Azoles and Polyenes Generates Reactive Oxygen Species Leading to Apoptosis", *Fems Yeast Research* **2010**, *10*, 570–578.

[317] S. Kim, E.-R. Woo, D. G. Lee, "Synergistic Antifungal Activity of Isoquercitrin: Apoptosis and Membrane Permeabilization Related to Reactive Oxygen Species in *Candida albicans*", *IUBMB Life* **2019**, *71*, 283–292.

[318] Y. Li, X. Jiang, J. Hao, Y. Zhang, R. Huang, "Tea Polyphenols: Application in the Control of Oral Microorganism Infectious Diseases", *Archives of Oral Biology* **2019**, *102*, 74–82.

[319] G. R. Teodoro, K. Ellepola, C. J. Seneviratne, C. Y. Koga-Ito, "Potential Use of Phenolic Acids As Anti-*Candida* Agents: A Review", *Frontiers in Microbiology* **2015**, *6*, 1420.

[320] P. W.-K. Tsang, H. M. H. N. Bandara, W.-P. Fong, "Purpurin Suppresses *Candida albicans* Biofilm Formation and Hyphal Development.", *PLOS ONE* **2012**, *7*, e50866.

[321] R. Tamai, M. Sugamata, Y. Kiyoura, "*Candida albicans* Enhances Invasion of Human Gingival Epithelial Cells and Gingival Fibroblasts by *Porphyromonas gingivalis*", *Microbial Pathogenesis* **2011**, *51*, 250–254.

[322] M. B. Lohse, M. Gulati, A. D. Johnson, C. J. Nobile, "Development and Regulation of Single- and Multi-Species *Candida albicans* Biofilms", *Nature Reviews Microbiology* **2018**, *16*, 19–31.

[323] J. Hasan, R. J. Crawford, E. P. Ivanova, "Antibacterial Surfaces: The Quest for a New Generation of Biomaterials", *Trends in Biotechnology* **2013**, *31*, 295–304.

[324] M. Kumorek, I. M. Minisy, T. Krunclová, M. Voršiláková, K. Venclíková, E. M. Chánová, O. Janoušková, D. Kubies, "pH-Responsive and Antibacterial Properties of Self-Assembled Multilayer Films Based on Chitosan and Tannic Acid", *Materials Science and Engineering: C* **2019**, 110493.

[325] Y. W. Cavalcanti, M. Wilson, M. Lewis, D. Williams, P. M. Senna, A. A. Del-Bel-Cury, W. J. d. Silva, "Salivary Pellicles Equalise Surfaces' Charges and Modulate the Virulence of *Candida albicans* Biofilm", *Archives of Oral Biology* **2016**, *66*, 129–140.

[326] R. Bürgers, S. Hahnel, T. E. Reichert, M. Rosentritt, M. Behr, T. Gerlach, G. Handel, M. Gosau, "Adhesion of *Candida albicans* to Various Dental Implant Surfaces and the Influence of Salivary Pellicle Proteins", *Acta Biomaterialia* **2010**, *6*, 2307–2313.

[327] M.-H. Pan, S.-Y. Lin-Shiau, C.-T. Ho, J.-H. Lin, J.-K. Lin, "Suppression of Lipopolysaccharide-Induced Nuclear Factor-κB Activity by Theaflavin-3,3'-digallate from Black Tea and Other Polyphenols through Down-Regulation of IκB Kinase Activity in Macrophages", *Biochemical Pharmacology* **2000**, *59*, 357–367.

[328] M. Feldman, S. Tanabe, A. Howell, D. Grenier, "Cranberry Proanthocyanidins Inhibit the Adherence Properties of *Candida albicans* and Cytokine Secretion by Oral Epithelial Cells.", *BMC Complementary and Alternative Medicine* **2012**, *12*, 6.

[329] A. Kumar, S. Dhamgaye, I. K. Maurya, A. Singh, M. Sharma, R. Prasad, "Curcumin Targets Cell Wall Integrity Via Calcineurin-Mediated Signaling in *Candida albicans*", *Antimicrobial Agents and Chemotherapy* **2014**, *58*, 167.

[330] Y. Ning, J. Ling, C. D. Wu, "Synergistic Effects of Tea Catechin Epigallocatechin Gallate and Antimycotics against Oral *Candida* Species", *Archives of Oral Biology* **2015**, *60*, 1565–1570.

[331] A. H. Nobbs, H. F. Jenkinson, "Interkingdom Networking within the Oral Microbiome", *Microbes and Infection* **2015**, *17*, 484–492.

[332] M. A. Al-Fattani, L. J. Douglas, "Biofilm Matrix of *Candida albicans* and *Candida tropicalis*: Chemical Composition and Role in Drug Resistance", *Journal of Medical Microbiology* **2006**, *55*, 999–1008.

[333] N. F. Della Vecchia, A. Luchini, A. Napolitano, G. D'Errico, G. Vitiello, N. Szekely, M. d'Ischia, L. Paduano, "Tris Buffer Modulates Polydopamine Growth, Aggregation, and Paramagnetic Properties", *Langmuir* **2014**, *30*, 9811–9818.

[334] A. Depla, E. Verheyen, A. Veyfeyken, M. Van Houteghem, K. Houthoofd, V. Van Speybroeck, M. Waroquier, C. E. A. Kirschhock, J. A. Martens, "UV-Raman and ^{29}Si NMR Spectroscopy Investigation of the Nature of Silicate Oligomers Formed by Acid Catalyzed Hydrolysis and Polycondensation of Tetramethylorthosilicate", *The Journal of Physical Chemistry C* **2011**, *115*, 11077–11088.

Appendix A

Appendix

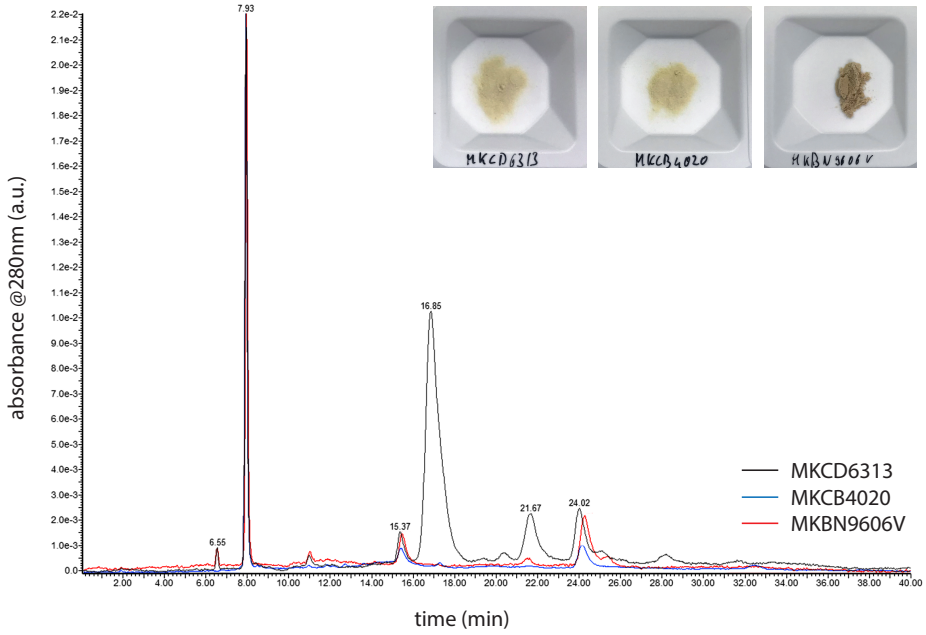

Figure A1: C18 reverse–phase HPLC. Commercially pure TA contains different phenolic molecules. All batches contained a high content of GA, which elutes at 8 min compared to TA at 24 min. TA MKCD6313 showed a major contamination eluting after 17 min. Lot MKBN9606V showed least contamination and was used for all studies.

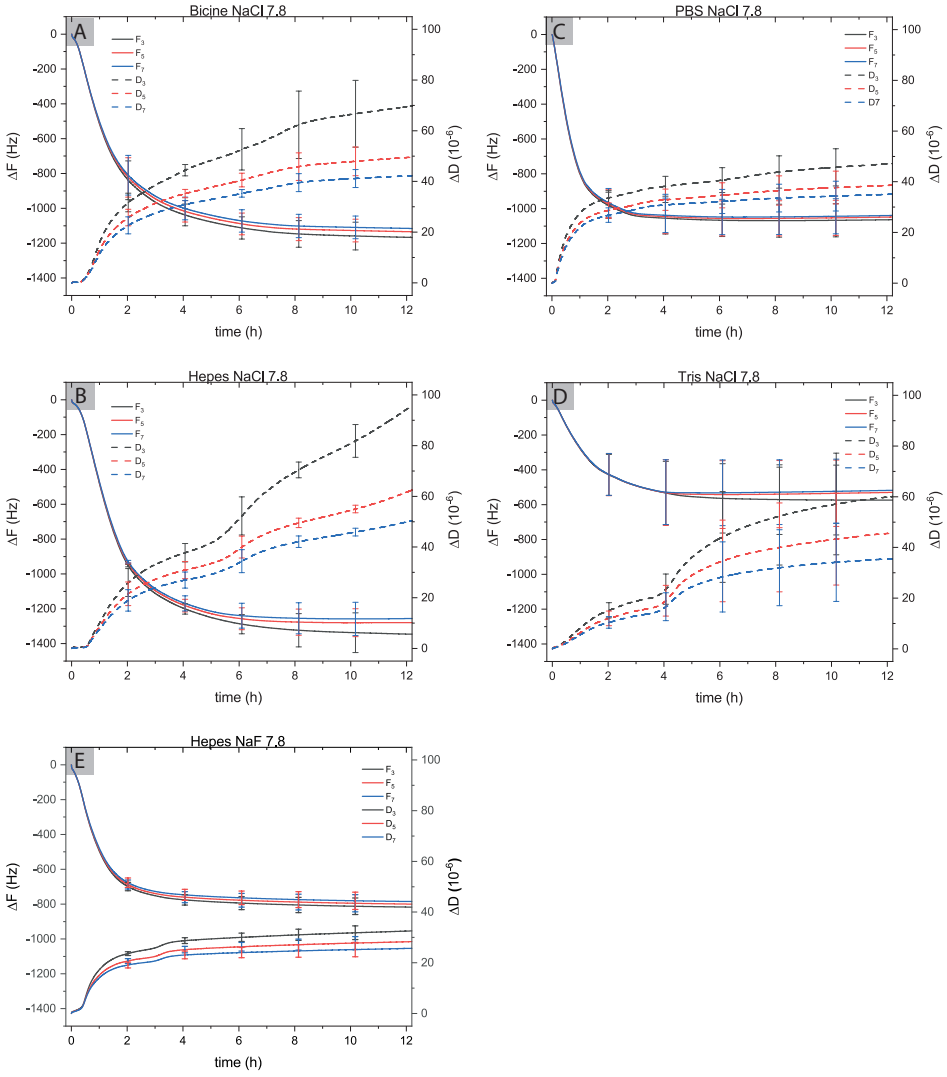

Figure A2: Due to the acidic properties of TA, coating solutions have to be buffered to maintain the same pH level throughout the experiment. Compatible organic buffers are either HEPES or bicine. Tris interacts with polyphenols via its primary amine group.[333] For inorganic buffers, sodium phosphate is more applicable compared to potassium phosphate, which interacts with polyphenols in the range between pH = 6 and pH = 11. Additionally, the ionic strength has to be adjusted with NaCl. Alternatively, NaF can be used.

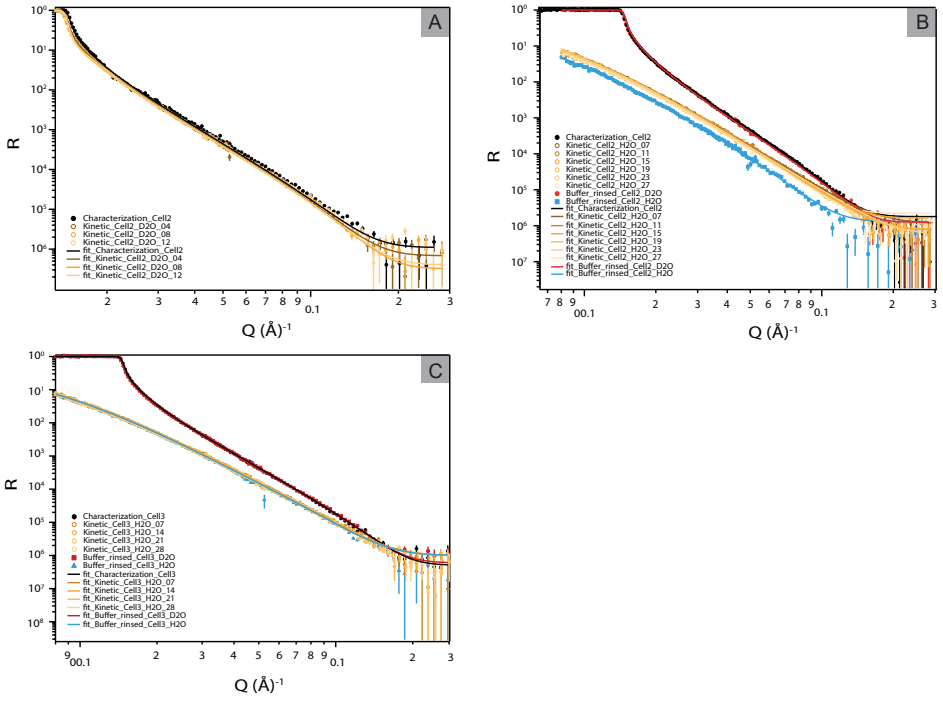

Figure A3: NR was used to characterize the morphology of TA coatings deposited under two pH conditions. (A) The initial experiment in heavy water (D_2O) showed no characteristic features in the data obtained for the full q-range. (B) Repeating the measurement in H_2O at pH = 7.8 and (C) pH = 6.8 also lacked a distinct fringe pattern. Similar to the measurement in D_2O the lack of features and the identical signal of final buffer rinse with the initial characterization suggested either no coating formation on the Si crystal, or lack of NR contrast.

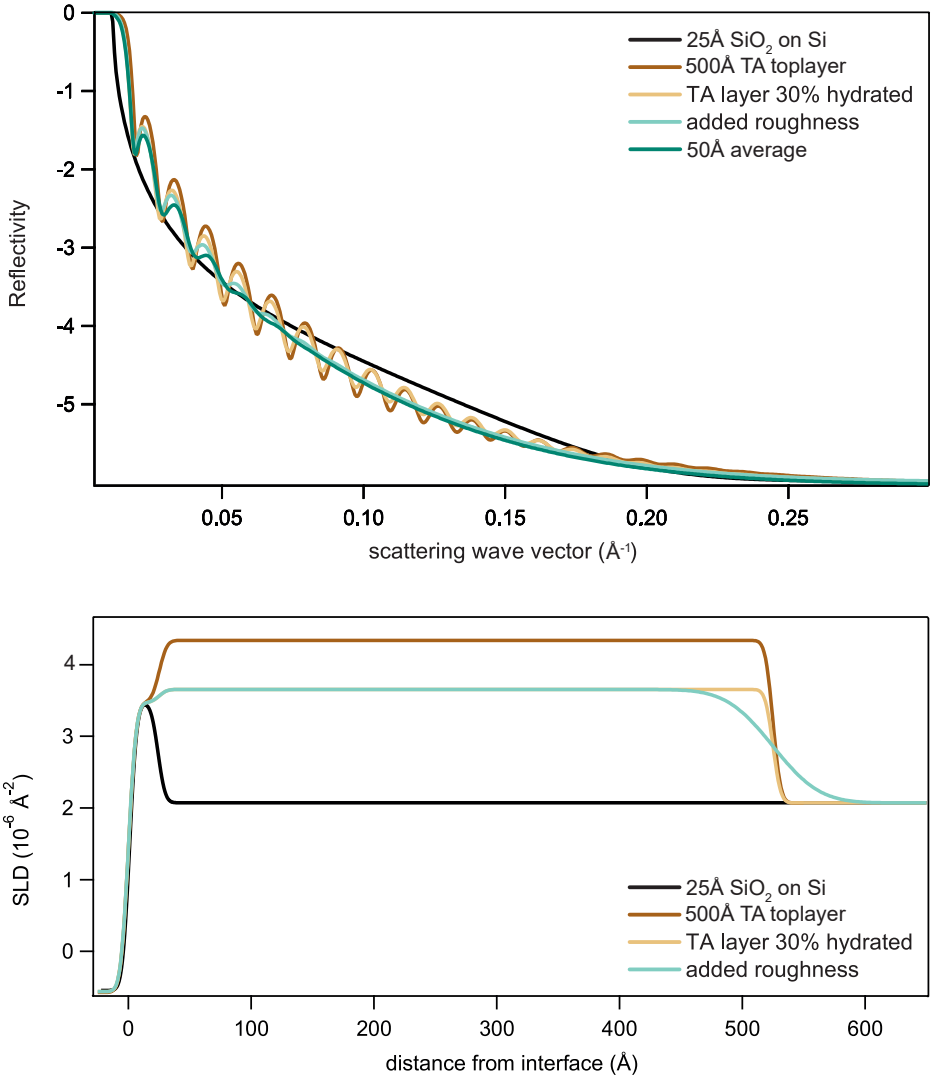

Figure A4: A characteristic reflection curve on a polished Si crystal with a 25 Å oxide layer results in no fringe pattern. Once a layer with a thickness of 50 nm is added, distinct fringes are expected. However, in case the layer is hydrated the contrast in SLD is reduced and the fringe pattern becomes less distinct. More striking is the effect of a surface roughness, which may occur due to adsorption of polymers or an uneven coating deposition. Finally, due to the limitation of the neutron flux, each time step requires a certain acquisition time. If the thickness increases within that time frame, the final signal is almost featureless due to the gradual signal average.

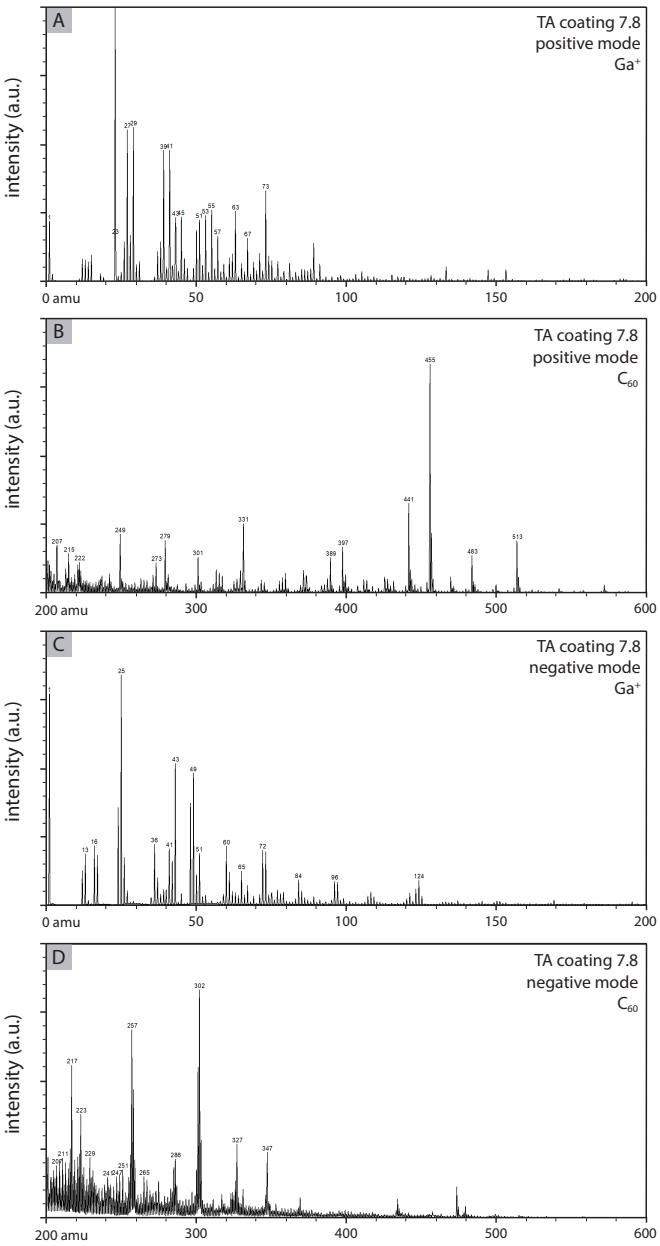

Figure A5: TOF–SIMS analysis of TA coating obtained in HEPES at pH = 7.8. The molecular structure of the coating was probed with C_{60} clusters, which have a lower ionization energy. However, in contrast to MALDI–TOF, no distinct fragmentation pattern was obtained, besides potential evidence of GA dimers with a mass of 302 Da (EA).

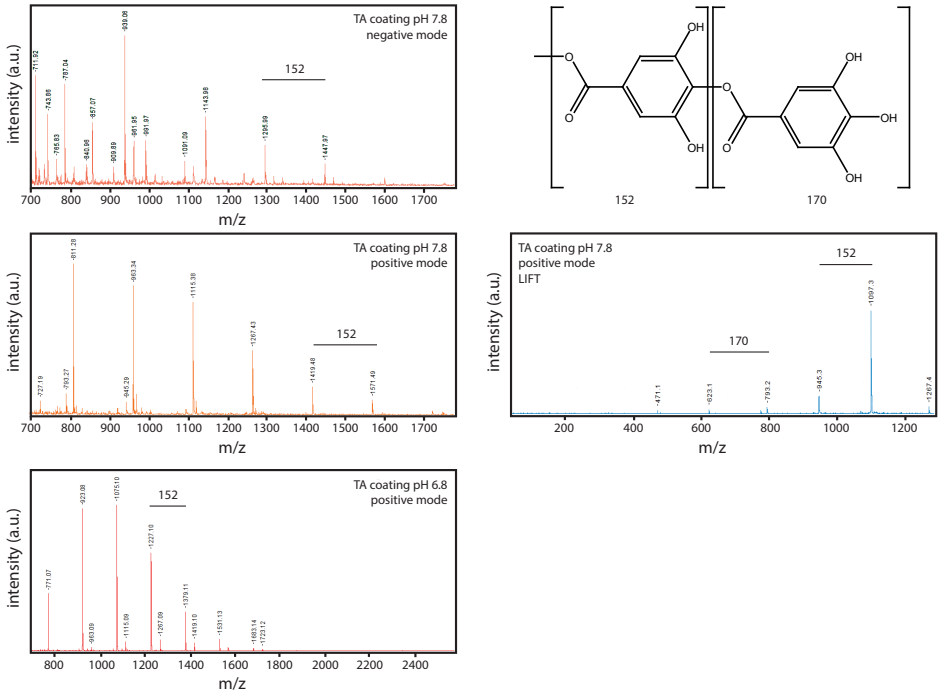

Figure A6: Surface MALDI–TOF of TA coatings using DHB as matrix showed a distinct fragmentation pattern of the molecule. The spectrum in positive mode shows intact TA as its sodium adduct at 1723 Da. Lower molecular weight fragments show the removal of galloyl units (152 Da) and GA (170 Da). The LIFT spectrum shows the secondary fragmentation pattern of the parent molecule, and corroborates the identification of TA with its structural subunits of GA and galloyl fragments.

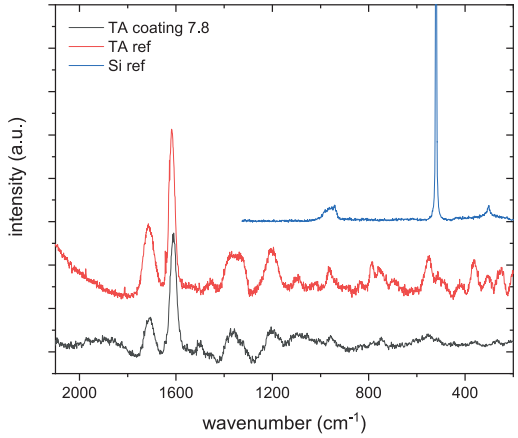

Figure A7: Surface analysis using a Raman microscope (Renishaw, inVia). Similar to FTIR, Raman spectroscopy did not result in any evidence of Si−O−Ar groups around $\nu = 1100\,\mathrm{cm}^{-1}$ in the TA coating (CSTR, HEPES pH = 7.8, 80 µM Si_{aq}, 600 mM NaCl).[201,334] The spectrum of the coating was recorded at a wavelength of 488 nm, whereas the spectra for both reference samples were obtained at 785 nm. TA showed high fluorescence at both IR laser wavelengths. Spectra were corrected for the baseline shift. Although the laser was pulsed with 10 exposures for each 10 seconds, visible coating degradation occurred during the measurement. The film thickness was approximately 350 nm to avoid interference with the signal of the Si substrate (Si−Si $\nu = 522\,\mathrm{cm}^{-1}$).

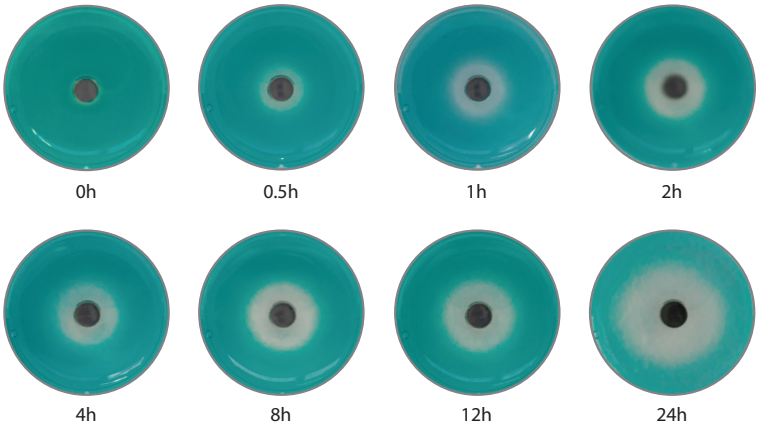

Figure A8: The antioxidant capacity of polyphenolic coatings was visualized in a radial diffusion method. The ABTS radical was embedded in an agar gel and coated coins were placed in the center of the cast gels. During the course of 24 h, the discoloration of the ABTS radicals away from the interface of the coin shows the radical scavenging capacity of the polyphenolic molecules, which are released from the coated surfaces.

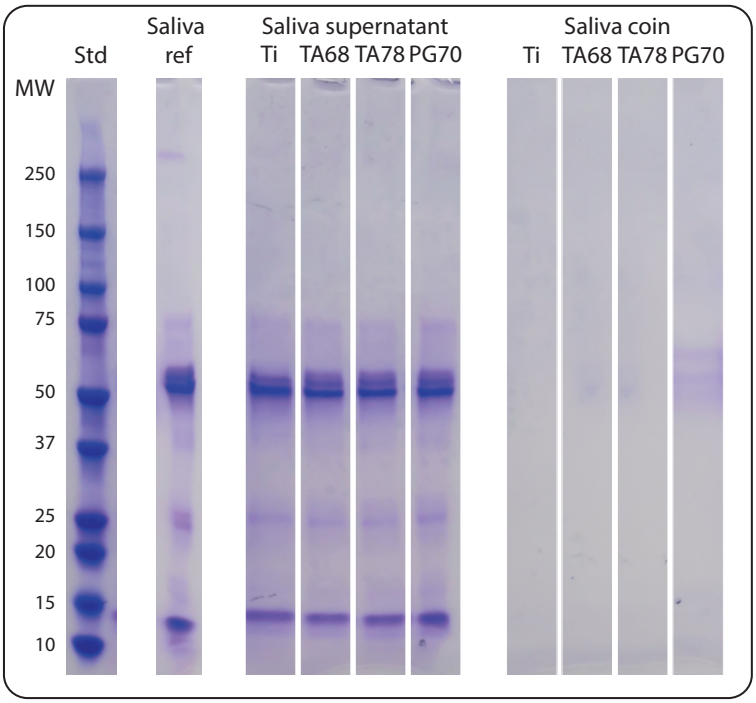

Figure A9: SDS–PAGE of salivary proteins. Saliva was incubated in presence of coated coins for 1 h to form a pellicle. The supernatant was collected, and the coins were sonicated for 10 min in 1 % SDS solution. The solution was then freeze–dried and resuspended in 100 µL water. The absorbance at λ =280 nm indicated concentrations below 1 mg mL^{-1}. The concentration of the saliva reference and supernatant samples was adjusted to 1 mg mL^{-1} before dilution with Laemmli sample buffer.

Papers

Paper II

Silicate-Phenolic Networks: Coordination-Mediated Deposition of Bioinspired Tannic Acid Coatings

II

Florian Weber, Wei-Chih Liao, Alejandro Barrantes, Matthias Edén, Hanna Tiainen

Published in *Chemistry – A European Journal*, May 2019, volume 4, pp. 9870–9874. DOI: 10.1002/chem.201902358.

ChemPubSoc Europe
DOI: 10.1002/chem.201902358
CHEMISTRY A European Journal Communication

Surface Chemistry

Silicate-Phenolic Networks: Coordination-Mediated Deposition of Bioinspired Tannic Acid Coatings

Florian Weber,[a] Wei-Chih Liao,[b] Alejandro Barrantes,[a] Mattias Edén,[b] and Hanna Tiainen*[a]

Abstract: Surface modification with polyphenolic molecules has been pursued in biomedical materials owing to their antioxidant, anti-inflammatory, and antimicrobial characteristics. Recently, the use of silicic acid (Si_{aq}) as a mediator for efficient surface deposition of tannic acid (TA) was reported, but the postulated Si-TA polymeric networks were not characterized. Herein, we present unambiguous evidence for silicate-TA networks that involve Si–O–C motifs by using solid-state NMR spectroscopy, further supported by XPS and ToF-SIMS. By using QCM-D we demonstrate the advantages of Si_{aq}, compared to using transition-metal ions, to improve the coating efficiency under mildly acidic conditions. The presented homogenous coating buildup and validated applicability in inorganic buffers broadens the use of TA for surface modifications in technological and biomedical applications.

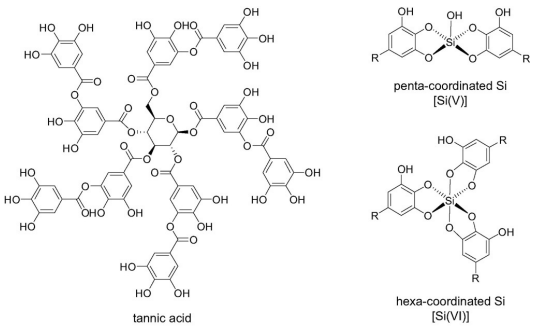

Scheme 1. Schematic illustration of tannic acid (TA), penta-coordinated Si [Si(V)] binding two TA ligands, and hexa-coordinated Si [Si(VI)] binding three TA ligands.

Polyphenolic molecules are well known for their antioxidant properties[1] and thus have been utilized in biomedical applications as anti-inflammatory,[2] antimicrobial,[3] and anticancer agents.[4] Due to the substrate-independent adhesive properties of catechol units, polyphenolic molecules have recently gained substantial attention toward creating novel bioinspired multifunctional material surfaces.[5] Tannic acid (TA) is a naturally derived hydrolysable polyphenolic molecule consisting of five to ten galloyl units on a central glucose ring (Scheme 1),[6] which account for its high antimicrobial and antioxidant capacity.[7] Albeit the use of polyphenolic surface functionalization to overcome challenges in medicine and biotechnology has been proposed,[8] to date, TA-modified interfaces are only found in a few applications, such as controlled drug delivery[9] and filtration membranes.[10]

Currently, two methods are applied to deposit TA onto surfaces: 1) self-assembly of a metal phenolic network (MPN) and 2) induced oxidative polymerization. MPNs exploit the strong interaction between vicinal diol groups and transition-metal ions.[11] Usually, these systems are based on Fe^{3+} and are conducted in mildly alkaline conditions.[12] Although MPNs have become the predominant method to create TA coatings, their drawback lies in the deposition of only one molecular layer per deposition cycle and the formation of complexation byproducts in solution.[13] Efforts have, therefore, been made to induce a continuous coating formation by slow conversion of Fe^{2+} to Fe^{3+}, yet with limited efficiency.[14] Induced oxidative polymerization is based on the spontaneous auto-oxidative polymerization of polyphenols in an alkaline environment[3c,15] or triggered by UV-light.[16] The stability of TA in alkaline conditions is, however, limited, and the auto-oxidation by dissolved oxygen leads to uncontrolled degradation of TA and precipitation of polymeric byproducts.[17]

Recently, we reported an alternative deposition method using silicic acid (Si_{aq}), which enables a continuous TA coating formation on titanium surfaces.[18] However, the structural role of Si_{aq} in the coating formation remained unknown. Herein, we provide direct evidence for the formation of silicate–TA networks by magic-angle spinning (MAS) NMR spectroscopy. These results are supported by X-ray photoelectron spectroscopy (XPS) and time-of-flight secondary ion mass spectroscopy (ToF-SIMS). Based on the formation of silicate–TA networks, we

[a] F. Weber, Dr. A. Barrantes, Prof. H. Tiainen
Department of Biomaterials, Institute of Clinical Dentistry
University of Oslo, P.O. Box 1109 Blindern, 0317 Oslo (Norway)
E-mail: hannati@odont.uio.no
[b] Dr. W.-C. Liao, Prof. M. Edén
Department of Materials and Environmental Chemistry
Stockholm University, 10691 Stockholm (Sweden)
Supporting information and the ORCID identification number(s) for the author(s) of this article can be found under:
https://doi.org/10.1002/chem.201902358.

present a novel deposition method in mildly acidic conditions for improved TA stability in solution compared to using transition-metal ions or oxidative conditions. By introducing a continuous-flow process and demonstrating the TA coating formation in inorganic buffers, we extend the applicability of TA coatings for technological and biomedical purposes, such as designing modified implant surfaces with reduced infection risk.[2]

We employed $^{1}H \rightarrow {}^{29}Si$ cross-polarization (CP) MAS NMR to investigate the coordination state of Si in two samples prepared with 99.7% ^{29}Si-enriched silicate ($^{29}Si_{aq}$; see the Supporting Information): TA-coated TiO_2 particles ($TA_{coating}$) prepared in an 80 μM $^{29}Si_{aq}$ solution, and TA precipitated with 1000 μM $^{29}Si_{aq}$ (TA_{prec}). The ^{29}Si CPMAS NMR spectra shown in Figure 1

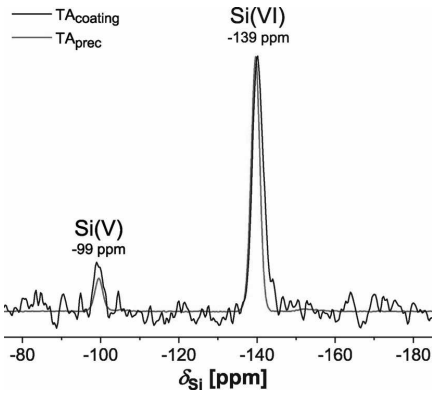

Figure 1. Solid-state ^{29}Si CPMAS NMR spectra recorded at 9.4 T and 7.00 kHz MAS from TA-coated TiO_2 particles in the presence of 80 μM $^{29}Si_{aq}$ solution ($TA_{coating}$), and from TA precipitated from a 1 mM $^{29}Si_{aq}$ solution (TA_{prec}). The NMR peaks at $\delta_{Si} = -99$ and $\delta_{Si} = -139$ ppm are assigned to ^{29}Si species coordinating five [Si(V)] and six [Si(VI)] phenolic O atoms of the TA ligands, respectively (Scheme 1).

reveal nearly identical ^{29}Si responses, which justifies using the Si-richer TA_{prec} specimen for the remaining NMR experimentation. From previously reported ^{29}Si chemical shifts involving Si–O–C bonds,[19] the two peaks at −99 and −139 ppm of Figure 1 are assigned to ^{29}Si coordinating five [Si(V)] and six [Si(VI)] phenolic O atoms, respectively, thereby complexing two and three galloyl motifs of TA (Scheme 1). These assignments are corroborated by the more rapid NMR-signal buildup observed from the $^{29}Si(V)$ sites (Figure S2, Supporting Information), the direct Si–OH bond of which implies a shorter ^{29}Si–^{1}H distance than their $^{29}Si(VI)$ counterparts, which solely feature Si–O–R motifs (Scheme 1). Further evidence for silicate-TA complexation is provided by the $^{13}C\{^{29}Si\}$ rotational-echo double-resonance (REDOR)[20] NMR results in Figure S3, of the Supporting Information. A significant ^{13}C NMR-signal attenuation is only observed from the aromatic ^{13}C moieties, meaning that they feature shorter internuclear distances to ^{29}Si than all other ^{13}C sites. This result accords with Si binding to the vicinal phenolic O positions of the TA molecule, as proposed in Scheme 1.

Both ^{29}Si NMR (Figures 1 and Figure S1, Supporting Information) and XPS (Figure S6) evidenced negligible SiO_2 contents in the TA coating. Hence, we conclude from Figure 1 and the integrated ^{29}Si NMR peak intensities of the quantitative ^{29}Si NMR spectrum of Figure S1 (Supporting Information) that ≈90% of all Si is hexa-coordinated by phenolic O atoms in the TA_{prec} and $TA_{coating}$ samples. Moreover, XPS and ToF-SIMS mappings verified that Si is distributed evenly across the polymeric TA network (Figure S8, Supporting Information).

Figure S4 shows ^{13}C CPMAS NMR spectra recorded from pristine TA (TA_{ref}), TA_{prec}, as well as oxidized TA (TA_{ox}), which was formed in a Si-free buffer solution at pH = 7.8. The NMR responses from TA_{prec} and TA_{ref} are similar, in which the latter accords with a previous report.[21] The main distinction is the emergence of a resonance at ≈150 ppm in the ^{13}C NMR spectrum of TA_{prec} that is attributed to ^{13}C–O–Si fragments based on the ^{13}C shift[22] and our $^{13}C\{^{29}Si$ REDOR NMR results (Figure S3, Supporting Information). The ^{13}C NMR peaks between 50 ppm and 80 ppm stem from the central glucose ring,[21] indicating an overall intact structure of TA upon its complexation with Si. In contrast, TA_{ox} revealed a distinctly different ^{13}C NMR spectrum (Figure S4, Supporting Information). The absence of resonances below 80 ppm suggests either an oxidation of the glucose ring or a cleavage of gallic acid ester bonds to form gallic acid residues. Either scenario is consistent with the ^{1}H NMR signal at 15.5 ppm observed from the TA_{ox} sample (Figure S5, Supporting Information), which is attributed to hydrogen-bonded acidic protons.

Identification of the formation of Si–O–C motifs, as well as successfully depositing TA under a N_2 atmosphere (Figure S9, Supporting Information), demonstrated that the complexation between Si_{aq} and TA constitutes the deposition of the polyphenolic network. Consequently, it shows that, unlike for other polyphenolic molecules, oxidative polymerization by dissolved O_2 is not required.[23] Given that oxidation of TA is associated with the formation of polymeric byproducts, both coating homogeneity and deposition efficiency benefit from restricting the oxidative polymerization. Therefore, we adjusted the solution pH and monitored the coating process in real-time (Figure S10, Supporting Information) using a quartz crystal microbalance (QCM-D). Figure 2 shows the thickness of TA coatings formed on titanium sensors under different pH conditions. For pH > 8.2, the rapid polymerization of TA impeded the deposition process. At pH = 7.8, the coating thickness was in accordance with previously reported values[15a] and the change from Bicine to HEPES did not result in a major deviation. By reducing the pH of HEPES, an increase in the coating thickness was observed as a result of reduced oxidation (Figure S11, Supporting Information). In contrast, a limited solubility of TA in BisTris manifested in a significantly lower coating thickness at pH = 7.0 compared to the equivalent coating formation in HEPES.

Since HEPES buffer covers both oxidizing and nonoxidizing pH conditions (Figure S11, Supporting Information), we characterized the structural properties of TA coatings at pH values of 6.8 and 7.8. The progression of the frequency and dissipation shifts at pH = 7.8 (Figure 3) attested that the adsorption of TA leveled out after 8 h. This effect is more perceivable in dissipa-

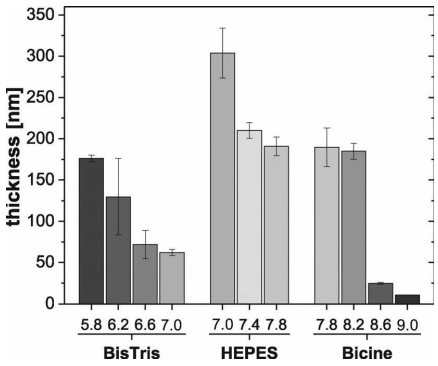

Figure 2. Averaged ($n_{rep}=3$) film thickness of TA coatings measured by QCM-D. The obtained values show the Voigt modeled thickness after 24 h adsorption time at different pH. Auto-oxidative polymerization impeded the deposition at pH > 8.2 and data represents the thickness before polymeric byproduct formation.

tion versus frequency ($\Delta D/\Delta F$) plots in which the deposition process of TA showed three distinct phases. An initial horizontal decrease of ΔF (Figure 3B, I) indicates a rigid layer. Subsequently a transition phase (II) resulted in increased viscoelastic properties until the third regime is reached, in which a vertical progression (III) denotes the increasing dissipative properties. Using nanoplasmonic spectroscopy (NPS), we further studied the initial coating formation in detail (Figure S13, Supporting Information). The comparison of the optical mass to the acoustic mass confirmed a low hydration of the TA layer during the first 30 min, followed by a gradual increase to ≈30% after 1 h (Figure S12, Supporting Information). Similarly, plotting $\Delta\lambda$ against ΔF and ΔD results in its structure–characteristic curve shape. Extending the analysis of NPS dry mass, we determined the layer thickness by means of ellipsometry and AFM. After 24 h, an in situ thickness of 191 ± 11 nm was obtained, which corresponded to 158 ± 3 nm (AFM: 132 ± 8 nm) in a dry state. From the lower dry state thickness, we conclude that the hydrated layer collapses and forms a rigid layer upon drying.

In buffered solution at pH = 6.8 (Figure 4), the initial adsorption kinetics was considerably slower compared to pH = 7.8. This may emanate from base catalytical processes, or from O–H dissociation of either silicic acid ($pK_A = 9.8$) or TA ($pK_A = 9.9$).[19c] However, compared to the deposition kinetics at pH = 7.8, no leveling out after 8 h was observed. In $\Delta D/\Delta F$ plots, a clear difference is noticeable, manifested in the absence of the third regime. It is likely that less TA reacts in oxidative polymerization processes at pH = 6.8 and thus more TA is available for the coating deposition, which led to a more homogenous layer thickness of 266 ± 2 nm after 24 hours in situ. Our combined assessment of the optical and acoustic mass revealed that the layer hydration was equivalent to the layer obtained at pH = 7.8 (Figure S12, Supporting Information). The time-de-

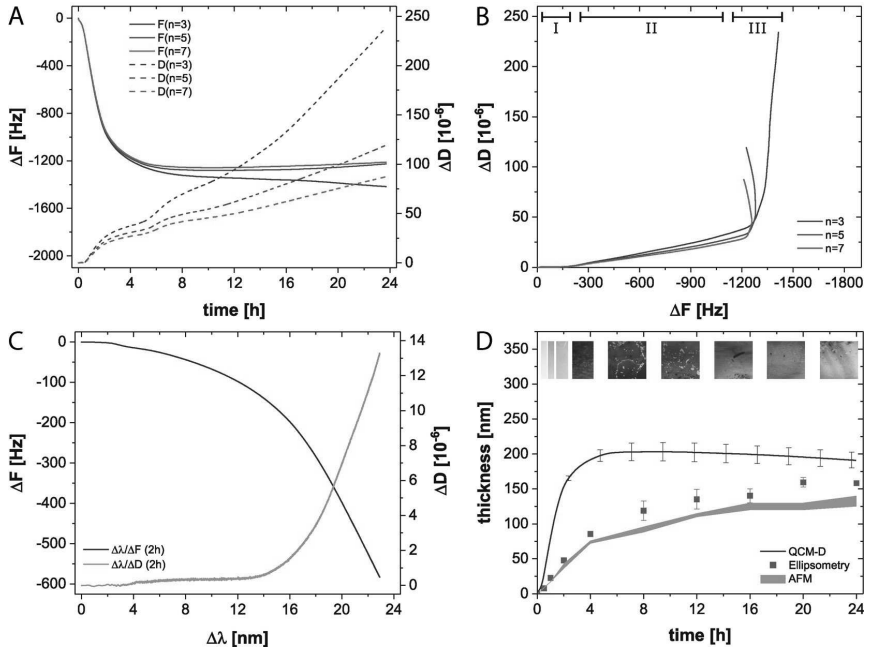

Figure 3. Deposition of TA coatings from HEPES at pH = 7.8. (A) Averaged ($n_{rep}=3$) and normalized frequency (ΔF) and dissipation shifts (ΔD) of the 3rd, 5th, and 7th QCM-D overtone (n) as a function of time and the correlated frequency versus dissipation plot (B). (C) Correlation between optical and acoustic mass. (D) In situ thickness compared to dry thickness of TA coatings (Inset: coated Si wafer).

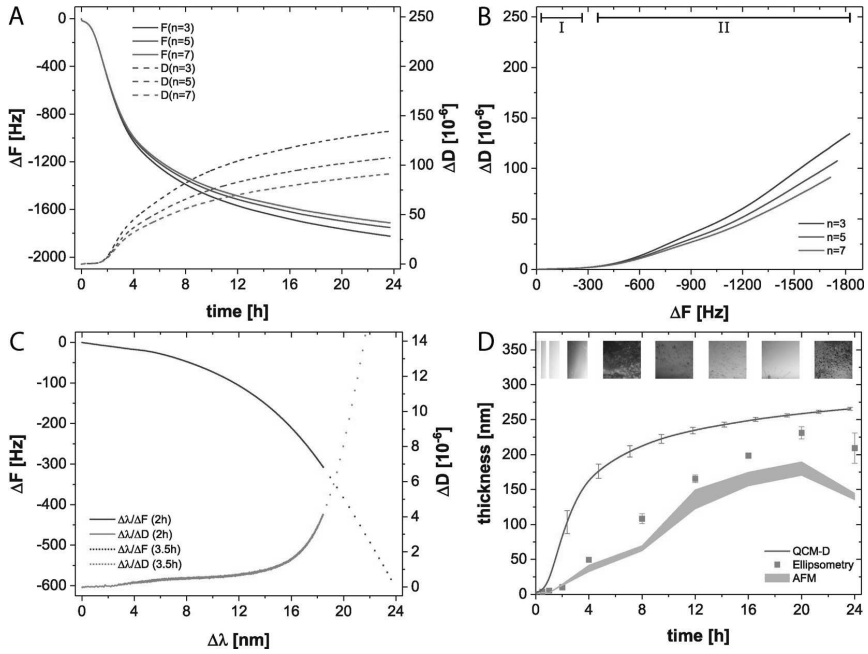

Figure 4. Deposition of TA coatings from HEPES at pH = 6.8. (A) Averaged ($n_{rep} = 3$) and normalized frequency (ΔF) and dissipation shifts (ΔD) of the 3rd, 5th, and 7th QCM-D overtone (n) as a function of time and the correlated frequency versus dissipation plot (B). (C) Correlation between optical and acoustic mass. (D) In situ thickness compared to dry thickness of TA coatings (Inset: coated Si wafer).

coupled plot of $\Delta\lambda$ against ΔF and ΔD resulted in the same characteristic curve shape and ascertained negligible structural differences between TA coatings obtained in either pH condition. Ellipsometry determined a thickness of 231 ± 9 nm (AFM: 180 ± 10 nm) after 16 h and confirmed the higher efficiency at pH = 6.8.

With an improved deposition efficiency, TA nanocoatings can be pushed towards microscale dimension and the deposition of higher amounts of TA is possible. Thereby the larger reservoir of TA may enable improved antibacterial and anti-inflammatory effects of TA coatings.[3b,5c] In order to break the boundaries of nanoscale polyphenolic coatings, the increased coating kinetics in alkaline conditions is a crucial requirement. Simultaneously, the formation of polymeric TA byproducts in solution must be avoided.

With Si as the coordinating species, the coating process can be changed from a batch reaction to a continuous-flow process (Figure S14, Supporting Information). By separating TA from Si_{aq}, TA can be kept stable at pH = 6.8 and fed with Si_{aq} at pH = 8.8, yielding a quadrupled TA-deposition compared to the batch process shown in Figure 3.

Moreover, we investigated the deposition process in alternative buffer systems for applications in which organic buffer molecules interfere with other chemical reactions. We demonstrated that TA coatings can be deposited in both citrate/phosphate and pure phosphate buffered solutions (Figure S15, Supporting Information). Tuning of the reaction speed can finally be performed by adjusting the pH and the ionic strength of the buffer.[15a,24]

In conclusion, we have presented direct experimental evidence for a complexation between silicate and TA that contributes to the deposition of TA coatings. The overall structurally intact TA molecules are expected to retain the antioxidant properties of the coating. By optimizing the solution pH, a prolonged and more homogenous deposition process was achieved. By demonstrating a continuous-flow process yielding high deposition rates, we establish a method that is commensurate with industrial demands, while giving a low rate of byproduct formation. For applications interfering with organic buffers, we have expanded the deposition of TA to inorganic buffers, which may open the utilization of TA coatings on implantable biomedical devices to prevent biofilm-associated infections and to improve the host tissue integration.

Experimental Section

Details of materials and methods, along with supplementary experimental data, can be found in the Supporting Information.

Acknowledgements

F.W., A.B., and H.T. acknowledge C.C. Steindal for EDS scans, S. Diplas for XPS measurements and related discussions, S. Kubo-

wicz for TOF-SIMS analysis, Insplorion A.B. for kindly providing the Acoulyte instrument and support with data analysis, and the Faculty of Dentistry, UiO for funding. W.C.L. and M.E. acknowledge funding from the Carl Trygger Foundation (CTS 17:130).

Conflict of interest

The authors declare no conflict of interest.

Keywords: coordination polymers · polyphenols · surface chemistry · tannic acid/silicate complexation · thin films

[1] a) N. S. Khan, A. Ahmad, S. M. Hadi, *Chem.-Biol. Interact.* **2000**, *125*, 177; b) C. Torres-León, J. Ventura-Sobrevilla, L. Serna-Cock, J. A. Ascacio-Valdés, J. Contreras-Esquivel, C. N. Aguilar, *J. Funct. Foods* **2017**, *37*, 176.

[2] X. Li, P. Gao, J. Tan, K. Xiong, M. F. Maitz, C. Pan, H. Wu, Y. Chen, Z. Yang, N. Huang, *ACS Appl. Mater. Interfaces* **2018**, *10*, 40844.

[3] a) T. J. Kim, J. L. Silva, Y. S. Jung, *Food Chem.* **2011**, *126*, 116; b) M. H. Lin, F. R. Chang, M. Y. Hua, Y. C. Wu, S. T. Liu, *Antimicrob. Agents Chemother.* **2011**, *55*, 1021; c) T. S. Sileika, D. G. Barrett, R. Zhang, K. H. A. Lau, P. B. Messersmith, *Angew. Chem. Int. Ed.* **2013**, *52*, 10766; *Angew. Chem.* **2013**, *125*, 10966.

[4] a) Y. Cao, K. B. Himmeldirk, Y. Qian, Y. Ren, A. Malki, X. Chen, *J. Nat. Med.* **2014**, *68*, 465; b) S. Nam, D. M. Smith, Q. P. P. Dou, Q. P. P. Dou, *Cancer Epidemiol. Biomarkers Prev.* **2001**, *10*, 1083.

[5] a) F. Reitzer, M. Allais, V. Ball, F. Meyer, *Adv. Colloid Interface Sci.* **2018**, *257*, 31; b) J. H. Ryu, P. B. Messersmith, H. Lee, *ACS Appl. Mater. Interfaces* **2018**, *10*, 7523; c) M. Cazzola, I. Corazzari, E. Prenesti, E. Bertone, E. Vernè, S. Ferraris, *Appl. Surf. Sci.* **2016**, *367*, 237; d) D. G. Barrett, T. S. Sileika, P. B. Messersmith, *Chem. Commun.* **2014**, *50*, 7265.

[6] R. W. Hemingway, P. E. Laks, *Plant polyphenols: synthesis, properties, significance, Vol. 59*, Springer Science & Business Media, **2012**.

[7] C. Sánchez-Moreno, J. A. Larrauri, F. Saura-Calixto, *Food Res. Int.* **1999**, *32*, 407.

[8] a) J. Guo, T. Suma, J. J. Richardson, H. Ejima, *ACS Biomater. Sci. Eng.* **2019**, DOI: 10.1021/acsbiomaterials.8b01507; b) A. Shavandi, A. E.-D. A. Bekhit, P. Saeedi, Z. Izadifar, A. A. Bekhit, A. Khademhosseini, *Biomaterials* **2018**, *167*, 91; c) Q. Wei, R. Haag, *Mater. Horiz.* **2015**, *2*, 567.

[9] a) J. Guo, Y. Ping, H. Ejima, K. Alt, M. Meissner, J. J. Richardson, Y. Yan, K. Peter, D. von Elverfeldt, C. E. Hagemeyer, F. Caruso, *Angew. Chem. Int. Ed.* **2014**, *53*, 5546; *Angew. Chem.* **2014**, *126*, 5652; b) T. Shutava, M. Prouty, D. Kommireddy, Y. Lvov, *Macromolecules* **2005**, *38*, 2850; c) V. Kozlovskaya, E. Kharlampieva, I. Drachuk, D. Cheng, V. V. Tsukruk, *Soft Matter* **2010**, *6*, 3596.

[10] X. Zhang, P.-F. Ren, H.-C. Yang, L.-S. Wan, Z.-K. Xu, *Appl. Surf. Sci.* **2016**, *360*, 291.

[11] a) A. R. S. Ross, M. G. Ikonomou, K. J. Orians, *Anal. Chim. Acta* **2000**, *411*, 91; b) M. McDonald, I. Mila, A. Scalbert, *J. Agric. Food Chem.* **1996**, *44*, 599; c) N. Slabbert, in *Plant polyphenols*, Springer, **1992**, pp. 421.

[12] a) M. A. Rahim, H. Ejima, K. L. Cho, K. Kempe, M. Müllner, J. P. Best, F. Caruso, *Chem. Mater.* **2014**, *26*, 1645; b) Q.-Z. Zhong, S. Pan, M. A. Rahim, G. Yun, J. Li, Y. Ju, Z. Lin, Y. Han, Y. Ma, J. J. Richardson, F. Caruso, *ACS Appl. Mater. Interfaces* **2018**, *10*, 33721; c) H. Ejima, J. J. Richardson, K. Liang, J. P. Best, M. P. van Koeverden, G. K. Such, J. Cui, F. Caruso, *Science* **2013**, *341*, 154.

[13] H. Ejima, J. J. Richardson, F. Caruso, *Nano Today* **2017**, *12*, 136.

[14] a) H. Lee, W. I. Kim, W. Youn, T. Park, S. Lee, T.-S. Kim, J. F. Mano, I. S. Choi, *Adv. Mater.* **2018**, *30*, 1805091; b) M. A. Rahim, M. Björnmalm, N. Bertleff-Zieschang, Q. Besford, S. Mettu, T. Suma, M. Faria, F. Caruso, *Adv. Mater.* **2017**, *29*, 1606717.

[15] a) S. Geißler, A. Barrantes, P. Tengvall, P. B. Messersmith, H. Tiainen, *Langmuir* **2016**, *32*, 8050; b) H. Lee, S. M. Dellatore, W. M. Miller, P. B. Messersmith, *Science* **2007**, *318*, 426.

[16] F. Behboodi-Sadabad, H. Zhang, V. Trouillet, A. Welle, N. Plumeré, P. A. Levkin, *Adv. Funct. Mater.* **2017**, *27*, 1700127.

[17] H. R. Devlin, I. J. Harris, *Ind. Eng. Chem. Fundamen.* **1984**, *23*, 387.

[18] F. Weber, A. Barrantes, H. Tiainen, *Langmuir* **2019**, *35*, 3327.

[19] a) I. F. Sedeh, L.-O. Öhman, S. Sjöberg, *Acta Chem. Scand.* **1992**, *46*, 933; b) S. D. Kinrade, J. W. Del Nin, A. S. Schach, T. A. Sloan, K. L. Wilson, C. T. G. Knight, *Science* **1999**, *285*, 1542; c) S. Bai, Y. Tsuji, Y. Okaue, T. Yokoyama, *J. Solution Chem.* **2011**, *40*, 348; d) O. Seiler, C. Burschka, M. Penka, R. Tacke, *Silicon Chem.* **2002**, *1*, 355; e) A. Weiss, A. Herzog, in *Biochemistry of Silicon and Related Problems* (Eds.: G. Bendz, I. Lindqvist, V. Runnström-Reio), Springer US, Boston, MA, **1978**, pp. 109; f) P. Bindu, B. Varghese, M. N. S. Rao, *Phosphorus Sulfur Silicon Relat. Elem.* **2003**, *178*, 2373.

[20] T. Gullion, J. Schaefer, *J. Magn. Reson.* **1989**, *81*, 196.

[21] F. H. Romer, A. P. Underwood, N. D. Senekal, S. L. Bonnet, M. J. Duer, D. G. Reid, J. H. van der Westhuizen, *Molecules* **2011**, *16*, 1240.

[22] D. F. Evans, A. M. Z. Slawin, D. J. Williams, C. Y. Wong, J. D. Woollins, *J. Chem. Soc. Dalton Trans.* **1992**, 2383.

[23] a) J. Saiz-Poseu, J. Mancebo-Aracil, F. Nador, F. Busque, D. Ruiz-Molina, *Angew. Chem. Int. Ed.* **2018**, *58*, 696; *Angew. Chem.* **2018**, *131*, 706; b) T. G. Barclay, H. M. Hegab, S. R. Clarke, M. Ginic-Markovic, *Adv. Mater. Interfaces* **2017**, *4*, 1601192.

[24] J. Guo, J. J. Richardson, Q. A. Besford, A. J. Christofferson, Y. Dai, C. W. Ong, B. L. Tardy, K. Liang, G. H. Choi, J. Cui, P. J. Yoo, I. Yarovsky, F. Caruso, *Langmuir* **2017**, *33*, 10616.

Manuscript received: May 22, 2019
Accepted manuscript online: May 27, 2019
Version of record online: July 1, 2019

CHEMISTRY
A European Journal

Supporting Information

Silicate-Phenolic Networks: Coordination-Mediated Deposition of Bioinspired Tannic Acid Coatings

Florian Weber,[a] Wei-Chih Liao,[b] Alejandro Barrantes,[a] Mattias Edén,[b] and Hanna Tiainen*[a]

Silicate-Phenolic Networks: Coordination Mediated Deposition of Bioinspired Tannic Acid Coatings

Table of Contents

Experimental section....2
Materials....2
Coating Preparation....2
Solid-State NMR....3
XPS....4
EDS....5
ToF-SIMS....5
QCM-D....5
NPS....5
Ellipsometry....6
AFM....6
UV-vis....6
Supporting information for solid-state NMR measurements....7
Supporting information for surface analysis....10
XPS....10
Si distribution determined by XPS, ToF-SIMS, and EDS....11
Supporting information for deposition of tannic acid coatings....12
QCM-D raw data....12
Spectrophotometric determination of TA oxidation....14
NPS data....14
CSTR type deposition of TA....15
TA deposition from inorganic buffers....16
CSTR setup....16
References....17

[a] F. Weber, Dr. A. Barrantes, Prof. H. Tiainen,
Department of Biomaterials, Institute of Clinical Dentistry,
University of Oslo,
P.O. Box 1109 Blindern, 0317 Oslo, Norway,
E-mail: hannati@odont.uio.no
[b] Dr. W.-C. Liao, Prof. M. Edén,
Department of Materials and Environmental Chemistry,
Stockholm University,
SE-106 91 Stockholm, Sweden

Experimental section

Materials

Tannic acid (ACS grade, MW = 1701.2, LOT#MKBN9606V) and sodium metasilicate pentahydrate (≥ 95%) were purchased from Sigma Aldrich. Unless otherwise stated, all materials were ACS grade and purchased from VWR.

Coating Preparation

Organic buffers were prepared by dissolving Bicine (≥ 99%, Sigma Aldrich), HEPES (BioPerformance, ≥ 99.5%, Sigma Aldrich), or BisTris (BioPerformance, ≥ 98%, Sigma Aldrich) at a concentration of 100 mM together with 600 mM NaCl in MilliQ water (18 MΩ cm). The pH was subsequently adjusted with 10 M NaOH or 5 M HCl to the needed level. NaOH stock solutions and prepared buffer solutions were stored in plastic bottles to avoid dissolving any silica ions from glassware.

Citrate buffer was prepared from 100 mM citric acid monohydrate (≥ 98%, Sigma Aldrich) and 200 mM disodium hydrogen phosphate (Na_2HPO_4, 98 – 102%; Sigma Aldrich) at a volume ratio of 17.6/82.34 for a final pH of 7.0. The buffer was supplemented with 600 mM NaCl and deviations from pH = 7.0 were corrected with 10 M NaOH or 5M HCl.

Phosphate buffer was prepared from 200 mM sodium dihydrogen phosphate (NaH_2PO_4, 98 – 102%; Sigma Aldrich) and 200 mM disodium hydrogen phosphate (Na_2HPO_4, 98 – 102%; Sigma Aldrich) at a volume ratio of 19.5/30.5. The solution was diluted with an equal amount of MilliQ water and supplemented with 600 mM NaCl. Deviations from pH = 7.0 were corrected with 10 M NaOH or 5 M HCl.

Tannic acid was dissolved in buffer solutions at a concentration of 1 mg/ml and stirred until fully dissolved. The concentration of 80 μM ortho-silicic acid (Si_{aq}) was adjusted from a 0.1 M stock solution of sodium metasilicate pentahydrate dissolved in MilliQ water.

Coatings prepared under continous flow conditions (CSTR setup) were obtained by seperating TA from Si_{aq} (Figure S16). TA at a concentration of 2 mg/ml was kept at acidic pH = 6.8 to prevent oxidation, while Si_{aq} at a concentration of 160 μM was adjusted to pH = 8.8. Both solution were mixed in a subsequent beaker (V_R = 6 ml) at a flow rate of 0.1 ml/min resulting in an average residence time of τ = 30 min. The solution pH in the CSTR was monitored and deviations from pH = 7.8 were adjusted by the pH level of the Si_{aq} feed.

As coating substrates, either polished titanium coins (grade IV) or silicon wafers (n-type, (100), Sigma Aldrich) were immersed in solution under gentle stirring. Prior to the coating process, Si wafers and Ti coins were treated for 15 min in an UV-Ozone chamber (Novascan PSD-UV4). Subsequently, the substrates were cleaned in 5/1/1 mixture of H_2O, 30% ammonia, 30% H_2O_2 to remove organic contaminants. Si wafers were finally treated with 10% HF for 10 min to create hydrophobic surfaces.

Chemical analytical experiments (XPS, EDS, ToF-SIMS) were conducted on Ti coins, which were coated with TA for 24 h in Bicine buffer at pH = 7.8 in presence of 80 μM Si_{aq}. AFM and ellipsometric measurements of TA coating thicknesses were evaluated on Si wafers. Note the different preparation procedures for the samples employed for the solid-state NMR experiments, as described below.

Solid-State NMR

Given the low Si contents in the samples (Table S3), all ^{29}Si NMR experimentation was conductedd on ^{29}Si-enriched samples, prepared using $^{29}SiO_2$ (99.7% enrichment; Buylsotope, Neonest AB, Sweden) dissolved 1.00 ml 10 M NaOH and added to HEPES buffer. The amounts of added $^{29}SiO_2$ yielded nominal Si concentrations of 80 μM and 1000 μM in the preparation of the "*TA precipitate"* (TA_{prec}) and the "*TA coating"* ($TA_{coating}$) specimens, respectivly. The pH of the solution was then adjusted to 7.8 using 10 M NaOH.

TA_{prec} was collected by filtering the reaction solution through a 0.2 μm nitrocellulose membrane after 24 h. The $TA_{coating}$ specimen was prepared by coating TiO_2 to mimic the native oxide layer of titanium surfaces described in the other experimental sections. The particles (sieved fraction with particle diameter between 100–180 μm) were suspended at a concentration of 1.5 mg/ml in TA solution for 1 h to avoid additional TA particle formation, followed by filtering through a nitrocellulose membrane (0.2 μm). The coated TiO_2 particles were subsequently washed with HEPES buffer solution. "*TA oxidation products"* (TA_{ox}), which formed at pH = 7.8 during 24 h in reaction solutions that did not contain any silicon, were collected by filtration (0.2 μm membrane). For comparison, the *pristine TA* precursor powder (TA_{ref}) was analyzed as received.

All ^{1}H, ^{13}C, and ^{29}Si MAS NMR experimentation was performed with Bruker Avance-III spectrometers at static magnetic fields (B_0) of 9.4 T or 14.1 T, which correspond to the respective ^{1}H/^{13}C/^{29}Si Larmor frequencies of 400.1/100.6/79.5 MHz and 600.1/150.9/119.2 MHz. Neat tetramethylsilane (TMS) was used to calibrate each ^{1}H, ^{13}C, and ^{29}Si chemical shift at 0 ppm. Fine powders of the TA_{prec}, $TA_{coating}$, TA_{ox}, and TA_{ref} samples were packed in 4 mm (outer diameter) zirconia rotors and ceiled with Kel-F caps. Throughout all Figures, all NMR spectra are for visualization purposes zoomed so as to comprise all relevant NMR signals, i.e., to emphasize the significant information.

Directly excited ("single-pulse") ^{1}H and ^{29}Si NMR spectra were recorded at 9.4 T and the MAS rate ν_r = 14.00 kHz, using 90° radiofrequency (rf) pulses operating at rf nutation frequencies of 54 kHz and 100 kHz for ^{29}Si and ^{1}H, respectively, with corresponding relaxation delays of 300 s and 5 s. These relaxation delays were selected from separate T_1 relaxation experiments to ensure quantitative NMR spectra. The total numbers of accumulated signal transients were 256 for ^{29}Si and 8 for ^{1}H. No ^{1}H decoupling was applied during the ^{29}Si NMR signal acquisitions.

^{1}H→^{13}C and ^{1}H→^{29}Si cross polarization (CP) NMR experiments performed at B_0 = 9.4 T employed MAS rates of 14.00 kHz for ^{13}C and 7.00 kHz for ^{29}Si. CP was established at the modified Hartmann-Hahn conditions

$$\nu_1^{\mathrm{H}} - \nu_1^{X} = n\,\nu_r, \qquad X = \{^{13}\mathrm{C}, ^{29}\mathrm{Si}\},$$

employing proton nutation frequencies ν_1^{H} of 43 kHz (n = −1) and 64 kHz (n = 1) for the ^{29}Si and ^{13}C NMR experiments, respectively. For both ^{29}Si and ^{13}C, the nutation frequency was ramped linearly[1] by ±5% around ν_1^{X} = 50 kHz. Contact-time periods of 4.0 ms and 2.0 ms were employed for all ^{29}Si and ^{13}C experiments, respectively (except for those shown in Figure S2). Heteronuclear ^{1}H decoupling during the NMR-signal acquisitions utilized the SPINAL-64 scheme[2] operating at ν_1^{H} = 83 kHz (5.8 μs ^{1}H pulses). Relaxation delays of 1.0 s were used for all ^{13}C CPMAS NMR experiments, whereas those involving ^{29}Si used 1.5 s and 3.0 s for the TA_{prec} and $TA_{coating}$ samples, respectively. Depending on the detected nucleus and sample,

6000–65000 accumulated transients were required to obtain NMR spectra of moderate to high quality (see Table S1).

The $^{13}C\{^{29}Si\}$ rotational-echo double-resonance (REDOR)[3] NMR experiments on the TA_{prec} specimen were performed at B_0 = 14.1 T and ν_r = 10.00 kHz, starting from ^{13}C magnetization generated by ramped $^1H \rightarrow {}^{13}C$ CP, employing ν_1^H = 42 kHz, ν_1^C = 32 kHz, and a contact time period of 2.0 ms. The REDOR protocol involves recording two separate NMR data sets for a given dipolar recoupling interval τ_{rec}:[3] (*i*) a "reference" NMR spectrum [$S_{ref}(\tau_{rec})$], which involves a Hahn-echo with a 180° rf-pulse (14.0 µs in our experiments) applied to the observed nuclei (^{13}C) to refocus chemical shifts; (*ii*) a "dipolar-dephased" spectrum [$S(\tau_{rec})$], for which additionally a rotor-synchronized train of 180° rf pulses (13.6 µs; ν_1^{Si} = 37 kHz) is applied to ^{29}Si in order to reintroduce the MAS-averaged ^{13}C–^{29}Si dipolar interactions.[3] Their presence results in an attenuation ("dephasing") of the ^{13}C NMR signals from all ^{13}C sites in close spatial proximity to ^{29}Si. Our experiments used τ_{rec} = 4.0 ms, with the rf phases of the 180° recoupling pulses cycled according to the XY8 scheme.[4] In all REDOR experiments, heteronuclear proton decoupling (ν_1^H = 67 kHz) were accomplished using continuous-wave (CW) and SPINAL-64[2] schemes during the dipolar-recoupling and NMR-signal acquisition periods, respectively. The relaxation delays were 3.0 s, and 12800 signal transients were collected for each part of the REDOR protocol.

Table S1: Number of accumulated transients used for the ^{13}C and ^{29}Si CPMAS NMR experiments.

Figure label	Sample	Number of transients
Figure 1	$TA_{coating}$	68408
	TA_{prec}	6144
Figure S1	TA_{prec}	6144
Figure S2	TA_{prec}	256 (512 for the contact time of 0.3 ms)
Figure S4	TA_{ref}	47752
	TA_{prec}	57344
	TA_{ox}	36864

XPS

Analysis of the silicon content and distribution was conducted on a Kratos XPS instrument (Kratos Analytical Ltd). Sprectra were obtained with a monochromated Al K_α radiation (15 kV, 10 mA) under charge compensation (2 A, 3.8 V). Survey spectra were measured with a pass energy of 160 eV, a step size of 1 eV, and a 200 ms dwell time. High-resolution spectra were obtained with a pass energy of 20 eV, a step size of 0.1 V, and a dwell time of 1000 – 2000 ms. Maps were acquired in parallel XPS imaging mode at a spatial resolution of 3 µm. The acquisition time was set to 300 s with a pass energy of 160 eV.

The data was processed in CasaXPS (Casa Software Ltd) by shifting the C_{1s} peak with the lowest binding energy to 285 eV. Peak fitting and deconvolution were performed with a Shirley background and a symmetric Gaussian/Lorentian line shape.

EDS

Coated Ti coins were analyzed regarding the atomic composition and surface morphology using an FEI Quanta 450 scanning microscope (Thermo Fisher Scientific) coupled to an X-Max^N Oxford 50 mm^2 analyzer (Oxford Instruments).

ToF-SIMS

ToF-SIMS analysis was performed using a PHI TRIFT V nanoTOF instrument (Ulvac-Phi Inc.) equipped with a 30 keV LIMG source. The primary ion beam (Ga^+) was set to the unbunched mode to be optimized for high lateral resolution (< 0.4 μm). The ^{28}Si isotope was detected in positive mode with an analyzed area of 100 μm × 100 μm and 30 μm × 30 μm in size. No charge compensation was required.

QCM-D

A QSense E4 (Biolin Scientific) quartz crystal microbalance (QCM-D) was used to monitor the real-time formation of TA nanocoatings. Ti sensors (QSX 310, Biolin Scientific) were used and cleaned according to the manufacturer's protocol before and after each experiment. The procedure includes sonication in 2% SDS, washing with MilliQ water and EtOH, and final UV-ozone treatment. The QCM-D chambers were cleaned with 2% SDS for 10 min and extensively flushed with water (> 15 min) prior to the experiment.

Before adsorption of tannic acid, sensors were equilibrated in buffer and a baseline was recorded. TA was flown through the cell at 0.1 ml/min at 21°C under gentle stirring of the solution (100 rpm). After the adsorption, the sensors and chambers were flushed with MilliQ water and 0.1 M HCl for 5 min to remove tannic acid. Subsequently, the chamber cleaning protocol was conducted as described before. All experiments were performed in triplicates (n_{rep} = 3).

The change in oscillation frequency (ΔF) and dissipation (ΔD) was continously monitored for the fundamental frequency and five overtones. For clarity, only the first three overtones are plotted. Calculations of layer thicknesses were performed with QTools Software (BiolinScientific, Version 3.1.33) using the extended viscoelastic model. Fits were obtained based on the 3rd (n = 3), 5th (n = 5), and 7th (n = 7) harmonic overtone and a power based shear dependence. The TA layer density was assumed to be 1046 kg/m^3,[5] accompanied by a measured fluid density of 1027 kg/m^3.

NPS

Nanoplasmonic spectroscopy (NPS) is a technique based on the concept of measuring the localized surface plasmon resonance (LSPR) and was conducted on an Acoulyte (Insplorion AB) instrument. The instrument allows simultanous recording of the optical mass and acoustic mass using the QCM-D equipment. TiO_2 coated sensors, provided by the manufacturer, were immersed in 2% SDS for 10 min, washed with MilliQ water, and UV-ozone treated prior to the experiment.

The coating procedure is performed as described in the QCM-D section. In short, sensors were equilibrated in buffer before TA was flown through the cell at 0.1 ml/min at 21°C. All experiments were conducted as duplicates (n_{rep} = 2).

The calculation of the optical mass was obtained with respect to the exponential decay of the plasmon signal (Equation S1). The adsorbed areal mass (Γ) depends on the layer thickness (d_s) obtained from QCM-D, the surrounding refractive index (n_{buffer}), and the refractive index (n_s) and the refractive index increment (dn/dc) of the layer. The difference in refractive index (Δn) is correlated with the change of the plasmon peak ($\Delta\lambda$), the sensitivity factor of the TiO_2 sensor (S_0 = 140 nm/RIU), and the characteristic decay length of the surface plasmon (L_Z = 30 nm).[6] The refractive index increment was determined to be 0.173 ± 0.01 ml/g.

$$\Gamma = d_s \frac{\Delta n}{dn/dc} = d_s \frac{\Delta\lambda}{S_0\left(1 - e^{\frac{-2d_s}{L_z}}\right) \cdot dn/dc} \tag{S1}$$

Ellipsometry

Coated Si wafers were analyzed using a Rudolf Auto EL III null ellipsometer (Rudolf Research). The instrument is equipped with a He-Ne laser (633 nm) probing the surface at an incident angle of 70°. A single layer calculation model was used to quantify the layer thickness of TA coatings. Therefore, the refractive index of tannic acid coatings was assumed to be equal to SiO_2 (n_R = 1.468). For each time point, three measurements on three individual wafers were acquired and averaged (n_{rep} = 9). Si wafers were coated in groups (G_1: 0.5 h – 4 h; G_2: 8 h – 16 h; G_3: 24 h). The thickness of the native oxide layer was measured on control wafers and subtracted from the reported results.

AFM

An atomic force microscope (MFP 3D, Asylum Research) was used to determine the coating thickness by scratching the coatings with a cantilever (ACS-240TS) and scanning across the edge of the scratched area. Three measurements were conducted at random positions on the sample surface to yield an average value (n_{rep} = 3).

UV-vis

Quantification of the oxidation of TA solutions was performed using a Lambda 25 spectrophotometer (Perkin Elmer). Spectra were recorded with a resolution of 1 nm. All samples were filtered through a 0.2 μm polyether sulfone syringe filter prior to the measurement. Due to strong adsorption in the UV-region samples were diluted 1/100 in their corresponding buffer solutions.

Supporting information for solid-state NMR measurements

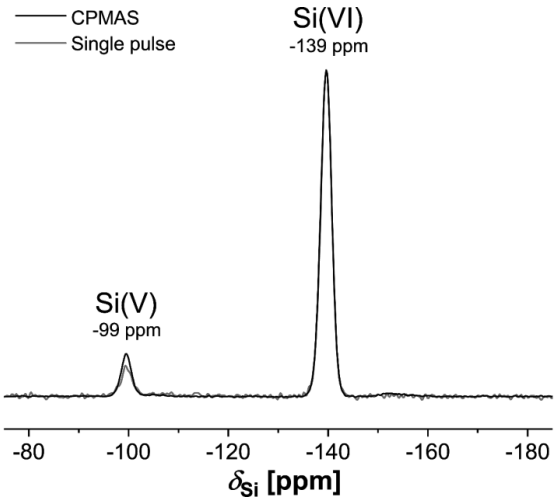

Figure S1: ^{29}Si NMR spectra recorded at B_0 = 9.4 T from the TA_{prec} sample, using either direct excitation by single pulses at 14.00 kHz MAS (red trace) or $^{1}H \rightarrow {}^{29}Si$ CP at 7.00 kHz (black trace). Note (*i*) the almost identical NMR-peak intensites/widths observed between the quantitative single-pulse NMR spectrum and that recorded using CP with a contact period of 4.0 ms, as well as (*ii*) the very similar CPMAS NMR spectra revealed for the TA_{prec} and $TA_{coating}$ samples in Figure 1. Altogether, this strongly suggests essentially identical relative Si(V) and Si(VI) populations in TA_{prec} and the TA-coated TiO_2 nanoparticles: these results justify using the NMR results from the TA_{prec} specimen as representative also for the $TA_{coating}$ sample, whose minute Si content (see Table S2) precludes any NMR experimentation other than the $^{1}H \rightarrow {}^{29}Si$ CP NMR results shown in Figure 1. Note that no traces of silica (which produces ^{29}Si resonances around –110 ppm[7]) is revealed from any of the NMR spectra shown above and in Figure 1.

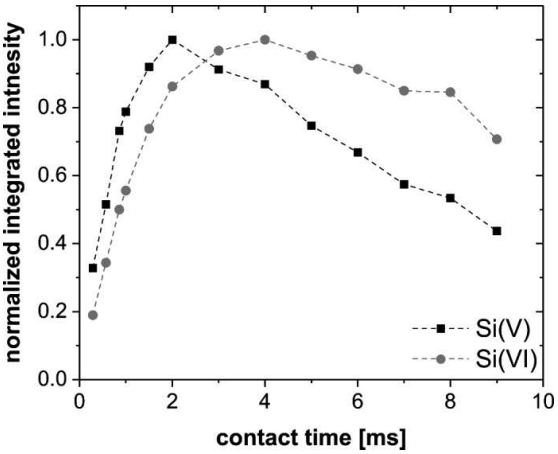

Figure S2: Integrated ^{29}Si CPMAS NMR peak-intensities plotted against the CP contact time-period for the resonances at –99 ppm and –139 ppm, which are associated with the ^{29}Si(V) and ^{29}Si(VI) sites of the TA_{prec} sample, respectively; see Figure S1. Each curve is normalized to a maximum integrated intensity of unity. The initial buildup-rate of the ^{29}Si NMR signal of each ^{29}Si(V) and ^{29}Si(VI) site grows as the inverse cube of its respective (***shortest***) ^{1}H–^{29}Si internuclear distance. Note the more rapid NMR-signal buildup from the ^{29}Si(V) sites relative to their ^{29}Si(VI) counterparts, as is expected from the presence of a Si(V)–OH linkage (as opposed to Si(VI)–O–C motifs only) in Scheme 1. We refer to Kolodziejski and Klinowski for general information about CPMAS NMR experimentation and its kinetics.[8]

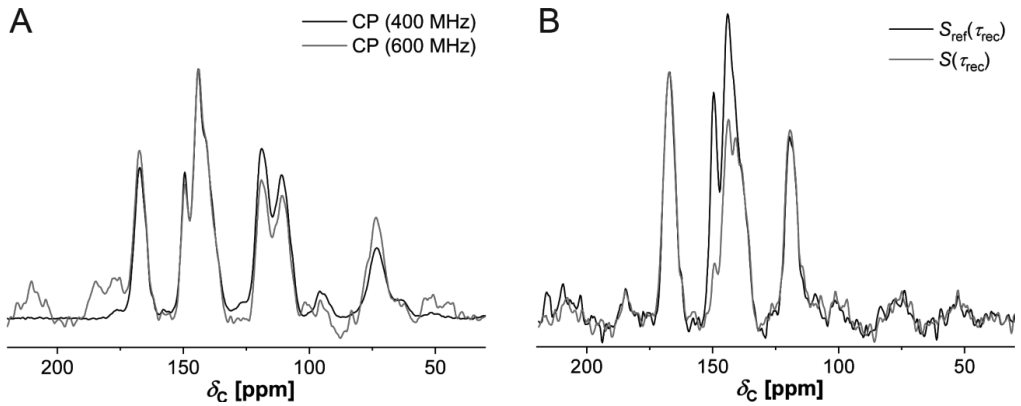

Figure S3: (A) ^{13}C CPMAS NMR spectra recorded from the TA_{prec} sample, and obtained either at B_0 = 9.4 T and ν_r = 14.00 kHz, or at B_0 = 14.1 T and ν_r = 10.00 kHz. (B) $^{13}C\{^{29}Si\}$ REDOR NMR spectra acquired at B_0 = 14.1 T and ν_r = 10.00 kHz, using a dipolar recoupling period of τ_{rec} = 4.0 ms, during which ^{13}C–^{29}Si dipolar interactions are activated: they lead to an NMR-signal attenuation ("dephasing") from all ^{13}C sites in close proximity to ^{29}Si [$S(\tau_{rec})$; red trace] relative to the "reference" portion of the REDOR protocol [$S_{ref}(\tau_{rec})$; black trace]. A significant dephasing is only observed for the ^{13}C resonances in the 135–50 ppm spectral range; they are associated with aromatic ^{13}C–O moieties of TA,[9] thereby evidencing their closer ^{13}C–^{29}Si distances relative to those of all other ^{13}C sites. The signal ~150 ppm reveals the strongest attenuation, and is therefore attributed to ^{13}C–O–Si motifs (also see Figure S4). The absence of ^{13}C resonances in the 50–110 ppm range in the REDOR NMR spectra [compare with the ^{13}C CPMAS spectrum in (A)] is attributed to a rapid T_2 relaxation of these ^{13}C sites. Consequently, our data do not permit drawing any conclusion about their proximities to Si.

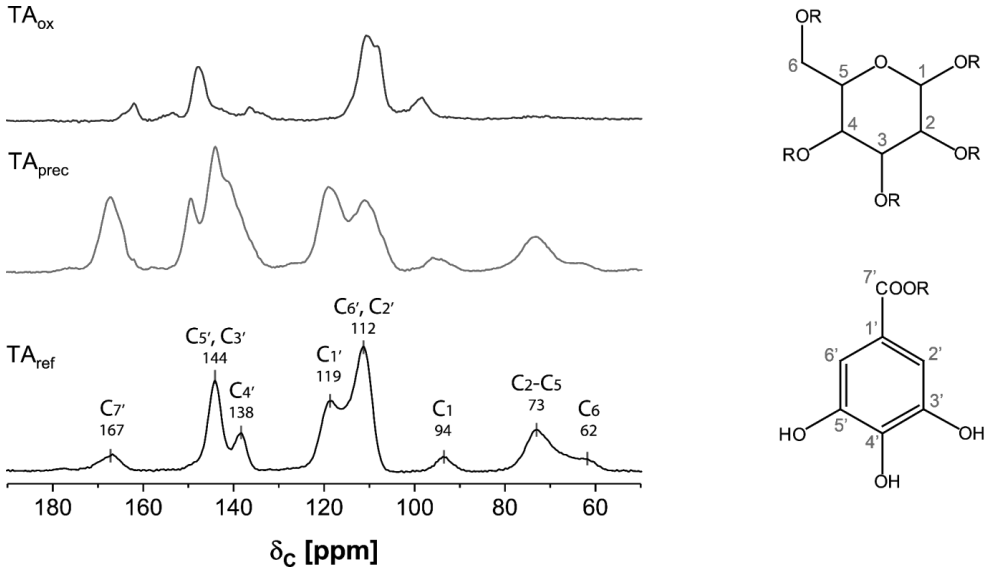

Figure S4: ^{13}C CPMAS NMR spectra recorded at B_0 = 9.4 T and 14.00 kHz MAS from pristine tannic acid (TA_{ref}), TA precipitated in presence of 1000 μM Si_{aq} (TA_{prec}), as well as the oxidative polymerization product (TA_{ox}). The indicated ^{13}C chemical shifts (in ppm) and peak assignments in the NMR spectrum of TA_{ref} refer to the C sites of the TA molecules labeled in the right panel.[9] Note the overall similar NMR results observed from the TA_{ref} and TA_{prec} samples, which mainly differ in the signal at δ_C ~150 ppm. This resonance is only observed from TA_{prec} and is attributed to ^{13}C–O–Si moieties (see Figure S3), as further supported by ^{13}C chemical shifts reported from solution NMR by Evans et al.[10]

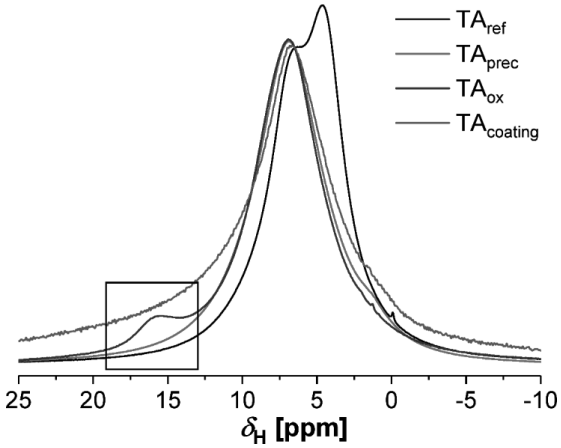

Figure S5: ^{1}H NMR spectra recorded at B_0 = 9.4 T and 14.00 kHz MAS from samples of pristine tannic acid (TA_{ref}), tannic acid precipitated in presence of 1000 μM Si_{aq} (TA_{prec}), oxidative polymerization products of tannic acid (TA_{ox}), and TA coated TiO_2 particles prepared in HEPES buffer (pH = 7.8) together with Si at a concentration of 80 μM ($TA_{coating}$). Note the minor peak at 15.5 ppm in the NMR spectrum from TA_{ox}, which is attributed to hydrogen-bonded carboxy moieties.

Supporting information for surface analysis

XPS

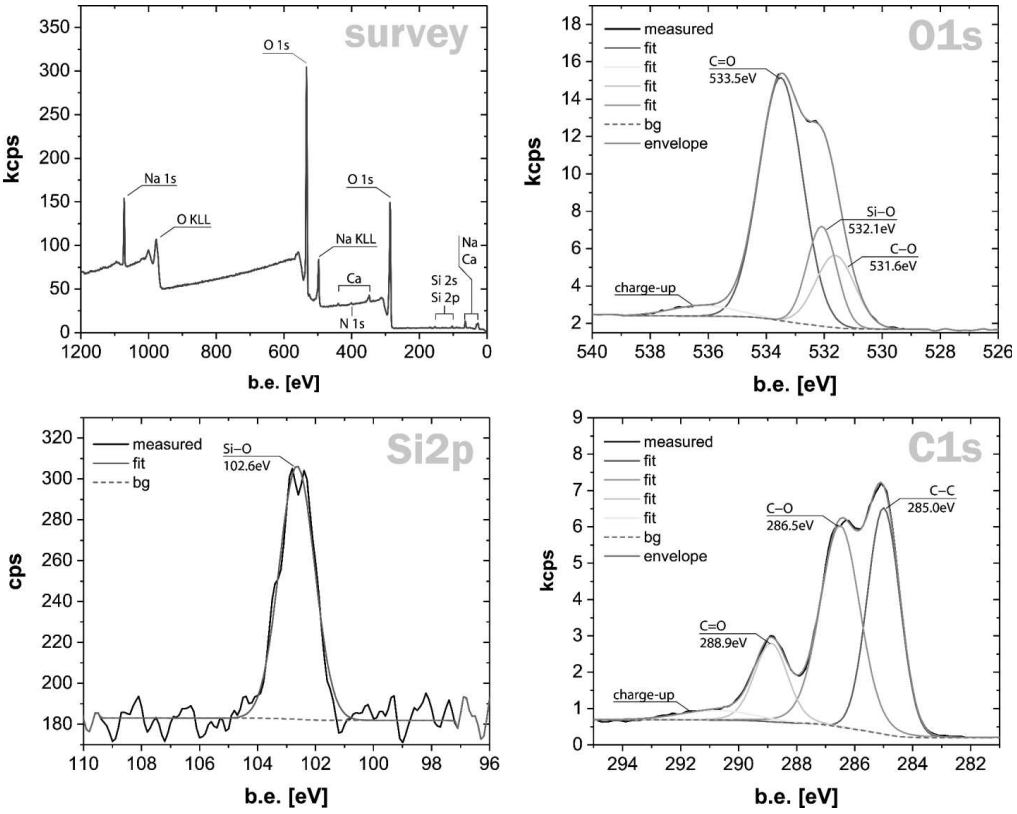

Figure S6: Chemical composition of TA coatings on titanium coins obtained in Bicine buffer supplemented with 80 μM Si_{aq} at pH = 7.8 determined by XPS. The survey scan indicated Na in the organic film, which may act as counter ions of deprotonated hydroxyl groups. Further, some Ca impurities are present. The high-resolution spectra of O 1s indicated three oxygen species, which were attributed to C=O, C–O, and Si–O bonds. The Si 2p peak is centered at 102.6 eV. Whilst the chemical state of Si could not be determined with sufficient reliability, the binding energy of Si excludes a pure SiO_2 phase.[11] It may rather be correlated to the bond length of hexa-coordinated Si–O–C bonds (Table S2). The C 1s spectrum shows three peaks indicating C=O, C–O, and C–C bonds.

Table S2: Correlation of bond length and binding energy in silicon compounds.

Type	Si–O (quartz)	Si–C	Si–O–R (hexa-coord.)	Si–Si
Bond length [pm]	161[12]	187.5[13]	170–190[14]	233[13]
Binding energy Si 2p [eV]	103.9[15]	102.5[15]	102.6[a]	99.3[16]

[a] *determined for Si in TA coatings on titanium surfaces*

Si distribution determined by XPS, ToF-SIMS, and EDS

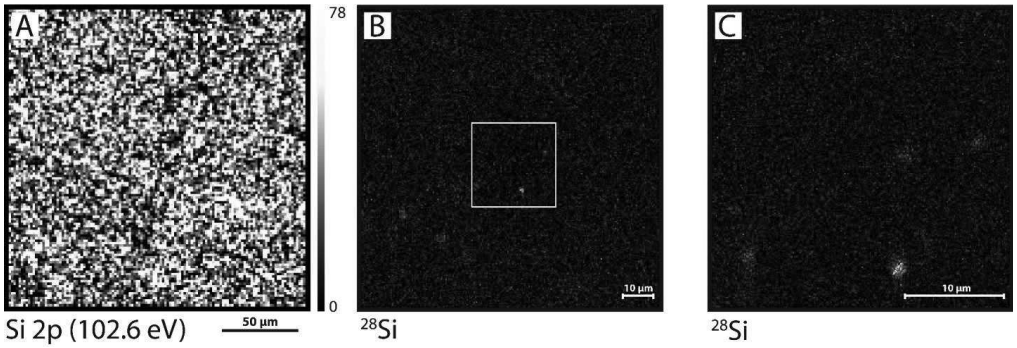

Figure S7: Representative distribution of Si in TA coatings on titanium coins from microscopic to submicroscopic scale: (A) Mapping of the Si 2p peak (102.6 eV) by XPS on an area of 200 × 200 µm. (B) ToF-SIMS mapping of ^{28}Si on an area of 100 × 100 µm and (C) subsequent high-resolution imaging of the center region. All measurements were performed on titanium coins coated with TA. The coating was obtained in Bicine buffered solution at pH = 7.8 supplemented with 80 µM Si_{aq} and a coating time of 24 h. The spacial resolution of 3 µm in XPS measurements did not allow to detect SiO_2 particles. However, the surface sensitive technique demonstrates the distribution of Si species throughout the measured area. This result was confirmed by high-resolution ToF-SIMS. Additionally, the higher spacial resolution detected some Si-rich areas which originate in particles as observed in SEM/EDS measurements (Figure S8), were detected.

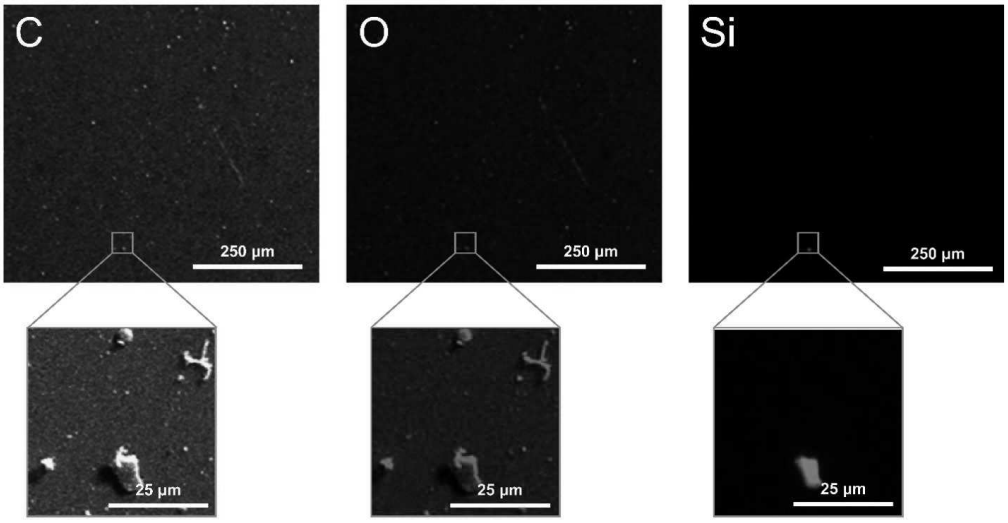

Figure S8: Representative EDS map of a Si-rich particle found on titanium surfaces coated with TA. The coating was obtained in Bicine buffer at pH = 7.8 for 24 h. A weak Si background signal was still obtained throughout the surface but the presence of particles suppressed the intensity in the false color map. The particles might originate from glassware or from the Si stock solution as ortho-silicic acid polymerization product.

Table S3: EDS-derived elemental contents (wt. %) of the samples used for solid-state NMR experiments.

Sample	[Si][a]	C	O	Si	Ti
TA_{prec}	1000 μM	48.8	46.2	2.3	–
$TA_{coating}$	80 μM	3.2	38.2	0.1	58.1

[a]*Nominal Si concentration during preparation.*

Supporting information for deposition of tannic acid coatings

QCM-D raw data

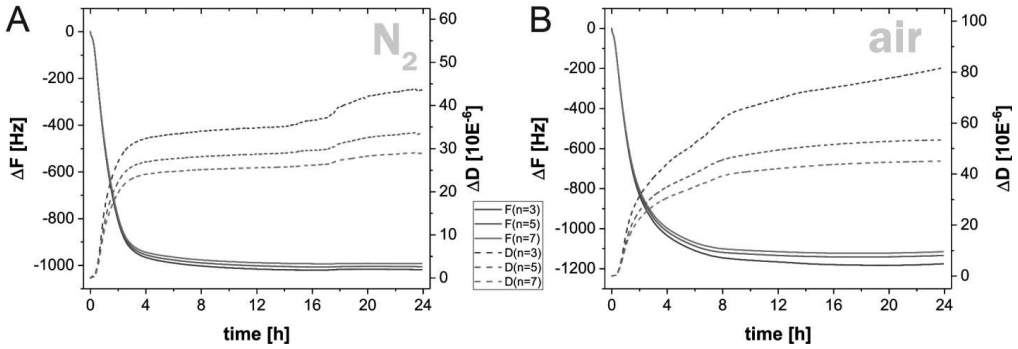

Figure S9: Averaged (n_{rep} = 3) progression of frequency and dissipation shifts of the 3rd, 5th, and 7th overtone (n) in QCM-D during deposition of TA on titanium sensors. Adsorption of TA from Bicine buffer at pH = 7.8 under depletion of oxygen (A) in comparison to the oxidative environment (B). Bicine buffer at pH = 7.8 was degassed prior to the experiment and constantly bubbled with nitrogen throughout the measurement. Under this condition, the colorless solution indicated no oxidation of TA. The reduced particle formation by oxidative polymerization also led to a more stable dissipation value in QCM-D during the course of a 24 h deposition process (note the different scale of the y-axes). The result indicates that oxidative polymerization by dissolved O_2 is not required for the formation of silicate-TA networks.

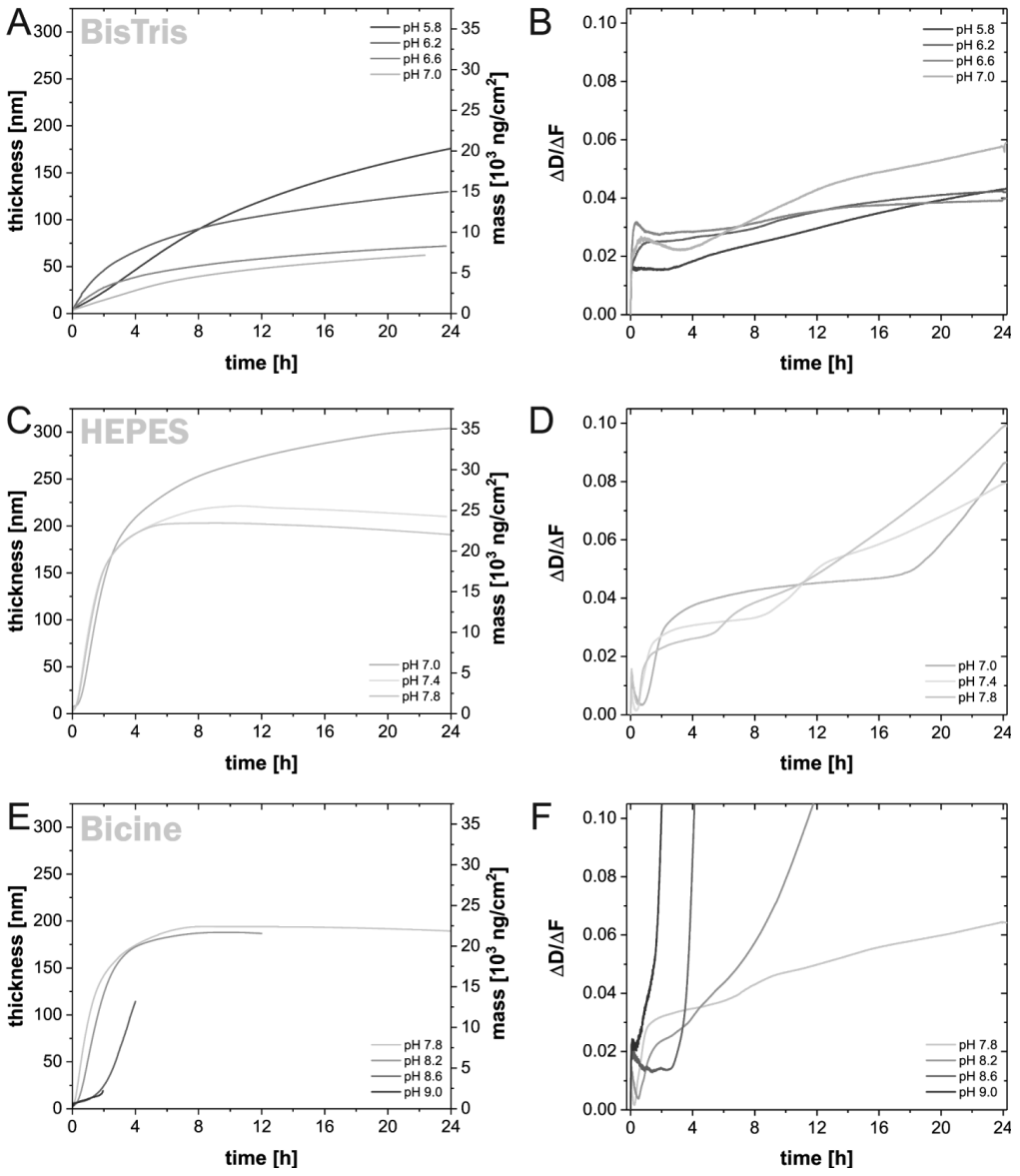

Figure S10: Averaged (n_{rep} = 3) progression of TA coating thickness calculated with the Voigt viscoelastic model (A, C, E). Additionally, the ratio of $\Delta D/\Delta F$ [10^{-6}Hz^{-1}] of the 3rd harmonic overtone is given in the panels to the right (B, D, F). Due to rapid oxidation and polymerization processes at pH above 8.6, the deposition efficiency was greatly impeded and the process was aborted after 2 h (pH = 8.6) and 1 h (pH = 9.0). Splitting overtones and increasing $\Delta D/\Delta F$ values were associated with the formation of polymeric byproducts. These polymers agglomerate and form particles, which sediment onto the sensor surface.[17]

Spectrophotometric determination of TA oxidation

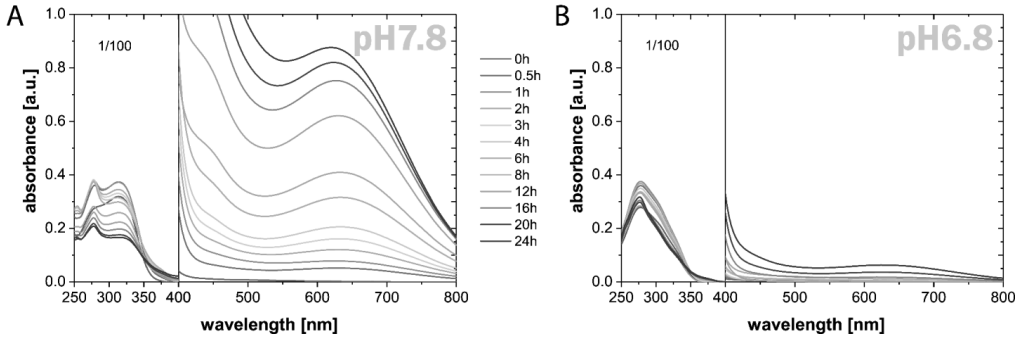

Figure S11: Representative progress of TA oxidation measured by UV-vis spectrophotometry. TA was dissolved in HEPES buffer at pH = 7.8 (A) and 6.8 (B). Solutions were exposed to air and gently stirred (100 rpm) during the course of 24 h. Prior to analysis, solutions were filtered through a 0.2 μm syringe filter. Due to strong adsorption in the UV region, samples were diluted (1/100) with buffer. The increased adsorption in the visible range is associated with the oxidation of the polyphenolic molecules.[18]

NPS data

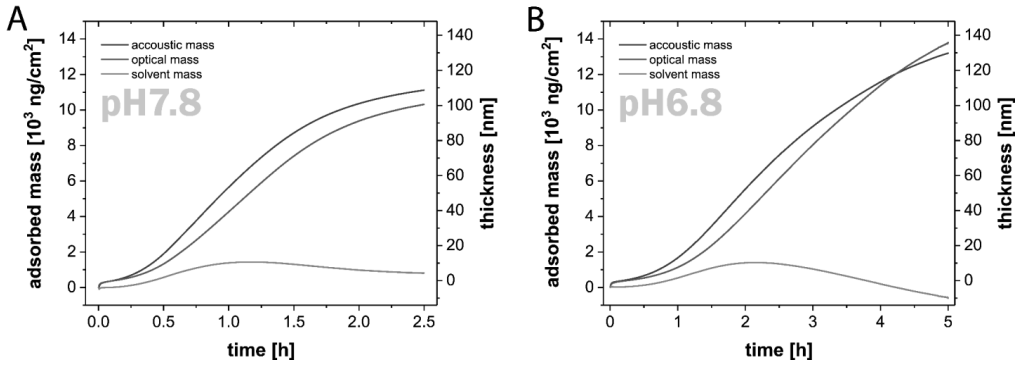

Figure S12: Representation of optical mass and acoustic mass of TA coatings determined by NPS and QCM-D respectively (n_{rep} = 2). Both conditions pH = 7.8 (A) and pH = 6.8 (B) show low hydration during initial formation of the coating followed by an increase. Once the penetration depth of NPS exceeds its characteristic probing depth of 30 nm the correlation starts to deviate and the estimation of the hydration decreases. Above 100 nm Equation S1 is no longer valid and the data cannot be interpreted correctly.

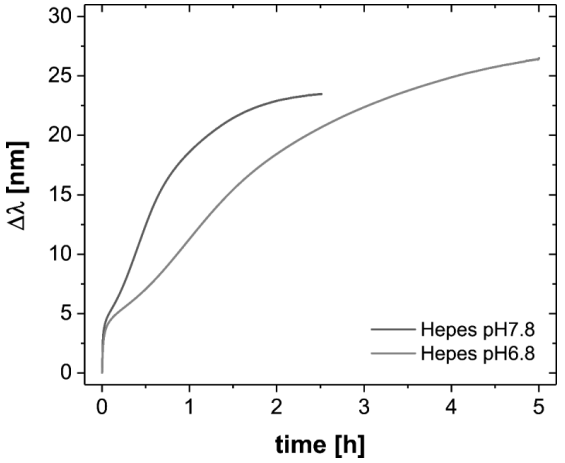

Figure S13: Averaged (n_{rep} = 2) shift of plasmon peak during the deposition of TA at pH = 6.8 and pH = 7.8. The measurements were conducted until the peak shift leveled off, indicating that the maximum penetration depth of the surface plasmon was reached. The variation in maximum peak shift might indicate a differing refractive index of layers obtained in oxidizing condition (pH = 7.8) compared to non-oxidizing conditions (pH = 6.8).

CSTR type deposition of TA

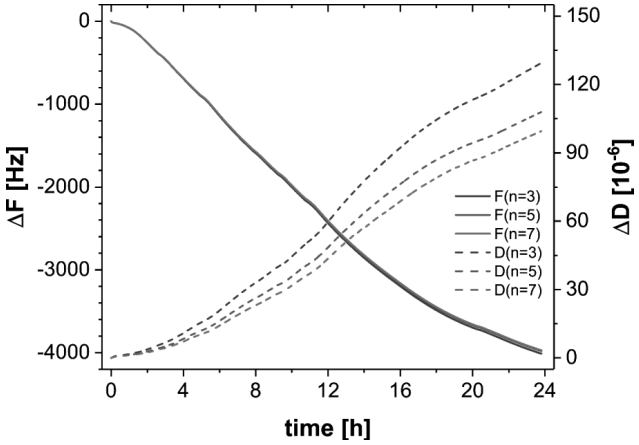

Figure S14: Averaged (n_{rep} = 4) and normalized frequency and dissipation shifts of the 3rd, 5th, and 7th QCM-D overtone (n) as a function of time. Graphs show the deposition of TA onto Ti surfaces in a continously stirred tank reactor (CSTR) setup with TA dissolved at pH = 6.8 and fed with Si_{aq} in alkaline condition (pH = 8.8) to result in a final pH-value of 7.8. The continuous deposition could be maintained throughout 24 h, owing to the reduced particle formation in the CSTR. Slight interferences in the slope of the QCM-D measurement were due to a change in reactant volume in the CSTR. The operation with a single peristaltic pump caused invariances in in- and out-flow of the CSTR (Figure S16).

TA deposition from inorganic buffers

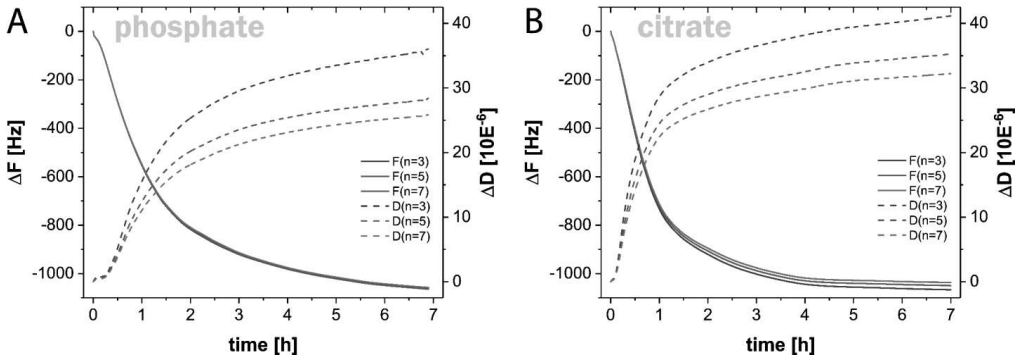

Figure S15: Averaged (n_{rep} = 3) progression of frequency and dissipation shifts of the 3rd, 5th, and 7th overtone (n) in QCM-D during deposition of TA on titanium sensors. Adsorption of TA from phosphate buffer (A) and citrate/phosphate buffer (B) that were both supplemented with 600 mM NaCl and 80 μM Si_{aq} at pH = 7.0.

CSTR setup

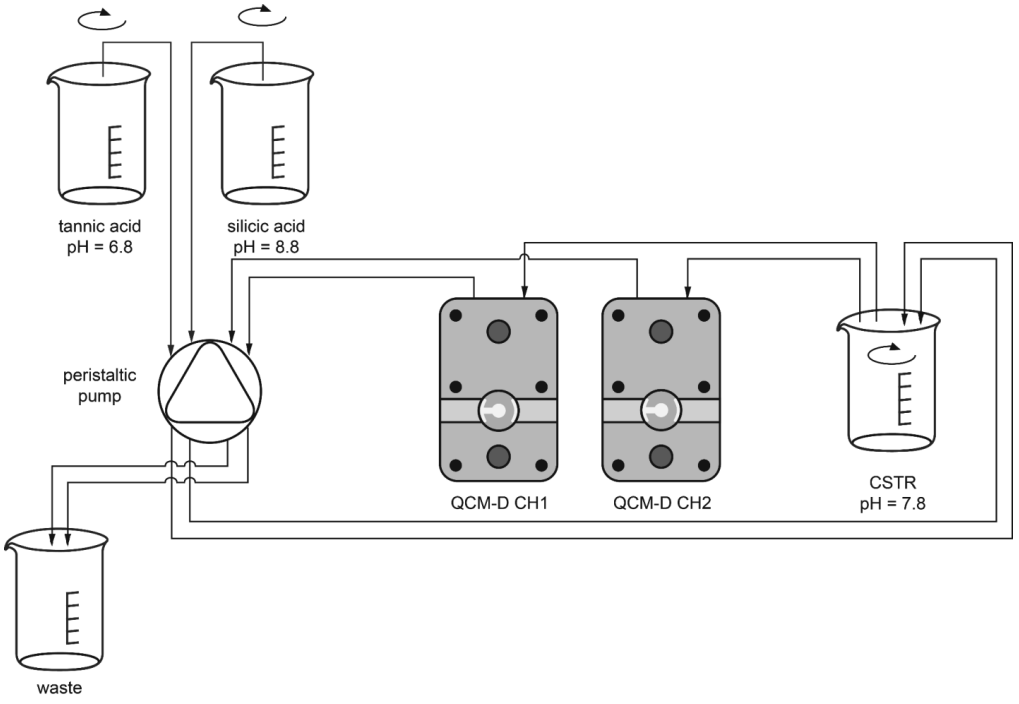

Figure S16: Flow chart of the continously stirred tank reactor (CSTR) setup for QCM-D measurements shown in Figure S14. Tannic acid was kept at mild acidic pH = 6.8 separated from silicic acid in alkaline condition. Mixing in the CSTR at a flow rate of 0.1 ml/min and a reaction volume of 6 ml resulted in an average residence time of 30 min. The solution in the CSTR was set to pH = 7.8 by adjusting the pH level of the silicic acid feed. The concentrations of TA and Si_{aq} in the CSTR were set equally to other QCM-D experiments to 1 mg/ml and 80 μM respectivly.

References

[1] G. Metz, X. L. Wu, S. O. Smith, *J. Magn. Reson. Ser. A* **1994**, *110*, 219.
[2] B. M. Fung, A. K. Khitrin, K. Ermolaev, *J. Mag. Reson.* **2000**, *142*, 97.
[3] T. Gullion, J. Schaefer, *J. Mag. Reson.* **1989**, *81*, 196.
[4] T. Gullion, D. B. Baker, M. S. Conradi, *J. Mag. Reson.* **1990**, *89*, 479.
[5] F. Weber, A. Barrantes, H. Tiainen, *Langmuir* **2019**, *35*, 3327.
[6] M. P. Jonsson, P. Jönsson, F. Höök, *Anal. Chem.* **2008**, *80*, 7988.
[7] M. Edén, *Annu. Rep. Prog. Chem., Sect. C: Phys. Chem* **2012**, *108*, 177.
[8] W. Kolodziejski, J. Klinowski, *Chem. Rev.* **2002**, *102*, 613.
[9] a) T. Kraus, Y. Zc, C. M Preston, R. A. Dahlgren, R. J Zasoski, *J. Chem. Ecol.* **2003**, *29*, 703; b) F. H. Romer, A. P. Underwood, N. D. Senekal, S. L. Bonnet, M. J. Duer, D. G. Reid, J. H. van der Westhuizen, *Molecules* **2011**, *16*, 1240.
[10] D. F. Evans, A. M. Z. Slawin, D. J. Williams, C. Y. Wong, J. D. Woollins, *J. Chem. Soc., Dalton Trans* **1992**, 2383.
[11] D. S. Jensen, S. S. Kanyal, N. Madaan, M. A. Vail, A. E. Dadson, M. H. Engelhard, M. R. Linford, *Surf. Sci. Spectra* **2013**, *20*, 36.
[12] A. F. Wells, *Structural inorganic chemistry*, 5th ed ed., Clarendon Press; New York: Oxford University Press, Oxford, **1984**.
[13] B. Beagley, J. J. Monaghan, T. G. Hewitt, *J. Mol. Struct* **1971**, *8*, 401.
[14] a) R. Tacke, A. Stewart, J. Becht, C. Burschka, I. Richter, *Can. J. Chem.* **2000**, *78*, 1380; b) K. Junold, J. A. Baus, C. Burschka, T. Vent-Schmidt, S. Riedel, R. Tacke, *Inorg. Chem.* **2013**, *52*, 11593; c) P. Bindu, B. Varghese, M. N. S. Rao, *Phosphorus Sulfur Silicon Relat. Elem.* **2003**, *178*, 2373.
[15] K. M. R. Kallury, U. J. Krull, M. Thompson, *Anal. Chem.* **1988**, *60*, 169.
[16] National Institute of Standards and Technology, *https://www.nist.gov/, (accessed 07 Jan 2019).*
[17] D. Johannsmann, I. Reviakine, R. P. Richter, *Anal. Chem.* **2009**, *81*, 8167.
[18] E. Haslam, in *Practical Polyphenolics: From Structure to Molecular Recognition and Physiological Action*, Cambridge University Press, **1998**.

Paper III

Tannic Acid Radicals in the Presence of Alkali Metal Salts and Their Impact on the Formation of Silicate-Phenolic Networks

Florian Weber, Einar Sagstuen, Qi-Zhi Zong, Tian Zheng, Hanna Tiainen

Published in *ACS Applied Materials & Interfaces*, November 2020, volume 12, issue 47, pp. 25457–52466. DOI: 10.1021/acsami.0c16946.

III

ACS APPLIED MATERIALS & INTERFACES

www.acsami.org

Research Article

Tannic Acid Radicals in the Presence of Alkali Metal Salts and Their Impact on the Formation of Silicate-Phenolic Networks

Florian Weber, Einar Sagstuen, Qi-Zhi Zhong, Tian Zheng, and Hanna Tiainen*

Cite This: *ACS Appl. Mater. Interfaces* 2020, 12, 52457−52466

Read Online

ACCESS | Metrics & More | Article Recommendations | Supporting Information

ABSTRACT: Polyphenolic molecules have become attractive building blocks for bioinspired materials due to their adhesive characteristics, capacity to complex ions, redox chemistry, and biocompatibility. For the formation of tannic acid (TA) surface modifications based on silicate-phenolic networks, a high ionic strength is required. In this study, we investigated the effects of NaCl, KCl, and LiCl on the formation of TA coatings and compared it to the coating formation of pyrogallol (PG) using a quartz-crystal microbalance. We found that the substitution of NaCl with KCl inhibited the TA coating formation through the high affinity of K^+ to phenolic groups resulting in complexation of TA. Assessment of the radical formation of TA by electron paramagnetic resonance spectroscopy showed that LiCl resulted in hydrolysis of TA forming gallic acid radicals. Further, we found evidence for interactions of LiCl with the Si_{aq} crosslinker. In contrast, the coating formation of PG was only little affected by the substitution of NaCl with LiCl or KCl. Our results demonstrate the interaction potential between alkali metal salts and phenolic compounds and highlight their importance in the continuous deposition of silicate-phenolic networks. These findings can be taken as guidance for future biomedical applications of silicate-phenolic networks involving monovalent ions.

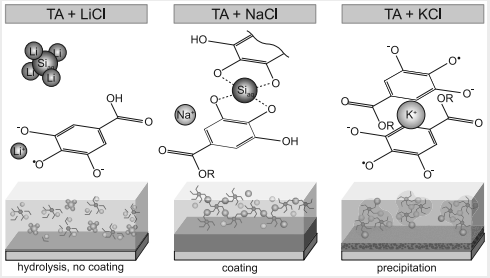

KEYWORDS: *polyphenols, surface modification, nanocoating, metal-phenolic networks, EPR*

INTRODUCTION

Naturally derived polyphenolic molecules have attracted great interest in creating novel and sustainable biomaterials based on green chemistry.[1−5] Their versatile interaction with interfaces originates from their molecular structure featuring catechol and galloyl groups that present an opportunistic reaction site for metal coordination and surface adhesion. Further, polyphenolic coatings can be utilized to create multifunctional surfaces via subsequent modifications, e.g., Michael additions.[4,6] Currently, the anti-oxidant properties of polyphenols are studied to create anti-inflammatory and anti-biofouling surfaces.[7−10] In these biologically relevant environments, salts are not only an important factor for biomolecular processes but also interact with polyphenolic molecules.[11]

Generally, the self-assembly and deposition process of polyphenolic layers depend on the type of polyphenol.[12] While tannic acid (TA) layers are commonly obtained through interaction with metal ions creating metal-phenolic networks (MPNs),[13] flavonoids, and low molecular weight polyphenols, such as dopamine and pyrogallol (PG), rely on oxidative polymerization.[14] Oxidation of phenolic molecules by dissolved oxygen results in their respective quinone form and is usually controlled by the solution pH.[15,16] Via oxidant induction or control of the pH, the coating formation of polyphenolic molecules can be regulated.[7,17] Additionally, diverse secondary interactions, such as π-stacking, π-cation interaction, hydrogen bonding, and electrostatic interactions affect the intermolecular interactions of polyphenols.[18] Therefore, the formation process is also controlled by the ionic strength. Optimal conditions to create MPNs and phenolic coatings were reported to be slightly alkaline with an ionic strength $\geq$0.5 M.[1,19]

Since multivalent ions strongly complex polyphenolic molecules and rapidly precipitate high molecular weight compounds, such as TA,[20] NaCl has been used to adjust the ionic strength in recent studies.[1,12,17,21,22] More focused investigations have later shown that the film thickness and particle morphology of TA-Fe^{III} based MPNs are highly dependent on the NaCl concentration. This relation has been attributed to changes in the hydration shell around the TA complexes.[23] Subsequently, the effect of other ions on TA-Fe^{III} networks was refined by Park et al., who concluded that the

Received: September 20, 2020
Accepted: November 9, 2020
Published: November 12, 2020

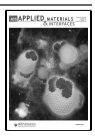

optimum ionic strength depends on the type of ion and decreases for ions with higher valency and atomic radius due to proposed charge screening effects.[24] Besides these charge screening effects, ions may also influence the reaction chemistry of phenolic compounds. The different interaction potentials of anions and cations with phenolic structures could influence the intermediary radical structures during oxidative polymerization reactions of polyphenols.[25−29] Evidence for changes in radical structures has been obtained studying the differences in quinone radicals generated by oxidation via horseradish peroxidase and H_2O_2 or NaOH oxidation.[30−32] In addition, stabilization of phenolic radicals by Zn^{2+} and Mg^{2+} are known effects.[33,34]

In this study, we investigated the interaction of silicate-phenolic networks with monovalent ions, Li^+, Na^+, and K^+ to optimize coating conditions and to elucidate the effect of their salts on the deposition of TA coatings. Using electron paramagnetic resonance (EPR), we probed different intermediary radical structures of TA in the presence of NaCl, KCl, and LiCl. A comparison to the formation of silica independent PG coatings allowed us to point out the specific interactions of the investigated salts with TA. We expect that these insights may impact future biomaterial research, which employs polyphenolic molecules as structural building blocks and comprise the use of monovalent ions in biological buffers.

MATERIALS AND METHODS

Materials. Tannic acid (MW = 1701.2, LOT#MKBN9606 V), pyrogallol (MW = 126.1), gallic acid (MW = 170.1), ellagic acid (≥95%, MW = 302.2), penta-galloyl glucose (≥96%, MW = 940.7), HEPES (BioPerformance, ≥99.5%), LiCl, LiOH, KCl, KOH, sodium metasilicate pentahydrate (orthosilicic acid, ≥95%), sodium persulfate ($Na_2(SO_4)_2$, ≥98%), and periodic acid (H_5IO_5, 99%) were purchased from Sigma-Aldrich. NaCl and NaOH were supplied by VWR. Sodium 3-(trimethylsilyl)propionate (TMSP, 2,2,3,3-D4, D = 98%) was supplied by Cambridge Isotope Laboratories. Ammonium molybdate (para)tetrahydrate (99%) was purchased from Alfa Aesar. Unless otherwise stated, all materials were ACS grade.

Polyphenolic Solutions. TA and PG were dissolved at a concentration of 1 mg/mL in Milli-Q water (18 MΩcm) containing 600 mM NaCl, KCl, or LiCl if not further specified. To avoid the influence of buffer molecules in spectroscopic techniques employed in this study, the pH was adjusted with specific amounts of 10 M base added to the solutions (Table 1). More data points can be found in Figure S1 of the ESI.

Table 1. Correlation of pH and Added Base to Aqueous Polyphenol Solutions

$V_{10Mbase}$ [μL/mL]	0	0.3	0.5	1.0
$pH_{TAsolution}$	∼4	∼8	∼9	∼11
$pH_{PGsolution}$	∼7	∼8	∼9	∼11

Coating Deposition. To compare the coating formation with previous experiments, TA and PG coatings were dissolved in 100 mM HEPES buffer containing 600 mM NaCl, KCl, or LiCl. The buffers were adjusted to pH 7.8 with NaOH, KOH, or LiOH, respectively. To form silicate-TA coatings, 80−100 μM orthosilicic acid (Si_{aq}) was added. Ø6 mm Ti coins were coated in 10 mL solutions under agitation at 30 rpm.

The real-time formation of polyphenolic coatings on Ti was monitored using a QSense E4 (Biolin Scientific) quartz crystal microbalance (QCM-D). Ti sensors (QSX 310, Biolin Scientific) were cleaned according to the manufacturer's protocol before and after each experiment. The procedure includes sonication in 2% SDS, washing with Milli-Q water and EtOH, and finally UV-ozone treatment. The QCM-D chambers were cleaned with 2% SDS for 10 min at 0.5 mL/min and extensively flushed with water (>15 min) prior to the experiment. Before the adsorption of polyphenols, sensors were equilibrated in the respective solvent for 20 min, and a baseline was recorded. The polyphenol solutions were gently stirred (100 rpm) during the measurement to provide sufficient O_2. Measurements were performed at a flow rate of 0.1 mL/min at 21°C. After the adsorption, the sensors and chambers were flushed with Milli-Q water and 0.1 M HCl for 5 min to remove the coating. All experiments were performed in triplicates ($n = 3$). Changes in frequency (ΔF) and dissipation (ΔD) were continuously monitored for the fundamental frequency and the 3rd, 5th, 7th, and 9th harmonic overtone. For clarity, only the first three harmonics are plotted. Calculations of the layer thickness were performed with QTools Software (BiolinScientific, Version 3.1.33) using the Voigt extended viscoelastic model. Fits were obtained based on the first three harmonic overtones and a power based shear dependence. The TA and PG layer densities were assumed to be 1046 and 1435 kg/m^3, respectively. Fluid density was set to 1027 kg/m^3.[22] Reported values should be taken as guidance.

Adhesion Force. Ti substrates (Ø6 mm coins) were coated for 24 h in 10 mL of HEPES buffer (pH 6.8) containing 1 mg/mL TA, Si_{aq}, and 600 mM NaCl. Then 10.28 μm polystyrene (PS) particles (100 μL, 10% w/v, Microparticles GmbH) were washed with 900 μL of Milli-Q water three times by centrifugation (1500g, 60 s) and removing of the supernatant. Subsequently, PS particles were incubated under constant stirring (400 rpm, 6 h) in 1 mL of TA solution (2 mg/mL TA in HEPES buffer pH 7.0 containing 600 mM NaCl and Si_{aq}). Then 500 μL aliquots of the dispersion were withdrawn into 1.7 ml plastic tubes and washed with Milli-Q water three times.

To attach a PS particle on a cantilever, the tipless MLCT-O10 cantilever (Bruker, spring constant ∼0.03 N/m) was lowered into a small amount of adhesive (two-part epoxy adhesive, Super Glue Corporation, U.S.A.) that was then promptly used to pick up a colloidal PS particle deposited on a glass slide. The modified cantilever was left at room temperature to allow the adhesive to dry and set for 24 h.

The atomic force microscopy (AFM) measurements were carried out by Cypher ES (Asylum Research, U.S.A.) with a colloidal probe in liquid. Prior to the measurement, both the TA coated Ti substrate and the colloidal probe were incubated in solutions for 10 min to reach equilibrium state. The spring constant of the colloidal probe was calibrated before taking force measurements. During the measurement, both the approaching and retracting velocity were kept at 500 nm/s. Between measurements in different solutions, the cantilever was washed with Milli-Q water and carefully dried to remove any residue on the colloidal probe. For each sample, at least 100 force curves were analyzed using Igor Pro 6.37.

Radical Formation. Electron paramagnetic resonance (EPR) spectra of polyphenolic radicals were recorded on a Bruker EleXsyS 560 SuperX X-band spectrometer using 25 μL quartz microcapillaries (Blaubrand, intraMark) inserted in a 4 mm Wilmad quartz tube positioned in the cavity by a Teflon rod. For all experiments, an ER4122SHQE cavity was used. The spectra were obtained at 0.50 mW input microwave power (i.e. 26 dB power attenuation), receiver gain of 55 dB, 0.01 mT modulation amplitude, a time constant of 81.92 ms, and a sweep time of 83.89 s. The magnetic field sweep width was 1 mT with a resolution of 1k points. Polyphenols were dissolved 1 h prior to the measurements. The pH was adjusted 1 min before each experiment under gentle agitation. Details on radical modeling can be found in the Supporting Information (SI). The signs of the hyperfine coupling (HFC) constant cannot be inferred from the experimental data; hence, only the absolute values are presented here.

Spectroscopic Structure Elucidation. *Fourier Transform Infrared (FTIR) Spectroscopy.* Identification of functional groups was performed with a PerkinElmer Spectrum 400 using a universal attenuated total reflection (ATR) sampler. Droplets of polyphenolic solutions were evaporated on the ATR crystal. Solutions containing LiCl did not fully dry and a LiCl·H_2O background had to be subtracted (Figure S2). Spectra were recorded at a resolution of 4 cm^{-1} and averaged over 16 measurements to improve the signal-to-noise ratio. The data was processed by correction for ATR, baseline subtraction, and normalization to the most intense peak at 1200 cm^{-1}.

https://dx.doi.org/10.1021/acsami.0c16946
ACS Appl. Mater. Interfaces 2020, 12, 52457−52466

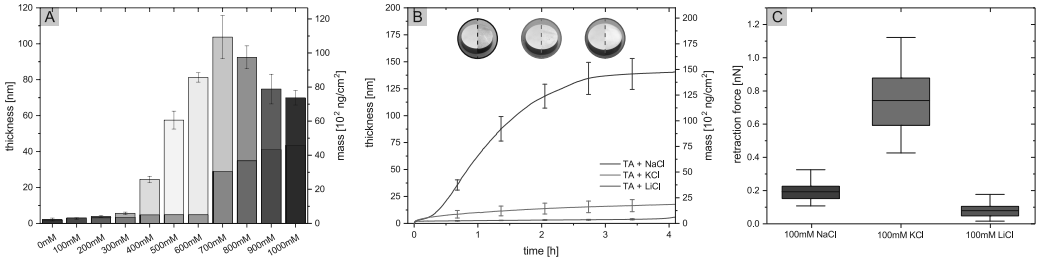

Figure 1. (A) Thickness and areal mass of tannic acid films deposited on Ti surfaces for 1 h determined by QCM-D. TA was dissolved in water supplemented with varying amount of NaCl, 80 μM Si_{aq} at pH 8 (n = 3). Control experiments without Si_{aq} are given in grey overlays. (B) Progression of thickness and areal mass during the coating process of TA followed by QCM-D (n = 3). TA was dissolved in 100 mM HEPES containing 600 mM salt and 100 μM Si_{aq} at pH 7.8. Insets show coated Ti coins (right). (C) Surface force between two TA coatings upon retraction of the AFM cantilever in 100 mM salt solutions. For each solution, 100 data points were collected. Boxplots show 25/75 percentiles, minima, maxima, and mean values.

UV–vis Spectroscopy. The electronic state of polyphenols was determined with a PerkinElmer Lambda 25 spectrophotometer using a quartz cuvette with 10 mm path length. Spectra were recorded at a resolution of 1 nm. Due to the high UV absorbance of polyphenolic molecules, 100× diluted samples were measured in the range of 220–400 nm.

Nuclear Magnetic Resonance (NMR) Spectroscopy. Solution ^{13}C NMR was performed on a Bruker AVII 600 instrument using 5 mm NMR tubes. Native TA was dissolved in heavy water (D_2O) at 100 mg/mL with TMSP as the internal reference. TA in the presence of 600 mM salts was dissolved in H_2O containing 10 vol. % D_2O due to solubility issues in pure D_2O. The concentration of Si_{aq} (8 mM) was stoichiometrically adjusted to the concentration of TA (100 mg/mL). Spectra were recorded at 150 MHz, 90° pulse, 0.9 s acquisition time, and 10 s delay time (d_1). Solution ^{29}Si NMR was performed on a Bruker AVII 400 instrument. Si_{aq} was dissolved at a concentration of 0.1 M in water containing 10 vol. % D_2O and TMSP as internal reference. Spectra were recorded at 79.5 MHz, 1.0 s acquisition time, and 5.0 s delay time (d_1).

Liquid Chromatography–Mass Spectrometry (LC-MS). TA solutions were separated from salts in a C18 SPE by washing with 10% formic acid and elution with acetonitrile. Then 1 μL aliquots were injected into a high-performance liquid chromatography system (HPLC) coupled to a 6495 triple quadrupole (TQ) MS (Agilent Technologies, Singapore) via an electrospray interface. The reverse-phase separation was performed at a flow rate of 0.6 mL/min on a C18 column (2.6 μm particle size, 3 mm inner diameter, 100 mm length, Kinetex) using water/formic acid (0.1% v/v) as solvent A and acetonitrile as solvent B in a stepwise gradient at 40 °C: 10–50% B (0–6 min), 50–100% B (6–6.5 min), held at 100% B for 1 min. MS spectra were recorded in negative mode.

TA Purification. TA was purified on a Biotage Selekt system using a Sfär C18 Duo (100 Å, 30 μm, 60 g) column. The same eluents as described above were used to run the gradient: 5% B (0–2 min), 5–45% B (2–5 min), and 100% B (5–10 min). The solvent was removed under reduced pressure and the TA fraction was re-dissolved in water and freeze-dried. Mass spectra were obtained using ESI-QTOF (maXis II ETD) in positive mode.

Silicomolybdic Assay. The concentration of monomeric orthosilicic acid was quantified via the complexation of silicic acid with ammonium molybdate according to an established protocol.[35] Si_{aq} containing salt solutions were prepared in Milli-Q water filtered twice through activated carbon to remove any potential interfering ions.[36] To 1.25 ml sample, 50 μL of 100 mg/mL ammonium molybdate solution was added and acidified with 50 μL of 1.5 M H_2SO_4 (pH 3). After 5 min stirring followed by 5 min settling time, the adsorption of the yellow β-complex was measured at λ = 400 nm.

RESULTS AND DISCUSSION

Characterization of the Ionic Strength Dependent Coating Deposition of Silicate-TA Networks. The deposition of TA coatings depended on the concentration of NaCl (Figure 1A). The continuous increase of the coating thickness of silicate-TA networks (Figure S3) with increasing ionic strength at pH 8 reached a maximum layer thickness in the presence of 700 mM NaCl. At a NaCl concentration c_{NaCl} < 300 mM, the QCM-D data indicated only the formation of a monolayer. At c_{NaCl} = 300 mM, a continuous deposition process was possible, which increased in efficiency between 400–600 mM NaCl. Above 600 mM NaCl we observed a cloudy solution, which was accompanied by a constant frequency and dissipation drift. Since the control experiment without Si_{aq} behaved similarly, we associate this effect with the interaction between TA and NaCl, resulting in limited TA deposition. As the NaCl concentration was further increased, more TA precipitated. Thus, unlike TA-Fe^{3+} networks, silicate-TA coatings did not benefit from NaCl concentrations beyond 600 mM.[23] The formation of TA aggregates in solution, which lowered the coating efficiency by reducing the amount of free reactive molecules, can be related to the described increase in the roughness of TA-Fe^{3+} network structures. This effect has been associated with cluster formation of TA molecules enabled by the charge screening effect of Na^+ ions.[23]

Coating Formation under Substitution of NaCl with KCl and LiCl. Upon exchanging NaCl with KCl and LiCl, we observed that the deposition of TA layers was negatively affected (Figure 1B). The coating process in NaCl showed three phases in $\Delta F/\Delta D$ plots (Figure S4) as reported before[21] and the TA layer reached a thickness of 140 ± 14 nm after 4 h. This correlates to a thickness of about 100 nm in dry state taken into account the hydration of the layer.[17] The K^+ based solutions turned turbid immediately upon mixing (see the SI video). This behavior was observed in a pH range between pH 6.0 and 9.0 and led to a significant loss of coating efficiency, resulting in a thickness of only 18 ± 6 nm after 4 h. Above pH 9, KCl led to the formation of TA coatings. However, NaCl did not result in a coating formation (Figure S5). In comparison, LiCl inhibited the coating formation and delayed the polymerization process substantially as the solutions were not turning turbid during the first 4 h. As a result, a layer thickness of only 3.1 ± 0.3 nm was obtained. Neither adjusting the pH in the range pH 6–11, nor lowering the LiCl concentration to 50 mM resulted in a successful deposition of TA beyond a monolayer. Further,

https://dx.doi.org/10.1021/acsami.0c16946
ACS Appl. Mater. Interfaces 2020, 12, 52457–52466

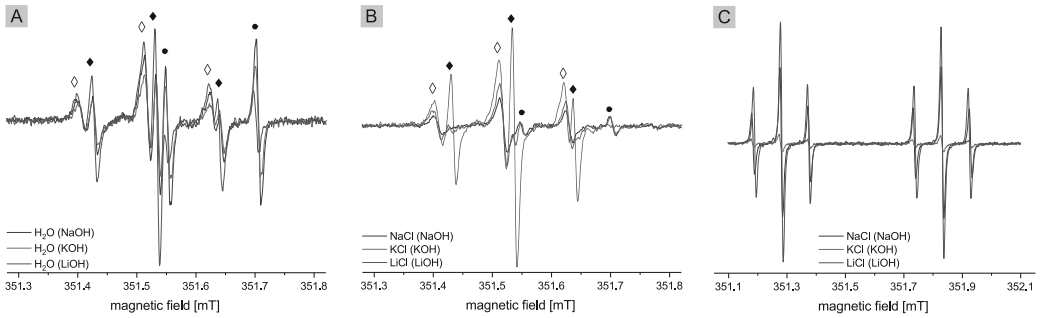

Figure 2. (A) EPR spectrum of 1 mg/mL TA dissolved in water and (B) 600 mM of either NaCl, KCl, or LiCl. All solutions were adjusted to pH 11. (C) EPR spectrum of 1 mg/mL PG dissolved in 600 mM of either NaCl, KCl, or LiCl at pH 11.

increasing the concentration of Si_{aq} to 1 mM led only to a slow deposition of TA reaching a layer thickness of 17.0 ± 0.3 nm after 4 h (Figure S6). Higher concentrations of Si_{aq} at pH 7.8 were not considered since Si_{aq} condensation caused a drifting QCM-D signal (Figure S7).

Although we have shown that silicate-phenolic networks did not form in the presence of KCl and LiCl, Fe^{+3} based metal-phenolic films can be assembled in the presence of both salts.[24] We suspect that the continuous built-up of silicate-TA networks behaved differently compared to Fe^{3+} based structures due to the interaction of TA and Si_{aq}. We hypothesize that the assembly of MPN films is mainly facilitated by the strong interaction between vicinal diol groups and Fe^{3+} compared to possibly weaker interactions of TA with silicic acid.[37] Contrary to the deposition of silicate-TA layers, PG coatings were successfully formed in all tested salt conditions (Figure S8). While the PG layer reached a higher thickness in the presence of KCl, some larger particles were formed after 12 h deposition time. This was also represented in QCM-D data showing splitting overtones. Opposed to the TA coating formation, the PG deposition was positively affected by LiCl and showed higher deposition rates than in NaCl.

The increased coating deposition of PG in LiCl solution supports our expectation that the different cations affect the formation of silicate-TA networks. To estimate the strength of cation-π complexes, the adhesion force between TA coated surfaces in the presence of salts was determined. Compared to NaCl and LiCl, KCl showed a significantly higher adhesion force between the surfaces (Figure 1C). Cation-π interactions are known to follow the stability order $Li^+ > Na^+ > K^+$ in the gas phase,[38] whereas the order changes in aqueous phase to $K^+ > Na^+$, Li^+ due to a reduction of the desolvation penalty of the larger K^+ ion.[25,27] Indeed, the high affinity of K^+ ions towards phenolic groups allows K^+ to replace Na^+ in polydopamine assemblies and to participate in competitive binding between other cations and aromatic compounds.[11,26,27] The high interaction potential of K^+ causes the increased retraction force (Figure 1C) and is also likely to induce the precipitation of TA in KCl solution near neutral pH. Thus, KCl is not well suited for our previously determined coating conditions, in which the layer thickness was increased.[17]

Intermolecular Interaction of TA in the Presence of Different Salts. The difference between the coating formation of TA and PG and the low interaction potential of TA with Li^+ raised the question of whether electrostatic interactions sufficiently explain the suppressed coating formation of TA in the presence of LiCl. Preventing the formation of TA coatings by LiCl could originate from two options: (i) interaction of Li^+ with TA or (ii) interaction of Li^+ with Si_{aq}. It is known that Li^+ is tightly coordinating H_2O, which may alter the TA hydration shell.[39] Further, the potential binding to TA hydroxyl reaction sites[23] and the high stability of ionic ($O^-\cdots Li^+$) complexes may cause irreversible Li^+ complexes with phenolic structures.[40,41] This effect is for example encountered in lithiation of the solid-state interface in energy storage materials.[42] Regarding interactions between Li^+ and Si_{aq}, an interaction preventing the assembly of silicate-TA networks may also be plausible, but evidence of any reactions under the conditions of this study were not found in literature. Therefore, we continued to evaluate whether the different salts have an effect on the reaction chemistry during the layer formation. Since the polyphenol chemistry is largely driven by their oxidation, we studied the formation of polyphenolic radicals to check whether these reaction intermediates are influenced by alkali metal salts.

Polyphenolic Radical Formation. In contrast to the pH used to obtain coatings, the pH had to be slightly increased for a reasonable EPR signal. While radicals could be observed at pH 9, the alkalinity of the solutions was further increased to pH 11 for kinetic and quantitative measurements. At this pH, TA presented two main radical triplets (◊, ♦) with 1:2:1 hyperfine splitting intensities and an additional radical doublet (●) with 1:1 hyperfine splitting (Figure 2A). By fitting radical models to the experimental data (Figure S9 and S10), we obtained the proton splitting constants (a^H), line widths (LW), and g-values of TA radicals (Table 2). Galloyl radicals typically form via a sequential proton loss electron transfer (SPLET) mechanism with the $4O^\bullet$ being the most stable radical (Scheme 1).[43,44] In agreement with this structure, the hyperfine splitting of R1 (♦) and R2 (◊) radicals is caused by the two equivalent protons in

Table 2. Parameters of TA and PG Radical Species

TA radical		equiv. protons	a^H [mT]	LW [mT]	g
1	(♦)	2	0.107	0.0035	2.0055
2	(◊)	2	0.112	0.0079	2.0056
3	(●)	1	0.152	0.0031	2.0050
4	(○)	1	0.052	0.0032	2.0054
PG radical		equiv. protons	a^H [mT]	LW [mT]	g
1		1	0.5514	0.0041	2.0054
		2	0.0995		

https://dx.doi.org/10.1021/acsami.0c16946
ACS Appl. Mater. Interfaces 2020, 12, 52457−52466

Scheme 1. Scheme of Gallic Acid (GA), Tannic Acid (TA), Pyrogallol (PG), and Ellagic Acid (EA) Radicals with Equivalent Protons Marked in the Same Color

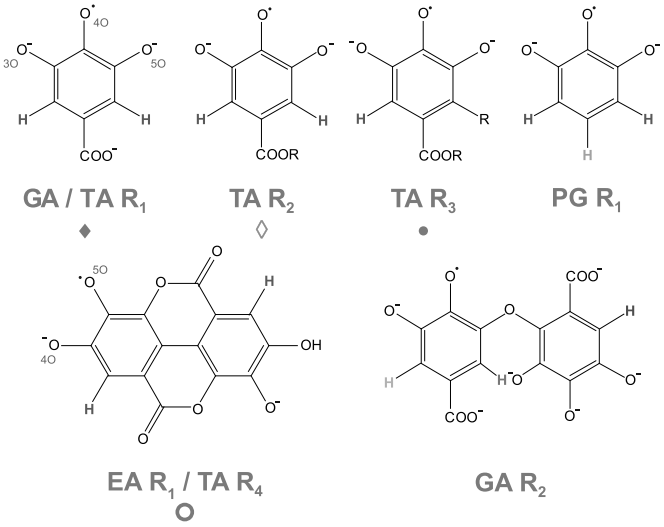

the galloyl group. The ♦-radical displayed HFC constant a^H = 0.107 mT and a LW equal to gallic acid (GA), the structural subunit of TA (Figure S11).[45] In comparison, the ◇ radical has a broader LW and slightly higher a^H.

The occurrence of two different radicals may be explained by differences in spin density or spin relaxation times in the outer galloyl group compared to the inner group. It has been proposed that both groups are chemically not equivalent with the inner galloyl groups being more prone to oxidation.[46] However, since we have found free GA in the commercial TA (Figure S12), and para-substitution in TA increases the coupling constant,[47] it is more likely that the R1 (♦) radical corresponds to free GA radicals. Under this assumption, R2 (◇) represents the radical of a galloyl ester group, which we have proven by comparing TA with penta-galloyl glucose (PGG) radicals (Figure S13). Thus, our results agree with previous studies determining the HFC constant of PGG radicals and gallate-ester radicals.[31,32] In addition, after purification of the commercial TA, we observed a spectrum with one ◇-radical triplet (Figure S14). Once the purified TA was subjected to higher pH, the second ♦-radical emerged in the spectrum indicating hydrolysis of the galloyl groups from TA, generating free GA.

R3 (●) however represents an unknown radical structure coupling with only one proton. Although phenolic molecules may form C−C bonds at C2 or C6 position, the coupling constant is unreasonably high and not comparable to C−C coupling observed in ellagitannins (Figure S15).[48] The low HFC constant a^H = 0.05 mT in ellagic acid indicates a low electron spin density at the meta position to the radical electron as indicated in Scheme 1. This stands in contrast to reports suggesting that this EA radical position is thermodynamically not the most stable species.[49] Further, the higher g-value of the ●-radical compared to ◇- and ♦-radicals may suggest the substitution of a phenolic ring proton with an electron donating group.[50] Recent quantum chemical studies have shown that hydrogen bonding affects the radicalization mechanism for various phenolic structures.[51] Yet these models need further experimental evidence to deduct the molecular structure of the ●-radical.

Altered Radical Formation in the Presence of Alkali Metal Salts. EPR spectra of saline TA solutions showed a significant salt dependent difference in the intensity of both ◇- and ♦-radical species and the absence of ●-radicals in the EPR spectra of TA solutions containing LiCl (Figure 2B). In the presence of NaCl and KCl, commercial TA preferably yielded a ◇-radical, whereas LiCl facilitated the formation of the ♦-radical. While radical parameters of both ♦- and ◇-radicals in NaCl and KCl solution did not differ from their corresponding signals without salt, LiCl appeared to slightly reduce the HFC constant compared to solutions without salt. This can be explained by influences in charge densities caused by the cation.[34,41] All salts produced lower intensities for ♦- and ◇-radicals (Figure S16). At pH 9, this effect was however canceled by Si_{aq} for NaCl and LiCl (Figure S16), which suggests a radical stabilizing effect similar to Zn^{2+}.[33,52]

We conducted further studies investigating whether the ●-radical is a specific form of oxidation product by inducing the radical formation chemically with periodic acid and sodium persulfate.[53,54] However, neither oxidant resulted in a significant change in the observed TA radical species (Figure S17). Further, no radicals could be detected in the sole presence of the oxidants. Since the oxidation in alkaline condition is strongly dependent on the oxygen update,[15] we next investigated the radical formation under varying O_2 uptake. We observed a new radical (○) displaying a doublet structure with a^H = 0.052 mT in vigorously shaken solutions (Figure S18). This species was observed directly at t = 0 min and appeared more stable than the other radical species. It is likely a reaction product of the oxidative coupling of GA,[55] since the similarity to EA radicals is striking (Figure S15).

To compare our observations for TA to the deposition of PG coatings, we further studied PG radicals (Figure 2C). At pH 11,

https://dx.doi.org/10.1021/acsami.0c16946
ACS Appl. Mater. Interfaces 2020, 12, 52457−52466

the EPR spectrum presented a doublet composed of 1:2:1 triplets with a^H = 0.551 and 0.099 mT, respectively (Table 2). This pattern originated from the two chemically different protons of PG (Scheme 1), with the para proton exhibiting the larger HFC constant. Both in LiCl and NaCl, PG displayed similar EPR signals at pH 11. KCl however led to a reduced intensity, which stands in contrast to the observed coating formation. The same result was also observed in solutions without the respective salt.

In conclusion, the structure of the ●-radical remained unexplained and we suggest it is a form of contamination in commercial TA since it did not appear in the purified TA spectra. However, we have shown that NaCl facilitated the formation of the TA radical, whereas in the presence of Li^+, GA radicals were observed. The formation of GA could be the reason for the reduced ability to form coatings since GA cannot be continuously deposited on surfaces.[22] The lower molecular weight GA potentially reacts faster with Si_{aq} and blocks the formation of TA coatings. Additionally, PG only showed one type of radical with a salt dependent intensity. This may explain why PG coatings were formed regardless of the type of salt.

pH Dependent TA Radical Distribution. After observing a salt dependent TA radical distribution, we investigated whether different salts have an effect on TA radicals at varying pH. With increasing pH, an increase in signal intensity (Figure S19) was accompanied by a change in the ratio of the two main ◊- and ♦-radicals (Figure 3A). In salt free solutions, both radicals were almost equally distributed at pH 11 and 12. Once the pH is further raised to pH 13, K^+ based solutions showed higher contents of the ◊-radical, while in NaOH the ratio is shifted more to the ♦-radical. Solutions adjusted with LiOH resulted in a ♦-radical dominated spectrum. Upon including salts, the K^+ and Na^+ based spectra indicated higher content of ◊-radicals throughout the whole pH range (Figure 3B). In contrast, LiCl increased the ratio of the ♦-radical even more compared to LiOH solutions. This corroborates our previous result with purified TA (Figure S14) showing that with increasing pH TA hydrolyses and breaks down to form GA subunits and that this process is reduced in NaCl and KCl but accelerated in LiCl solution. The HFC parameters of ◊- and ♦-radicals further showed a decrease in LiCl solution with increased LiOH concentration to a^H = 0.102 mT and a^H = 0.108 mT respectively (Table S3). Further, the decreasing coupling constant indicates strong Li-coordination to the phenol group affecting its electron distribution. Similar ion specific interactions have been observed in anhydrous environment.[56] These results support our initial observation that LiCl has a distinct role in the formation of GA radicals. Further, the trend allows us to extrapolate to pH level closer to the coating conditions for which we expect similar behavior.

Time Dependent TA Radical Stability. Radicals are short-lived intermediary structures and key structures in oxidative reactions.[47] Hence, we investigated the decay of the radicals over time. TA radicals at pH 12 were stable for more than 3.5 h in NaOH, KOH, and LiOH solution (Figure 3C–E). However, the presence of the respective salts compromised TA radical lifetime, as the signals decayed before 3.5 h. In the course of the decay, the intensity of the ◊ radical continuously decreased and diminished earlier than the ♦-radical. This may indicate a transformation of the ◊ radical to the ♦-radical and a subsequent radical termination. Thus, this time dependent signal reduction also supports the suspected hydrolysis reaction. Coincidentally this timespan correlates with the kinetically

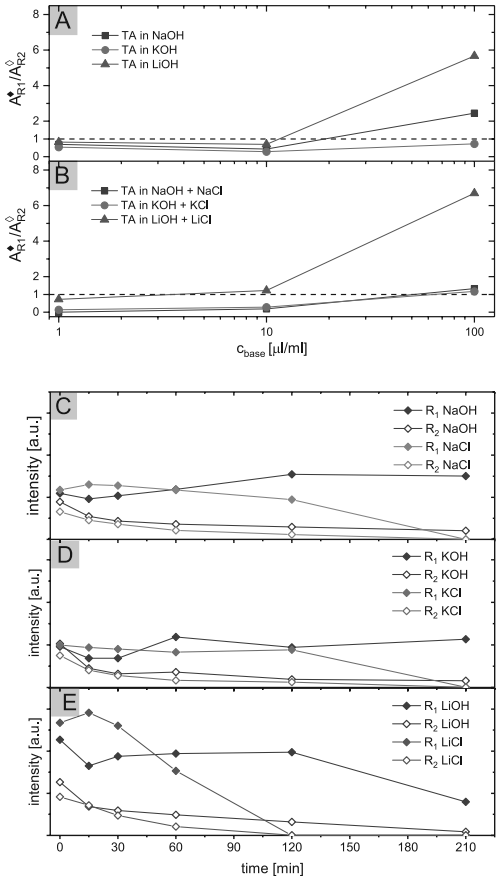

Figure 3. (A) Ratios of modeled peak areas of TA radical 1 (♦) vs radical 2 (◊) in water and (B) salt containing solutions. (C) Time dependent radical decay of TA dissolved in Na^+, (D) K^+, and (E) Li^+ containing solutions at pH 12.

fastest period of the coating formation suggesting that radicals could play a key role in this process.[17,21]

Spectroscopic Structure Analysis. A clear limitation of the EPR measurements is however the raised pH compared to the coating condition. TA coatings could not be obtained in NaCl solution above pH 9 (Figure S5). Only in KCl it was still possible, presumably due to retaining of the TA radical structure. However, we expect that reactions occur already at lower pH, which only get accelerated in alkaline pH. To support our EPR results showing that Li^+ ions alter the electronic structure of polyphenols also at coating conditions, we studied the UV–vis spectra of TA for different pH levels.

The absorption peak of pristine TA at 275 nm changed upon pH induced oxidation and resulted in two peaks appearing at 234 and 324 nm due to deprotonation (Figure 4A).[57] These decayed above pH 11, indicating that the molecules have lost their initial structure (Figure S20). While we did not observe significant differences in TA solutions adjusted with any of the bases NaOH, KOH, or LiOH, the addition of salts resulted in

https://dx.doi.org/10.1021/acsami.0c16946
ACS Appl. Mater. Interfaces 2020, 12, 52457–52466

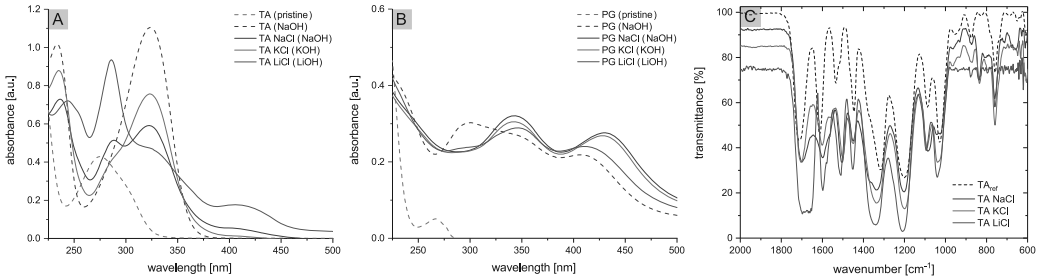

Figure 4. (A) UV−vis spectra of TA and (B) PG at concentrations of 0.01 mg/mL. Solutions were supplemented with 600 mM NaCl, KCl, or LiCl and adjusted to pH 7. For representation, the respective polyphenolic solution without salt is added in dashed lines. (C) FTIR spectra of TA supplemented with 600 mM NaCl, KCl, or LiCl and adjusted to pH 8.

the appearance of a peak at 290 nm at pH 7. In solutions containing NaCl, the peak at 290 nm was distinct while in KCl it existed only as a shoulder of the 324 nm peak and in LiCl it was the main peak of the spectrum. These peaks may be an indication for the formation of GA and EA, which show peaks around 290 nm (Figure S21).[58] These results confirm our EPR and LC-MS results and point out that LiCl leads to hydrolysis of TA.

We further analyzed the spectra of PG with the hypothesis that we observe less distinct differences between the added salts. While PG dissolved in water showed a peak at 268 nm, three peaks merged at 300, 335, and 410 nm after increasing the pH with NaOH, KOH, or LiOH (Figure S22). Adding salts to PG solutions at pH 7 reduced the peak at 300 nm resulting in a double peak at 345 and 430 nm (Figure 4B). The lack of significant differences in the PG spectra confirm the hypothesis and support the salt independent coating formation of PG.

Since we had evidence for the creation of GA and EA, we investigated whether we can determine changes in the chemical structure of TA solutions by FTIR. The presence of salts resulted in minor peak shifts and peak broadening of TA spectra at pH 8 compared to pristine TA (Figure 4C). However, the peak broadening was primarily induced by the change in pH (Figure S23). These peak shifts in the range of 2−5 cm^{-1} have been observed for K- and Li-phenolates[59] as well as for Fe-TA network structures.[60] The most dominant differences are (i) the shift of the C═C stretching vibration from 1534 to 1505 cm^{-1}, (ii) the broadening and shift of phenolic C−O and C−H bending vibrations from 1316 to 1340 cm^{-1} (Table S4), and (iii) the shift of the C−H bending vibration from 1030 to 1040 cm^{-1} in alkaline conditions. These differences correlate to EA and GA spectra (Figure S23D) and may thus indicate the formation of EA and GA upon oxidation of TA. The addition of 100 μM Si_{aq} in Li^+ and K^+ systems did not lead to changes in the spectra. However, Na^+ systems with Si_{aq} showed variations in the peak-to-peak intensities for absorption bands at 1598 cm^{-1}, 1504 cm^{-1}, 1087 cm^{-1} and 1026 cm^{-1}. Although FTIR results are not suitable for an absolute structure determination due to the high similarity of TA, GA, and EA spectra, the obtained results indicate a plausible mixture of the compounds. Moreover, TA precipitate (TA_P), we observed during the coating formation, showed typical oxidation induced peak shifts for both NaCl and LiCl containing solutions (Figure S24),[22] whereas KCl captured TA in its non-oxidized form.

Additionally, we conducted NMR experiments to check for changes caused by the interaction between TA and Na^+, K^+, or Li^+. The ^{13}C NMR of TA showed a typical spectrum and no apparent changes in the presence of salts and Si_{aq} were observed (Figure S25). Similar to LC-MS (Figure S12), ^{13}C NMR of TA solutions showed the presence of free gallic acid. A correlation with emerging C−O−Si bonds could not be obtained to study the interaction of TA and Si_{aq} as described by solid-state NMR.[17] Precipitation occurring during the course of the measurement likely excluded the cross-linked TA molecules from being NMR active.

Interaction of Na^+, K^+, and Li^+ with Si_{aq}. We investigated the potential of salts to interact with Si_{aq} inhibiting the formation of silicate-phenolic networks by blocking silicic acid. ^{29}Si NMR experiments of 0.1 M Si_{aq} showed a major peak for silicic acid (Q^0) followed by minor peaks of Si polycondensates with Q^1 and Q^2 states (Figure S26).[61] Only minor shifts of 0.2 and 0.3 ppm occurred in the solutions containing 600 mM NaCl or LiCl, respectively, which can be explained by ion-pairing.[62] However, more elaborate experiments have previously shown irreversible complexation of silicate anions with Li^+.[63] We could not determine these interactions by NMR and our sole observation that Si_{aq} interacts with LiCl is based on QCM-D data that showed a significantly reduced Si_{aq} condensation in LiCl solution (Figure S7D).

Finally, we evaluated the amount of free silicic acid in solutions containing NaCl, KCl, and LiCl by a silico-molybdic assay. The assay resulted in an equal amount of free Si_{aq} irrespective of the added salts. The linear correlation between the absorbance of the silico-molybdic complex was maintained until the capacity of the assay was reached well beyond the concentration of Si_{aq} used to obtain TA coatings (Figure S27).[35] Although we did not observe a reduction of free silicic acid we take into account that the acidic pH may shift the dissociation of the weak silicic acid (pK_A = 9.8) towards neutral charge, thus limiting its interaction with cations and not representing reactions at the coating condition.

■ CONCLUSION

We have taken a closer look at the effects of different salts and their concentration on the silica (Si_{aq}) mediated coating formation of tannic acid (TA). Our results revealed that 600 mM NaCl is required to effectively form silicate-phenolic networks. Substitution with KCl resulted in strong interaction with TA leading to precipitation near neutral pH, whereas LiCl prevented any deposition of TA coatings beyond a monolayer.

Using EPR, we obtained insight into the salt dependent radical formation during the oxidation of TA. While NaCl

https://dx.doi.org/10.1021/acsami.0c16946
ACS Appl. Mater. Interfaces 2020, 12, 52457−52466

promoted the formation of TA radicals, LiCl resulted in the formation of GA radicals. LiCl is likely contributing to hydrolytic cleavage of the galloyl ester bonds of TA and thereby inhibiting the formation of silicate−TA networks. In contrast, pyrogallol (PG) coatings, which do not rely on Si_{aq} crosslinking, were independent on the type of alkali metal cation and EPR spectra did not show a salt dependent radical formation. Although EPR experiments were conducted at elevated pH, supporting spectroscopic experiments corroborated that LiCl results in hydrolysis of TA also under coating conditions. Further, we obtained indications that LiCl interacts with Si_{aq}, preventing the formation of silicate-TA networks.

In summary, we highlight that charge screening may not be the only important interaction of alkali metal salts in the chemistry of silicate-phenolic networks. Depending on the coating mechanism, the specific interactions between polyphenols and cations must be taken into consideration to obtain desired reaction conditions in biologically relevant environments. Our EPR data lays the fundament for further quantum chemical investigations of phenolic radicals. This may find application in further investigations into the chemistry of polyphenols, e.g., whether TA radicals are a prerequisite to form silicate-phenolic networks.

■ ASSOCIATED CONTENT

Supporting Information

The Supporting Information is available free of charge at https://pubs.acs.org/doi/10.1021/acsami.0c16946.

Details on EPR modeling, QCM-D raw data, and supplementary UV−vis, EPR, and FTIR spectra (PDF)

Turbidity of the K^+ based solutions immediately upon mixing (MP4)

■ AUTHOR INFORMATION

Corresponding Author

Hanna Tiainen − *Department of Biomaterials, Institute of Clinical Dentistry, University of Oslo, Oslo 0317, Norway;* orcid.org/0000-0003-2757-6213; Email: hanna.tiainen@odont.uio.no

Authors

Florian Weber − *Department of Biomaterials, Institute of Clinical Dentistry, University of Oslo, Oslo 0317, Norway*

Einar Sagstuen − *Department of Physics, University of Oslo, Oslo 0317, Norway;* orcid.org/0000-0003-4261-1398

Qi-Zhi Zhong − *Centre of Excellence in Convergent Bio-Nano Science and Technology, Department of Chemical Engineering, The University of Melbourne, Melbourne 3010, Australia*

Tian Zheng − *Materials Characterisation and Fabrication Platform, Department of Chemical Engineering, The University of Melbourne, Melbourne 3010, Australia*

Complete contact information is available at: https://pubs.acs.org/10.1021/acsami.0c16946

Author Contributions

The manuscript was written by contributions of all authors. All authors have given approval to the final version of the manuscript.

Funding

This work was financially supported by the Research Council of Norway (Grant No. 302590), UiO Life Science, and through the Norwegian NMR Package in 1994 for the Department of Chemistry and the Faculty of Mathematics and Natural Sciences at the University of Oslo.

Notes

The authors declare no competing financial interest.

■ ACKNOWLEDGMENTS

We kindly acknowledge the help from Frode Rise (University of Oslo) with NMR measurements and related discussions, Hellen Collins (University of Adelaide), Jelle Lahnstein (University of Adelaide), and Helle Wangensteen (University of Oslo) for support with LC-MS experiments.

■ ABBREVIATIONS

TA, tannic acid; PG, pyrogallol; GA, gallic acid; EA, ellagic acid; PGG, penta-galloyl glucose; Si_{aq}, silicic acid dissolved in water; MPN, metal-phenolic network; HFC, hyperfine coupling

■ REFERENCES

(1) Sileika, T. S.; Barrett, D. G.; Zhang, R.; Lau, K. H. A.; Messersmith, P. B. Colorless Multifunctional Coatings Inspired by Polyphenols Found in Tea, Chocolate, and Wine. *Angew. Chem., Int. Ed.* **2013**, *52* (41), 10766−10770.

(2) Ejima, H.; Richardson, J. J.; Caruso, F. Metal-Phenolic Networks as a Versatile Platform to Engineer Nanomaterials and Biointerfaces. *Nano Today* **2017**, *12*, 136−148.

(3) Ryu, J. H.; Messersmith, P. B.; Lee, H. Polydopamine Surface Chemistry: A Decade of Discovery. *ACS Appl. Mater. Interfaces* **2018**, *10* (9), 7523−7540.

(4) Guo, J.; Suma, T.; Richardson, J. J.; Ejima, H. Modular Assembly of Biomaterials Using Polyphenols as Building Blocks. *ACS Biomater. Sci. Eng.* **2019**, *5* (11), 5578−5596.

(5) Lee, H. A.; Ma, Y.; Zhou, F.; Hong, S.; Lee, H. Material-Independent Surface Chemistry Beyond Polydopamine Coating. *Acc. Chem. Res.* **2019**, *52* (3), 704−713.

(6) Quideau, S.; Deffieux, D.; Douat-Casassus, C.; Pouységu, L. Plant Polyphenols: Chemical Properties, Biological Activities, and Synthesis. *Angew. Chem., Int. Ed.* **2011**, *50* (3), 586−621.

(7) Chen, Y.; Liu, Q. Oxidant-Induced Plant Phenol Surface Chemistry for Multifunctional Coatings: Mechanism and Potential Applications. *J. Membr. Sci.* **2019**, *570-571*, 176−183.

(8) Yang, S.; Xu, Y.; Lin, Q.; Bai, Y.; Zan, X.; Ye, Q. A Bio-Inspired, One-Step but Versatile Coating onto Various Substrates with Strong Antibacterial and Enhanced Osteogenesis. *Chem. Commun.* **2019**, *55* (14), 2058−2061.

(9) Zhao, X.; Zhang, R.; Liu, Y.; He, M.; Su, Y.; Gao, C.; Jiang, Z. Antifouling Membrane Surface Construction: Chemistry Plays a Critical Role. *J. Membr. Sci.* **2018**, *551*, 145−171.

(10) Li, X.; Gao, P.; Tan, J.; Xiong, K.; Maitz, M. F.; Pan, C.; Wu, H.; Chen, Y.; Yang, Z.; Huang, N. Assembly of Metal−Phenolic/Catecholamine Networks for Synergistically Anti-Inflammatory, Antimicrobial, and Anticoagulant Coatings. *ACS Appl. Mater. Interfaces* **2018**, *10* (47), 40844−40853.

(11) Hong, S.; Wang, Y.; Park, S. Y.; Lee, H. Progressive Fuzzy Cation-Π Assembly of Biological Catecholamines. *Sci. Adv.* **2018**, *4* (9), eaat7457.

(12) Barrett, D. G.; Sileika, T. S.; Messersmith, P. B. Molecular Diversity in Phenolic and Polyphenolic Precursors of Tannin-Inspired Nanocoatings. *Chem. Commun.* **2014**, *50* (55), 7265−7268.

(13) Rahim, M. A.; Ejima, H.; Cho, K. L.; Kempe, K.; Müllner, M.; Best, J. P.; Caruso, F. Coordination-Driven Multistep Assembly of Metal−Polyphenol Films and Capsules. *Chem. Mater.* **2014**, *26* (4), 1645−1653.

(14) Liebscher, J. Chemistry of Polydopamine − Scope, Variation, and Limitation. *Eur. J. Org. Chem.* **2019**, *2019*, 4976−4984.

(15) Marklund, S.; Marklund, G. Involvement of the Superoxide Anion Radical in the Autoxidation of Pyrogallol and a Convenient

Assay for Superoxide Dismutase. *Eur. J. Biochem.* **1974**, *47* (3), 469−474.
(16) Zeng, L.; Ma, M.; Li, C.; Luo, L. Stability of Tea Polyphenols Solution with Different Ph at Different Temperatures. *Int. J. Food Prop.* **2017**, *20* (1), 1−18.
(17) Weber, F.; Liao, W.-C.; Barrantes, A.; Edén, M.; Tiainen, H. Silicate-Phenolic Networks: Coordination Mediated Deposition of Bioinspired Tannic Acid Coatings. *Chem. - Eur. J.* **2019**, *25*, 9870−9874.
(18) Saiz-Poseu, J.; Mancebo-Aracil, J.; Nador, F.; Busque, F.; Ruiz-Molina, D. The Chemistry Behind Catechol-Based Adhesion. *Angew. Chem., Int. Ed.* **2019**, *58* (3), 696−714.
(19) Ejima, H.; Richardson, J. J.; Liang, K.; Best, J. P.; van Koeverden, M. P.; Such, G. K.; Cui, J.; Caruso, F. One-Step Assembly of Coordination Complexes for Versatile Film and Particle Engineering. *Science* **2013**, *341* (6142), 154−157.
(20) Slabbert, N. Complexation of Condensed Tannins with Metal Ions. In *Plant Polyphenols*; Springer: Berlin, 1992; pp 421−436.
(21) Geißler, S.; Barrantes, A.; Tengvall, P.; Messersmith, P. B.; Tiainen, H. Deposition Kinetics of Bioinspired Phenolic Coatings on Titanium Surfaces. *Langmuir* **2016**, *32* (32), 8050−8060.
(22) Weber, F.; Barrantes, A.; Tiainen, H. Silicic Acid Mediated Formation of Tannic Acid Nanocoatings. *Langmuir* **2019**, *35* (9), 3327−3336.
(23) Guo, J.; Richardson, J. J.; Besford, Q. A.; Christofferson, A. J.; Dai, Y.; Ong, C. W.; Tardy, B. L.; Liang, K.; Choi, G. H.; Cui, J.; Yoo, P. J.; Yarovsky, I.; Caruso, F. Influence of Ionic Strength on the Deposition of Metal−Phenolic Networks. *Langmuir* **2017**, *33* (40), 10616−10622.
(24) Park, T.; Kim, W. I.; Kim, B. J.; Lee, H.; Choi, I. S.; Park, J. H.; Cho, W. K. Salt-Induced, Continuous Deposition of Supramolecular Iron(Iii)−Tannic Acid Complex. *Langmuir* **2018**, *34* (41), 12318−12323.
(25) Kumpf, R.; Dougherty, D. A Mechanism for Ion Selectivity in Potassium Channels: Computational Studies of Cation-Pi Interactions. *Science* **1993**, *261* (5129), 1708−1710.
(26) Park, S.; Kim, S.; Jho, Y.; Hwang, D. S. Cation−Π Interactions and Their Contribution to Mussel Underwater Adhesion Studied Using a Surface Forces Apparatus: A Mini-Review. *Langmuir* **2019**, *35* (48), 16002−16012.
(27) Lu, Q.; Oh, D. X.; Lee, Y.; Jho, Y.; Hwang, D. S.; Zeng, H. Nanomechanics of Cation−Π Interactions in Aqueous Solution. *Angew. Chem., Int. Ed.* **2013**, *52* (14), 3944−3948.
(28) Zhang, J.; Xiang, L.; Yan, B.; Zeng, H. Nanomechanics of Anion−Π Interaction in Aqueous Solution. *J. Am. Chem. Soc.* **2020**, *142* (4), 1710−1714.
(29) Tóth, I. Y.; Szekeres, M.; Turcu, R.; Sáringer, S.; Illés, E.; Nesztor, D.; Tombácz, E. Mechanism of in Situ Surface Polymerization of Gallic Acid in an Environmental-Inspired Preparation of Carboxylated Core−Shell Magnetite Nanoparticles. *Langmuir* **2014**, *30* (51), 15451−15461.
(30) Tollin, G.; Steelink, C. Biological Polymers Related to Catechol: Electron Paramagnetic Resonance and Infrared Studies of Melanin, Tannin, Lignin, Humic Acid and Hydroxyquinones. *Biochim. Biophys. Acta, Biophys. Incl. Photosynth.* **1966**, *112* (2), 377−379.
(31) Severino, J. F.; Goodman, B. A.; Kay, C. W. M.; Stolze, K.; Tunega, D.; Reichenauer, T. G.; Pirker, K. F. Free Radicals Generated During Oxidation of Green Tea Polyphenols: Electron Paramagnetic Resonance Spectroscopy Combined with Density Functional Theory Calculations. *Free Radical Biol. Med.* **2009**, *46* (8), 1076−1088.
(32) Bors, W.; Michel, C.; Stettmaier, K. Electron Paramagnetic Resonance Studies of Radical Species of Proanthocyanidins and Gallate Esters. *Arch. Biochem. Biophys.* **2000**, *374* (2), 347−355.
(33) Kalyanaraman, B. Characterization of O-Semiquinone Radicals in Biological Systems. In *Methods in Enzymology*; Academic Press: New York, 1990; Vol. *186*, pp 333−343.
(34) Alegría, A. E.; Sanchez-Cruz, P.; Rivas, L. Alkaline-Earth Cations Enhance Ortho-Quinone-Catalyzed Ascorbate Oxidation. *Free Radical Biol. Med.* **2004**, *37* (10), 1631−1639.
(35) Coradin, T.; Eglin, D.; Livage, J. The Silicomolybdic Acid Spectrophotometric Method and Its Application to Silicate/Biopolymer Interaction Studies. *Spectroscopy* **2004**, *18* (4), 567−576.
(36) Goher, M. E.; Hassan, A. M.; Abdel-Moniem, I. A.; Fahmy, A. H.; Abdo, M. H.; El-sayed, S. M. Removal of Aluminum, Iron and Manganese Ions from Industrial Wastes Using Granular Activated Carbon and Amberlite Ir-120h. *Egypt. J. Aquat. Res.* **2015**, *41* (2), 155−164.
(37) Huang, S.-P.; Li, W.; Franz, K. J.; Albright, R. L.; Fish, R. H. Polymer Pendant Ligand Chemistry. 3. A Biomimetic Approach to Selective Metal Ion Removal and Recovery from Aqueous Solution with Polymer-Supported Sulfonated Catechol and Linear Catechol Amide Ligands. *Inorg. Chem.* **1995**, *34* (11), 2813−2819.
(38) Reddy, A. S.; Sastry, G. N. Cation [M = H^+, Li^+, Na^+, K^+, Ca^{2+}, Mg^{2+}, Nh^{4+}, and Nme^{4+}] Interactions with the Aromatic Motifs of Naturally Occurring Amino Acids: A Theoretical Study. *J. Phys. Chem. A* **2005**, *109* (39), 8893−8903.
(39) Ikeda, T.; Boero, M.; Terakura, K. Hydration of Alkali Ions from First Principles Molecular Dynamics Revisited. *J. Chem. Phys.* **2007**, *126* (3), 034501.
(40) Remko, M.; Rode, B. M. Effect of Metal Ions (Li^+, Na^+, K^+, Mg^{2+}, Ca^{2+}, Ni^{2+}, Cu^{2+}, and Zn^{2+}) and Water Coordination on the Structure of Glycine and Zwitterionic Glycine. *J. Phys. Chem. A* **2006**, *110* (5), 1960−1967.
(41) Flint, N. J.; Tabner, B. J. Linewidth Alternation, as a Result of Intramolecular Cation Migration, in the Electron Spin Resonance Spectrum of the 1,4-Naphthoquinone Radical Anion. *J. Chem. Soc., Faraday Trans. 1* **1987**, *83* (1), 167−176.
(42) Zhang, G.; Yang, Y.; Zhang, T.; Xu, D.; Lei, Z.; Wang, C.; Liu, G.; Deng, Y. Fe^{iii} Chelated Organic Anode with Ultrahigh Rate Performance and Ultra-Long Cycling Stability for Lithium-Ion Batteries. *Energy Storage Mater.* **2020**, *24*, 432−438.
(43) Đorović, J.; Marković, J. M. D.; Stepanić, V.; Begović, N.; Amić, D.; Marković, Z. Influence of Different Free Radicals on Scavenging Potency of Gallic Acid. *J. Mol. Model.* **2014**, *20* (7), 2345.
(44) Chen, Y.; Xiao, H.; Zheng, J.; Liang, G. Structure-Thermodynamics-Antioxidant Activity Relationships of Selected Natural Phenolic Acids and Derivatives: An Experimental and Theoretical Evaluation. *PLoS One* **2015**, *10* (3), e0121276−e0121276.
(45) Eslami, A. C.; Pasanphan, W.; Wagner, B. A.; Buettner, G. R. Free Radicals Produced by the Oxidation of Gallic Acid: An Electron Paramagnetic Resonance Study. *Chem. Cent. J.* **2010**, *4*, 15.
(46) Janošević, A.; Ćirić-Marjanović, G.; Šljukić Paunković, B.; Pašti, I.; Trifunović, S.; Marjanović, B.; Stejskal, J. Simultaneous Oxidation of Aniline and Tannic Acid with Peroxydisulfate: Self-Assembly of Oxidation Products from Nanorods to Microspheres. *Synth. Met.* **2012**, *162* (9), 843−856.
(47) Scott, A. I. Oxidative Coupling of Phenolic Compounds. *Q. Rev., Chem. Soc.* **1965**, *19* (1), 1−35.
(48) Yoshida, T.; Yoshimura, M.; Amakura, Y. Chemical and Biological Significance of Oenothein B and Related Ellagitannin Oligomers with Macrocyclic Structure. *Molecules* **2018**, *23* (3), 552.
(49) Marković, Z.; Milenković, D.; Đorović, J.; Dimitrić Marković, J. M.; Lučić, B.; Amić, D. A Dft and Pm6 Study of Free Radical Scavenging Activity of Ellagic Acid. *Monatsh. Chem.* **2013**, *144* (6), 803−812.
(50) Dixon, W. T.; Kok, P. M.; Murphy, D. Calculations of G-Factors of Phenoxyl Radicals, Phenol Radical Cations and Alkyl Aryl Ether Radical Cations. *J. Chem. Soc., Faraday Trans. 2* **1978**, *74* (0), 1528−1531.
(51) Spiegel, M.; Andruniów, T.; Sroka, Z. Flavones' and Flavonols' Antiradical Structure−Activity Relationship—a Quantum Chemical Study. *Antioxidants* **2020**, *9* (6), 461.
(52) Felix, C. C.; Sealy, R. C. O-Benzosemiquinone and Its Metal Chelates. Electron Spin Resonance Investigation of Radicals from the Photolysis of Catechol in the Presence of Complexing Metal Ions. *J. Am. Chem. Soc.* **1982**, *104* (6), 1555−1560.

https://dx.doi.org/10.1021/acsami.0c16946
ACS Appl. Mater. Interfaces 2020, 12, 52457−52466

(53) Liu, B.; Burdine, L.; Kodadek, T. Chemistry of Periodate-Mediated Cross-Linking of 3,4-Dihydroxylphenylalanine-Containing Molecules to Proteins. *J. Am. Chem. Soc.* **2006**, *128* (47), 15228−15235.
(54) Weidman, S. W.; Kaiser, E. T. The Mechanism of the Periodate Oxidation of Aromatic Systems. Iii. A Kinetic Study of the Periodate Oxidation of Catechol. *J. Am. Chem. Soc.* **1966**, *88* (24), 5820−5827.
(55) Malinda, K.; Sutanto, H.; Darmawan, A. Characterization and Antioxidant Activity of Gallic Acid Derivative. *AIP Conf. Proc.* **2017**, *1904* (1), 020030.
(56) Lucken, E. A. C. 814. Ion-Association and Specific Solvation in the Electron Spin Resonance Spectra of Semiquinones. *J. Chem. Soc.* **1964**, 4234−4240.
(57) Ou, R.; Wei, J.; Zhao, C.; Gu, Q.; Zhu, H.; Li, X.; Nguyen, N. S.; Wan, L.; Forsyth, M.; Wang, H. Monovalent Cation-Phenolic Crystals with Ph Reversible Crystal Transformation. *Chem. - Eur. J.* **2019**, *25*, 12281−12287.
(58) Simić, A. Z.; Verbić, T. Ž.; Sentić, M. N.; Vojić, M. P.; Juranić, I. O.; Manojlović, D. D. Study of Ellagic Acid Electro-Oxidation Mechanism. *Monatsh. Chem.* **2013**, *144* (2), 121−128.
(59) Kotorlenko, L. A.; Aleksandrova, V. S. Spectral Manifestations of Change in Electronic Structure in Phenol-Phenolate Anion-Phenoxy Radical Series. *Theor. Exp. Chem.* **1982**, *18* (1), 97−99.
(60) Díaz Hidalgo, R. J.; Córdoba, R.; Nabais, P.; Silva, V.; Melo, M. J.; Pina, F.; Teixeira, N.; Freitas, V. New Insights into Iron-Gall Inks through the Use of Historically Accurate Reconstructions. *Heritage Sci.* **2018**, *6* (1), 63.
(61) Brunet, F.; Cabane, B.; Dubois, M.; Perly, B. Sol-Gel Polymerization Studied through Silicon-29 Nmr with Polarization Transfer. *J. Phys. Chem.* **1991**, *95* (2), 945−951.
(62) McCormick, A. V.; Bell, A. T.; Radke, C. J. Evidence from Alkali-Metal Nmr Spectroscopy for Ion Pairing in Alkaline Silicate Solutions. *J. Phys. Chem.* **1989**, *93* (5), 1733−1737.
(63) McCormick, A. V.; Bell, A. T.; Radke, C. J. Influence of Alkali-Metal Cations on Silicon Exchange and Silicon-29 Spin Relaxation in Alkaline Silicate Solutions. *J. Phys. Chem.* **1989**, *93* (5), 1737−1741.

https://dx.doi.org/10.1021/acsami.0c16946
ACS Appl. Mater. Interfaces 2020, 12, 52457−52466

Supplementary Information

Tannic acid radicals in presence of alkali metal salts and their impact on the formation of silicate-phenolic networks

Florian Weber[1], Einar Sagstuen[2], Qi-Zhi Zhong[3], Tian Zheng[4], Hanna Tiainen[1*]

[1]Department of Biomaterials, Institute of Clinical Dentistry, University of Oslo, P.O. Box 1109, Blindern, 0317 Oslo, Norway

[2]Department of Physics, University of Oslo, Norway

[3]Centre of Excellence in Convergent Bio-Nano Science and Technology, Department of Chemical Engineering, The University of Melbourne, Australia

[4]Materials Characterisation and Fabrication Platform, Department of Chemical Engineering, The University of Melbourne, Australia

Table of Contents

Abbreviations 2

Supplementary Methodological Information 2

EPR modeling: 2

Supplementary Figures 3

pH of polyphenolic solutions 3

ATR-FTIR $LiCl{\cdot}H_2O$ background 4

Supplementary QCM-D data 5

Supplementary EPR figures 12

UV-vis absorption spectra 24

FTIR absorption spectra 27

^{13}C and ^{29}Si NMR spectra 30

Silico-molybdic assay 32

References 32

Abbreviations

Tannic acid (TA), penta-galloyl glucose (PGG), pyrogallol (PG), gallic acid (GA), ellagic acid (EA), aqueous sodium meta silicate (silicic acid, Si_{aq}).

Supplementary Methodological Information

EPR modeling:

Individual radicals of TA, GA, and PG were modeled from different datasets, which were normalized to a peak-to-peak amplitude of 2000 (Figure S9 & Figure S10). TA radical spectra were aligned to the radical field position of the ♦ radical species. The set of four different radicals R1 (♦), R2 (◊), R3 (•), and R4 (O) was then verified with the experimental data of TA under high O_2 uptake directly after shaking (Figure S18B, 0 min), which showed peaks of all four radical species. All simulations were performed on a computer equipped with a 64 bit Intel 4-core processor with the software WinSim (V. 1.0, 2002)[a] running under Windows 7.[1] Estimated uncertainties of g-values were ≤ 0.0001, hyperfine coupling (a^H) ≤ 0.002 mT. The signs of the hyperfine couplings may be positive or negative, but can not be inferred directly from the experimental spectra. Thus, only the absolute values are presented in the Tables.

Ratios of the TA radicals ♦ and ◊, given in Figure 3A and 3B, were obtained by modeling the individual radicals for each experimental dataset. For the decay rates given in Figure 3C – 3E, double integration of the raw data peaks at 351.4 mT was performed instead. We compared this semi-quantitative method to the full modeling approach for the data and concluded that the estimation via the experimental peak area resulted in sufficient data quality. Note that the overlap of the peaks in the raw data however does not allow for absolute quantification.

[a] retrieved from https://www.niehs.nih.gov/research/resources/software/tox-pharm/tools/index.cfm on March 19th, 2019.

Supplementary Figures

pH of polyphenolic solutions

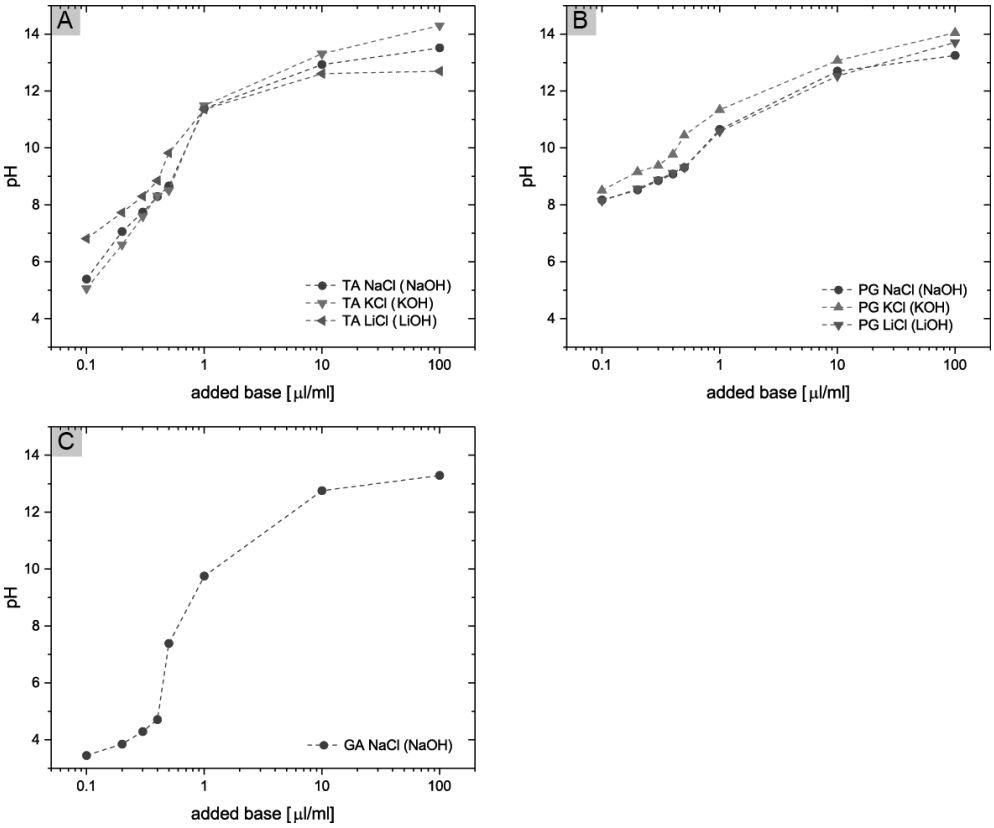

Figure S1: (A) Sequential increase of pH with the addition of defined volumes of 10 M NaOH, KOH, or LiOH to 1 mg/ml tannic acid, (B) pyrogallol, or (C) gallic acid solutions. All solutions contained 600 mM of the respective alkali metal chloride. Note that the LiOH concentration was 1 M due to its solubility limit but corrected by the volume. For simplification, 10 M notation is used throughout the ESI.

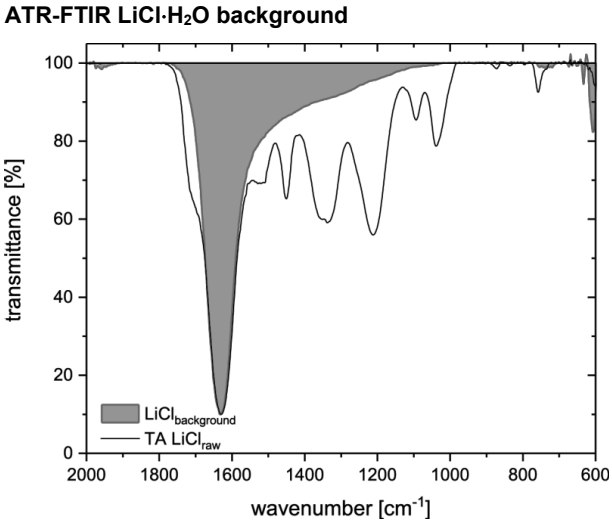

Figure S2: FTIR measurements of dried liquid droplets on an ATR crystal. For LiCl, we subtracted a LiCl·H_2O background (pink) from the TA sample spectrum.

Supplementary QCM-D data

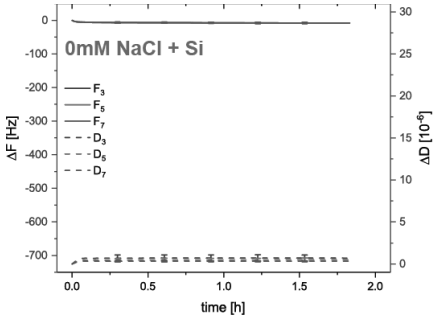

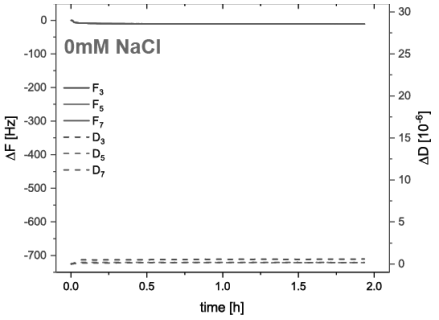

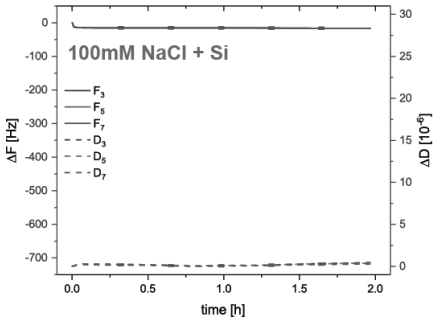

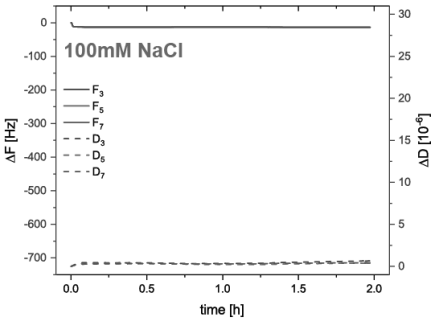

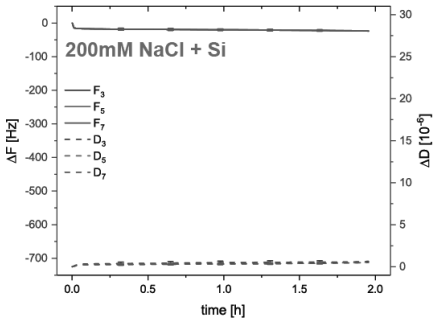

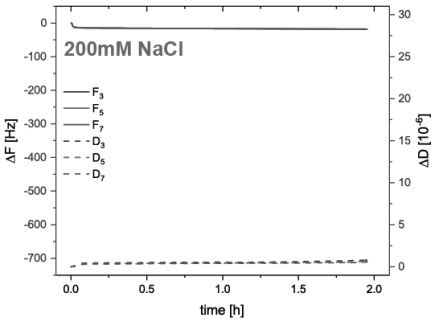

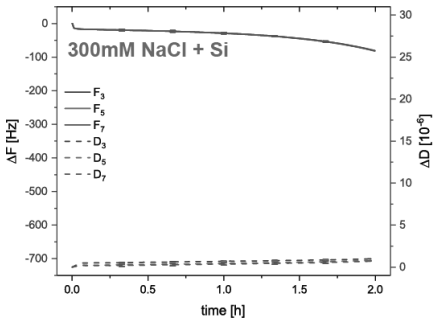

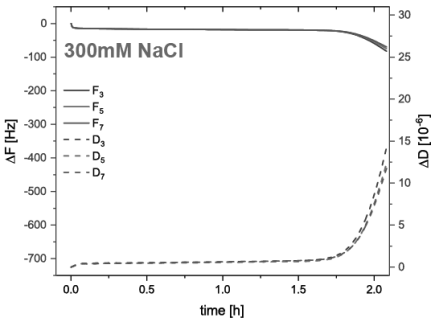

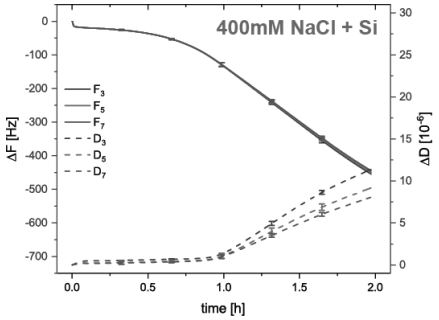
400mM NaCl + Si
ΔF [Hz]
ΔD [10⁻⁶]
time [h]
F3
F5
F7
D3
D5
D7

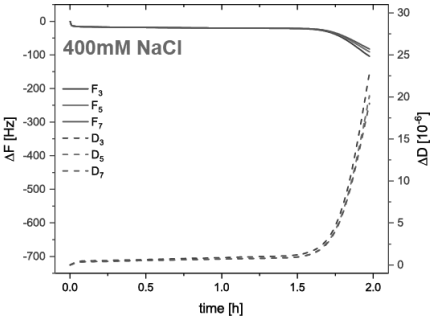
400mM NaCl
ΔF [Hz]
ΔD [10⁻⁶]
time [h]
F3
F5
F7
D3
D5
D7

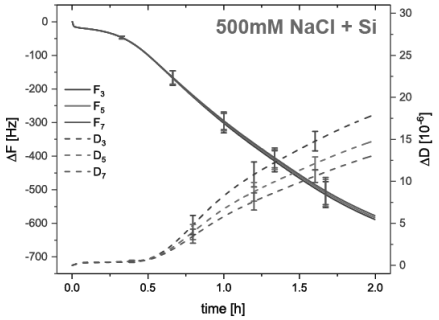
500mM NaCl + Si
ΔF [Hz]
ΔD [10⁻⁶]
time [h]
F3
F5
F7
D3
D5
D7

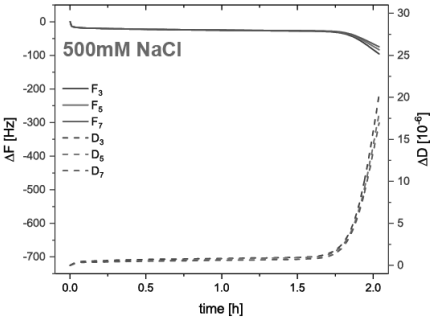
500mM NaCl
ΔF [Hz]
ΔD [10⁻⁶]
time [h]
F3
F5
F7
D3
D5
D7

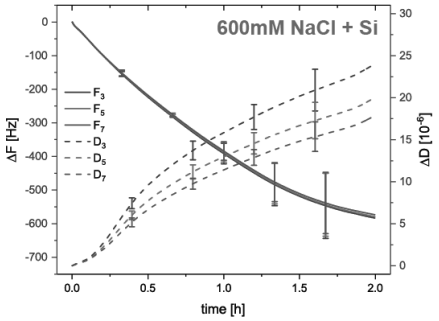
600mM NaCl + Si
ΔF [Hz]
ΔD [10⁻⁶]
time [h]
F3
F5
F7
D3
D5
D7

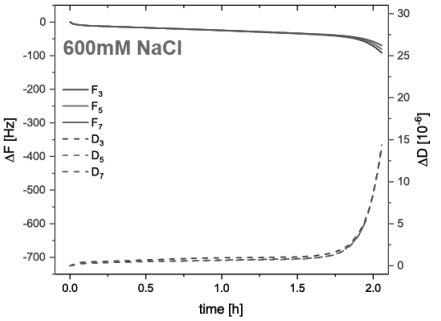
600mM NaCl
ΔF [Hz]
ΔD [10⁻⁶]
time [h]
F3
F5
F7
D3
D5
D7

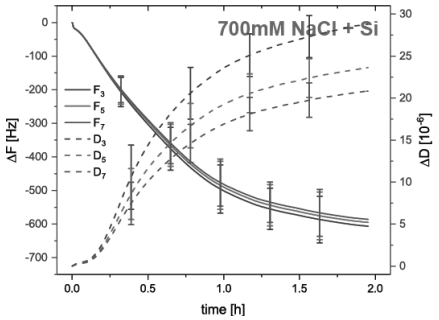
700mM NaCl + Si
ΔF [Hz]
ΔD [10⁻⁶]
time [h]
F3
F5
F7
D3
D5
D7

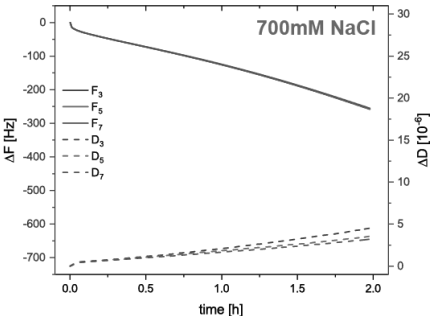
700mM NaCl
ΔF [Hz]
ΔD [10⁻⁶]
time [h]
F3
F5
F7
D3
D5
D7

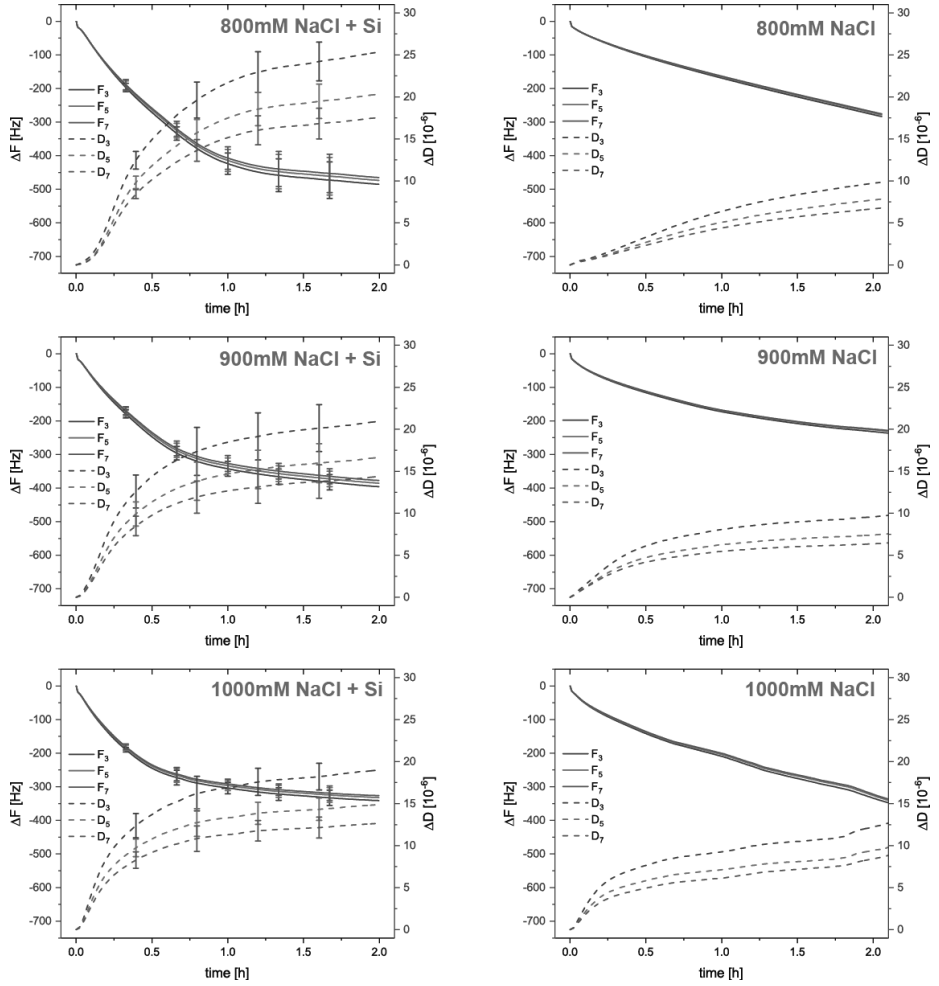

Figure S3: QCM-D raw data for the NaCl dependent coating formation of TA. Presented are averaged (n = 3) changes in frequency (ΔF) and dissipation (ΔD) for the 3rd, 5th, and 7th, harmonic overtone. TA was dissolved in water at 1 mg/ml at given ionic strengths compared to HEPES buffer during other QCM-D experiments. This decision was made to correlate effects with experiments at pH exceeding the buffer capacity of HEPES. The pH was adjusted to pH = 8 with 0.3 µl/ml 10 M NaOH and solutions were supplemented with 80 µM Si_{aq}. Control measurements were conducted without the addition of Si_{aq}. Error bars denote standard deviations. Note that the drift in control experiments for experiments containing ≥ 700 M NaCl is not caused by a stable layer formation but is rather an effect of particles since flushing with buffer caused an instant return of the signal to the baseline. Analysis of the data in Figure 1A of the manuscript was performed at the 1 h mark to avoid any influence of the particle formation, which causes splitting overtones and a leap in dissipation.

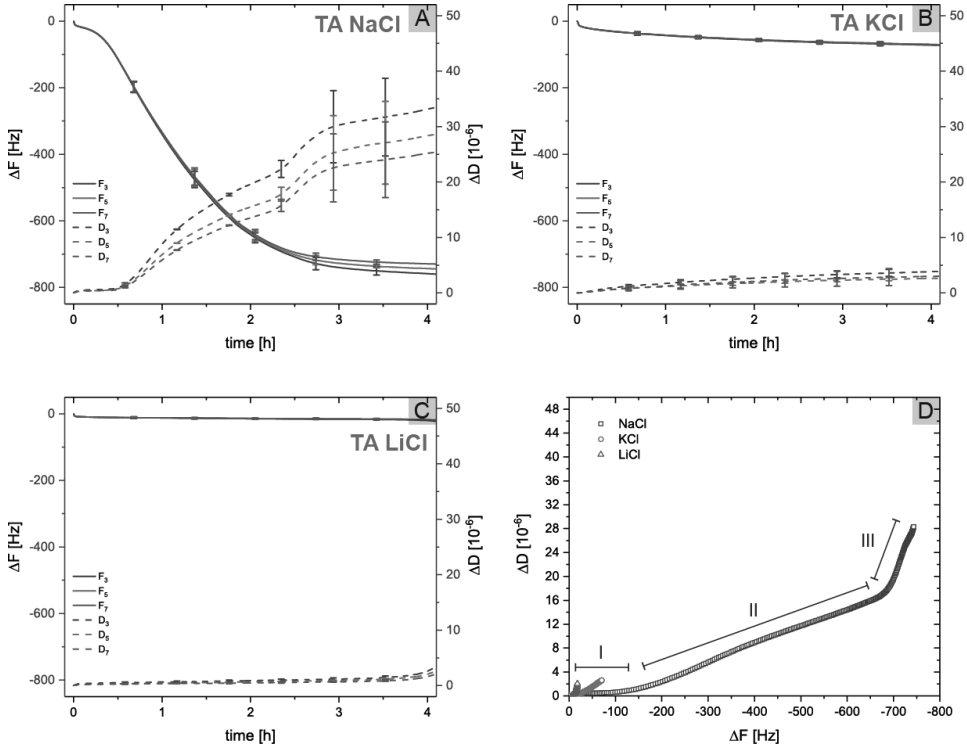

Figure S4: QCM-D raw data of the continuous layer formation of tannic acid (TA) in HEPES buffered solutions at pH = 7.8 with different alkali metal salts. The concentration of (A) NaCl, (B) KCl, and (C) LiCl was 600 mM and the pH was adjusted with NaOH, KOH, and LiOH respectively. Plots show the average change of frequency (ΔF) and dissipation (ΔD) from three individual experiments (n = 3) with error bars denoting standard deviations. (D) Plots of $\Delta F/\Delta D$ for the 5th harmonic show distinct three phases (I, II, and III) of TA adsorption in NaCl compared to KCl and LiCl. In phase I rapid adsorption is forming a ridig layer. Phase II is characterised by a continous build-up with increasing dissipation. In the last phase, the deposition of TA comes to an end and the process is governed by loose binding of reacted polymers to the surface.

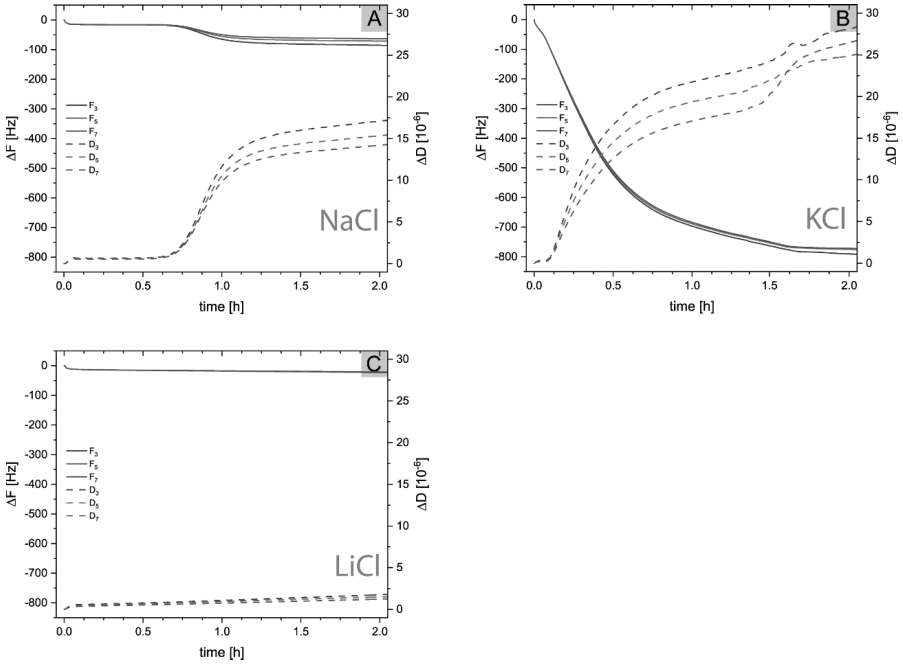

Figure S5: Coating formation of TA followed by QCM-D. (A) TA was dissolved in water containing 600 mM NaCl at pH = 9 using 0.5 µl/ml 10 M NaOH. Solutions turned immediately orange and particles could be observed after 40 min. (B) TA dissolved in 600 mM KCl solution at pH = 9 using 0.5 µl/ml 10 M KOH. Solutions stayed green in color but turned from an initially clear solution turbid after 15 min. (C) TA in 600 mM LiCl solution at pH = 9 using 0.5 µl/ml 10 M LiOH. The color appeared orange similar to NaCl solution. However, no particle formation was observed for 4 h of the experiment.

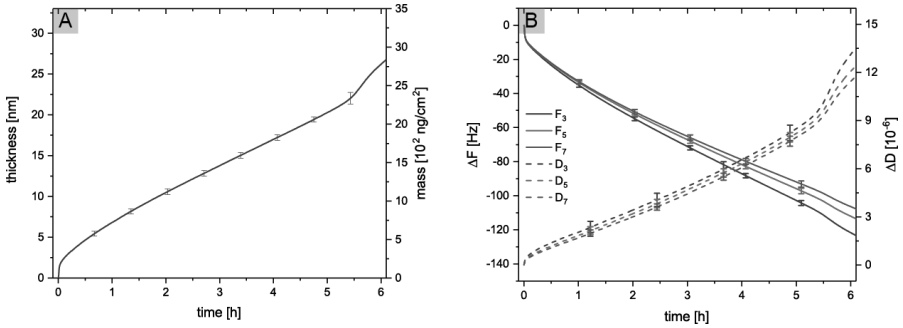

Figure S6: (A) Progression of the coating thickness of TA dissolved in HEPES at pH = 7.8 supplemented with 600 mM LiCl and 1 mM Si_{aq}. (B) The corresponding change in frequency (ΔF) and dissipation (ΔD) of panel A given as an average of three experiments (n = 3) for the 3rd, 5th, and 7th harmonic overtones. After 6 h an incline in dissipation and splitting in overtones indicated the overlaying effect of particle formation. 1 mM Si_{aq} was chosen as upper limit to prevent auto-condensation of silicic acid in slightly alkaline conditions (Figure S7). Error bars denote standard deviations.

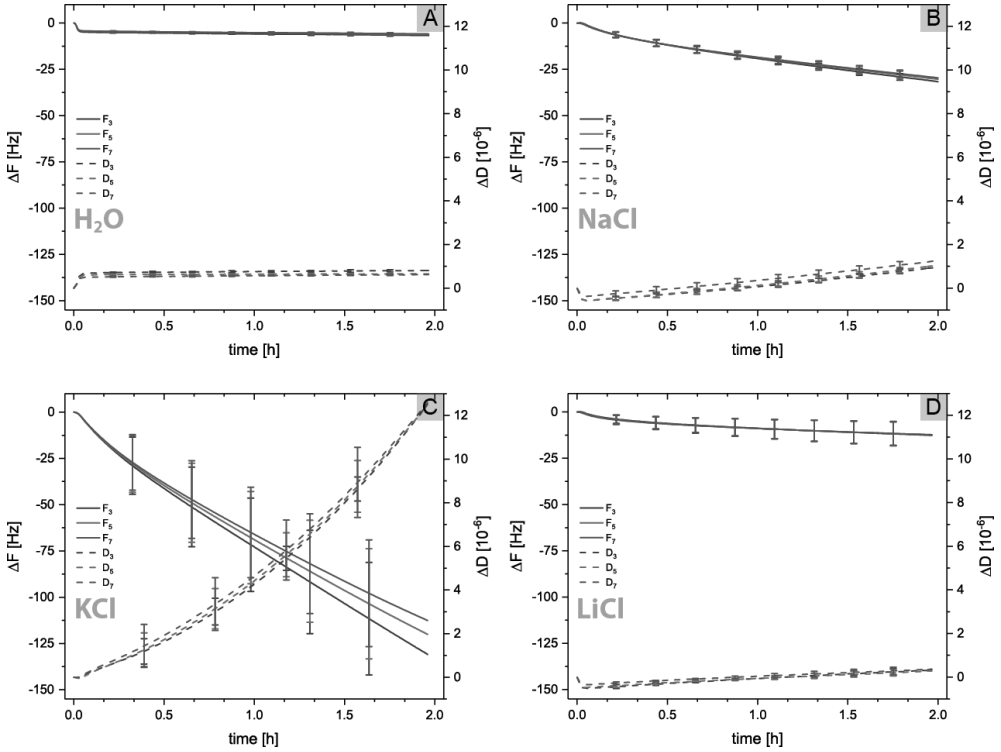

Figure S7: Reaction of 10 mM Si_{aq} in water and 100 mM HEPES at pH = 7.8 supplemented with 600 mM NaCl, KCl, LiCl. Graphs show the change in frequency (ΔF) and dissipation (ΔD) as average of three experiments (n = 3) for the 3rd, 5th, and 7th harmonic overtones. (A) Si_{aq} dissolved in water remains stable in solution with an average frequency shift of -6 ± 0.5 Hz related to changes in viscoelastic properties of the solution and adsorption to the Ti surface. (B) Si_{aq} in NaCl containing buffer solution displayed a slow continuous layer build-up. (C) Even more pronounced was the formation of either a SiO_2 layer in presence of KCl or a large change in the viscosity of the solution.[2] Both SiO_2 layers reaching -30 ± 2 Hz from NaCl and -120 ± 31 Hz from KCl solution had to be dissolved in alkaline condition for 1 h. Thus we expect that this behavior did not only result from changes in the bulk fluid. (D) In presence of LiCl the silica layer formation was strongly inhibited showing a decrease in frequency of -12 ± 7 Hz after 2 h. Error bars denote standard deviations.

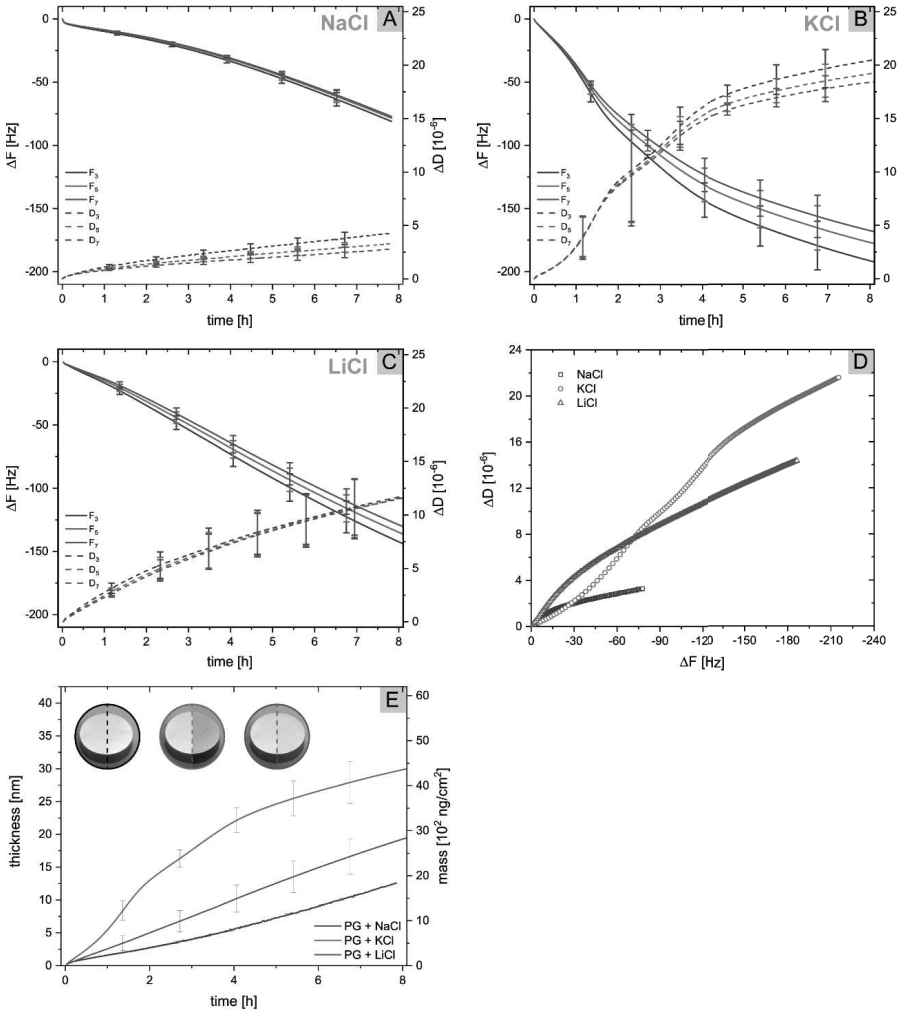

Figure S8: Progression of the change in frequency (Δ*F*) and dissipation (Δ*D*) as average of three experiments (n = 3) for the 3rd, 5th, and 7th harmonics monitored by QCM-D. (A) PG dissolved in HEPES at pH = 7.8 supplemented with 600 mM NaCl, (B) 600 mM KCl, (C) 600 mM LiCl. (D) Plot of dissipation vs frequency for the 5th harmonic representing the kinetics and layer characteristics of PG. The PG deposition process in KCl systems is subject to higher variance and larger particles were observed forming in the system in comparison to PG in NaCl and LiCl solution. Kinetically, the deposition of PG in LiCl and NaCl was similar but higher dissipation in LiCl indicates a less rigid layer, possibly due to a higher water content. In KCl solution, PG exhibits faster initial deposition kinetics, which led to a more rigid structure until the layer became more dissipative. (E) Progression of thickness and areal mass during the coating process of PG. Note that for calculation of the film thickness a fixed layer density was used and potential ion-dependent changes in layer density were not accounted for.[3, 4] The insets show coated Ti coins (right) versus Ti reference coins (left). Error bars denote standard deviations.

Supplementary EPR figures

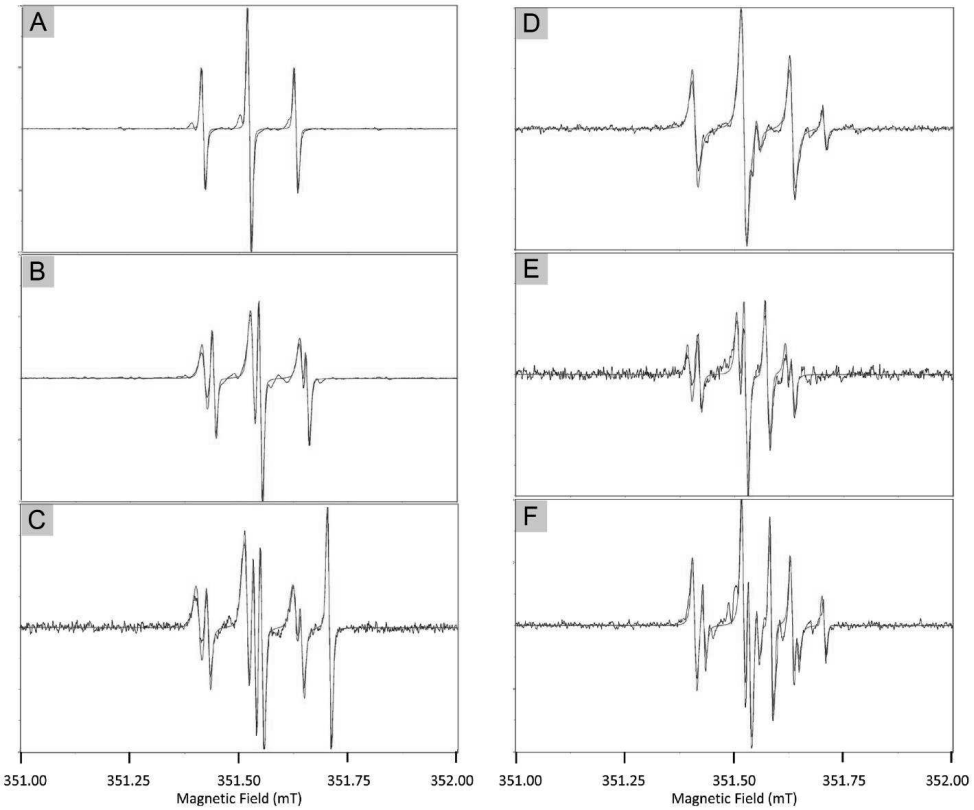

Figure S9: Experimental (black) and simulated (red) EPR spectra from various mixtures of single radical patterns. The magnetic field scale is common whereas the resonance frequencies in each panel were slightly different so that the same radical pattern in different panels are not aligned. (A) Radical R1, frequency ν = 9867.342 MHz, correlation factor CF = 0.9825. (B) Radical R1 (35%) and radical R2 (65%), ν = 9867.3339 MHz, CF = 0.9823. (C) Radical R1 (28%), radical R2 (50%) and radical R3 (22%), ν = 9867.333 MHz, CF = 0.9791. (D) Radical R2 (95%) and radical R3 (5%), ν = 9867.380 MHz, CF = 0.9793. (E) Radical R1 (30%), radical R2 (42%), and radical R4 (27%), ν = 9867.342 MHz, CF = 0.9304. (F) Radical R1 (20%), radical R2 (57%), radical R3 (6%), and radical R4 (17%), ν = 9867.407 MHz, CF = 0.9867. For detailed results and listing of all parameters, please refer to Table S1.

Table S1: Simulated TA radical parameters of Figure S8

Panel	Radical	Equiv. protons	a^{H} [mT]	LW [mT]	g	Weight [%]
A	R1	2	0.1068	0.0034	2.00556	100
B	R1	2	0.1074	0.0034	2.00541	35
	R2	2	0.117	0.0073	2.00551	65
C	R1	2	0.1073	0.0042	2.00548	28
	R2	2	0.1108	0.0083	2.00558	50
	R3	1	0.1537	0.0038	2.00481	22
D	R2	2	0.1113	0.0086	2.00558	95
	R3	1	0.1514	0.0038	2.00496	5
E	R1	2	0.1069	0.0034	2.0054	30
	R2	2	0.1121	0.0083	2.00564	42
	R4	1	0.0530	0.0049	2.00541	27
F	R1	2	0.1073	0.0042*	2.00548	20
	R2	2	0.1121	0.0046*	2.00558	57
	R3	1	0.1526	0.0031	2.00497	6
	R4	1	0.0522	0.0032	2.00537	17

*unusual linewidths likely caused by overlapping peaks in this particular spectrum

Figure S10: Experimental (black) and simulated (red) EPR spectra from various mixtures of single radical patterns. (A) GA radical R1 (17.5%) and radical R2 (82.5%), frequency ν = 9867.420 MHz, correlation factor CF = 0.9921. (B) PG radical R1 (100%), ν = 9867.434 MHz, CF = 0.9931. For detailed results and listing of all parameters, the reader is referred to Table S2.

Table S2: Parameters of modeled gallic acid (GA), pyrogallol (PG), ellagic acid (EA), and penta-galloyl glucose (PGG) radicals.

Radical	Equiv. protons	a^H [mT]	LW [mT]	g	Weight [%]
GA R1	2	0.107	0.0045	2.00560	82.5
GA R2	1	0.079	0.0043	2.00547	17.5
	1	0.030			
	1	0.015			
PG R1	2	0.0995	0.0041	2.0054	100
	1	0.5514			
EA R1	1	0.0509	0.0041	2.00536	100
PGG R1	2	0.1068	0.0038	2.00549	51
PGG R2	2	0.1105	0.0091	2.00557	59

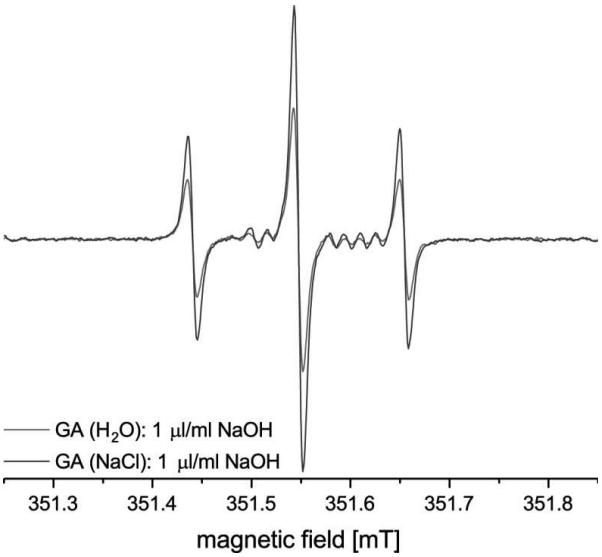

Figure S11: EPR spectrum of 1 mg/ml gallic acid dissolved in water or 600 mM NaCl solution and adjusted with 1 µl/ml 10 M NaOH (pH = 9). A 1:2:1 hyperfinesplitting of the major radical peaks originate from fully dissociated hydroxyl groups and the equal interaction of the unpaired electron of the O$^{\bullet}$ radical with each of the two protons of the benzene ring.[5] The weaker resonance is due to partially deprotonated gallic acid, which features three inequivalent protons (Scheme 1).[6]

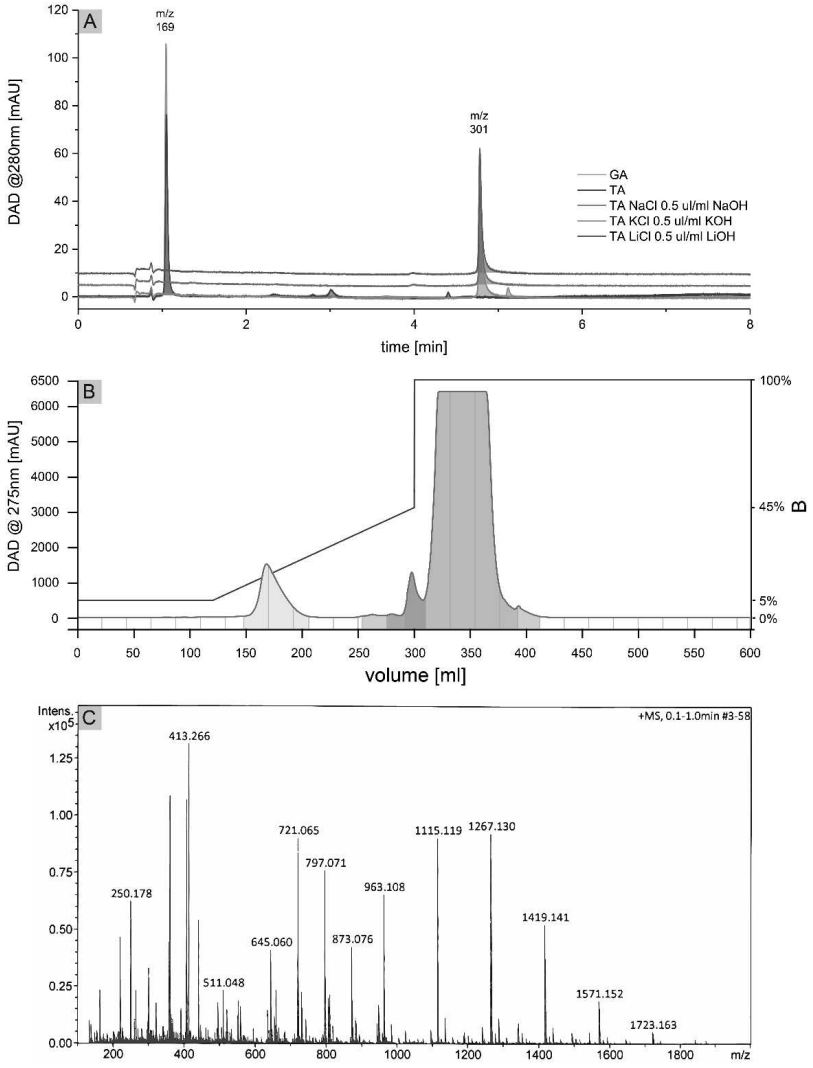

Figure S12: (A) LC-MS chromatogram (DAD 280 nm) of TA oxidized in 600 mM NaCl, KCl, and LiCl solution at pH = 11 after solid-phase extraction (SPE). Mass spectroscopy was performed on a triple quadrupole MS in MS2 mode. Pristine TA showed a high content of GA ($[M-H]^-$ = 169 m/z) in the chromatogram with its higher molecular weight compounds eluting after 8 min giving rise to a broad undefined peak. After the oxidation, a peak with a mass of 301 m/z ($[M-H]^-$) indicates the presence of ellagic acid. (B) Purification of commercial TA using water:formic acid (0.1 v/v) as solvent A and acetonitrile as solvent B at a flow rate of 50 ml/min. The TA fraction (green) eluting after approximately 6 min was collected for ESI-QTOF and EPR analysis. (C) Mass spectra showed masses up to 1723 m/z indicating the presence of unfragmented Na-adducts of TA.

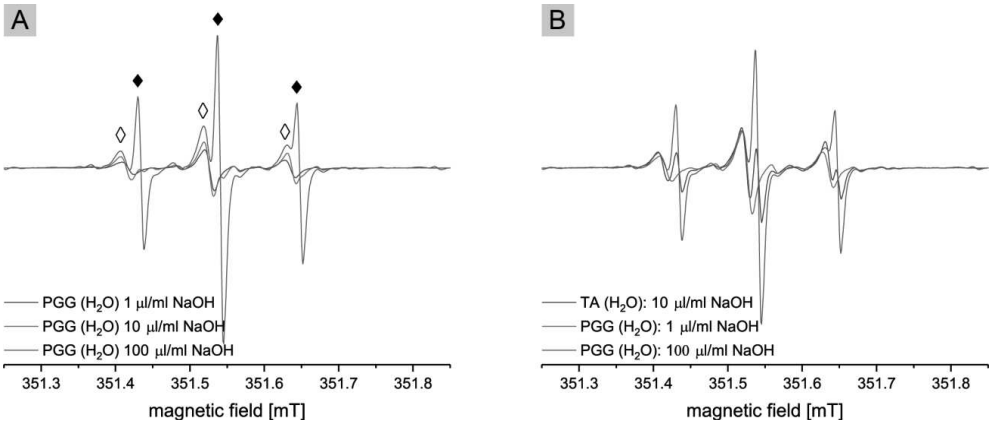

Figure S13: (A) EPR spectrum of 1 mg/ml penta-galloyl glucose (PGG) dissolved in water adjusted with given amounts of 10 M NaOH. The ◊-triplet with 1:2:1 hyperfinesplitting and hyperfine coupling constant $a^{H} = 0.111$ mT at low pH resembles the R2 radical of TA. Further details on the modeled radical can be found in Table S2. Once the pH is raised with NaOH, PGG spectra showed a transition of the R2 to an R1 radical (♦) with a coupling constant $a^{H} = 0.107$ mT. (B) TA spectrum overlayed with both states of PGG.

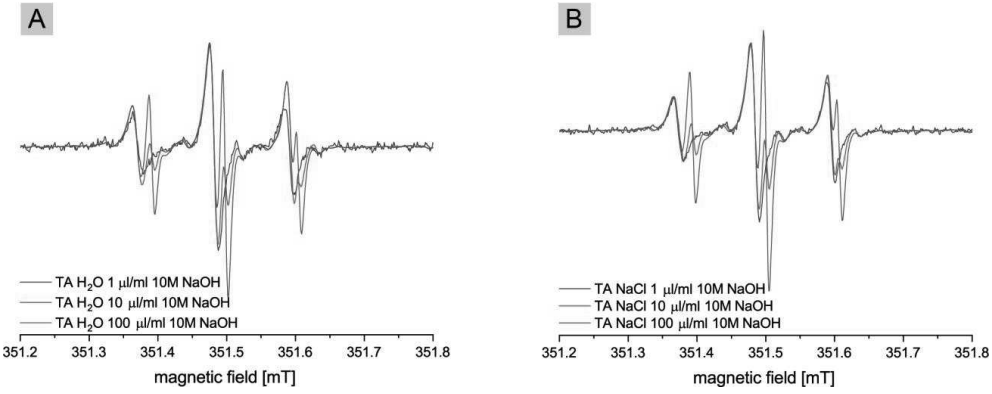

Figure S14: (A) EPR spectra of purified TA dissolved in water or (B) 600 mM NaCl solution adjusted with given amounts of 10 M NaOH. For improved visibility, peak amplitudes were normalized to the center peak of the R2 radical. At low pH = 9, a single triplet can be observed representing the R2 radical similarly to PGG. With increasing pH, the second R1 triplet emerges. This indicates the hydrolysis of galloyl ester bonds and the release of free gallic acid. Note that both PGG (Figure S13) and purified TA did not contain signs of the R3 (●) radical, which may indicate that R3 originates from an impurity in the commercial TA.

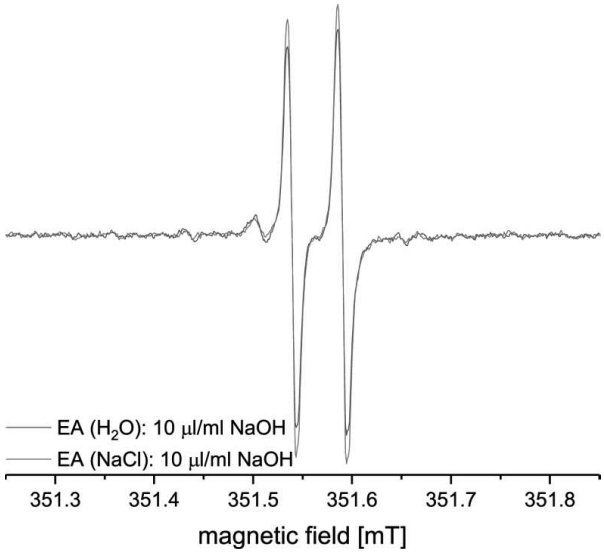

Figure S15: EPR spectrum of 1 mg/ml ellagic acid (EA) dissolved in water or 600 mM NaCl solution adjusted with 10 µl/ml 10 M NaOH. The doublet with 1:1 hyperfinesplitting originates from the single proton in the benzene ring structure. Details to the modeled radical can be found in Table S2. Due to the low hyperfine coupling constant a^{H} = 0.05 mT, the radical electron is likely located at the vicinal O atom.[7] The vicinal position has also been shown to be the most stable conformation provided by the greatest delocalization of the radical anion in water.[8]

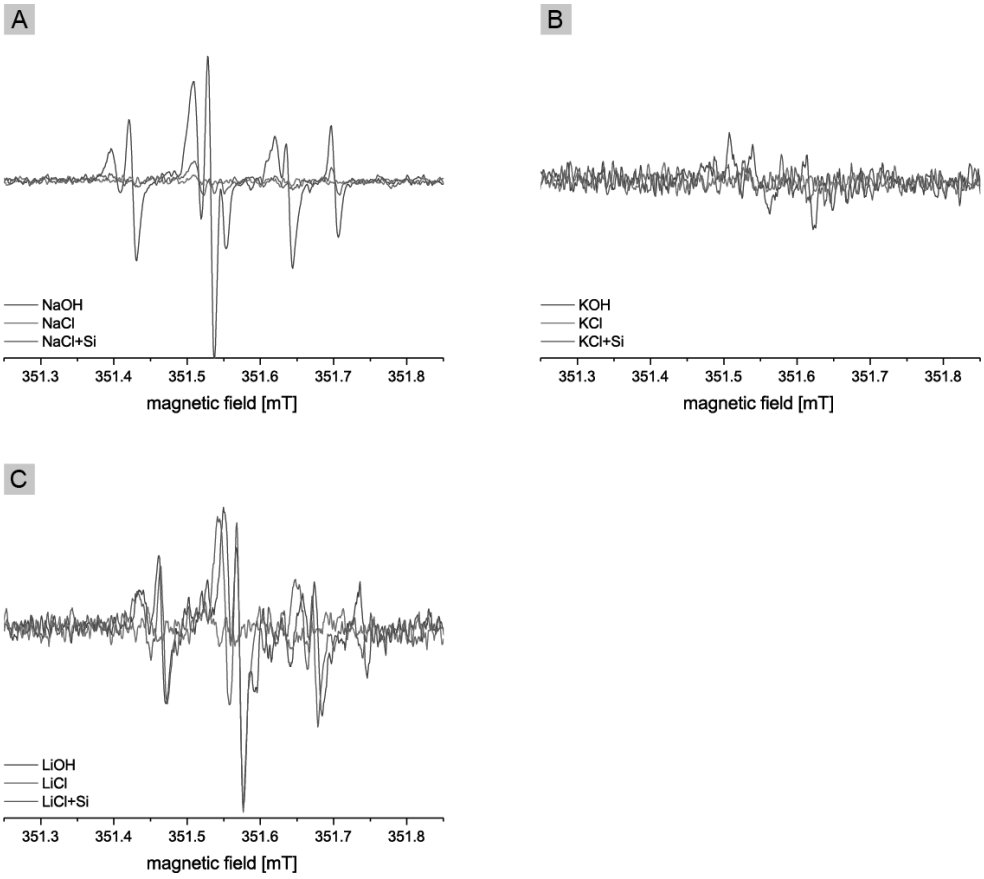

Figure S16: EPR spectra of 1 mg/ml tannic acid dissolved in water or 600 mM salt solution. (A) Na^+, (B) K^+, and (C) Li^+ containing solutions were adjusted with 0.5 µl/ml 10 M NaOH, KOH, LiOH, respectively. The pH of the solutions was approximately pH = 9 and Si_{aq} was supplemented at a concentration of 100 µM. Note that under the addition of silicic acid, the pH may slightly increase by 0.5 and that KCl systems at these pH conditions showed interactions of TA with K^+ resulting in turbid solutions. All spectra represent added sums of 4 scans with a time constant twice as long as for experiments with ≥ 1 µl/ml 10 M alkaline solution (163.8 ms).

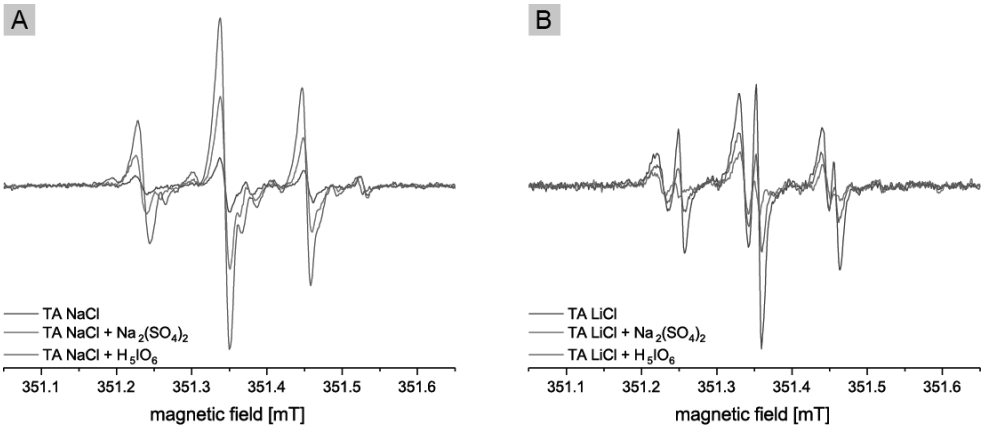

Figure S17: (A) Radical formation under influence of oxidants: 1 mg/ml tannic acid was dissolved in either 600 mM NaCl or (B) 600 mM LiCl solution adjusted to pH = 11 with 1 µl/ml 10 M NaOH, and LiOH, respectively. Although samples within each graph originate from the same solution, the absolute signal intensity is not an indication for the radical quantity but only considered as a trend. Note that all experiments were conducted at elevated pH since oxidants on their own did not form any detectable phenolic radicals (data not shown). Further, at high pH, persulfate radical anions may also react with hydroxyl anions to form persulfate anions and hydroxyl radicals, which would not directly show in the TA radical spectrum.[9]

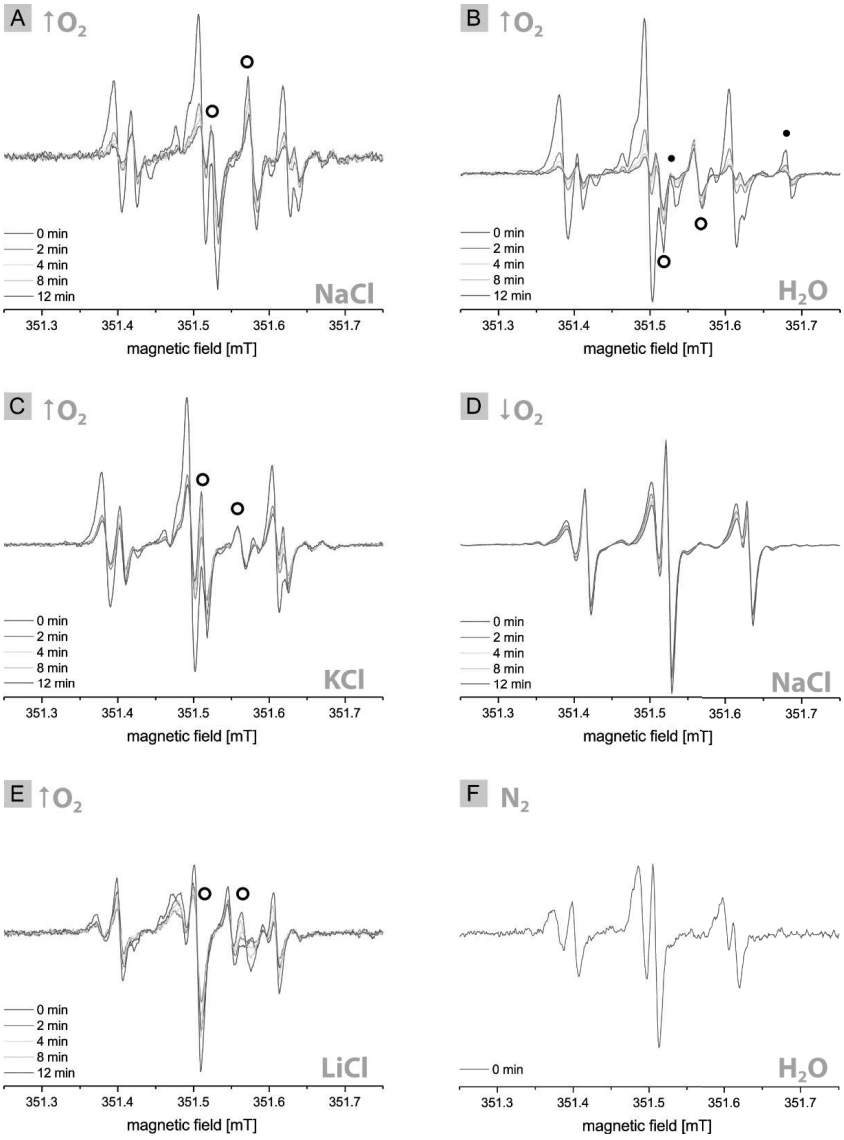

Figure S18: (A, D) EPR spectra of 1 mg/ml tannic acid dissolved in 600 mM NaCl, (B) water, (C) KCl, or (E) LiCl solution adjusted with 10 µl/ml 10 M NaOH, KOH, LiOH respectively. (A, B, C, E) Solutions were shaken vigorously for 60 s until they obtained a dark red color and analyzed immediately afterward. The transformation of the signal was then monitored for up to 12 min. (D) In comparison, under low oxygen uptake (short mixing and limitation of O_2 uptake by diffusion under static condition), the radical R4 (O) is not observed. (F) The same observation was made for a TA solution with 1 µl/ml 10 M NaOH and purged with nitrogen, indicating that R4 and R3 are formed by reactions with oxygen.

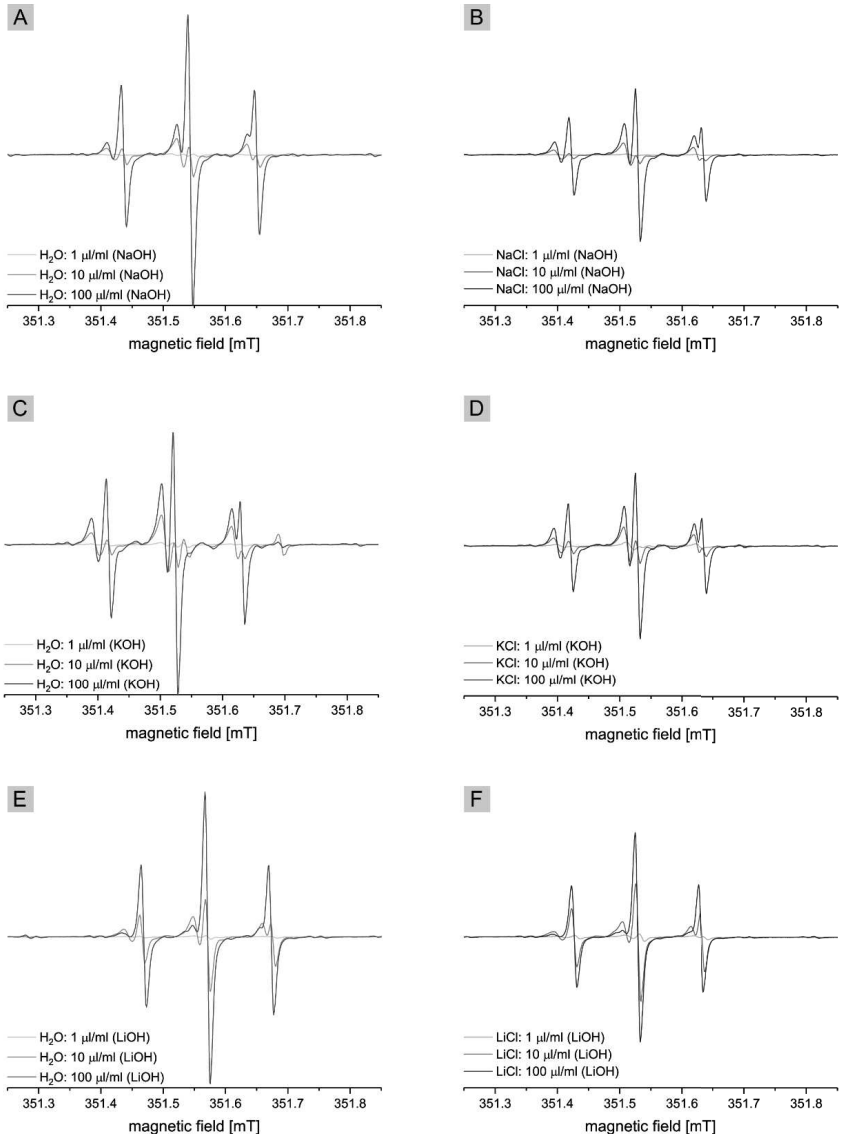

Figure S19: (A, C, E) EPR spectra of 1 mg/ml tannic acid dissolved in water or (B, D, F) 600 mM salt solution adjusted with given amounts of 10 M NaOH (A, B), KOH (C, D), LiOH (E, F). Increasing pH gave rise to an increased intensity of the sharp radical triplet (♦) compared to the broad triplet (◊). In general, at higher pH, the signal intensity of salt containing solutions was lower compared to the respective water based solution.

Table S3: Quantitative ratio of tannic acid radicals in solution with different pH, metal cation, and metal salt content. Additionally, the abnormal decrease in hyperfine coupling is given for Li^+ solutions.

	R1 (♦)			R2 (◊)		
µl/ml base	1	10	100	1	10	100
NaOH	41 %	30 %	71 %	59 %	70 %	29 %
NaOH + NaCl	0 %	16 %	57 %	100 %	84 %	43 %
KOH	35 %	22 %	42 %	65 %	78 %	58 %
KOH + KCl	12 %	22 %	54 %	88 %	78 %	46 %
LiOH	45 % 0.106 mT	41 % 0.105 mT	85 % 0.102 mT	55 % 0.110 mT	59 % 0.110 mT	15 % 0.109 mT
LiOH + LiCl	42 % 0.103 mT	55 % 0.103 mT	87 % 0.102 mT	58 % 0.109 mT	45 % 0.101 mT	15 % 0.108 mT

UV-vis absorption spectra

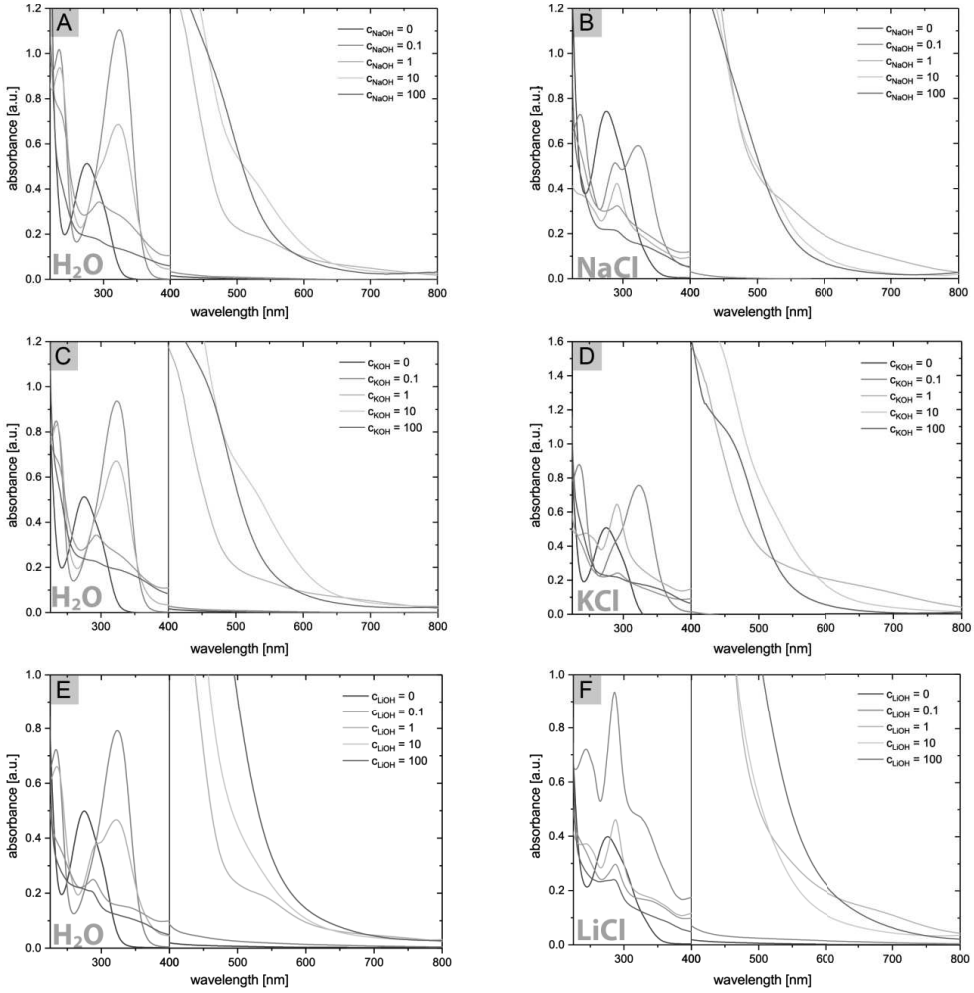

Figure S20: (A, B) UV-vis spectrophotometric assessment of the electronic configuration of TA in Na^+, (C, D) K^+, and (E, F) Li^+ containing solutions. The salt concentrations in panels B, D, and F were set to 600 mM. The pH was adjusted in given increments in µl/ml of 10 M of the respective alkaline solution (0.1 µl/ml ~ pH = 7; 1 µl/ml ~ pH = 11, 10 µl/ml ~ pH = 12, 100 µl/ml ~ pH = 13). Spectra were taken 1 h after preparation. Due to a high absorbance in the UV region, graphs display the spectrum of 1/100 diluted samples in the range of 220 – 400 nm. Upon pH-induced oxidation, all solutions turned from colorless via green to a red color. A high peak to valley difference between the two peaks at 234 nm and 324 nm further indicated a high galloyl content up to pH = 11 with no formation of intramolecular bonds.[10]

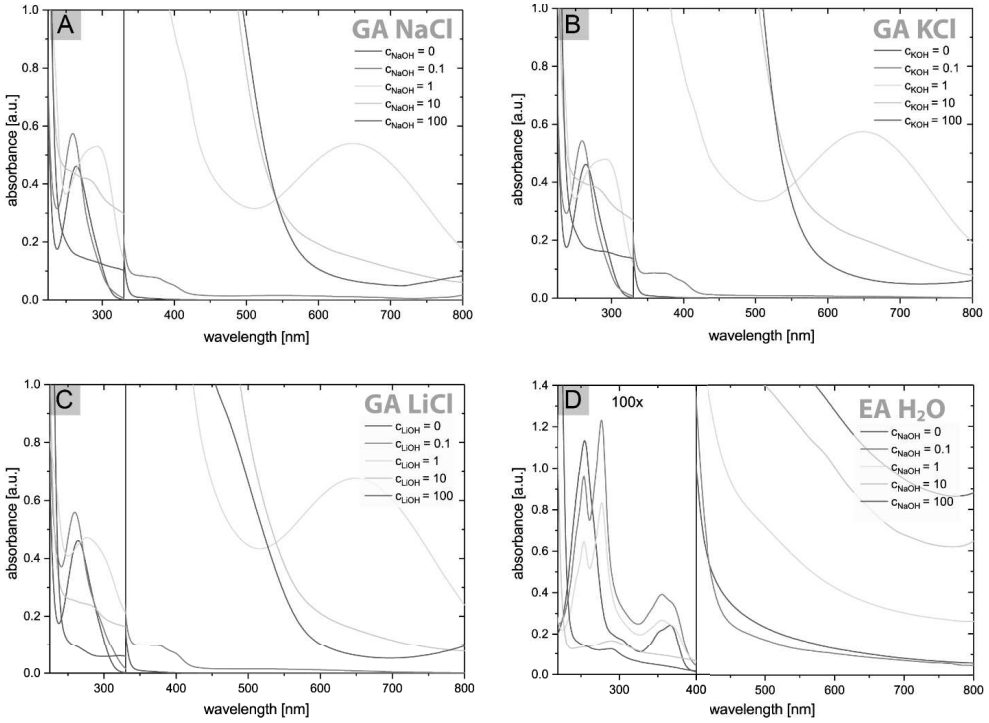

Figure S21: (A) UV-vis spectra of 1 mg/ml gallic acid (GA) in 600mM NaCl, (B) KCl, and (C) LiCl containing solutions. (D) Spectra of 1 mg/ml ellagic acid dissolved in water. The pH was adjusted in given increments in µl/ml of 10 M of the respective alkaline solution. Spectra were taken 1 h after preparation. Due to a high absorbance in the UV region, graphs display the spectrum of 1/100 diluted samples in the range of 220 – 400 nm. Pristine GA displays a single peak at 265 nm. Once the pH is slightly increased, this peak shifts to 260 nm and 290 nm. Subsequently, GA appears to react to EA indicated by the emerging second peak at 355 nm that corresponds to a similar peak position in EA (D).

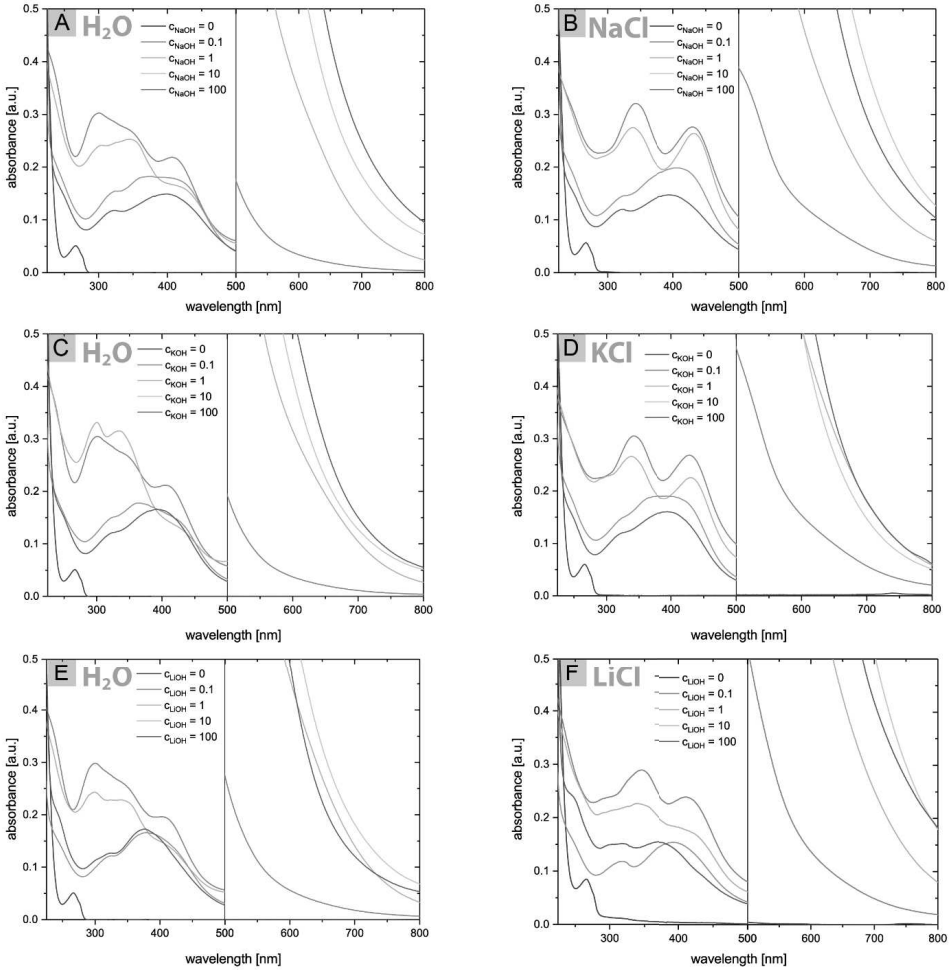

Figure S22: (A, B) UV-vis spectrophotometric assessment of the electronic configuration of PG in Na^+, (C, D) K^+, and (E, F) Li^+ containing solutions. The salt concentrations in panels B, D, and F were set to 600 mM. The pH was adjusted in given increments in µl/ml of 10 M of the respective alkaline solution (0.1 µl/ml ~ pH = 8; 1 µl/ml ~ pH = 11, 10 µl/ml ~ pH = 12, 100 µl/ml ~ pH = 13). Spectra were taken 1 h after preparation. Due to a high absorbance in the UV region, graphs display the spectrum of 1/100 diluted samples in the range of 220 – 500 nm.

FTIR absorption spectra

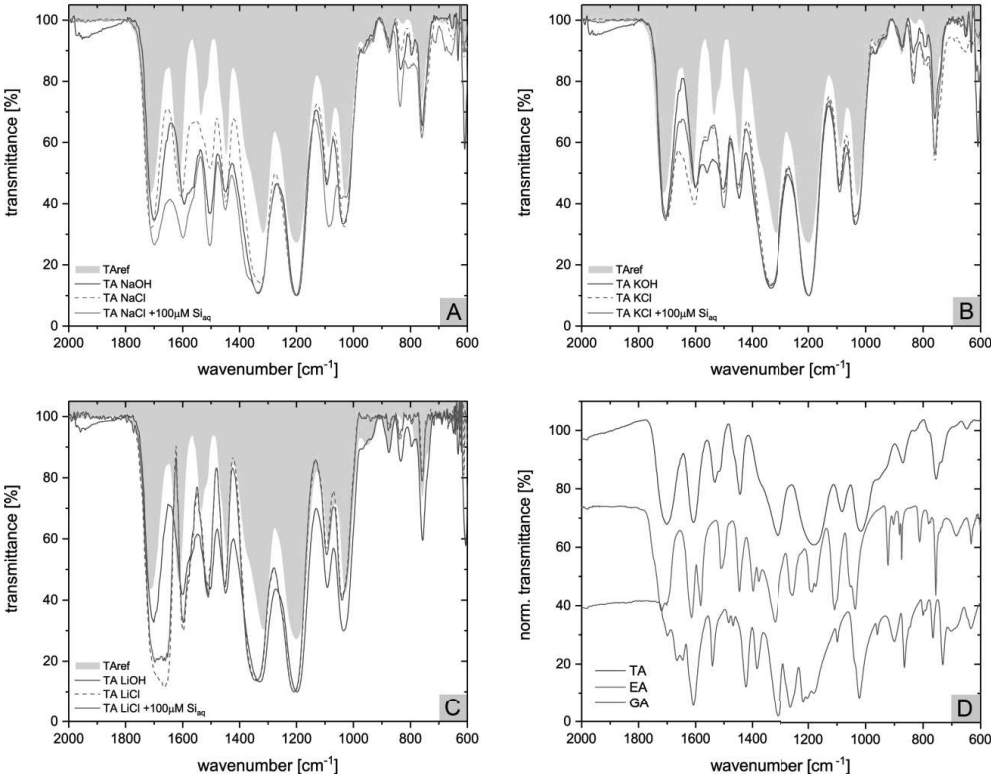

Figure S23: FTIR spectra of TA solutions dried on a diamond ATR crystal. (A) Na^+, (B) K^+, and (C) Li^+ containing solutions were adjusted to pH = 8 with 0.3 µl/ml 10 M NaOH, KOH, and LiOH, respectively. NaCl, KCl, and LiCl concentrations were set to 600 mM. LiCl solutions exhibited a peak at 1631 cm^{-1}, which was subtracted from TA solutions containing LiCl after normalization (Figure S2). (D) Spectra of tannic acid (TA), ellagic acid (EA), and gallic acid (GA) reference powders.

Table S4. Vibrational modes of tannic acid

Vibrational mode				assignment[c,11]
TA_{ref}[a]	TA NaCl[b]	TA KCl[b]	TA LiCl[b]	
1714	1689	1707	1689	ν C=O
1614	1598	1601	1598	ν aromatic C=C
1534	1504	1500	1510	ν aromatic C=C
1446	1448	1449	1451	ν aromatic C=C ν C–O β O–H
1373				β C–H
1316	1338	1338	1340	γ O–H γ aromatic C–H
1200	1200	1200	1209	β C–H ν C–O
1087	1087	1090	1094	γ C–H β –OH β aryl C–O
1029	1043	1038	1040	σ C–H
874	872	872	874	β aryl C–O γ C–H
	836	836	838	β C–H
758	760	759	759	β C–OH σ aromatic C=C

[a] dissolved in water
[b] dissolved in water containing 600 mM salt adjusted to pH = 11 with NaOH, KOH, or LiOH respectively
[c] ν-stretching, σ-out of plane bending, β-bending/deformation, γ-in plane bending

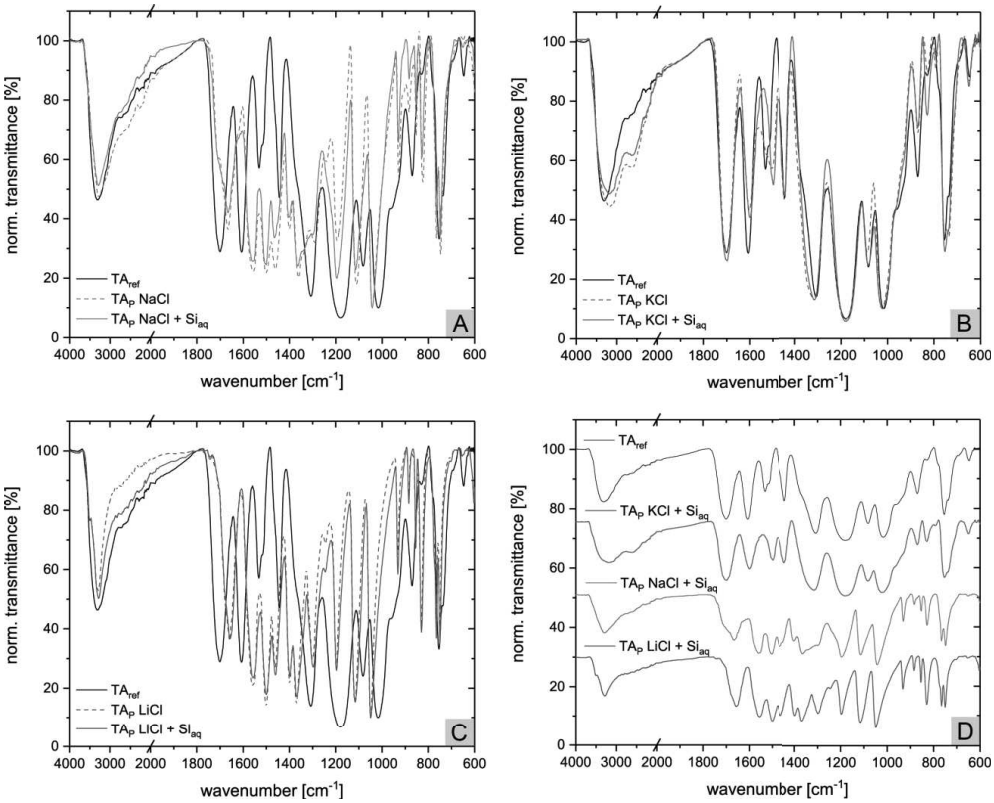

Figure S24: (A) Tannic acid polymerization products (TA_P) precipitated after oxidation in 100 mM HEPES at pH = 7.8, supplemented with 600 mM NaCl, (B) KCl, or (C) LiCl, and optionally 100 µM Si_{aq}. Particles, which sedimented after 24 h, were filtered off, washed with buffer, and dried at 60°C. TA_P collected from Na^+ and Li^+ systems showed typical oxidation. K^+, which showed strong precipitation captured TA in non-oxidized form. (D) A comparison between NaCl and LiCl shows some minor differences in the peak intensities in the range between 1400 cm^{-1} and 1250 cm^{-1}.

^{13}C and ^{29}Si NMR spectra

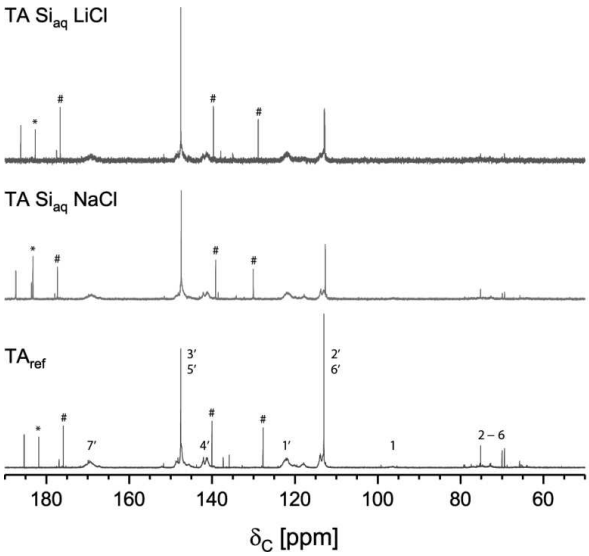

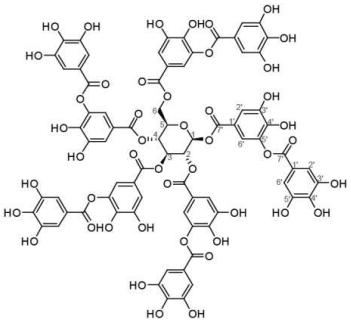

Figure S25: ^{13}C NMR spectrum recorded at 150 MHz of 100 mg/ml native TA and TA solutions adjusted with 600 mM salt and 8 mM $Si_{aq.}$ Peak shifts are given relative to TMSP (*). TA showed typical ester peaks at 169 ppm, phenolic carbons at 147 ppm, 141 ppm, 121 ppm, and 113 ppm, and alkyl carbons between 96 ppm and 65 ppm originating from the central glucose unit. Additional peaks marked with (#) may result from free gallic acid.[12] TA_{ref} was dissolved at 100 mg/ml in D_2O. TA was dissolved in LiCl and NaCl solution at 100 mg/ml in H_2O containing 10 v.% D_2O due to solubility issues in pure D_2O. Note that due to the long NMR run, we tried to keep the sample stable and did not raise the pH. Thus EA was likely not formed in these experiments.

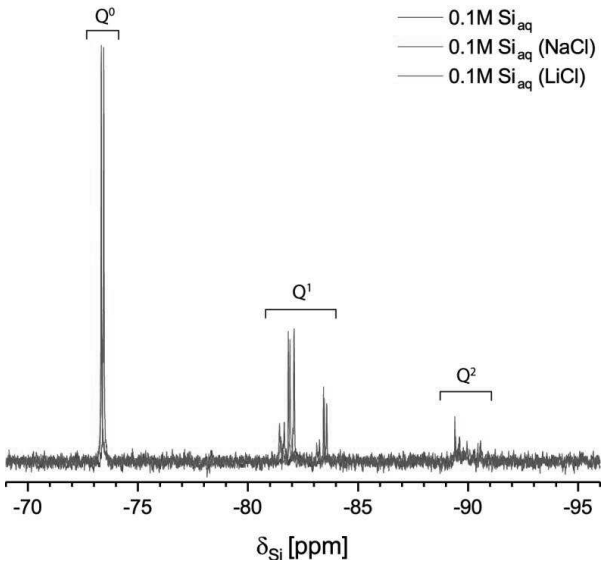

Figure S26: ^{29}Si NMR spectra of native 0.1 M Si_{aq} solution (H_2O containing 10 v.% D_2O) and 0.1 M Si_{aq} solution in the presence of 600 mM salt. Spectra were recorded at 150 MHz. Peaks at δ = -73.4 ppm, -81.6 ppm to -83.6 ppm, and -89.6 ppm were assigned to free silicic acid (Q^0) and its condensation products (Q^1, Q^2).

Silico-molybdic assay

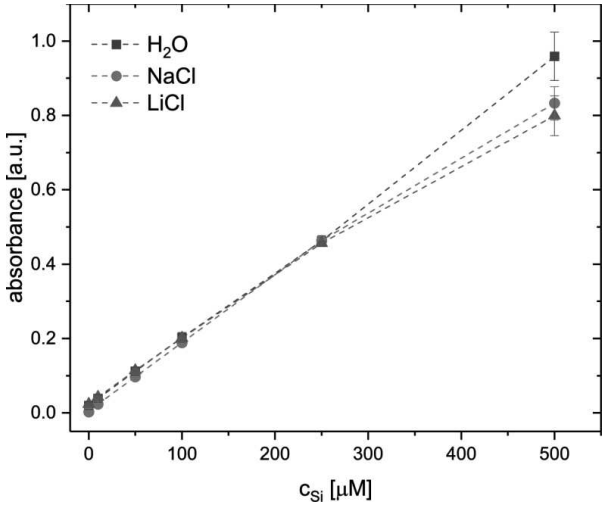

Figure S27: Quantification of the concentration of free silicic acid via the silico-molybdic assay. The concentration of Si_{aq} (c_{Si}) is directly proportional to the absorbance of the complex at $\lambda = 400$ nm. Si_{aq} was dissolved in water or 600 mM salt solution at pH = 3 according to the assay protocol.[13]

References

1. Duling, D. R., Simulation of Multiple Isotropic Spin-Trap EPR Spectra. *J Magn Reson Ser B* **1994,** *104* (2), 105-110.
2. Voinova, M. V.; Rodahl, M.; Jonson, M.; Kasemo, B., Viscoelastic acoustic response of layered polymer films at fluid-solid interfaces: continuum mechanics approach. *Phys Scr* **1999,** *59* (5), 391.
3. Dinnebier, R. E.; Pink, M.; Sieler, J.; Stephens, P. W., Novel Alkali-Metal Coordination in Phenoxides: Powder Diffraction Results on C6H5OM (M = Li, Na, K, Rb, Cs). *Inorg Chem* **1997,** *36* (16), 3398-3401.
4. Herbst-Gervasoni, C. J.; Gau, M. R.; Zdilla, M. J.; Valentine, A. M., Crystal structures of sodium-, lithium-, and ammonium 4,5-di-hydroxy-benzene-1,3-di-sulfonate (tiron) hydrates. *Acta Crystallogr E Crystallogr Commun* **2018,** *74* (Pt 7), 918-925.
5. Eslami, A. C.; Pasanphan, W.; Wagner, B. A.; Buettner, G. R., Free radicals produced by the oxidation of gallic acid: An electron paramagnetic resonance study. *Chem Cent J* **2010,** *4*, 15.
6. Oniki, T.; Takahama, U., Free radicals produced by the oxidation of gallic acid and catechin derivatives. *J Wood Sci* **2004,** *50* (6), 545-547.
7. Steenken, S.; Neta, P., Transient Phenoxyl Radicals: Formation and Properties in Aqueous Solutions. In *The Chemistry of Phenols*, Rappoport, Z., Ed. 2016.
8. Marković, Z.; Milenković, D.; Đorović, J.; Dimitrić Marković, J. M.; Lučić, B.; Amić, D., A DFT and PM6 study of free radical scavenging activity of ellagic acid. *Monatsh Chem* **2013,** *144* (6), 803-812.
9. Delavaran Shiraz, A.; Takdastan, A.; Borghei, S. M., Photo-Fenton like degradation of catechol using persulfate activated by UV and ferrous ions: Influencing operational parameters and feasibility studies. *J Mol Liq* **2018,** *249*, 463-469.
10. Salminen, J. P.; Karonen, M.; Sinkkonen, J., Chemical Ecology of Tannins: Recent Developments in Tannin Chemistry Reveal New Structures and Structure–Activity Patterns. *Chem Eur J* **2011,** *17* (10), 2806-2816.
11. Ricci, A.; Olejar, K. J.; Parpinello, G. P.; Kilmartin, P. A.; Versari, A., Application of Fourier Transform Infrared (FTIR) Spectroscopy in the Characterization of Tannins. *Appl Spectrosc Rev* **2015,** *50* (5), 407-442.
12. SDBS. https://sdbs.db.aist.go.jp/sdbs/cgi-bin/direct_frame_disp.cgi?sdbsno=806 (accessed 11. September, 2019).
13. Coradin, T.; Eglin, D.; Livage, J., The silicomolybdic acid spectrophotometric method and its application to silicate/biopolymer interaction studies. *J Spectrosc* **2004,** *18* (4), 567-576.